High-power broadband absorptive waveguide filters

Tinus Stander

Dissertation presented for the degree of Doctor of Philosophy
in Engineering at the University of Stellenbosch

Promoter: Prof. P. Meyer
December 2009

Declaration

By submitting this dissertation electronically, I declare that the entirety of the work contained therein is my own, original work, that I am the owner of the copyright thereof (unless to the extent explicitly otherwise stated) and that I have not previously in its entirety or in part submitted it for obtaining any qualification

Date: ________________________

Abstract

Keywords – Absorptive Filter, Waffle-Iron Filter, Transversal Broadwall Waveguide Slots, Harmonic Pad

This dissertation presents a synthesis method for broadband high-power absorptive microwave filters by cascading a wide stop-band waffle-iron filter with an absorptive harmonic pad.

The classical image impedance synthesis methods for waffle-iron filters are updated to allow for non-uniform boss patterns, which enable control over both the stop-band attenuation and pass-band reflection of the filter. By optimising an accurate circuit model equivalent, computationally intensive numerical EM optimisation are avoided. The non-uniform waffle-iron filter achieves the same electrical specification as similar filters in literature, but in a smaller form factor. The prototype presented displays less than -21 dB in-band reflection over 8.5 - 10.5 GHz, with stop-band attenuation in excess of 50 dB over the harmonic bands 17 - 31.5 GHz and 30 dB over the 34 - 42 GHz. The prototype is designed to handling 4 kW peak power incident in the transmitted band, and is 130 mm in length. Minimal full-wave tuning is required post-synthesis, and good agreement is found between synthesised and measured responses. Additionally, a completely novel oblique waffle-iron boss pattern is proposed.

For the absorptive harmonic pad, transversal broadwall slots in rectangular waveguide, coupling to an absorptive auxiliary guide, are investigated in the presence of standing wave surface current distributions. An accurate circuit model description of the cascaded structure is developed, and optimised to provide a required level of input match in the presence of an arbitrary reflective filter. Using numerical port parameter data of the waffle-iron filter, a harmonic pad is developed that provides -12.5 dB input reflection match across the band 17 - 21 GHz with up to 1 kW peak incident power handling capability, yet is only 33 mm in length. Again, good agreement is found between synthesised and measured responses of the cascaded structure.

Opsomming

Sleutelwoorde – Absorberende Filter, Wafelyster filter, Transversale Breëwand Golfleiergleuwe, Harmoniekdemper

Hierdie proefskrif stel 'n sintesetegniek voor vir wyeband, hoëdrywing absorberende mikrogolffilters deur 'n kaskade kombinasie van 'n verlieslose wafelysterfilter met 'n wye stopband, en 'n absorberende harmoniekdemper.

Die klassieke sintesemetodes vir wafelyster filters word aangepas om nie-uniforme tandpatrone toe te laat, wat beheer oor beide die filter se stopband attenuasie en deurlaatband weerkaatsing moontlik maak. Deur die optimering van 'n akkurate stroombaanmodel van die filter kan berekeningsintensiewe numeriese EM optimering vermy word. Die nie-uniforme wafelysterfilter behaal dieselfde spesifikasies as soortgelyke gepubliseerde filters, maar is meer kompak. Die vervaardigingsprototipe handhaaf minder as -21 dB intreeweerkaatsing oor die deurlaatband van 8.5 - 10.5 GHz, asook attenuasie van meer as 50 dB oor die stopband 17 - 31.5 GHz en 30 dB oor 34 - 42 GHz. Die prototipe is ontwerp om 4 kW intree kruindrywing te hanteer in die deurlaatband, en is 130 mm lank. Die metode vereis minimale verstellings tydens volgolf simulasie, en die meetresultate stem goed ooreen met die gesintetiseerde gedrag. 'n Nuwe skuinstandpatroon word ook voorgestel vir wafelyster filters.

Vir die harmoniekdemper word transversale breëwandgleuwe in reghoekige golfleier wat koppel na 'n absorberende newegolfleier ondersoek in die teenwoordigheid van staandegolfpatrone in oppervlakstroom. 'n Akkurate stroombaanmodel van 'n gleufkaskade word ontwikkel, en geoptimeer om 'n vereiste intreeweerkaatsing te bewerkstellig in samewerking met 'n arbitrêre weerkaatsende filter. Deur gebruik te maak van poortparameterdata van die wafelysterfilter word 'n 33 mm lange hamoniekdemper ontwikkel wat 'n maksimum intreeweerkaatsing van -12.5 dB oor die band 17 - 21 GHz handhaaf vir kruindrywingsvlakke van tot 1 kW. Goeie ooreenstemming tussen gesintetiseerde en gemete resultate word weereens waargeneem vir die volledige saamgestelde struktuur.

Acknowledgments

The work presented in this dissertation could not have been completed without the dedicated support and encouragement of my promoter, Prof. Petrie Meyer. His knowledge and guidance in technical matters is only matched by his interest in his students' welfare and personal development. Prof. P.W. van der Walt and Dr Werner Steyn from Reutech Radar Systems also provided invaluable inputs throughout the development process, for which I am grateful. I also wish to thank Prof. Heinz Chaloupka at the Bergische Universität Wuppertal, and Prof. Ian Hunter at the University of Leeds, who were kind enough to host me in their respective research groups. The project relied heavily on simulation software and academic licenses graciously provided by Computer Simulation Technology GmbH and Applied Wave Research, Inc. I am also indebted to Wessel Croukamp and Theuns Dirkse van Schalkwyk for the manufacturing of both prototypes. Drs Andrew Guyette and Douglas Jachowski of the US Naval Research Laboratory deserve special mention for providing insights and reading material on absorptive filtering.

My parents spared themselves no cost or inconvenience to support me throughout my academic career, and this document is a testament to their prayers, dedication and support. I am also grateful to my friends and my cell group, who were always ready with cuppa or a pint when I could spare the time, and a kind word of support when I couldn't. My office mates in E206 over the years (Dirk, Parick, André, Shaun, Madelé, Evan, Sunel and Karla) were always helpful in technical matters when things were serious, and up for a discussion or a laugh (or some Nama Rouge) when things were not-so-serious. The same goes for my colleagues and friends in Wuppertal and Leeds (who helped me adapt to life abroad) and my friends on the PhD Phorums (for constantly reminding me that I'm not alone). Finally, I wish to thank Mia for carrying me through the last year's ups and downs. Whether by delivering a home-cooked meal at the office, sending a million postcards to the UK, or simply listening and praying, she was always there. *Dankie, skat.*

This project was supported financially by the National Research Foundation and Reutech Radar Systems (Pty) Ltd.

Dit is die Here wat die wysheid gee,
uit Sy mond kom die kennis en die insig.

– Spreuke 2:6

Contents

List of Tables

List of Figures

Chapter 1

Introduction

Microwave filters are an integral part of any microwave system, whether in radar, satellite communications or any number of other applications. Generally, filtering is achieved by passive near-lossless filters, which maintain band selectivity by reflecting out-of-band energy from the input port back to the source device or network. These filters feature close to 0 dB reflection across all frequencies except the transmission band, as shown in Fig. 1.1 as S_{11A}, with a negligible proportion of untransmitted energy absorbed by dissipation.

An absorptive filter, in contrast, attenuates out-of-band energy by absorbing it inside the filter, rather than reflecting it back to the source. The device effects near-lossless transmission with out-of-band reflection far below 0 dB, as shown in Fig. 1.1 as S_{11B}. The reduction in reflection may be across all frequencies, or isolated to specific required absorption bands, as shown in Fig. 1.1 as S_{11C}.

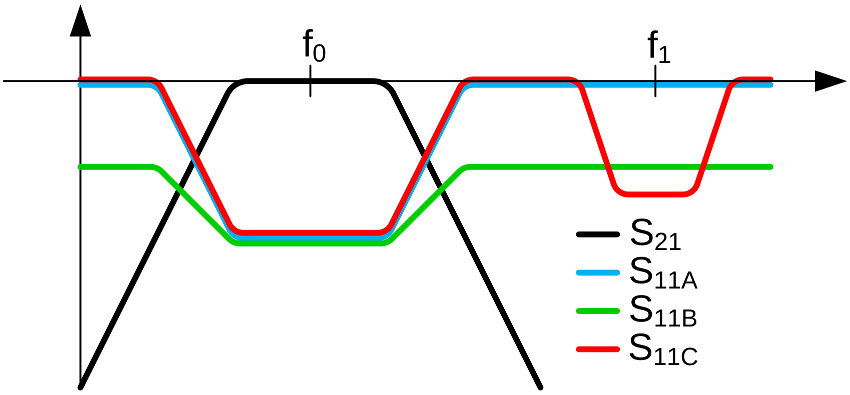

Figure 1.1: Example transmission and reflection responses of lossless and absorptive band-pass filters.

Absorptive filters are used when reflected out-of-band can have significant adverse effects on the source device or network.

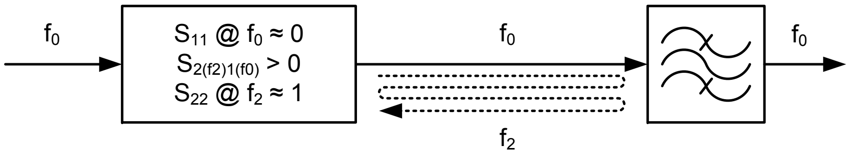

(a) General application.

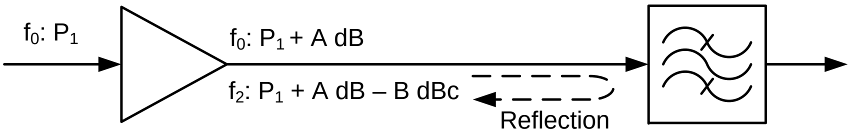

(b) Application with amplifiers.

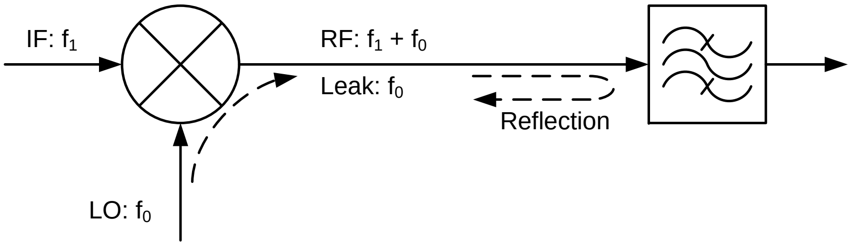

(c) Application with mixers.

Figure 1.2: Common applications of absorptive filters.

Consider, for instance, the cascade of a filter and an arbitrary network or device in Fig. 1.2(a). The device is matched for an incident signal at f_0, performing some function on it before re-transmitting it to the rest of the network. If the device creates a spurious signal at f_2, it has to be isolated from the rest of the subsequent network by a cascaded filter. The filter rejects the incident f_2 by reflecting it back to the source device.

If, additionally, the device features a poor output reflection match at f_2, the spurious signal is reflected, again, back to the filter, where it is again rejected and reflected to the source. Eventually, a resonance at f_2 is formed on the line connecting the device and the spurious rejection filter. Depending on power levels and the nature of the device, this could either inhibit the proper operation of the device, or in extreme cases, lead to component damage.

If the magnitude of the reflection at the filter (for f_2) is reduced to below 0 dB, the reflected signal is effectively attenuated, and the magnitude of the standing wave pattern at f_2 is reduced to levels that do not inhibit the operation of the device.

A typical example of such an arrangement is shown in Fig. 1.2(b). When RF amplifiers are driven into saturation, as usually is the case with power amplifiers in pulsed and CW radar transmitters, they generate harmonic products at integer multiples of the transmit signal frequency. These harmonics may not be radiated by the antenna. If the harmonic components are suppressed with reflective filters, they are reflected back to the amplifier where they can affect the voltage and current waveforms. This can lead to reduced output power or a ripple in the frequency response of the transmitter. A high-power broadband absorptive filter is clearly preferred for this application.

Another application, with lower power handling requirements, is the cascade of a mixer and a filter in Fig. 1.2(c). The filter is placed to prevent the leaked LO signal from the mixer to propagate to the rest of the system. However, the magnitude of the reflected leakage signal may, for some applications, be sufficient to severely degrade the mixer's performance. The conventional approach would be to place an attenuator between the mixer and the filter. This would attenuate the reflected leakage incident at the mixer's output, but would also attenuate the signal. If the reflective filter is replaced by an absorptive filter, the magnitude of this reflection can be reduced to an acceptable level.

1.1 State of the art

Numerous examples of absorptive filters, or other structures with some absorptive filtering properties, exist in literature. For high-power broadband applications, the most common solution is the *leaky wall* filter. These filters attenuate an incident travelling wave in waveguide by coupling energy to an exterior structure through a series of appropriate apertures, usually narrow slots [1]. The exterior structure may either be longitudinal auxiliary waveguides placed in parallel to the main guide [2, 3] or individual waveguides for each aperture [1, 4, 5, 6]. In both cases, the transmission band cut-off is determined by the cut-off frequency of the auxiliary waveguides, above which the energy is coupled to the auxiliary guides and dissipated inside the guides' absorptive loads. Typical commercial X-band filters achieve -40 dB S_{21} and -7.5 dB S_{11} over a stop-band that covers three harmonics [7]. Moreover, they can operate at 500 W CW and 5 kW peak, but are bulky devices of around 300 mm in length. Additionally, very little control over the shape of the transmission band reflection response is possible. A more complete discussion of leaky wall filters is presented in §2.4.

Another common approach to absorptive filtering is cascading a high-power non-reciprocal or four-port device with a reflective filtering structure, such as circulators [8] or -3 dB / 90° quadrature hybrids in both planar [9, 10] and waveguide implementations [11, 12]. The incident signal is coupled, through the device, to a network that features an input reflection match at some frequencies, but full reflection at others. At reflection frequencies, the reflected signal is directed to a third port as the filter's output, whereas at matched frequencies, the network absorbs an incident signal, and no energy is reflected to the output port. In all cases, the input and output ports remain isolated, and an input reflection match is achieved across all frequencies. These solutions are limited by the power handling capabilities and bandwidths of the coupling devices, as discussed in §2.6.

Absorptive filtering can also be achieved by dual phase path cancellation [13, 14, 15], with one path being a low-Q notch filter, and the other a lossy band-pass filter. At most frequencies, the low-Q notch filter allows for lossless transmission, and the lossy band-pass filter does not affect the signal's propagation. However, at a chosen frequency, the signal attenuated by the notch filter is recombined out-of-phase with a signal of equal magnitude transmitted (with significant dissipative attenuation) by the band-pass filter. This cancellation results in a high-Q notch, matched at all frequencies. Though inherently simple, the solution only provides absorptive filtering over very narrow bandwidths, as discussed in §2.5.

Some digital spectrum shaping filters [16, 17, 18] and gain slope equalisers [19] have also been demonstrated to exhibit absorptive filtering properties. Though synthesisable solutions, they generally feature transmission responses unfavourable from a strictly harmonic rejection perspective (slow roll-off, pass-band rounding), and have only been implemented for low-power planar applications with lumped-element dissipative components. They are discussed further in §2.10 and §2.12.

A number of other structures with frequency selective absorption properties have been proposed, but not developed into synthesised absorptive filters. Lossy dielectric resonators in waveguide [20, 21] (§2.7), planar etched rings with lumped element resistors placed in waveguide [22, 23] (§2.8) and quarter-wavelength chokes in stainless steel circular waveguide [24] (§2.9) all exhibit resonance absorption: the absorption of the energy incident on the structure at its resonant frequency (by dielectric heating, dissipation in surface mount resistors, or dissipation by the finite conductivity of the waveguide material, respectively), whilst not affecting transmission at other frequencies. Due to the limited power handling capability of the surface mount resistors used in etched rings, they are unsuitable for high-power applications. The lossy dielectric resonators require exact synthesis of material properties ($\tan\delta$ and ϵ_r), and the stainless steel chokes (though capable of operation at very high power levels) require wide-band transitions from circular waveguide to rectangular waveguide.

Additionally, no general cascaded insertion loss synthesis theory exists by which to synthesise filters based on these components, even though all three can be represented by simple lossy resonator circuit models. The theories available for lossless [25, 26, 27] and predistorted [28] filters are not applicable to absorptive filter synthesis, as shown in §2.2. The best attempts at finding such a theory are discussed in §2.3, and rely on even-odd reflection synthesis of symmetrical absorptive networks [29, 30], Baum cycles [31, 32] or non-series-parallel realisations [33, 34].

If absorption is restricted to specific bands, as illustrated by S_{11C} in Fig. 1.1, a particular solution is of interest. A *harmonic pad*, as discussed in §2.11 [35, 36, 37, 38, 39], is effectively any device that features frequency selective absorption in a specific band and lossless transmission elsewhere. If such a device is cascaded with a broadband reflective filter, signals in the transmission band of the reflective filter are passed with very little attenuation, while signals in the stop-band are redirected and absorbed by the harmonic pad. In this way, the input match of a specific harmonic band may be improved without affecting the transmitted band. This solution has been proposed [1, 35, 39], but no implementations have been published.

Implementations of harmonic pads using 0 dB couplers over the signal bandwidth have been published [37, 36], but these limit the filter transmission bandwidth to that achievable by the coupler. The use of leaky wall filters as harmonic pads is suggested [35, 37], but has not been developed in literature to date.

For a reflective filter in such an application, a very wide stop-band is required. Coupled resonator waveguide filters are high-power devices suitable to be used as reflective filters in conjunction with a harmonic pad, but their stop-band capabilities are limited by spurious transmission spikes at multiples of the centre frequency [26]. Corrugated waveguide filters [26, 40] and waffle-iron filters [41, 42, 43] (discussed in Chapter 3) have spurious-free stop-bands over multiple harmonics, but waffle-iron filters have the added advantage of maintaining identical stop-band responses for all incident waveguide modes, which make these filters the recommended [38] choice for such an application. However, the classical synthesis theories for waffle-iron filters [25, 44] are fairly limited, and rely on uniform boss dimensions and spacing which does not allow direct control over the in-band reflection response. Recent publications [45, 46, 47] have synthesised waffle-iron filters with non-uniform boss patterns, but rely on computationally intensive mode matching (MM) or finite element method (FEM) optimisation of the filter dimensions.

1.2 Proposed solution outline

This dissertation develops a high-power broadband absorptive filter by cascading a harmonic pad and a lossless filter with a wide reflective stop-band in WR-90 waveguide. A compact slotted waveguide structure is used as a harmonic pad, designed to efficiently absorb the standing wave created by a specific reflective filter at its stop-band frequencies, without affecting the in-band transmission or reflection response of the filter. A non-uniform waffle-iron filter is implemented as reflective filter, with the synthesis method improved to allow for greater control over the transmission band reflection response without the need for full-wave optimisation.

To guide the design process, the specifications as set out in Table 1.1 will serve as development goals. Additionally, the design is required to operate at 8 kW peak and 500 W average power levels over the transmission band at an altitude of 3000 m, with -15 dBc power handling capability required for the second filter harmonic.

Table 1.1: Target specifications for absorptive filter development.

		S_{11} [dB]	S_{21} [dB]
8.5 - 10.5	GHz	< -25	> -1
17 - 21	GHz	< -15	< -65
25.5 - 31.5	GHz	< -10	< -60
34 - 42	GHz	–	< -55

1.3 Original contributions

This dissertation will demonstrate the following original contributions:

- An accurate circuit model based synthesis method for non-uniform waffle-iron filters is presented, allowing control over both the filter's stop-band attenuation and in-band reflection response. This method relies on optimisation of a circuit model, instead of the computationally intensive full-wave optimisation.
- A general design algorithm for developing a compact harmonic pad designed for a specific reflective filter, is developed. This method, which also relies on computationally inexpensive circuit model optimisation, is used in conjunction with an accurate simplified circuit model representation of transversal broadwall waveguide slots to develop an harmonic pad capable of high-power broadband absorption.
- A cascaded combination of a harmonic pad and a waffle-iron filter to form an absorptive filter with excellent stop-band attenuation and absorption, is presented. This structure is significantly more compact than the commercially available absorptive filters.
- In addition to the contributions mentioned previously, the dissertation also proposes a completely new class of ultra-compact waffle-iron filters with oblique boss patterns. Methods to increase the spurious-free operating bandwidth of transversal broadwall slots are also demonstrated.

1.4 Dissertation layout

Chapter 2 provides an extensive review of the published literature on absorptive filtering solutions, highlighting the need for a novel approach. Chapter 3 presents the circuit model based synthesis algorithm for non-uniform and oblique waffle-iron filters, as well as measured results of a manufactured prototype. Chapter 4 investigates the use of transversal broadwall slots and auxiliary absorptive waveguides to synthesise harmonic pads, and also presents a manufactured prototype. Finally, Chapter 5 concludes the dissertation with an evaluation of both synthesis methods, and recommendations for future development.

Chapter 2

Literature review

2.1 Introduction

This chapter examines the state of the art of absorptive filtering, reviewing different approaches and evaluating each approach's ability to address the problem stated in the previous chapter. A quick review of classical lossless microwave filter theory is also included, to state clearly its applicability to the stated problem. The chapter concludes with a general summary of the shortcomings of current solutions, and highlights the need for a novel approach.

2.2 Synthesis of lossless and dissipative filters

The general synthesis of lossless microwave filters by insertion loss methods is the subject of an extensive body of literature [25, 26, 27]. The classical synthesis of two-port networks by insertion loss methods was first proposed by Sydney Darlington [33], and has since replaced image impedance synthesis [25] as the mainstay of filter synthesis techniques. In short, Darlington proved that any positive real function can be synthesised as an input impedance function (known as a Foster reactance function [48]) of a lossless passive reciprocal two-port network, terminated in a load resistor. This lossless network may be decomposed into sections of first- or second-order sections, each of which produce a single transmission zero at infinity or zero frequency ("A" and "B"-sections), a finite real frequency zero ("C"-sections) or complex transmission zeros ("D"-sections). These sections are comprised of linear reactive components: inductors, capacitors and transformers.

A key step in the insertion loss synthesis approach is the calculation of an input impedance

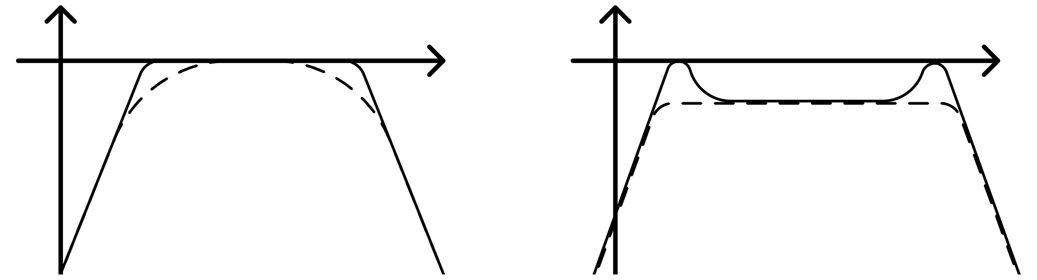

(a) Ideal lossless synthesised filter (–), and response with lossy components (– –).

(b) Predistorted lossless synthesised filter (–), and response with lossy components (– –).

Figure 2.1: Transmission response of filters with lossy components, with and without predistorted synthesis.

function from a synthesised transmission approximation function. In lossless synthesis, this is done by using the Feldtkeller equation

$$|S_{11}|^2 + |S_{21}|^2 = 1 \tag{2.1}$$

to establish a unique relationship between the transmission and reflection response of a lossless network. If, however, energy is to be dissipated (neither transmitted, nor reflected), the previous identity is invalidated. This means that the synthesis of a prescribed input impedance no longer guarantees a specified transmission response.

In addition to this effect on the synthesis approach, finite dissipation has important practical implications as well. Not only does it increase the in-band insertion loss, but it also makes the transmission response over the band uneven by increasing the roll-off at the band edges, creating “round” transmission shoulders, as shown in Fig. 2.1(a). From a synthesis perspective, this corresponds to a shift of transfer poles toward $-\sigma$ on the complex plane.

An approach frequently taken in this case is to design a filter to have a prescribed level of in-band transmission loss (effected by the finite dissipation of the filter components), but with a flat transmission band. This technique is called predistortion [26, 28] and involves synthesising a lossless filter with its transfer poles shifted a distance $+\sigma_p$ on the complex plane, a value determined by the uniform finite Q of the resonators or reactive components used. This has the effect of creating a lossless transmission response with transmission peaks (0 dB) at the band edges (shown in Fig. 2.1(b)) which, in the presence of finite dissipation, creates a flat transmission band.

Though synthesised finite dissipation is an eventual effect of predistortion, the synthesis itself remains that of a lossless network. Even if lossy theoretical resonators were to be considered, the bulk of the dissipation still occurs in-band (rather than out-of-band, as is required of an absorptive filter). An independent synthesis of absorption response, as required with an absorptive filter, is still not possible.

2.3 General synthesis theory of absorptive filters

A variation of the predistortion technique involves synthesis of filters with non-uniform resonator Q, where the loss is distributed throughout the network [28, 29]. By making the distribution of loss through the network the function of a synthesis process (unlike predistortion, where all resonators are assumed to have equal Q) the synthesis of filters with frequency selective absorption becomes possible.

The unique relationship between transmission and reflection in a lossless filter, which is ordinarily lost in the presence of dissipation, can be regained if the filter is constrained to be symmetric. In this case, even and odd mode admittances Y_e and Y_o can be defined, where Y_e is the input admittance at either port for even excitation, and Y_o that for odd excitation of the two ports. These are related to the network's transmission and reflection parameters by

$$\begin{aligned} S_{21} &= \frac{Y_e - Y_0}{(1+Y_e)(1+Y_o)} \\ S_{11} &= \frac{1 - Y_e Y_0}{(1+Y_e)(1+Y_o)} \end{aligned} \tag{2.2}$$

Even and odd reflection coefficients can now be defined as

$$\begin{aligned} S_{11} + S_{21} &= \frac{(1+Y_o)(1-Y_e)}{(1+Y_e)(1+Y_o)} \\ &= \frac{1-Y_e}{1+Y_e} \\ &= S_e \end{aligned} \tag{2.3}$$

$$\begin{aligned} S_{11} - S_{21} &= \frac{(1+Y_e)(1-Y_o)}{(1+Y_e)(1+Y_o)} \\ &= \frac{1-Y_o}{1+Y_o} \\ &= S_e \end{aligned} \tag{2.4}$$

where S_e is the even mode reflection coefficient, and S_o the odd mode reflection coefficient. Note that the definition of S_e requires the cancellation of an $(1 + Y_o)$ factor, and that of S_o requires the cancellation of $(1 + Y_e)$. This is only possible if all system poles are assigned either to S_e or to S_o. It is because of these constraints of symmetrical networks that a unique relationship between S_{11} and S_{21} is established, even in the presence of dissipation.

The method has, as yet, only been implemented to synthesise input reflection functions with 0 dB reflection at infinite frequencies ([29, 49, 30, 50, 51, 52], among others). There is, however, no inherent restriction in the method that requires this choice. In principle, it could be adapted to synthesise an absorptive filter with infinite frequency reflection less than 0 dB, or even filters with less out-of-band reflection than in-band insertion loss (if some in-band dissipation is permitted).

Unfortunately, though the method produces an positive real input impedance, the required component extractions tend to be either non-real or negative values, or require asymmetric pole placements, ruling out the use standard Darlington sections. The use of Baum cycles [31, 32] or Bott-Duffin [33] and other non-series-parallel realisations [34] have proven more effective than simple cascade synthesis, but significant efforts have, as yet, not produced an implementable circuit model for an absorptive filter using this method. A single, general theory of absorptive filtering remains elusive.

2.4 Leaky wall filters

Leaky wall filters are one of the oldest known solutions for achieving attenuation by absorption, rather than reflection. A large and well-established body of literature exists on the solution type. In its simplest form, a leaky wall filter comprises simply of a cascade of slots in rectangular [2] or coaxial [3] waveguide, which couple to a single auxiliary waveguide with absorptive end-loads, as shown in Fig. 2.2(a). These apertures, though having a minimal effect at transmission frequencies, “leak” a travelling wave into the auxiliary guiding structure at frequencies above the auxiliary guide cut-off. Since this auxiliary structure contains some absorptive material, the signal is not transmitted at the auxiliary guide ports, but dissipated in the guide. The filter’s level of attenuation and reflection is determined by the number and spacing of the coupling apertures, whilst the filter’s transmission band edge is determined solely by the cut-off frequency of the auxiliary guide f_c. Greater control may be achieved by sectioning the auxiliary guide into distinct absorptive resonating cavities, allowing each aperture to terminate into its own auxiliary waveguide cavity at the expense of decreasing the absorptive bandwidth of each slot [1]. Performance may be enhanced further by bending the leaky wall main guide into a spiral [38], though this increases the manufacturing complexity.

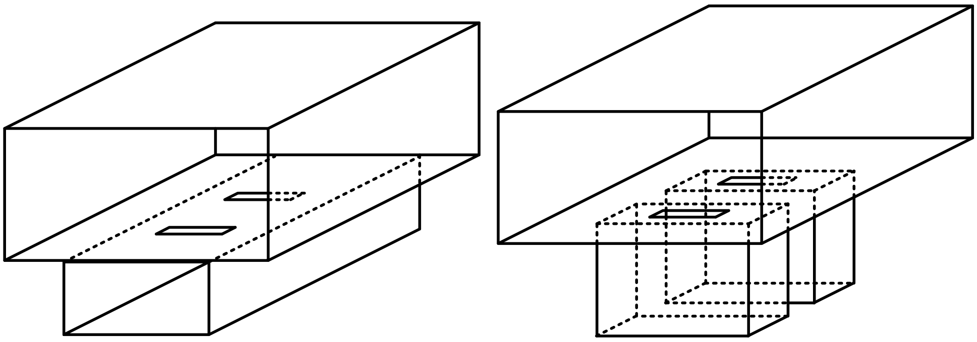

(a) Single auxiliary guide. (b) Multiple auxiliary guides.

Figure 2.2: Leaky wall filter configurations for two slots.

A more advanced design is achieved by allowing each aperture to couple into its own auxiliary waveguide, terminated by an absorptive load, as shown in Fig. 2.2(b). Since these waveguides are much longer than the previously noted sectioned cavities in leaky wall filters, they support a coupled waveguide travelling wave mode, and not a single cavity resonance mode. These waveguides may be rectangular [4, 1], elliptic [5] or round [6], and the coupling is determined by the size and shape of the aperture. The transmission band edge of the filter is determined by the cut-off frequency f_c of the auxiliary waveguides, which is above the highest required transmission frequency. These filters are inherently low-pass, with the lower operating frequency determined by the cut-off wavelength of the main guide.

With the notable exception of the study in [4] (where an approximate uniform structure is analysed to determine the attenuation constant), there is no published synthesis procedure for leaky wall filters that involves more than choosing auxiliary waveguides with a suitable f_c and selecting the minimum number of sections to achieve the required attenuation.

The single auxiliary guide structures described in [2, 1, 53] typically achieve better than 0.3 dB insertion loss and an input reflection coefficient of below -20 dB across the transmission band, with around 30 dB insertion loss and less than -14 dB reflection at moderately high frequencies. The performance may be enhanced by lengthening the filter and adding more cascaded apertures.

Far superior performance is achieved with individual auxiliary guided structures [5, 6], with in-band transmission loss of less than 0.1 dB and input reflection of below -25 dB across the transmission band, whilst absorbing second, third and fourth harmonics with more than 30 dB insertion loss and around -15 dB input reflection.

Current commercial filters [7] include filters that achieve -20 dB input reflection and 0.5

dB insertion loss across the X-band band, maintaining -40 dB S_{21} and -7.5 dB S_{11} over the 16.4 - 37.2 GHz stop-band. This specific filter can operate at 500 W CW and 5 kW peak, and is 300 mm in length.

Leaky wall filters are inherent low-pass, high-power filters, but allow for very little insertion loss control over the transmission band. Since an average coupling value for a transversal slot is only -10 dB [3], typical examples require 50 - 200 coupling apertures to achieve 40 dB insertion loss, and the more advanced designs require an individually machined auxiliary waveguide for each aperture. Though the reward for the complex manufacturing is very broad-band absorption, a simpler solution might provide the required absorption of specific harmonic bands.

2.5 Dual phase path cancellation

Dual phase path cancellation, though an intuitively simple arrangement, has received little interest before the advent of the 21^{th} century, where it has been fueled by interest in compact, frequency-agile filter solutions. Two independent bodies of literature exist on dual phase path cancellers. The first, an example of which can be found in [13], considers two parallel network blocks, as shown in Fig. 2.3(a). If total resonance absorption at a single frequency is assumed, a unique definition of T_2 exists for any given T_1. If T_1 is now assumed to be a lossy transmission line of length $\lambda/4$, it is found that T_2 takes the form of a cascade of lossy resonators, as shown in Fig. 2.3(b). By combining the two, T_2 acts as a phase inverter, recombining the signals out-of-phase. This creates a transmission null by absorbing the energy in the lossy structures, thus keeping the input reflection coefficient low. In this case, two coupled resonators (in the T_2 path) are required to absorb a single frequency.

A second approach is proposed in [14], where the model is presented as the out-of-phase combination of a low-Q notch filter, and a band-pass filter with high insertion loss, as shown in Fig. 2.3(c). The resulting response is a high-Q notch matched at all frequencies. This theory is later adapted for frequency-agile cascaded [15] and biquad [54] resonators, as well as a single dual-mode [10] resonator. Here, the required absorption is achieved by the losses associated with the substrate the filter is etched on, without the need for explicitly including absorptive material in the filter.

The current implementations of this technique are all on planar media around S and C band (1 - 2 and 2 - 4 GHz) and display input reflection coefficients at all frequencies of

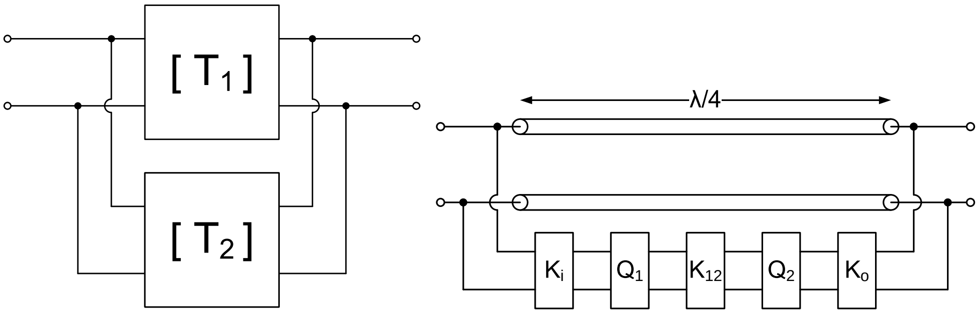

(a) Osipenkov's two arbitrary network blocks.

(b) The resulting Osipenkov synthesis.

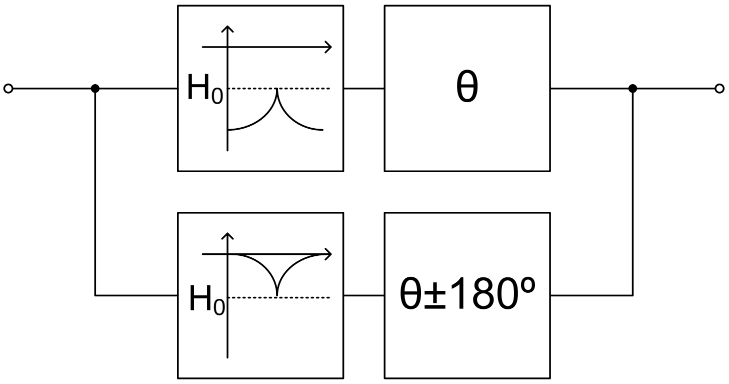

(c) Jachowski's approach.

Figure 2.3: Dual phase-path cancellation approaches.

-10 dB or better, with most (like [15] and later work) featuring -20 dB or better input reflection at resonance. The magnitude of the insertion loss of the transmission nulls vary from 35 dB in [10] to an impressive 120 dB in [13].

The only attempt at wider bandwidths is made in [54], where the concept is demonstrated for a fourth-order network with 0.5% bandwidth.

This class of solution is features an exact analytical synthesis method and maintains adequate input match over all frequencies. It is, however, inherently restricted to notch and narrow-band implementations.

2.6 Directional reflection mode filters

The first examples of directional reflection mode filters precede even leaky wall filters, but recent interest into this topology has been driven by research into frequency-agile applications in planar media. Two distinct solution types may be categorised as directional reflection mode filters. The first [8] uses a circulator as non-reciprocal device, as shown in Fig. 2.4(a). The filter's input is connected to port 1, some lossy network connected to 2, and the output to 3. Incoming signals at transmission frequencies are reflected off the network at 2 and directed to 3, whilst out-of-band signals are absorbed by the network at 2. The reflection response of the network at 2 is then, effectively, the transmission response of the filter, whilst port 1 is matched at all frequencies (provided that port 3 is terminated in a matched load). This approach is limited by the bandwidth and finite isolation of practical circulators.

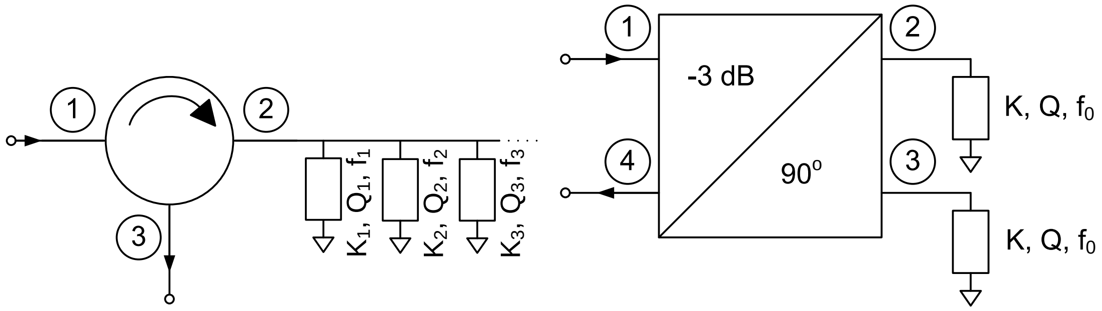

(a) Using a circulator.

(b) Using a -3 dB / 90° hybrid coupler.

Figure 2.4: Reflection mode filter topologies.

Another approach involves replacing the circulator with a -3 dB / 90° hybrid coupler, as shown in Fig. 2.4(b). Ports 1 and 4 are, respectively, the input and output of the filter, whilst 2 and 3 are connected to two lossy resonators with identical coupling K, quality factor Q and centre frequency f_0. At $f \neq f_0$, ports 2 and 3 are effective open circuits, and a signal incident from 1 experiences full reflection at both ports. These reflected signals then recombine in-phase at port 4, but 180° out-of-phase at port 1, allowing for transmission. At f_0, the resonators act like matched loads, and no signal is reflected back to either port 1 or port 4. In both cases, port 4 remains isolated from port 1, and the filter remains matched at all frequencies.

Early implementations used high-power waveguide quadrature hybrids with high cut-off waveguides and resistive end-loads [12] or lossy dielectric resonating cavities [11] acting as loads, whilst later publications use lumped element [9, 10] and Schottky diode [51] resonators as loads. Again, the bandwidth of the 90° hybrid becomes the determining factor in this class of filters.

The earliest waveguide implementations [12] achieved 500 MHz bandwidth at 9.3 GHz, with -19 dB in-band and -14 dB out-of-band reflection coefficient. The earliest planar implementations [9] were matched notch filters, with more than 30 dB insertion loss at 1.5 GHz whilst maintaining better than -15 dB match from DC to 3 GHz. Variable absorption from -2 to -30 dB has also been demonstrated in [51]. Reflection mode filters could potentially operate as absorptive filters in high-power environments, but the bandwidth will always be limited by the bandwidth of the directional structure (circulator or quadrature hybrid).

2.7 Cascaded lossy dielectric resonators

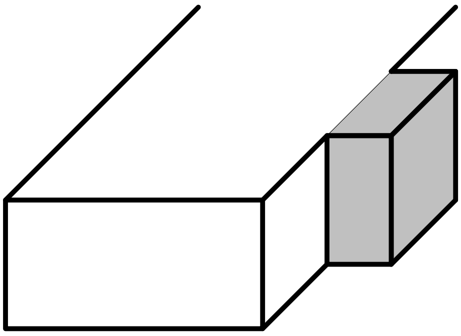

Figure 2.5: Lossy dielectric resonator stub.

Another approach to absorptive filtering is resonance absorption, achieved by cascading lossy dielectric resonators along rectangular waveguide. These may be placed in the main guide [20] or partially fill waveguide sidewall stubs [21], as shown in Fig. 2.5. By numerical optimisation of both the dimensions and electrical properties (relative permittivity ϵ_r and loss tangent $\tan\delta$) of these resonators, notch or band-stop filters may be synthesised that are matched at all frequencies.

Absorption of up to 50% per resonator has been documented, with a cascade of two resonators achieving up to -35 dB harmonic suppression. Another interesting application is alternate cascading of dielectrically loaded and empty cavities, which causes dissimilar input reflection coefficients at the two ports. At the resonant frequency of the two cavities, one port may exhibit full reflection, with the other port achieving a -20 dB input reflection match. A full filter synthesis would require either a full numerical optimisation of these dielectric resonators, or a general theory of absorptive filtering. In both cases, these solutions require exact synthesis of both the permittivity and loss tangent of the dielectric material. Also, applying this solution in a high-power environment could compromise the resonators due to dielectric heating.

2.8 Etched loaded rings in waveguide

Much like the previous technology, absorptive resonators can be constructed as shown in Fig. 2.6. A ring, or two rings, are etched on a substrate and placed in rectangular waveguide normal to the incident wave. These rings are then loaded with some lumped element. The original publication [55] uses SMD capacitors and inductors, but later papers implement absorptive rings with lumped element resistors [22] and varactor diodes [56], as well as a combination [57]. The cascadability was also demonstrated in [56], with further enhancements in the circuit model description and synthesis techniques of cascaded rings in [23]. The operation of this type of filter is based on the incident TE_{10} mode, which couples to the ring at the ring's resonant frequency, creating a circular current. As the current flows, energy is dissipated in the loaded lumped elements. The latest results reported by [57] indicate a typical input reflection of below -5 dB, with 30 dB insertion loss at resonance.

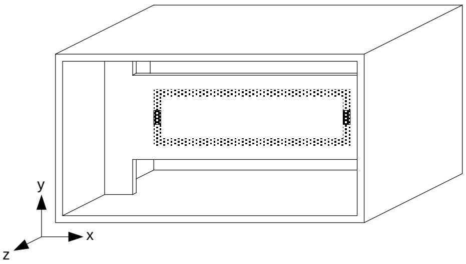

Figure 2.6: Etched ring in rectangular waveguide, loaded with surface mount resistors.

As with the previous technology, this structure is inherently a waveguide solution. However, the use of small surface-mount devices with limited power handling capability makes it unattractive for high-power applications.

2.9 Chokes in stainless steel circular waveguide

Absorptive resonators can also be constructed by placing chokes in circular stainless steel waveguide [24], shown in Fig. 2.7. At the frequency where the depth of the choke around the guide is approximately $\lambda/4$, the $\vec{H}$-field (and, consequently, surface current) concentrates in the choke. The relatively low conductivity of stainless steel causes dissipation at this frequency of increased surface current density. By cascading two chokes at a specific distance of separation (referred to as a matched pair), greater absorption is achieved than the sum total two individual chokes. Such matched pairs are shown to suppress an

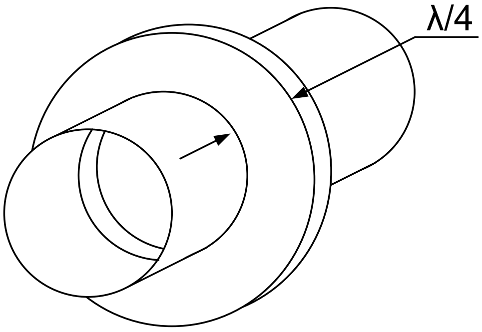

Figure 2.7: Single choke in circular waveguide.

harmonic at 11.4 GHz by as much as 20 dB (10 dB in a 2.5% bandwidth around 11.4 GHz) whilst maintaining a return loss of below -30 dB [24]. More remarkably, the filter can easily maintain operation at 22.5 kW CW.

This topology achieves resonance absorption, but the filter synthesis would again require a general synthesis theory or extensive numerical optimisation. What makes this solution particularly attractive, is the very high power handling capability, as well as the fact that no special absorptive material is required in construction. Circular waveguide is, however, required for its operation, and the transition from circular to rectangular waveguide provides a unique set of challenges (especially over the bandwidth required by the initial specification).

2.10 Digital spectrum shaping

A number of digital spectrum shaping filters have been shown to exhibit absorptive filtering properties.

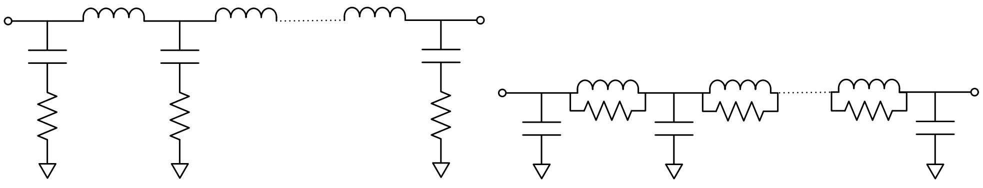
(a) Loaded capacitors. (b) Loaded inductors.

Figure 2.8: Digital spectrum shaping circuits with absorptive filtering properties.

In [16], a lumped-element LC filer implemented in microstrip and coplanar waveguide was adapted for optimal group delay by placing a lumped element resistor in series with each capacitor, as shown in Fig. 2.8(a). Not only did the group delay response improve, but the filter exhibited below 0 dB reflection at higher levels of insertion loss, which is the very definition of absorptive filtering.

Another publication, by Djordjević *et al* [17], aims to design a filter with quasi-Gaussian transmission response by examining different configurations of resistive loading in lumped element LC filters. Again, the result was the synthesis of an absorptive low-pass filter (Shown in Fig. 2.8(b)), later adapted to a band-pass topology [18].

Even simple designs, as shown in [16], can exhibit 20 dB insertion loss with below -15 dB input reflection coefficient at sufficiently high frequency. The absorption does however give the filter a slow roll-off, which makes it an unappealing solution from an attenuation perspective. Similar results where achieved in [17].

The results in [18] are somewhat unique since the principle of band-pass absorptive filtering is demonstrated without the need for multiple phase paths. The filter prototype features -15 dB match across all frequencies, with less than 2 dB insertion loss around 1 GHz. As before, the filter's response is marked by slow roll-off. Due to the planar medium of implementation, no power handling data has, as yet, been published.

The techniques published above may, in future, be adapted to synthesise generalised absorptive filters, since they demonstrate clear absorptive filtering properties.

2.11 Harmonic pads

An completely different approach to absorptive filtering is proposed by Leo Young in [35, 36, 37], with brief references elsewhere in literature [25, 38, 1, 39, 58]. The solution requires a *harmonic pad*, which is defined as any network device with near-lossless transmission in a band, and matched attenuation out-of-band, to be cascaded with a traditional reflection-mode filter, as shown in Fig. 2.9.

The purpose of the harmonic pad is to absorb **some** out-of-band energy (f_1 in Fig. 2.9) in both the transmitted and reflected directions. This distinguishes it from frequency-selective absorptive solutions, where the absorptive structure itself carries the full burden of stop-band attenuation. The cascaded pad serves only to improve the input match out-of-band, and may be designed for a specified input match level, as well as specific harmonic bands.

Shortened leaky wall filters have been proposed as possible implementations of harmonic pads [1, 35, 39] but no example of the development of leaky wall filters for the express

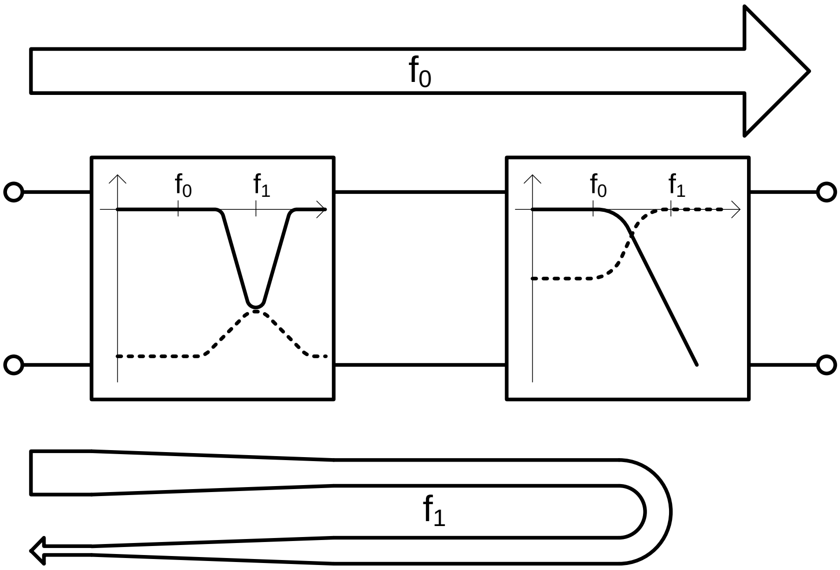

Figure 2.9: Layout and operation of harmonic pad (left), used in conjunction with reflective filter (right) to form an absorptive filter. Example parameters S_{21} (–) and S_{11} (– –) of both blocks are shown.

purpose of implementation as harmonic pads, has been published to date. The use of a helical transmission line filter (discussed in §2.12) is demonstrated in [58], but the design features greater than 2 dB insertion loss across the transmission band.

Young himself published two developments of harmonic pads both using 0 dB couplers. The first uses a branch-line coupler with reflective filters in its branches [36], to form an device that integrates filtering and harmonic pad functions. This design features below 0.3 dB insertion loss and below -19 dB input reflection coefficient over an 12% bandwidth around 1.3 GHz, with below -10 dB reflection from 2.3 to 7 GHz. The structure is, however, difficult to design and expensive to manufacture [37].

The second approach uses a cascade of two -3 dB Riblet short-slot couplers [37] to form a 0 dB coupler from the input port of the harmonic pad to the reflective filter, whilst terminating the coupler's other two ports in matched loads. This is done to avoid the need for coupling over the full stop-band of the filter, which is the main restriction in the use of -3 dB hybrids in reflection mode filters. Two devices were tested, one with broadwall coupling, the other with sidewall coupling. Both feature input reflection coefficients of below -32 dB and less than 0.13 dB insertion loss across a 7.2% transmission band around 2.8 GHz. The sidewall couplers suppress up to the fifth harmonic (up to 16.2 GHz) to below -7 dBc, whilst broadwall couplers achieve similar results, but only up to the third harmonic cut-off (10.8 GHz). Similar to the previously discussed -3 dB hybrids, limited transmission bandwidth is achievable with 0 dB couplers.

Without exception, *waffle-iron* filters are proposed as companion reflective filters, due to their very wide spurious-free stop-bands, compactness and multi-mode operating capability [38].

2.12 Other solutions

A number of other papers feature structures or designs with inherent absorptive filtering properties.

2.12.1 Gain equalisers

As with the digital spectrum shaping filters mentioned previously, gain equaliser circuits [19] (as shown in Fig. 2.10) have been shown to exhibit absorptive filtering characteristics. These models are synthesised with transmission line sections and lumped element resistors, and are cascadable. Again, no general synthesis theory is provided, and no high-power implementations exist.

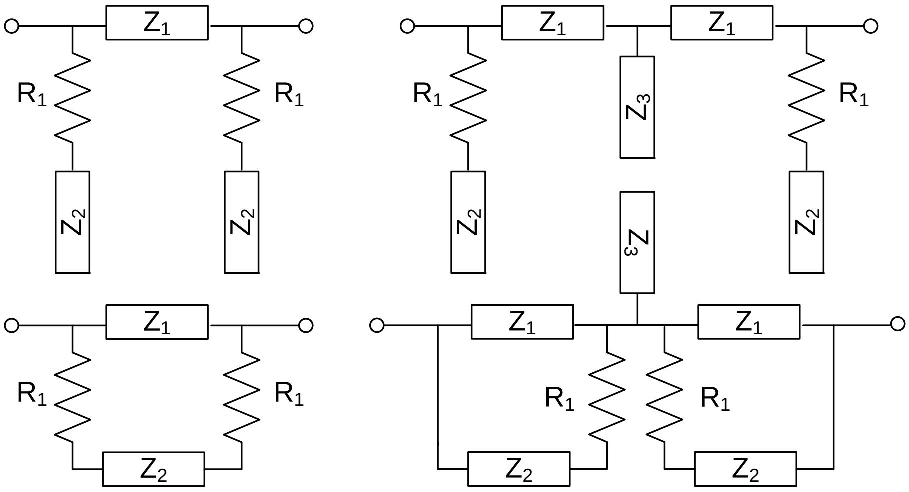

Figure 2.10: Four two-port gain equaliser circuits with absorptive filtering properties. All lines are one quarter wavelength at centre frequency.

2.12.2 Uniform line etched on absorptive material

An approach that requires no filter synthesis, is to use ferrites as substrates in planar transmission lines [59, 60]. Here, at frequencies where the ferrite is saturated, near-lossless transmission occurs, with absorption at higher frequencies. This is inherently a planar solution, and since filter cut-off frequency is determined by the material properties of the ferrite, the synthesisable transmission band is limited by the available ferrite materials.

2.12.3 Ferrite slab in waveguide

An alternative use of ferrites is the *field rotation filter* proposed in [61]. A flat sheet of magnetized ferrite is placed in the floor of a rectangular waveguide, creating a transmission notch which is perfectly matched at all frequencies. The notch frequency is adjusted by changing the magnetization of the ferrite. This is a true high-power waveguide solution, but the magnetization of ferrites is an undesirable manufacturing step, and the filter is inherently narrow-band.

2.12.4 Voltage controlled attenuator with frequency-selective FET's

By arranging FET transistors into a π-network [62], the inherent dissipative and frequency-selective properties of these components may be exploited to achieve frequency-selective absorption. This is, however, a weak filtering solution, with poor selectivity and dependence on the electrical properties of the packaging.

2.12.5 Helical transmission line filters

A helical transmission line filter resembles a coaxial line with a centre conductor bent into the shape of a tapered helix, and the outer conductor lined with absorptive material [58, 38]. The helix is an open periodic structure, which allows propagation along the helical centre conductor in an 8% bandwidth around a centre frequency, with all other frequencies radiated by the helix antenna into the surrounding absorptive material. Though capable of wide stop-bands and high power handling capability, the structure only achieves adequate input reflection match when connected by coaxial ports, and would require ultra-wideband transitions to operate in a waveguide system.

2.12.6 Non-directional narrow-band coupling

The last absorptive filtering solution proposed (somewhat similar to the use of 0 dB couplers in [37]) uses a narrow-band non-directional coupler to couple to an output port, as has been done with coupling to an antenna in [63]. The device consists of a narrow-band non-directional coupler, connected on one side to an input port and a matched load, and to an output port on the other side. Over a narrow transmission band, most of the energy incident on the coupler is directed to the output port, with very little dissipated in the matched load. Outside the coupling bandwidth, the incident signal passes through the one side of the coupler unaffected, and is dissipated in the matched load. In both cases, an input reflection match is maintained. This approach requires coupling $k > 0.9$, and would necessarily lead to a very narrow transmission band.

2.13 Conclusion

An extensive overview of theoretical and practical examples of absorptive filtering, has been provided. Of these, very few operate at high power levels in waveguide, and even fewer over significant bandwidths.

None of the planar devices (digital spectrum shaping filters, dual phase path cancellation devices, etched loaded rings in waveguide) are capable of maintaining operation at incident power levels up to 8 kW, and feature other disadvantages such as slow stop-band roll-off (in the case of digital spectrum shaping filters) and narrow bandwidth (dual phase path cancellers). Reflection mode filters, whether implemented using circulators or -3 dB / 90° hybrids, are limited by the operating bandwidth of the coupling device (as well as by finite isolation, in die case of circulators). Even though the operating bandwidth might cover the required pass-band of 8.5 - 10.5 GHz, it would require development of a special ultra-wideband device to maintain operation above 40 GHz. Lossy dielectric resonators require exact material property synthesis, and the operation of circular stainless steel chokes would be limited to the bandwidth of the transitions from circular to WR-90 waveguide required.

For high-power broadband applications, the leaky wall filter offers the best current solution for broadband high-power absorptive filtering. If, however, absorption alone is used for attenuation, the required device would be in excess of 300 mm in length. The same level of attenuation over the same multiple harmonic stop-band can be achieved by a significantly smaller, lighter and cheaper reflective filter [38]. The published implementations of 0 dB couplers as harmonic pads [37, 36] demonstrates the effectiveness of this approach, but this solution is limited by the achievable bandwidth of the 0 dB couplers. Leaky wall filters do not suffer this bandwidth restriction.

Employing a shortened leaky wall filter as a harmonic pad (as proposed, but not developed, in [35, 37, 1]) in cascade with a wide-band reflective filter, offers a number of advantages over using a leaky wall filter in isolation, or using couplers as harmonic pads.

- The burden of stop-band attenuation is transferred to the reflective filter, which means that the target specification for absorption is no longer -65 dB (the attenuation of the filter) but only -15 dB (the required input reflection match).
- The harmonic pad can be synthesised to target specific absorptive bands, unlike the unavoidable full-band absorption performed by the leaky wall filter in isolation or using 0 dB couplers in the transmitted band. This leads to a further reduction in size.
- A single aperture absorbs more energy from a standing wave (created by the stop-band reflection of the reflective filter) than it does from a travelling wave, further reducing the number of apertures required.
- By synthesising a custom harmonic pad for a specific reflective filter, phase interaction and specific local maxima in standing wave surface current can be exploited to further reduce the number of apertures required to achieve a prescribed level of absorption.
- The in-band signal is not required to couple through any (hybrid or 0 dB) coupling device, which means that the transmission bandwidth of the solution is not limited by any coupling bandwidth.

As suggested by [35, 25, 38, 36, 37, 39] and others, a waffle-iron filter offers the best option as broadband reflective filter. The synthesis of this type of filter is discussed in the next chapter.

Chapter 3

Non-uniform and oblique waffle-iron filters

3.1 Introduction

Waffle-iron low-pass filters were first invented by Seymour B. Cohn *et al* at the Stanford Research Institute in 1957 [41, 42, 43] and have since become a popular solution for harmonic suppression. This is due to the wide stop-band, typically covering up to the four times the cut-off frequency [64], which may be extended even further by cascading two or three waffle sections [65]. Another advantage is that all propagating $\mathrm{TE_{m0}}$ modes [1] have the same cut-off frequency [44], unlike the equally well known corrugated waveguide filters [40]. The classical structure, as shown in Fig. 3.1, consist of uniform multi-ridged rectangular waveguide, with equal width transverse grooves, forming rows and columns of rectangular bosses or pegs on the waveguide floor and ceiling. Later designs replace these square bosses with round pegs [66], which increased the power handling capability by 1.3 [65]. Since the spacing between opposing peg ends are typically less than full-height waveguide, the filter is matched using stepped or tapered E-plane sections.

The main drawback to these filters is that both classical synthesis methods, outlined in [25] as *Cohn's Corrugated Filter Data Design* and *T-Junction Equivalent Circuit of Marcuvitz Design*, only allow for the synthesis of a specified stop-band, with no direct control over pass-band response. The only reference made to pass-band match is that it is considered good practice choose the upper stop-band frequency $f_1 > 1.43 f_c$, the actual highest required transmission frequency.

Recognising the restrictions uniform bosses place on the response of the filter, a number of

---

[1] All non-$\mathrm{TE_{m0}}$ modes are reflected by the transition to the reduced height main guide.

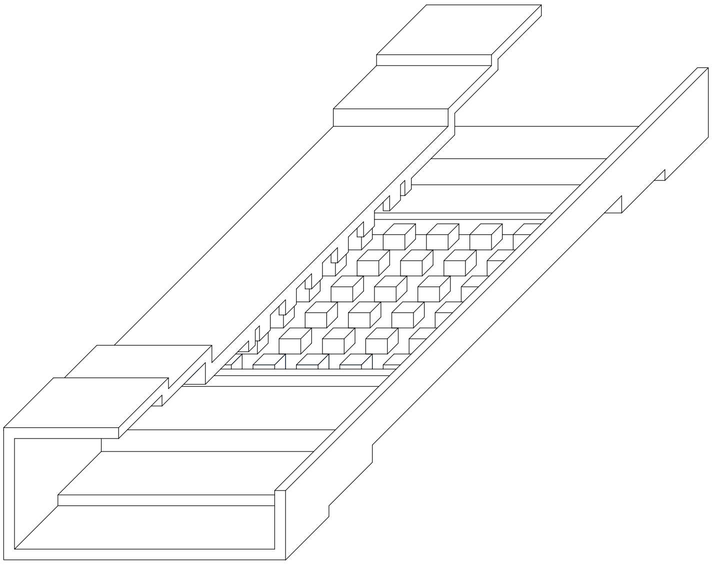

(a) Cut-away perspective view.

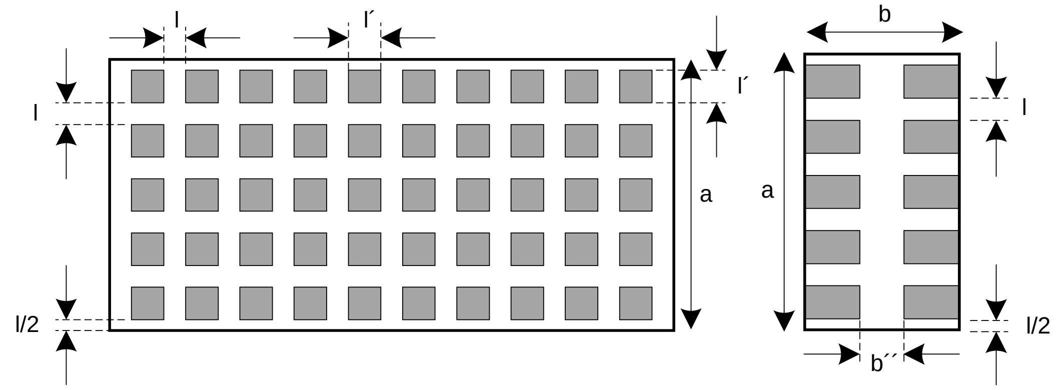

(b) Sectioned top view.

(c) Sectioned front view.

Figure 3.1: Classical uniform waffle-iron filter.

CAD solutions have been developed in recent years [45, 46, 47]. The waffle iron structure is modeled by a series of general scattering problems, or solved utilising hybrid mode matching (MM) / finite element method (FEM), which allows transversal grooves to be optimised for both adequate stop-band response, as well as equiripple transmission across a defined frequency band. Traditional synthesis methods are, however, used for initial values [47].

This chapter will revisit the circuit model based synthesis of [25], but apply it to the non-uniform waffle iron filters proposed by [45], [46] and [47]. Secondly, this circuit model based approach will be used to investigate waffle-iron filters with bosses rotated for oblique incidence to the dominant TE_{10} mode propagation, in that way synthesising a phase path along the TEM propagation directions.

3.2 Classical synthesis techniques

Two classic synthesis methods exist for waffle-iron filters. The first is based on Cohn's corrugated waveguide filter data, the other, Marcuvitz's models for waveguide stubs. Both rely on image impedance methods to match a specific periodic section below a cut-off frequency f_1, and pick an infinite attenuation frequency f_∞ below an upper stop-band frequency f_2, as shown in Fig. 3.2. Transmission occurs below f_c, and the stop-band between f_1 and f_2. No particular transmission or reflection is required between f_c and f_1, which makes this a so-called "buffer-band" between the transmitted and rejected bands.

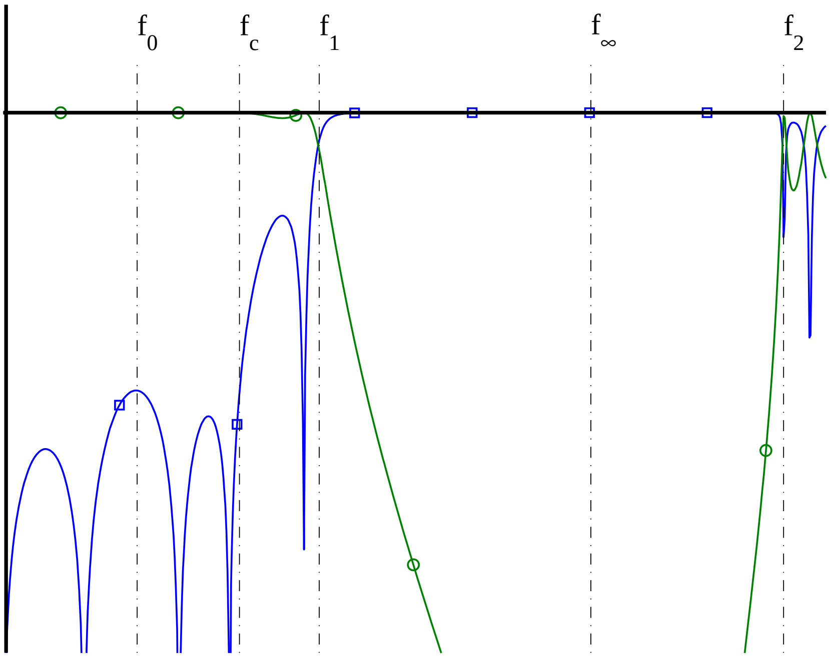

Figure 3.2: Definition of frequencies f_0, f_c, f_1, f_∞ and f_2 for waffle-iron filters.

A short description of each method is provided here.

3.2.1 Cohn's corrugated waveguide filter model synthesis

The first method, by Cohn [25], involves first designing a corrugated waveguide filter to render the required stop-band, replacing references to guide wavelength λ_{g0} by free-space wavelength λ_0. Once the transversal groove widths (forming the corrugations) are determined, identical longitudinal grooves are placed to achieve TEM filtering (the details of this step is discussed in §3.4.1), and b' (the spacing between two opposing solid ridges in a corrugated waveguide filter) is reduced to b'' to compensate for the decrease in shunt capacitance of the discontinuity. The image impedance calculations rely on the circuit model shown in Fig. 3.3, where the transmission lines of alternating impedance Z_1 and Z_2 represent the section of reduced height and full height (of b' and b) waveguide of lengths l and l', respectively. The shunt capacitance C_2 compensates for transition effects, and C_1 for capacitance between two adjacent corrugations.

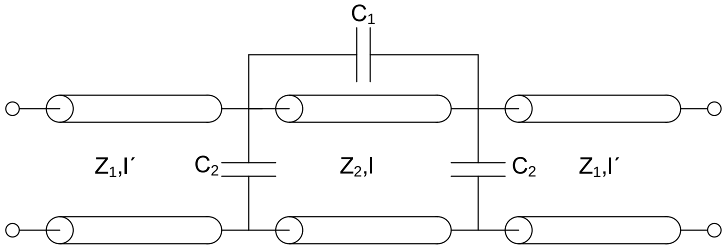

Figure 3.3: Cohn's corrugated waveguide filter model, single section.

The synthesis method does not involve the circuit model itself, but rather uses the design graphs published in [67], which provide dimensions for the required stop-band frequencies. The synthesis (based on equations and figures in [25]) proceeds as follows:

1. Choose the upper cut-off frequency f_c and upper stop-band frequency f_2.
2. Select frequencies f_1 and f_∞, based on the rules of thumb $f_1 > 1.43 f_c$ and $f_\infty \approx 0.8 f_2$.
3. Choose values for b' and l/b.
4. Use the selections in Step 3, as well as λ_1/λ_∞, to find b_0/λ_1 and b/λ_1 from Fig. 7.04-5. Subsequently, calculate b_0, b and l.
   (a) Iterate steps 2-4 until satisfactory values of b and l are found.
5. Use Fig. 7.04-6 to calculate parameter G, and Eq. 7.04-14 to find l'
   (a) Iterate steps 2-5 until a satisfactory value of l' is found.
6. Use Eq. 7.04-16 to calculate the b_T, the height of the main guide providing an optimal match to the waffle-iron filter, and Eq. 7.05-1 to calculate the boss spacing b''.
   (a) Iterate steps 2-6 until a satisfactory value of b'' is found.

From the trial-and-error nature of the synthesis, it is clear that it is a time-consuming approach which requires several iterations to find a design. Further more, it is only accurate for $l/b' > 1$ (i.e, shallow, wide transversal grooves), and grows increasingly inaccurate for smaller b'/b . This is due to the field distribution inside the transversal grooves becoming less like those of the full-height guide (Fig. 3.4) and more like those of short-circuited waveguide stubs. For cases of $l/b' \leq 1$ and arbitrary b'/b, designs based on Marcuvitz's waveguide T-junctions yield better results.

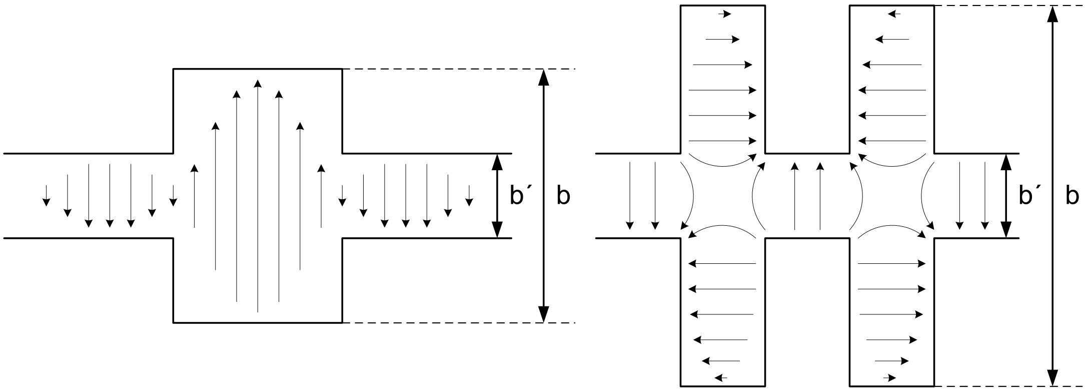

Figure 3.4: TE$_{10}$ $\vec{E}$-field distributions in waveguide height variations which support stepped-impedance (left) and short-circuited series stub (right) models, respectively.

3.2.2 Marcuvitz's waveguide T-junction model synthesis

As with the previous method, designs based on Marcuvitz's data synthesise filter dimensions in terms of free-space (rather than TE$_{10}$ waveguide mode) wavelength. The transversal grooves are not, however, modelled as sections of high impedance transmission lines, but rather lengths of short-circuited series waveguide stubs, also shown in Fig. 3.4. An electric wall is placed in the H-plane between the bosses, to simplify the analysis.

The circuit model used for these sections is shown in Fig. 3.5, as first published in the classical text by Nathan Marcuvitz [68]. It compensates for capacitive discontinuities in the E-plane (C_a), but also energy stored at the discontinuity planes (L_b, C_d) and inductive coupling to the groove (L_c). It is valid for stub widths and boss spacings of less than $\lambda/2$. Two electrical equivalents (using single reactances and reference plane shifts, respectively) are also published in [68]. For each of the three models, analytical equations are provided, as well as design graphs.

The design proceeds in much the same way as the previous method, with initial selections of the relevant frequencies and dimensions b', l' and l. Dimension b is chosen to ensure the stubs have an equivalent length (with consideration to the shifted reference plane) of

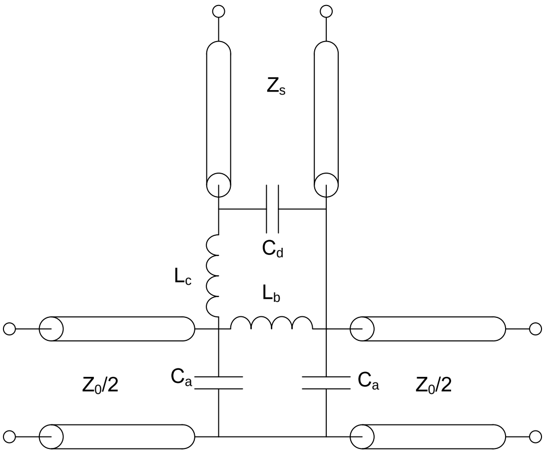

Figure 3.5: Marcuvitz's model for reactive compensation of waveguide discontinuities, as used in waffle-iron filter synthesis. The circuit makes use of electrical symmetry.

$\lambda_\infty/4$. Eq. 4 in [44] is then used to calculate f_1 and f_2. This process is iterated (with adjustments to b', l and l') until a satisfactory stop-band response is found. Finally, b'' is calculated using Eq. 7.05-1 in [25], and b_T (the terminating guide height) using Eq. 7.07-7.

3.2.3 Half-inductive and half-capacitive terminations

A lumped element equivalent of a stepped impedance filter model uses capacitors to represent sections of low impedance line, and inductors as an equivalent of high impedance lines [69]. If this equivalency is applied to waffle-iron filters, transversal rows of bosses (which correspond to sections of low impedance line, under Cohn's stepped impedance line model description) are referred to as capacitive sections, whereas sections of transversal grooves are referred to as inductive sections. Classical waffle-iron filter boss patterns are designed to terminate at either side with either half width ($l/2$) transversal grooves, or half width ($l'/2$) rows of bosses, as shown in Fig. 3.6. This is referred to as half-inductive and half-capacitive terminations, respectively. In terms of Marcuvitz's model, these correspond to terminations in either half-impedance stubs, or half lengths of main guide.

The differences in transmission and reflection response of the two filters are shown in Fig. 3.6(b). In each case, the filter is of 6th order with b_T, b'', l and l' all set to 1.875 mm and b to 9.375 mm. Both filters are of equal length and width $a = 22.5$ mm, with seven longitudinal grooves (the outer two of which are of width $l/2$). The half-inductive model has a total of 7 transversal grooves of which the first and last are of width $l/2$, and 6 rows of bosses of length l'. The half-capacitive model has 7 rows of bosses of which the first

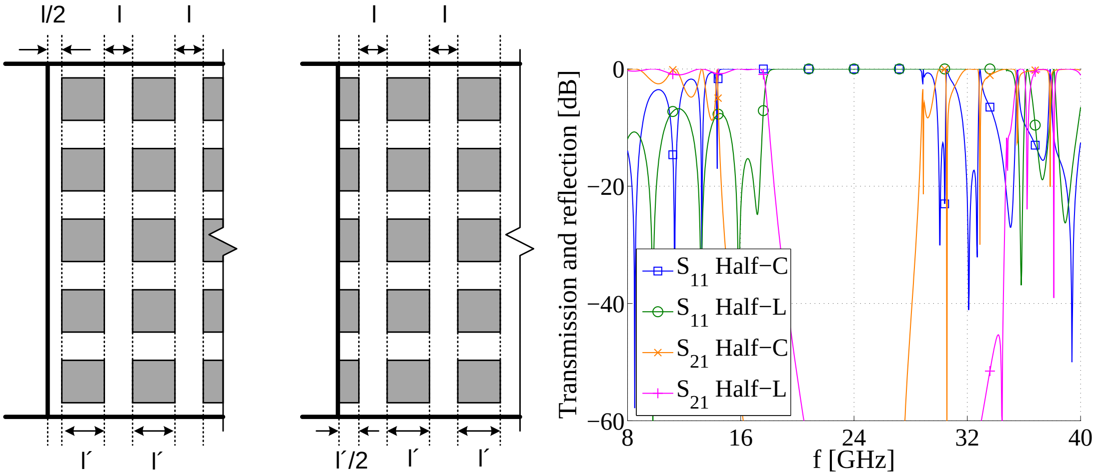

(a) Boss patterns with half-inductive (left) and half-capacitive (right) inputs.

(b) Comparative electrical responses.

Figure 3.6: Comparative responses of uniform filters with half-capacitive and half-inductive input sections.

and last are of width $l'/2$, and 6 transversal grooves of width l.

The half-inductive filter exhibits a bandwidth improvement of 23% both in transmission band (given the same waveguide lower cut-off frequency due to the identical main guide width a) and stop-band, as well as 5 dB lower in-band reflection response than the half-capacitive filter, in keeping with the findings of [66]. If the wider stop-band is not required, the half-capacitive filters have the advantage that, for equivalent dimensions (and therefore, power handling capability), the width of the buffer band is reduced. The increased input reflection can easily be corrected by adjusting the input waveguide height. A choice of half-inductive or half-capacitive inputs may therefore be made based on the filter specifications.

3.3 Non-uniform filters

A simple extension on the classical design methods is to allow for non-uniform boss length l' and transversal groove width l, as shown in Fig. 3.7. This would allow control over the transmission response, as well as better prediction of the stop-band without the time-consuming iterative designing. Until now, this has only been possible using full-wave optimisation [45, 46, 47], a time-consuming and computationally intensive process.

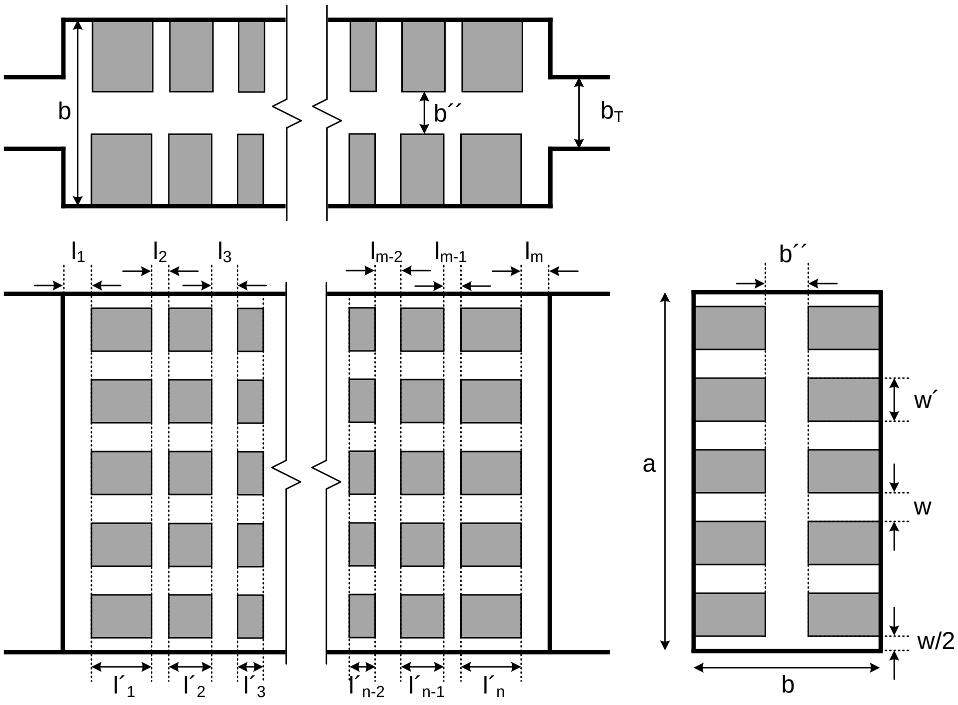

Figure 3.7: Non-uniform waffle-iron filter dimensions.

In this work, a new technique based on fast and simple circuit optimisation, is presented. This method relies on simple, yet accurate circuit models of non-uniform waffle-iron filters.

3.3.1 Circuit model

As a first step in the proposed technique, simple and accurate circuit model representations of non-uniform waffle-iron filters need to be identified. This is done by comparing S-parameters of various circuit model prototypes to the full-wave simulation results of a half-capacitive non-uniform filter. The dimensions of the full-wave model are used to construct equivalent circuit models based on different synthesis approaches; effectively, applying each synthesis process in reverse.

For the purpose of verifying the accuracy of a proposed circuit model, the choice of half-capacitive or half-inductive termination is arbitrary. This is because an accurate circuit model representation of a non-uniform boss pattern would be accurate for an arbitrary boss or groove width at either end of the filter, effectively negating the need for an explicit half-inductive or half-capacitive termination. For classical synthesis techniques, the half-inductive filter is clearly advantageous. However, in this case, the half-capacitive model is chosen simply for its lower f_2, requiring full-wave simulation at lower frequencies and, therefore, less simulation time.

The models described are the best ones found after extensive inquiries and experimentation on numerous non-uniform waffle-iron filters. For the sake of clarity, detailed descriptions of the alternative choices which yield poorer results (implementing or omitting reactive compensation, using λ_0 or λ_g, calculating impedances based on b' or b'') are omitted.

The dimensions of the full-wave model used to benchmark the circuit models, are based on uniform model dimensions in [25], with some random variations to boss lengths and transversal groove widths to create the non-uniform boss pattern.

In all cases, the circuit models are constructed and simulated in *AWR Microwave Office 8.02*, and compared to a full-wave simulation model in *CST Microwave Studio 2009.*

Cascaded stepped-impedance line model

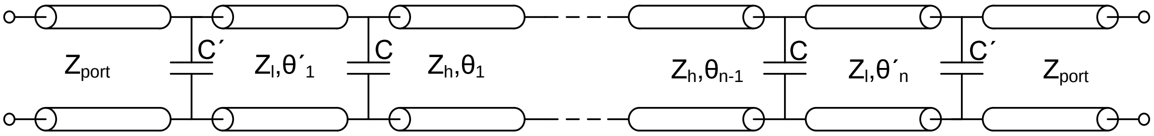

Figure 3.8: Stepped-impedance circuit model with incomplete reactive compensation.

The first circuit model approach evaluated is the stepped-impedance model shown in Fig. 3.8, with reactive compensation for steps in waveguide height as prescribed in Fig. 5.07-11 in [25]. The line impedance is approximated as directly proportional to waveguide height [25]. The terminating guide height b_T is used as the 1 Ω reference height, with all other impedances calculated as $Z_x = b_x/b_T$. The height b', calculated from Eq. 7.05-1 in [25], is used to calculate the low line impedance Z_l, and not the actual boss spacing b''. This is done to include the effect of the longitudinal grooves into the model. The main cavity height b is used to calculate the high impedance line Z_h. Lastly, the port impedance Z_0 is determined from the value b_0 calculated from Eq. 7.05-2 in [25]. The electrical line lengths of the ideal transmission lines in the circuit model are based on the lengths l and l' as fractions of TE_{10} wavelength λ_g at a transmission frequency of 10 GHz.

Except for the omission of the capacitors placed in parallel with the high impedance lines, this model is similar to the one used in Cohn's corrugated waveguide model (Fig. 3.3). The significant difference is that this model is based on TE_{10} longitudinal propagation, and not TEM propagation. All dimensions and circuit parameters are shown in Table 3.1, with the full-wave and circuit simulated results shown in Fig. 3.9.

Table 3.1: Stepped-impedance circuit model parameters derived from benchmark non-uniform filter dimensions. All dimensions refer to Fig. 3.7.

Full-wave	[mm]	Circuit	[Ω] / [°] / [F]
a	22.86	f_0	10 GHz
b	8	Z_h	2.67
b_T	3	Z_{port}	0.75
b''	2	Z_l	0.79
l_1	2.5	θ_1	22.63
l_2	2.2	θ_2	19.92
l_3	2.2	θ_3	19.92
l_4	2.5	θ_4	22.63
l'_1	1.2	θ'_1	10.87
l'_2	2.4	θ'_2	21.73
l'_3	2.2	θ'_3	19.92
l'_4	2.4	θ'_4	21.73
l'_5	1.2	θ'_5	10.87
w	2.286	C	8.488×10^{-12}
w'	2.286		

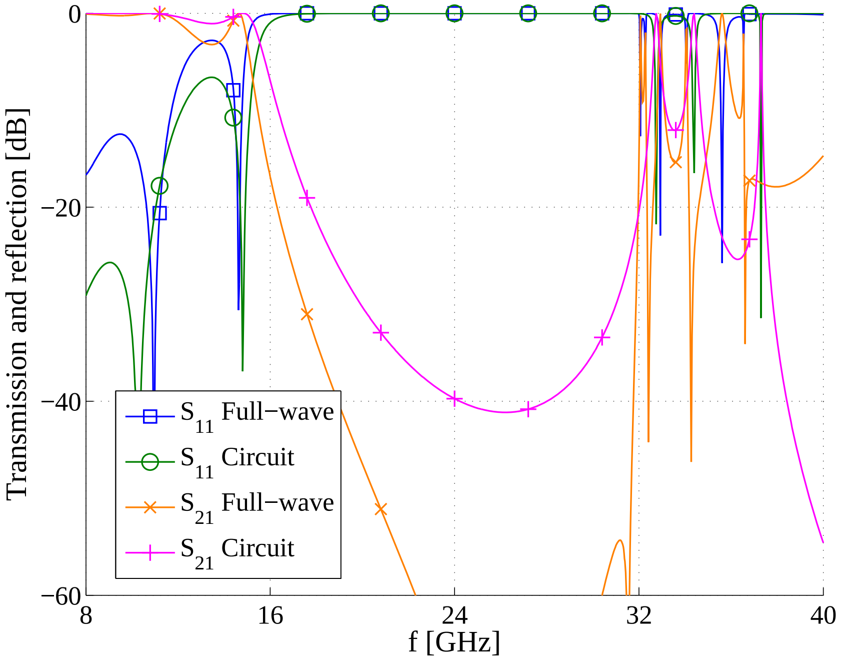

Figure 3.9: Evaluation of stepped-impedance circuit model for non-uniform filters.

The model predicts f_1 and f_2 to within 2%, and the maximum in-band reflection coefficient to within 5 dB. The accuracy of the placements of f_1 and f_2 confirms the validity of the choice in wavelength, opting for TE_{10} λ_g instead of TEM λ_0. However, it underpredicts the stop-band roll-off both at the upper and lower edge, as well as the maxiumum attenuation. The reason lies the field distributions in the transversal grooves, shown in Fig. 3.10.

The electric field on the symmetric E-plane of the filter is shown at a transmission frequency of 10 GHz (Fig. 3.10(a)) and a stop-band frequency of 26 GHz (Fig. 3.10(b)). For a stepped-impedance line, the expectation is a y-directed $\vec{E}$-field (where y is directed in the height of the main guide, and x over the width) over the full height of the transversal groove, as shown in Fig. 3.4. This is not the case.

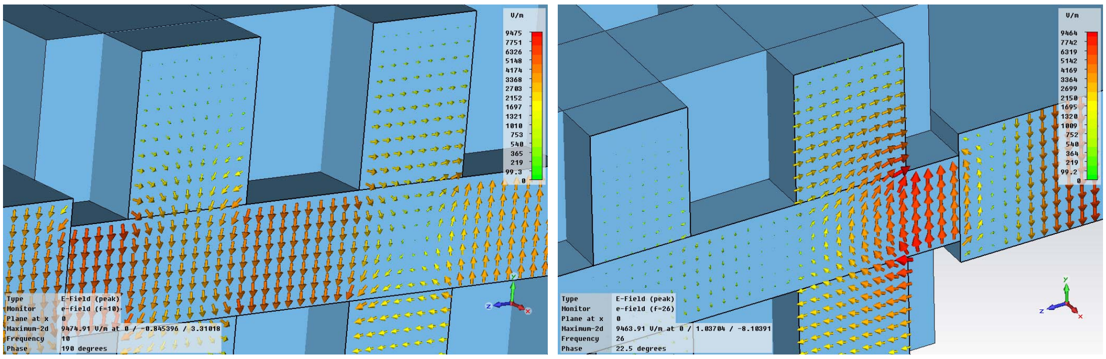

Type E-Field (peak)
Monitor e-field (f=10)
Plane at x 0
Maximum-2d 9474.91 V/m at 0 / -0.845396 / 3.31018
Frequency 10
Phase 190 degrees

Type E-Field (peak)
Monitor e-field (f=26)
Plane at x 0
Maximum-2d 9463.91 V/m at 0 / 1.03704 / -8.10391
Frequency 26
Phase 22.5 degrees

(a) $\vec{E}$-field distribution at 10 GHz.

(b) $\vec{E}$-field distribution at 26 GHz.

Figure 3.10: Electrical field distributions inside non-uniform filters.

What is found, is an y-directed $\vec{E}$-field over the height of the waveguide between the bosses (supporting a transmission line model in these sections), but an z-directed $\vec{E}$-field in the transversal groove decreasing for higher values of y (similar to that shown in Fig. 3.4 for short-circuited series stubs). This field distribution is even more prominent at the first transversal groove at stop-band operation. The internal field distribution therefore does not support a stepped-impedance circuit model, but rather a short-circuited series stub model. This is in line with the observation that the stepped-impedance model is best suited for "wide shallow grooves" [42], which is not the case here.

Short-circuited series stub model

In keeping with the previously observed field distributions, a short-circuited quarter-wavelength stub model is used for the second class of circuit model. The model, shown in Fig. 3.11, is identical to the one used in Marcuvitz's data, except that (as with the previous example) λ_0 is substituted with λ_g. Impedances Z_0, Z_s and line lengths θ_i (as

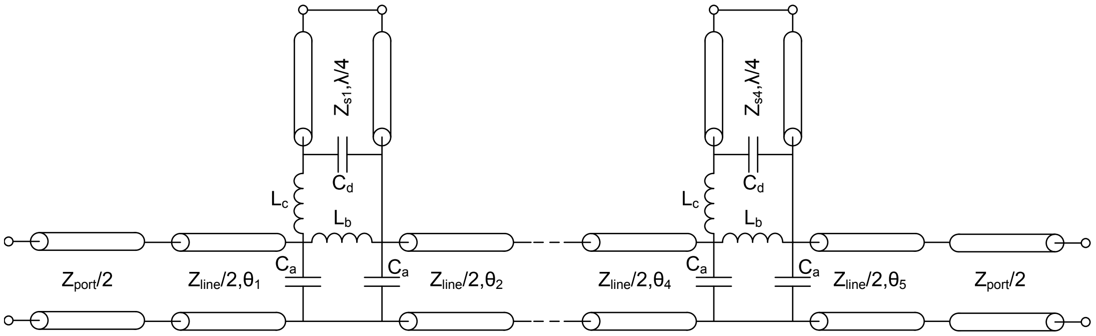

Figure 3.11: Short-circuited series stubs circuit model with full reactive compensation.

shown in Fig. 3.11) are determined as with the stepped-impedance model. A notable difference from the previous stepped-impedance model shown in Fig. 3.8, is the absence input- and output discontinuity capacitor C'. Given the small step from b_T to b'', the capacitor does not contribute significantly to the accuracy of the model, and is therefore omitted.

The circuit model values are shown in Table 3.2, with its S-parameters in Fig. 3.12 compared to the same full-wave model S-parameters used to evaluate the stepped-impedance model. Stub lengths are chosen $\lambda_g/4$ length at f_∞.

The following should be noted on the use of this model:

- Ideal TEM lines are used in circuit modelling, whereas it is assumed that the waveguide filter operates with TE_{10} waveguide lines. It is therefore necessary to transform the resulting frequency response of the circuit model to an equivalent waveguide response by a frequency transformation. It follows that the waveguide specifications would then also have to be transformed to TEM frequencies for circuit optimisation.
- The reactive compensation values are calculated at a specific wavelength. In all cases, this wavelength is chosen as the the TE_{10} mode guide wavelength λ_g at the centre of the transmission band, since it is here that accuracy is required for the synthesis of the in-band reflection response.
- Single values of C_a, L_b, L_c and C_d are used throughout the circuit, based on an average transversal groove width[2] l. This is done to simplify the circuit optimisation processes, which would otherwise require a re-calculation of each reactive element each time a stub or line impedance is altered. The model, though simple to use, is only valid for for near-uniform boss patterns.

---

[2] The notable exception is in half-inductive filters, where the narrow transversal groove is explicitly modeled as $l/2$.

Table 3.2: Short-circuited series stub model parameters derived from benchmark non-uniform filter dimensions.

Full-wave	[mm]	Circuit	[GHz] / [Ω] / [°] / [F] / [H]
a	22.86	f_0	7.5461
b	8	f_∞	25.85
b_T	3	Z_{port}	1
b''	2	Z_{line}	1.052
l_1	2.5	Z_{s1}	1.315
l_2	2.2	Z_{s2}	1.157
l_3	2.2	Z_{s3}	1.157
l_4	2.5	Z_{s4}	1.315
l'_1	1.2	θ_1	10.87
l'_2	2.4	θ_2	21.73
l'_3	2.2	θ_3	19.92
l'_4	2.4	θ_4	21.73
l'_5	1.2	θ_5	10.87
w	2.286	C_a	2.691×10^{-12}
w'	2.286	L_b	556.842×10^{-12}
		L_c	7.888×10^{-12}
		C_d	393.2658×10^{-15}

- An electric wall is placed along the central xz-plane of the filter, as with the model in [68].
- As the stepped-impedance model is better suited for shallow, wide grooves, so this model is better suited for narrow, deep grooves ($l/b' \leq 1$).
- The reactive values are calculated based on the formulas provided in [68]. Recent publications have presented more accurate equivalent representations of waveguide T-junctions [70], but rely on more complex computation, and do not provide generalised formulas for the simple circuit representation crucial to this synthesis method.

Despite these restrictions, the model predicts the lower stop-band frequency f_1 to within 2.7% and the upper stop-band frequency f_2 to within 1%. The reflection levels in the transmission band are modelled more accurately, though the frequencies of the reflection maxima predicted 12% higher by the circuit model than by the full-wave simulation. The most significant feature of this model, though, is the improved prediction of stop-band roll-off. This enables the designer to determine the required filter order during circuit synthesis.

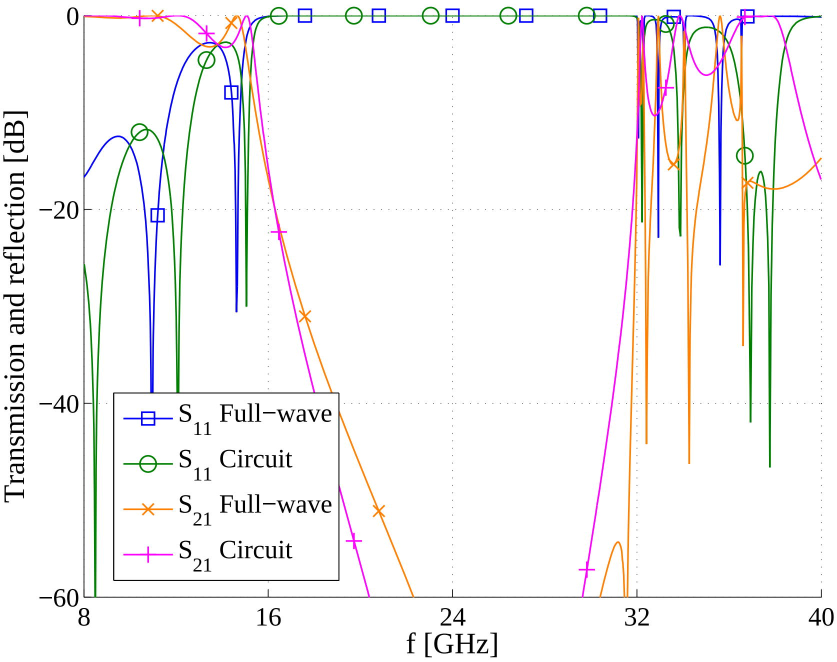

Figure 3.12: Evaluation of short-circuited stub model description of non-uniform filters.

3.3.2 Suppression of higher order modes

The above results only show the S-parameters of the dominant TE_{10} mode. However, since the stop-band of the filter extends above the cut-off frequencies of higher order modes, it is imperative that the operation of the filter be verified for these modes as well. In fact, it is specifically because of the suppression of higher order modes that waffle-iron filters are preferred above corrugated waveguide filters.

To verify the suppression of higher order modes, S_{11} and S_{21} for the TE_{20} and TE_{30} mode excitation of the filter in Table 3.2 are shown in Fig. 3.13(a). These modes are shown to be subject to the same attenuation in their respective propagating bands as the fundamental mode. This is the significant advantage waffle-iron filters hold over corrugated waveguide filters, where higher order modes have to be considered individually [71, 26].

Of more concern, is the cross-coupling between the TE_{10} and TE_{30} modes, as shown in Fig. 3.13(b). The output magnitude of the TE_{30} mode can reach levels comparable to the stop-band attenuation required by the filter, and will be exacerbated by asymmetries due to manufacturing tolerances. This effect should be investigated and considered in any final design.

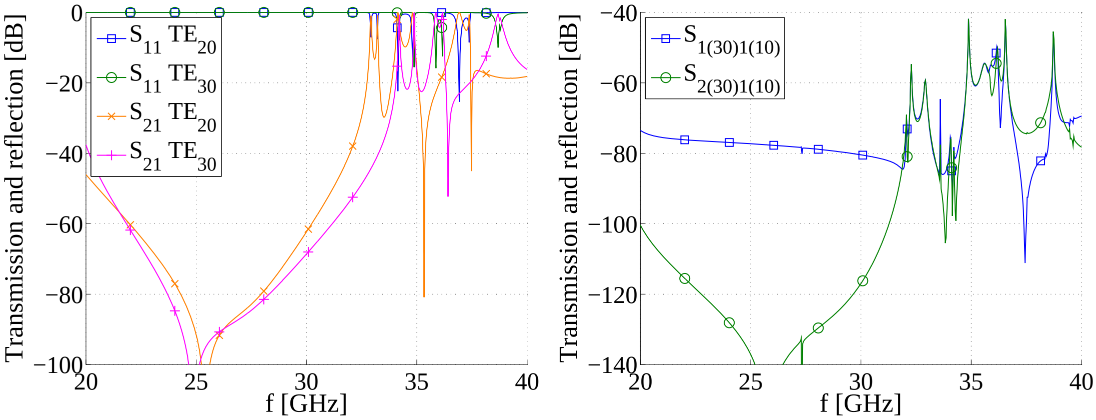

(a) TE_{20} and TE_{30} transmission and reflection responses.

(b) Coupling between the odd modes TE_{10} and TE_{30}.

Figure 3.13: Higher-order modes in non-uniform waffle-iron filters.

3.3.3 Synthesis example

To illustrate the synthesis procedure, a waffle-iron filter is synthesised to meet specification set “A” in Table 3.11. The first step is to transform the TE_{10} specification frequencies to TEM frequencies by the relation

$$f_{\text{TEM}} = \frac{c}{2\pi}\sqrt{\left(\frac{2\pi f_{\text{TE10}}}{c}\right)^2 - \left(\frac{\pi}{a}\right)^2} \tag{3.1}$$

to the values in Table 3.3

Table 3.3: Transformation of TE_{10} specification frequencies to TEM optimisation frequencies.

	f [GHz]	TE_{10}	TEM
Transmission band	Lower	8.5	5.41
	Upper	10.5	8.20
First stop-band	Lower	17	15.68
	Upper	21	19.95
Second stop-band	Lower	25.5	24.64
	Upper	31.5	30.81
f_∞		24.25	23.35

These frequencies will be used as targets for circuit model optimisation.

At this point, the classical transmission line filter synthesis using Kuroda’s identities [69] might be considered. Unfortunately, this synthesis theory (apart from not taking into account reactive transition effects) relies on uniform stub and line lengths, which is exactly the restriction this synthesis method is designed to overcome. Modern synthesis techniques for corrugated waveguide filters [26] rely on uniform line lengths and non-uniform stub lengths, neither of which are true here. In the absence of a synthesis theory for non-uniform cascaded lines and stubs, circuit model optimisation is implemented.

Electrical line lengths will be optimised around a frequency of 6.87 GHz, which corresponds to a TE_{10} mode f_0 of 9.5 GHz. The short-circuited stubs will have an electrical length of 90° at $f_\infty = 23.35$ GHz. This corresponds to an initial stub length of $\lambda_{g\infty}/4 = 3.21$ mm and an overall height $b = 2 \times l_s + b'' = 8.42$ mm, as illustrated in Fig. 3.7.

The physical dimension a is chosen as 22.86 mm, to allow matching to standard WR-90 waveguide without the need for H-plane steps. Maximum power handling capability (discussed in §3.5) motivates a choice of $b'' = 2$ mm. A half-capacitive approach is chosen due to width and the proximity of the stop-band to the transmission band.

Next, initial values of $\theta_{(i)}$ and $Z_{s(i)}$ have to be selected. Initial values of $l \approx l' \approx w \approx w' \approx b''$ are chosen, in an attempt to create an even geometry inside the filter. This is assumed to result in an even electric field distribution, avoiding localised $\vec{E}$-field breakdown at high power levels. In line with this choice, all bosses and transversal grooves are given an initial length of $l = l' = 2$ mm, with the first and last rows of bosses being of length $l'/2$ (in keeping with the half-capacitive approach). To allow for an integral number of longitudinal grooves of equal length, w and w' are chosen as 2.286 mm, which renders approximately square bosses. This is done as a further effort to create an even geometry in the filter. This choice allows for 4 equal-width longitudinal grooves of width w, and another two along the sides of width $w/2$, as well as five longitudinal rows of bosses of width w'.

The boss lengths l' are calculated as fractions of guide wavelength at 9.5 GHz

$$\begin{aligned}\theta &= \frac{l'}{\lambda_g} \times 360 \\ &\approx 16.5^\circ\end{aligned}$$

These same electrical lengths are then used as initial TEM line lengths at 6.87 GHz in the circuit model (with the exception of θ_1 and θ_{n+1}, which are chosen as 8.25° due to the half-capacitive input). Since $b'' = l$, the values of Z_0, Z_l and $Z_{s(i)}$ are all set to 1 Ω. Finally, the formulas provided in [68] are used to calculate the circuit parameters (based on the previously selected initial dimensions) of $C_a = 2.78 \times 10^{-12}$ F, $L_b = 654.79 \times 10^{-12}$ H, $L_c = 7.63 \times 10^{-12}$ H and $C_d = 562.83 \times 10^{-15}$ F. It is important to note that the model in [68] is defined in terms of solid waveguide ridges, without longitudinal grooves. This means that b'' cannot be used in these calculations, but rather the effective solid-ridge boss spacing of b', which is found by an iterative solution of the relation provided in [25]

$$b' = b'' \left(\frac{l'}{l+l'} + \frac{2}{\pi} \frac{l}{l+l'} \left[\arctan\left(\frac{b''}{l}\right) + \log\left(\sqrt{1 + \left(\frac{l}{b''})\right)^{2}} \right) \frac{b''}{l} \right] \right)^{-1} \tag{3.2}$$

A circuit optimiser is now used to optimise the values of Z_l, $Z_{s(1,2,\ldots,n)}$, f_∞ and $\theta_{(1,2,\ldots,n+1)}$. To allow synthesis of an electrically symmetrical structure, and to reduce the number of optimisation variables, symmetrical stub impedances and line lengths are chosen equal (eg. $Z_{s(1)} = Z_{s(n)}$, $\theta_{(i+1)} = \theta_{(n)}$). It is important to note that a **localised** optimiser is required, to ensure final values which preserve the quasi-uniform nature of the boss pattern. Excessive dimensional adjustments would invalidate the uniform choice of reactive compensation (since it is determined for an average geometry), and could lead to the violation of the requirement of narrow, deep grooves. Initially, $n = 6$ transversal grooves are modelled and optimised, but the stop-band roll-off is found inadequate. Repeating the procedure for $n = 8$ transversal grooves proved satisfactory.

The result of this optimisation is shown in Table 3.4, as well as the resulting dimensions in Table 3.5. An additional parameter generated by the circuit model optimisation is $f_{1(TEM)}$, the upper stop-band frequency, which will be used to design b_T.

After these values are recorded, the resulting changes have to be applied to the physical dimensions. The TEM frequencies f_∞ and f_1 are converted back to TE$_{10}$ frequencies $f_1 = 15.28$ GHz and $f_\infty = 26.86$ GHz. The new value of l_s is then calculated as $\lambda_{g\infty}/4 = 2.88$ mm and the new value of b as 7.75 mm.

Next, the transversal groove widths l_i are calculated based on the relative rescaled values of stub impedances $Z_{s(i)}$ and line impedance Z_l. It follows that

$$l_i = \frac{Z_{s(i)}}{Z_l} b'' \tag{3.3}$$

given that the value of b'' remains fixed, for the purpose of maintaining the power handling capability of the filter. Similarly, the boss lengths are rescaled proportional to the optimised values of θ_i by the relation

$$l'_i = \frac{\theta_i \lambda_{g0}}{360} \tag{3.4}$$

where λ_{g0} is the wavelength of the filter centre frequency $f_0 = 9.5$ GHz.

The impedance $Z_0 = 1\ \Omega$ is referenced to a waveguide height b_0. Its value is found by the relative change of Z_l as

$$b_0 = \frac{b' Z_0}{Z_l} \tag{3.5}$$

which enables the calculation of the final terminating guide height b_T as

$$b_T = \frac{b_0}{\sqrt{1-\left(\frac{f_0}{f_1}\right)^2}} \tag{3.6}$$

Table 3.4: Progressive development of short-circuited stub circuit model values for non-uniform filter.

Parameter	Initial	Optimised
f_0	6.878	6.878
f_∞	23.347	26.050
Z_{port}	1	1
Z_{line}	1	0.825
Z_{s1}	1	1.102
Z_{s2}	1	1.052
Z_{s3}	1	1.129
Z_{s4}	1	1.036
Z_{s5}	1	1.036
Z_{s6}	1	1.129
Z_{s7}	1	1.052
Z_{s8}	1	1.102
θ_1	8.25	10.88
θ_2	16.50	18.22
θ_3	16.50	18.52
θ_4	16.50	17.87
θ_5	16.50	18.43
θ_6	16.50	17.87
θ_7	16.50	18.52
θ_8	16.50	18.22
θ_9	8.25	10.88
C_a	2.776×10^{-12}	2.776×10^{-12}
L_b	645.778×10^{-12}	645.778×10^{-12}
L_c	7.625×10^{-12}	7.625×10^{-12}
C_d	562.833×10^{-15}	562.833×10^{-15}

The full-wave simulation results of the resulting structure are shown in Fig. 3.14. To improve this response, full-wave tuning of only two parameters need to be performed. The stop-band is adjusted by tuning[3] b, and the pass-band reflection by tuning b_T. This is indicated in Table 3.5 by the amount of tuning in brackets. All other dimensions remain unchanged from their values calculated by the synthesis process. This representation is followed in all following tables as well.

---

[3] "Tuning" refers to manual adjustment of specific dimensions in a full-wave simulation to achieve a specific change in electrical response, whereas optimisation refers to a programmed algorithm incrementally changing all dimensions, with a specific electrical response as goal function. Tuning is, therefore, far less time consuming and computationally intensive than optimisation.

Table 3.5: Progressive development of physical dimensions for example non-uniform waffle-iron filter. Dimensions indicated as (–) remain unchanged.

Dimension [mm]:	Initial	From circuit optimisation	Full-wave tuned
a	22.86	22.86	–
b	8.42	7.75	**8.20** (+5.8%)
b_T	–	3.66	**4.48** (+22.4%)
b''	2	2.00	–
l_1	2	2.67	–
l_2	2	2.55	–
l_3	2	2.74	–
l_4	2	2.51	–
l_5	2	2.51	–
l_6	2	2.74	–
l_7	2	2.55	–
l_8	2	2.67	–
l'_1	2	1.32	–
l'_2	2	2.21	–
l'_3	2	2.24	–
l'_4	2	2.16	–
l'_5	2	2.23	–
l'_6	2	2.16	–
l'_7	2	2.24	–
l'_8	2	2.21	–
l'_9	2	1.32	–
w	2.286	2.286	–
w'	2.286	2.286	–

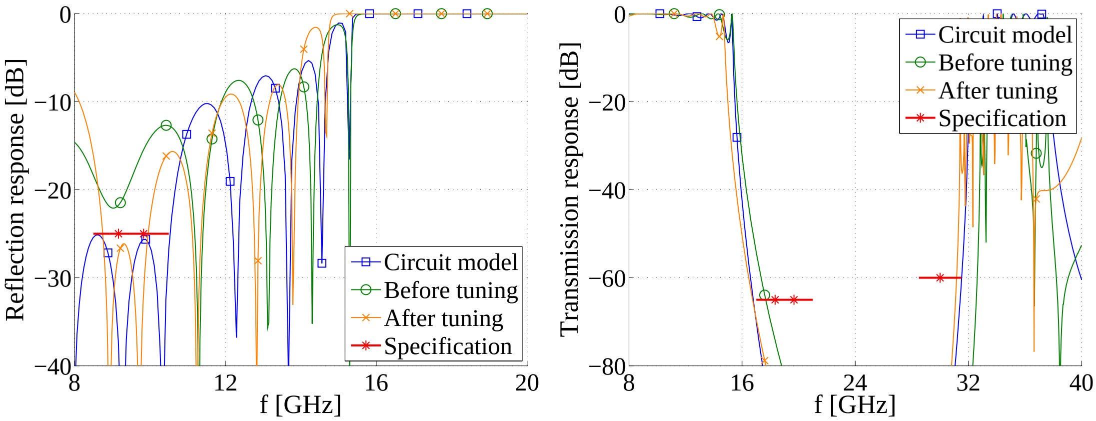

(a) Reflection response

(b) Transmission response

Figure 3.14: Example synthesis of non-uniform filter.

To compensate for the remaining inaccuracy in synthesis, i.e. that of the reduced transmission bandwidth (12.8% achieved, compared to 21% synthesised), it is simply necessary to optimise the circuit model for 40% wider transmission bandwidth than is required by the specification. It is for this reason that later examples are optimised to wider goals than required by specifications for similar levels or reflection.

3.3.4 Synthesis evaluation

The model suffers from slight inaccuracy in the transmission band reflection response (particularly the frequency shift in local maxima and minima of reflection), and the transmission bandwidth is narrower than that predicted by the circuit model. This inaccuracy can be compensated for in synthesis by optimising the circuit model for 40% wider goal functions than is required by the eventual filter. The required dimensional adjustments to improve the input reflection coefficient and stop-band attenuation are easy to perform, since the input reflection coefficient is predominantly a function of b_T, and the stop-band centre predominantly a function of b. It is also important to point out that no full-wave adjustments to other internal dimensions (l_i' or l_i) are required, which highlights the first-iteration synthesis accuracy of the model. Ultimately, the model is a useful representation of non-uniform waffle-iron filters, and is used for further development.

3.4 Oblique waffle-iron filters

All waffle-iron filter boss patterns (both uniform and non-uniform) discussed up to now, rely on perturbations normal to the propagation of an incident $\mathrm{TE_{m0}}$ modes. The next section proposes a novel approach to boss pattern design by synthesising perturbations at an oblique angle of incidence to the propagating $\mathrm{TE_{m0}}$ modes.

3.4.1 Diagonal TEM propagating mode perturbation

A $\mathrm{TE_{m0}}$ mode propagating in rectangular waveguide can also be described as the sum of two diagonally propagating TEM modes in the guide [72, 73], as shown in Fig. 3.15. The propagating angle of the diagonal mode θ is such that the path length from sidewall to sidewall is a multiple of half a free-space wavelength λ_0. Any considered TEM phase path is, therefore, only valid at multiples of some fixed frequency f_0. In corrugated waveguide filters, frequency selectivity is achieved by periodic variations in the $\mathrm{TE_{m0}}$ transmission path. Since different $\mathrm{TE_{m0}}$ modes have different wavelengths at a specific frequency of propagation, the physical width of the corrugation corresponds to a synthesised phase length only for a single mode, usually the fundamental $\mathrm{TE_{10}}$ mode. This is why corrugated waveguide filters have dissimilar transmission and reflection responses for different incident modes [40].

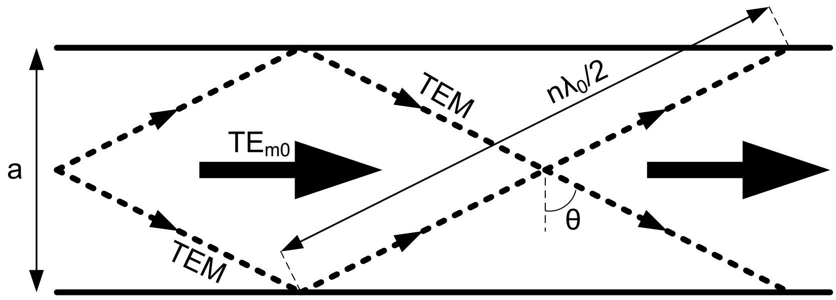

Figure 3.15: Decomposition of $\mathrm{TE_{m0}}$ modes into diagonal TEM modes.

By cutting uniform longitudinal grooves into the solid ridge corrugations, as is done to create waffle-iron filters, uniform perturbations along the TEM propagating phase paths are formed. In this view, it is effectively the TEM mode that is filtered, and since all propagating $\mathrm{TE_{m0}}$ modes decompose into the same two diagonal TEM paths at a specific frequency, the filter has similar transmission responses for all incident $\mathrm{TE_{m0}}$ modes [41, 42]. Furthermore, because of the reduced waveguide height b' leading into the filter, the orthogonal $\mathrm{TE_{0n}}$ modes are reflected before reaching the filter, and may safely be neglected during synthesis.

Two restrictions apply when perturbing these reflected TEM phase paths. Consider two plane waves propagating in directions A and B, as shown in Fig. 3.16(a). Placing a corrugation across the waveguide to perturb $\mathrm{TEM_A}$ would require a ridge be placed across the waveguide width along $X-X'$, normal to the incident plane wave. Similarly, the other propagating plane wave $\mathrm{TEM_B}$ requires a ridge along $Y-Y'$. Placing these two ridges as indicated would cause incidence of $\mathrm{TEM_A}$ on $Y-Y'$ at an oblique angle θ', and similarly $\mathrm{TEM_B}$ on $X-X'$, leading to unequal propagation distances from source to ridge for different parts of the plane wave. By choosing $\theta = 45°$, as shown in Fig. 3.16(b), the oblique incidence to the plane wave is avoided. In this case, a TEM plane wave may either propagate with normal incidence to a ridge, or propagate parallel to a ridge. By choosing this value of θ, the width of the waveguide a is made a function of the desired synthesis frequency f_0 by the $n\lambda_0/2$ relationship previously discussed.

Another restriction is illustrated in Fig. 3.16(c), where paths A and B are both perturbed by a phase length ϕ by ridges X and Y formed by $X-X'$ to X_1-X_1' and $Y-Y'$ to Y_1-Y_1', respectively. From the illustration, it is clear that ridge X perturbs not only phase path A, but also B, though a phase length $n\pi/2$ further than the perturbation of ridge Y. The result, from a synthesis perspective, is that any phase path perturbation has to repeat every $n\lambda_0/4$, where n is determined by the reflection angle θ and the guide width a. Physically, this restriction requires axial symmetry along the length of the waveguide of any chosen perturbation pattern.

In traditional uniform waffle-iron filters, both these restrictions are inherently satisfied by forming ridged perturbations with uniformly spaced square or circular bosses, as shown in Figs. 3.17(a) and 3.17(b). Instead of using solid ridges for perturbation, as is the case with corrugated waveguide filters, solid ridges are approximated by perforated diagonal ridges (shown in Fig. 3.17(d)). The uniform bosses provide a uniform perturbation path along several different angles of inclined TEM propagation (corresponding to different frequencies), provided the centre-to-centre spacing of the bosses are a small fraction of a wavelength [42].

If, at a single specified frequency f_0, the uniform pattern is adapted to allow immediate transition from open to ridged guide, "diamond" (45° rotated square) bosses are formed, as shown in Fig. 3.17(c). This leads to a perturbation normal to a TEM path, but oblique to $\mathrm{TE_{m0}}$ propagation. As before, the phase paths are periodically perturbed by a ridged obstacle subject to the restrictions previously stated. The previously stated restriction of

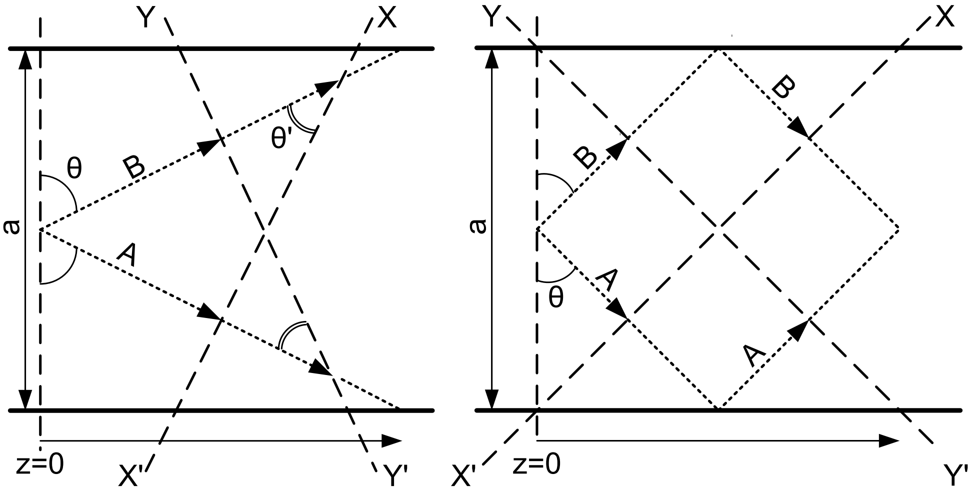

(a) Non-45° inclined ridges (b) 45° inclined ridges

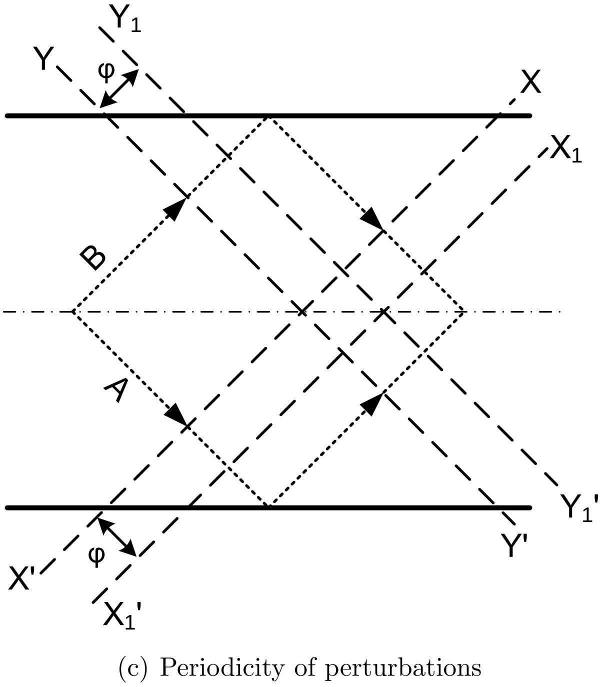

(c) Periodicity of perturbations

Figure 3.16: Restrictions to TEM phase path perturbation.

small dimensions compared to wavelength, still applies.

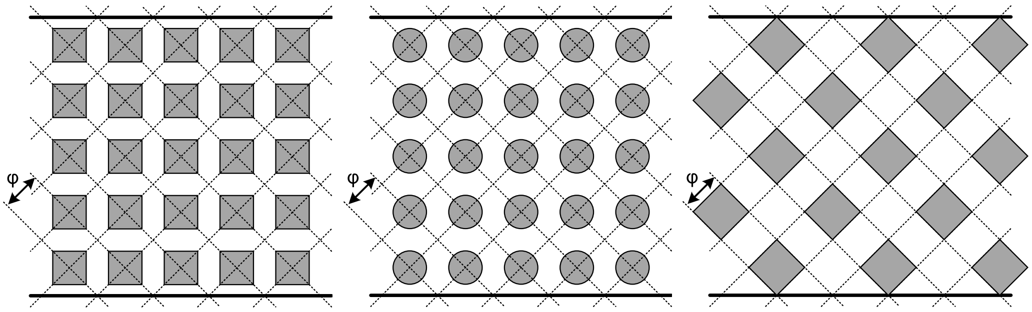

(a) Regular square bosses. (b) Regular round bosses. (c) Regular diamond bosses.

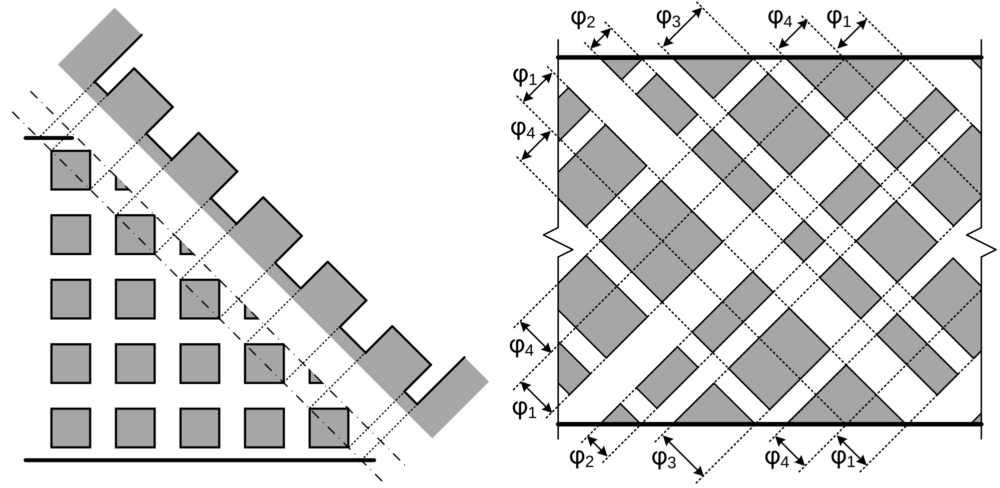

(d) Sectioned boss pattern view, showing approximation of full ridge.

(e) Oblique diamond bosses.

Figure 3.17: Different uniform and oblique boss patterns.

Just as in the preceding non-uniform synthesis, the diamond pattern in Fig. 3.17(c) may be altered to allow for non-uniform values of boss length ϕ. A typical oblique waffle pattern is shown in Fig. 3.17(e), where a sequence of line lengths ϕ_1, ϕ_2, ϕ_3 and ϕ_4, as well as unequal groove widths, are repeated. If an adequate circuit model description of this structure can be found, it would lead to the same control over both the transmission and in-band reflection responses of the filter, as previously shown for the non-uniform case.

3.4.2 Circuit model

As before, the synthesis of the boss pattern in Fig. 3.17(e) requires an accurate circuit model description. Both stepped-impedance and short-circuited stub models will be re-evaluated for this topology, using a prototype full-wave model loosely based on the dimensions of the non-uniform filter evaluated in the previous section.

What should be noted for this topology, is that a half-capacitive approach is followed consistently. A half-inductive step (ϕ_1 in Fig. 3.17(e)) creates a triangular prism cavity in the corners of the boss pattern, of which the cross-sectional length is a poor indication of either stub impedance or stepped line length. The half-capacitive stub, though still ill-defined as a line length, does not create the additional inconvenience of a cavity resonance.

Stepped-impedance model

The first synthesis approach uses the same capacitively compensated stepped-impedance model used for the non-uniform filters, as shown in Fig. 3.8. The example model uses a square pattern of $a = 26.729$ mm, which means the overall length of diagonal TEM propagation is $\sqrt{2}a$, or 37.8 mm. This is equal to λ_0 at $f_0 = 7.94$ GHz, the centre frequency of the filter. Inside a diagonal length of $\lambda_0/2$, four transversal grooves of unequal width are placed (with symmetry around the point $\lambda/4$). In reference to Fig. 3.17(e), this means that $\phi_1 = \phi_5$ and $\phi_2 = \phi_4$. The half-capactive short boss length ϕ_5 and ϕ_1 are combined in the middle of the filter to form one average sized boss, as ϕ_1 and ϕ_4 are merged in Fig. 3.7 for the case of four bosses.

Since the synthesised phase path is TEM, and not TE_{10}, no frequency transformation is required between the physical and electrical models. Using f_0 as frequency, electrical lengths of the high impedance (l_i) and low impedance (l_i') lines are established as shown in Table 3.6.

As before, line impedances Z_{port}, Z_l and Z_h are calculated by

$$Z_i = \frac{b_i}{b_0} Z_0$$

where b_0 is calculated from Eq. 7.05-2 in [25], and a reference value of $Z_0 = 1\ \Omega$ is chosen. The actual boss separation b'' (not the equivalent full-ridge separation b', as was used in the previous non-uniform synthesis) is used to calculate low impedance line, whilst b is still used to calculate the high impedance. Unlike the non-uniform model, there is no uniform longitudinal boss width w' or groove width w, since w and w' are, effectively, l and l', respectively. This requires the use of mean values of l and l' to be used in Eq. 3.2 to calculate b'. This establishes b' as 2.3746. The resulting circuit model parameters are shown in Table 3.6.

A comparison of the full-wave and circuit simulated results is shown in Fig. 3.18(a). Apart from the similar general shape of the response, there is little correspondence between the

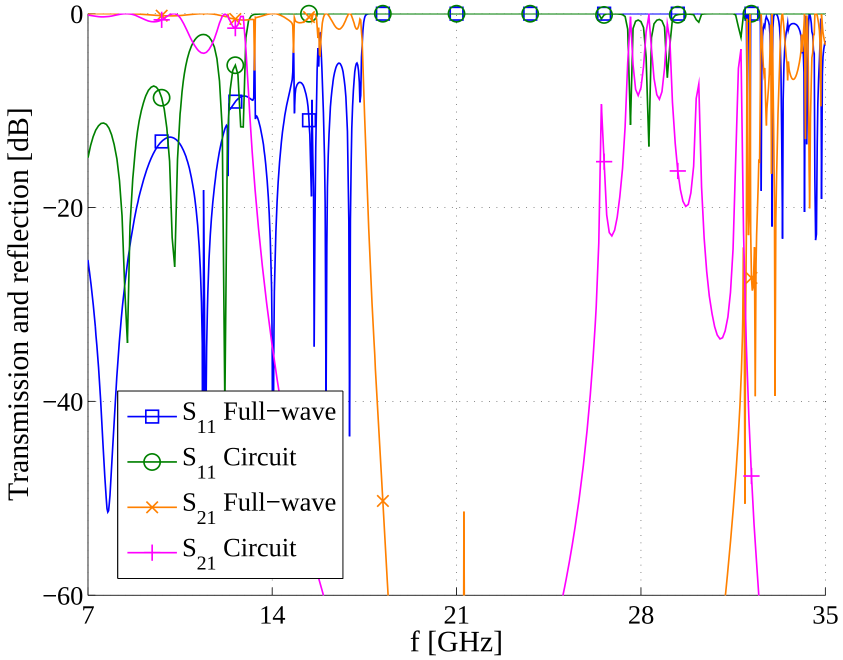

(a) Electrical response.

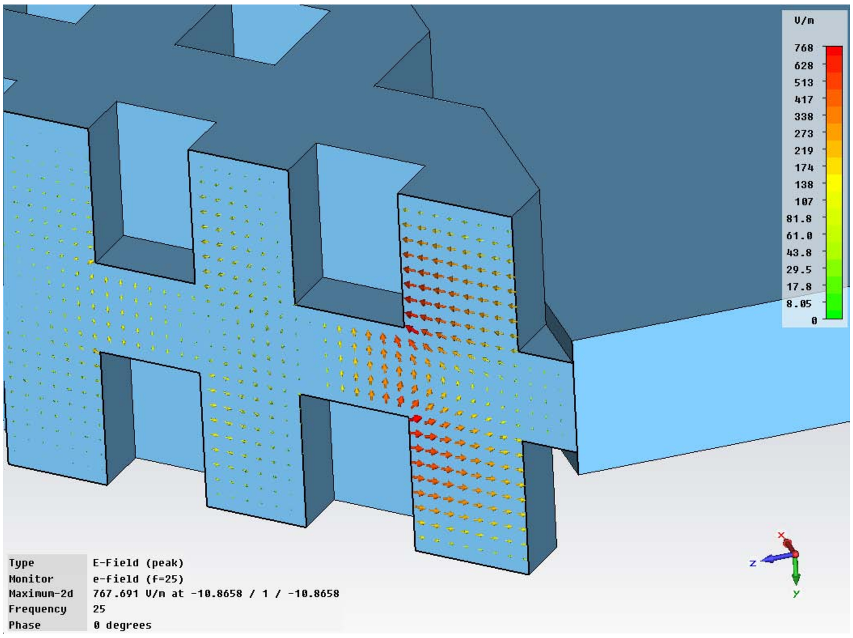

Type E-Field (peak)
Monitor e-Field (f=25)
Maximum-2d 767.691 V/m at -10.8658 / 1 / -10.8658
Frequency 25
Phase 0 degrees

(b) $\vec{E}$-field distribution at 26 GHz.

Figure 3.18: Evaluation of stepped-impedance circuit model for oblique filters.

Table 3.6: Stepped-impedance model parameters derived from benchmark oblique filter dimensions.

Full-wave	[mm]	Circuit	
a	22.86	f_0 [GHz]	7.937
b	8	Z_h	3.00
b_T	3	Z_{port}	1.12
b''	2	Z_l	0.89
l_1	2.5	θ_{h1}	23.81
l_2	2.2	θ_{h2}	20.95
l_3	2.2	θ_{h3}	20.96
l_4	2.5	θ_{h4}	23.81
l'_1	1.2	θ_{l1}	11.43
l'_2	2.4	θ_{l2}	22.86
l'_3	2.2	θ_{l3}	20.95
l'_4	2.4	θ_{l4}	22.86
l'_5	1.2	θ_{l5}	11.43
		C	7.425×10^{-12}

circuit and full-wave models' S-parameter responses. This is due to the $\vec{E}$-field distribution (shown in Fig. 3.18(b)) which does not support a stepped impedance transmission line model. The approach is dismissed as inadequate, and not considered for further development.

Short-circuited series stubs

The development of the short-circuited series stub model is identical to that used previously for non-uniform filters (using the same circuit model shown in Fig. 3.11), except for two key aspects. Firstly, f_{TE10} and λ_g is replaced by f_{TEM} and λ_0 in calculating f_∞ and θ_i. Secondly, average values of l and l' are used instead of w and w' to calculate the reactive compensation for the Marcuvitz model [68]. The synthesis centre frequency f_0 is derived from the cross-sectional length of the filter $\sqrt{2}a$, as with the stepped-impedance model. The resulting parameters and electrical responses are shown in column #1 of Fig. 3.19.

As seen in Fig. 3.19(a), this circuit model is less accurate applied to oblique filters than it is when applied to non-uniform filters. This is attributed to the fact that the $\theta = 45°$ propagation path of Fig. 3.15 is only valid at multiples of a single frequency: in this case, 7.937 GHz. The stop-band is estimated at 18.7% lower than in the full-wave simulation, and the reflection levels at local maxima differ by as much as 3.7 dB. Although the roll-off is better predicted than was the case with the stepped-impedance model, significant full-wave tuning would be required post-synthesis for this model to be used in a design

Table 3.7: Short-circuited stub model parameters derived from benchmark oblique filter dimensions.

Full-wave	[mm]	Circuit	#1	#2
a	22.86	f_0	7.937 GHz	7.937 GHz
b	8	f_∞	25 GHz	25 GHz
b_T	3	Z_{port}	1.124	2.572
b''	2	Z_l	0.89	2.0
l_1	2.5	Z_{s1}	0.937	2.5
l_2	2.2	Z_{s2}	0.824	2.2
l_3	2.2	Z_{s3}	0.824	2.2
l_4	2.5	Z_{s4}	0.937	2.5
l'_1	1.2	θ_1	11.43	11.43
l'_2	2.4	θ_2	22.86	22.86
l'_3	2.2	θ_3	20.95	20.95
l'_4	2.4	θ_4	22.86	22.86
l'_5	1.2	θ_5	11.43	11.43
		C_a	2.5233×10^{-12}	–
		L_b	513.0047×10^{-12}	–
		L_c	6.667×10^{-12}	–
		C_d	638.342×10^{-15}	–

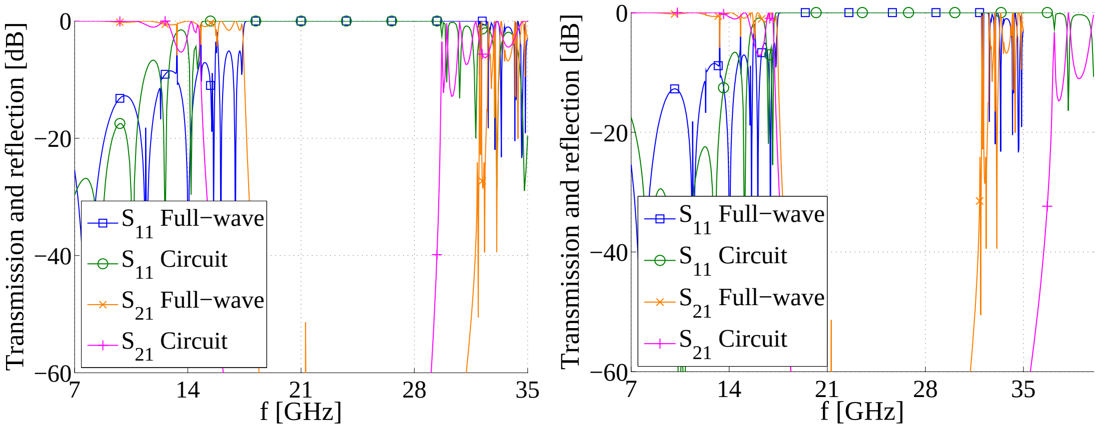

(a) Electrical response, synthesised.

(b) Electrical response, simplified model.

Figure 3.19: Evaluation of short-circuited stub model description of oblique filters.

algorithm.

In light of this required full-wave tuning, the model is simplified by

- Removing all reactive compensation (C_a, L_b, L_c and C_d)
- Omitting the rescaling step from b'' to b' to calculate Z_l
- Foregoing the use of f_1 to calculate b_T, instead using b_0 (still derived from b') as input impedance reference

The response of this highly simplified model shown in Fig. 3.19(b) (with circuit parameters shown in column #2 of Table 3.7) over-estimates f_2 by 15.7%, but f_1 to within 1.5%. Input reflection levels are not tracked as accurately, but the frequencies of local minima and maxima are better estimated (typically to within 12%).

Even though both short-circuited stub models are more accurate than the stepped-impedance model, neither achieve the same level of correspondence with full-wave simulated results as was achieved with the Marcuvitz model and non-uniform filters. More full-wave tuning would be required post-synthesis for oblique filters than for non-uniform filters, whichever model is chosen for further development. However, the same predominant tuning parameters (b_T for input reflection match, b for stop-band centre) apply. To keep the design process as simple as possible, the simpler of the two models is retained for further synthesis of oblique filters.

3.4.3 Synthesis example

Using the simplified short-circuited series stub model, an example filter is designed by optimisation of the circuit model parameters. The optimisation was perfomed with specification set “A” in Table 3.11 as target. A detailed diagram of the oblique boss pattern is shown in Fig. 3.20. Different initial choices are made as to dimensions and operating frequency (compared to the non-uniform filter synthesis), since the filter is more constrained in its design. Dimension a is now a function of a predetermined synthesis frequency f_0, which is selected as the centre of the transmission band. For specification “A”, $f_0 = 9.5$ GHz, which requires a value of

$$\begin{aligned} a &= \frac{\lambda_0}{\sqrt{2}} \\ &= 22.33 \text{ mm} \end{aligned}$$

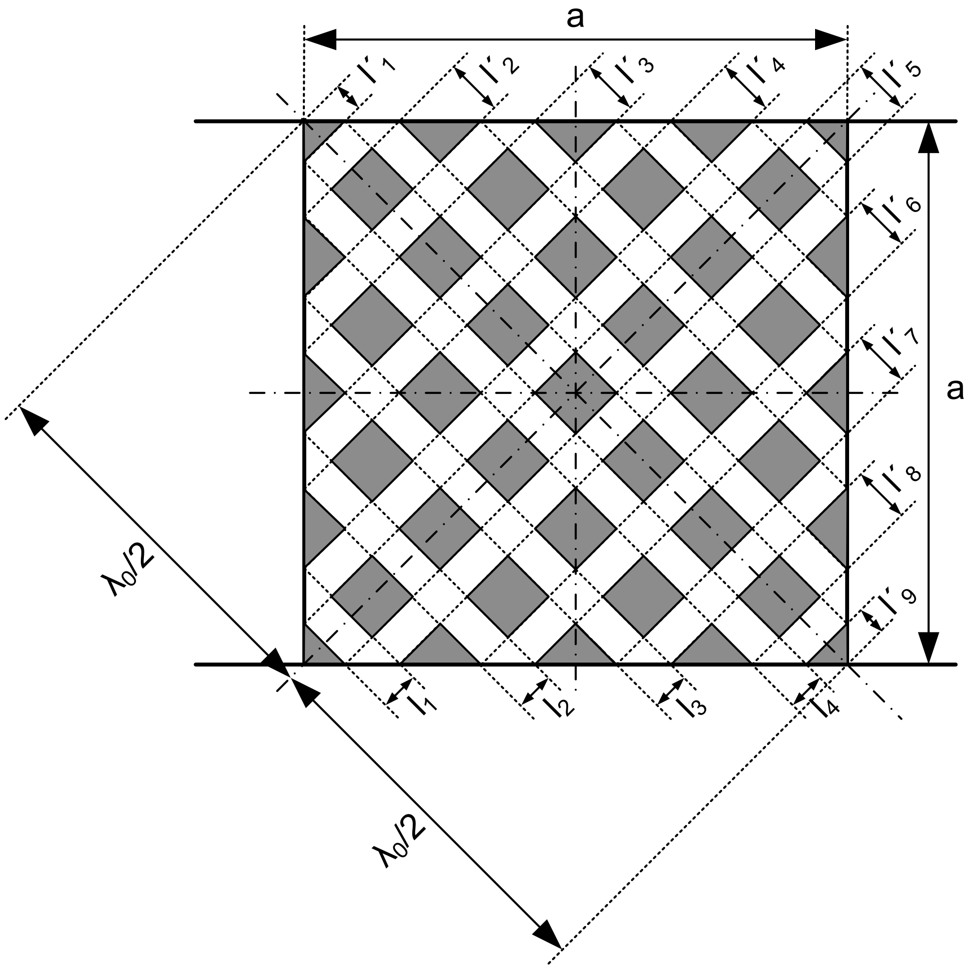

Figure 3.20: Example oblique waffle-iron filter boss pattern. Dimensions not to scale.

As before, initial impedances are chosen as $Z_{\text{port}} = Z_l = Z_{s(i)} = 1\ \Omega$. The total TEM phase path length of the filter is 2π. Since the synthesised boss pattern has to repeat every $n\pi/2$ (Fig. 3.16(c)), and the filter width allows for $n = 2$ half-wavelengths between the sidewalls (Fig. 3.15), a phase path of length π is synthesised, and then repeated. A total filter order of $n = 8$ was found to achieve sufficient stop-band roll-off in previous syntheses, and is used again. This means that 4 evenly-spaced transversal grooves are used in each half-section. This leaves initial values of $\theta_{2..n} = 22.5°$, with half-capacitive end-sections $\theta_{1,n+1} = 11.25°$. This corresponds to free-space physical lengths of $l = l' = 1.97$ mm. Since an initial value choice of $Z_l = Z_{s(i)}$ is made, b'' is also set to 1.97 mm. Average values of $l \approx l' \approx 1.97$ mm are used in Eq. 3.2 to calculate $b' = 2.29$ mm, which in turn is used to select $b_T = 2.29$ mm by the initial value choice of $Z_{\text{port}} = Z_l$.

Lastly, f_∞ (the frequency at which the stubs are quarter-wavelength) is chosen as the centre of the stop-band at 24.25 GHz. This requires a stub length (at f_0) of $\theta_s = 35.25°$, which translates to an initial dimension of $b = 8.15$ mm.

Using a random local optimiser[4], the parameters Z_l, $Z_{s(i)}$, θ_i and θ_s are optimised, as shown in Table 3.8. Since the second half of the total λ_0 phase length has to repeat the pattern of the first $\lambda_0/2$, only $Z_{s(1..4)}$ and $\theta_{(1..5)}$ are optimised. Port symmetry is preserved by constraining $Z_{s(i)} = Z_{s(n+1-i)}$ and $\theta_{(i)} = \theta_{(n+2-i)}$. Lastly, it is noted that l'_5 is actually the sum of two half-capacitive line lengths, namely the last and first lines of the two $\lambda_0/2$ halves of the synthesis.

The line lengths are calculated by their fractions of λ_0 as

$$l'_i = \frac{\theta_i}{360}\lambda_0 \tag{3.7}$$

To ensure the total phase length is λ_0, the sum of the transversal stub widths is calculated as

$$\sum_{i=1}^{n} l_i = \lambda_0 - \sum_{i=1}^{n+1} l'_i \tag{3.8}$$

The groove widths l_i are considered directly proportional to the stub impedances $Z_{s(i)}$. It follows that the sum of the groove widths $\sum l_i$ is also directly proportional to the sum of the stub impedances $\sum Z_{s(i)}$. This is used to calculate the boss separation b'' from the optimised Z_l as

$$b'' = \frac{Z_l}{\sum_{i=1}^{n} Z_{s(i)}} \sum_{i=1}^{n} l_i \tag{3.9}$$

after which the individual stub impedances may be calculated as

$$Z_{s(i)} = \frac{l_i}{b''} Z_l \tag{3.10}$$

as well as the total height b

$$b = 2 \times \frac{\theta_s}{360}\lambda_0 + b'' \tag{3.11}$$

Finally, mean values of l_i and l are used to calculate b', which in turn is used to calculate $b_0 = b_T$ as before.

Using these calculated dimensions, full-wave tuning of b (re-centering of the stop-band), b'' (increasing the width of the stop-band) and b_T (improving the input reflection coefficient) are all that is required to meet the specification. Note that none of the other internal dimensions (l_i, l'_i) need adjustment, which indicates encouraging first-iteration accuracy.

There are, however, clear indications of spurious resonances in the "buffer band" (the frequency band between the synthesised transmission band and stop-band), which are unaccounted for in the circuit model representation of the filter. These will be discussed in the next section.

---

[4] An optimiser is used in the absence of a non-uniform transmission line filter synthesis theory, as discussed previously.

Table 3.8: Progressive development of short-circuited stub model values for oblique filter.

Parameter	Initial	Optimised
f_0	9.5	9.5
θ_s	34.89	39.01
Z_{port}	1	1
Z_{line}	1	0.882
Z_{s1}	1	1.027
Z_{s2}	1	0.998
Z_{s3}	1	0.998
Z_{s4}	1	1.027
Z_{s5}	1	1.027
Z_{s6}	1	0.998
Z_{s7}	1	0.998
Z_{s8}	1	1.027
θ_1	11.25	12.37
θ_2	22.5	27.94
θ_3	22.5	22.01
θ_4	22.5	27.94
θ_5	22.5	24.74
θ_6	22.5	27.94
θ_7	22.5	22.01
θ_8	22.5	27.94
θ_9	11.25	12.37

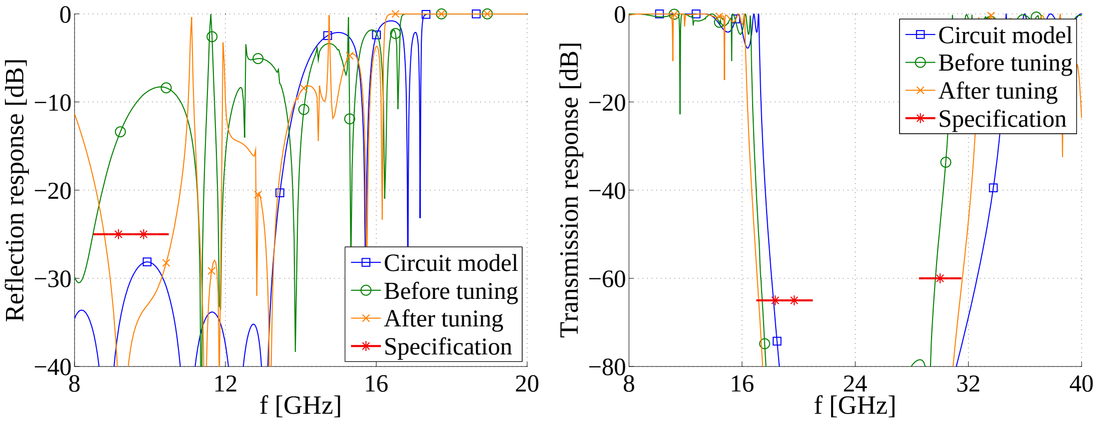

(a) Reflection response (b) Transmission response

Figure 3.21: Example synthesis of non-uniform filter.

Table 3.9: Progressive development of physical dimensions for oblique filter. Dimensions indicated as (–) remain unchanged.

Dimension [mm]	Initial	From circuit optimisation	Full-wave tuned
a	22.33	22.33	–
b	8.15	8.32	**7.82** (-6.0%)
b_T	1.93	1.93	**2.45** (+26.9%)
b''	1.97	1.48	**1.14** (-23.0%)
l_1	1.97	1.72	–
l_2	1.97	1.67	–
l_3	1.97	1.67	–
l_4	1.97	1.72	–
l_5	1.97	1.72	–
l_6	1.97	1.67	–
l_7	1.97	1.67	–
l_8	1.97	1.72	–
l'_1	0.99	1.09	–
l'_2	1.97	2.45	–
l'_3	1.97	1.93	–
l'_4	1.97	2.45	–
l'_5	1.97	2.18	–
l'_6	1.97	2.45	–
l'_7	1.97	1.93	–
l'_8	1.97	2.45	–
l'_9	0.99	1.09	–

3.4.4 Spurious resonances

The spurious resonances in the response of the oblique filter at 11.66, 12.51, 15.93 and 15.15 GHz are of some concern. These correspond with Eigenmodes of the cavity housing the bosses, as shown in Fig. 3.22. They are, however, not accounted for by synthesis techniques or ordinary cavity resonance predictions.

These Eigenmodes exist in any (uniform, non-uniform or oblique) waffle-iron filter, according to [74]. The spurious resonances are grouped in two bands of quasi-$\mathrm{TE_{m0}}$ modes[5], above and below the stop-band (respectively). Classical literature, eg. [25], holds that ideal uniform waffle-iron filters do not excite these modes, for two reasons. Firstly, all $\mathrm{TE_{m0}}$ modes for $m > 1$ are evanescent in the transmission band of interest. Secondly, the dominant $\mathrm{TE_{10}}$ mode exhibits a different symmetry to that of the Eigenmodes.

In practical (uniform and non-uniform) waffle-iron filters, quasi-$\mathrm{TE_{m0}}$ mode resonances for even values of m may arise due to manufacturing inaccuracy [74, 75], particularly because

---

[5] The complexity of the cavity rules out the existence of conventional rectangular cavity Eigenmodes.

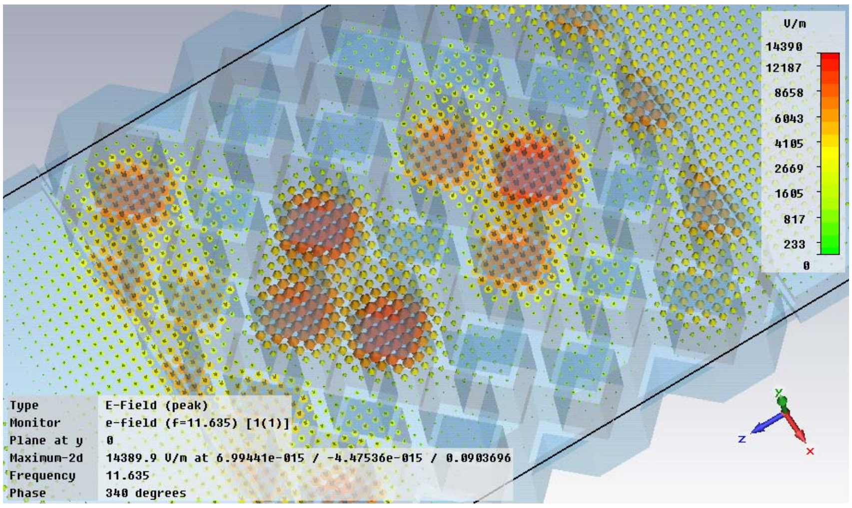

Type E-Field (peak)
Monitor e-field (f=11.635) [1(1)]
Plane at y 0
Maximum-2d 14389.9 V/m at 6.99441e-015 / -4.47536e-015 / 0.0903696
Frequency 11.635
Phase 340 degrees

(a) Quasi-TE_{102} at 11.66 GHz.

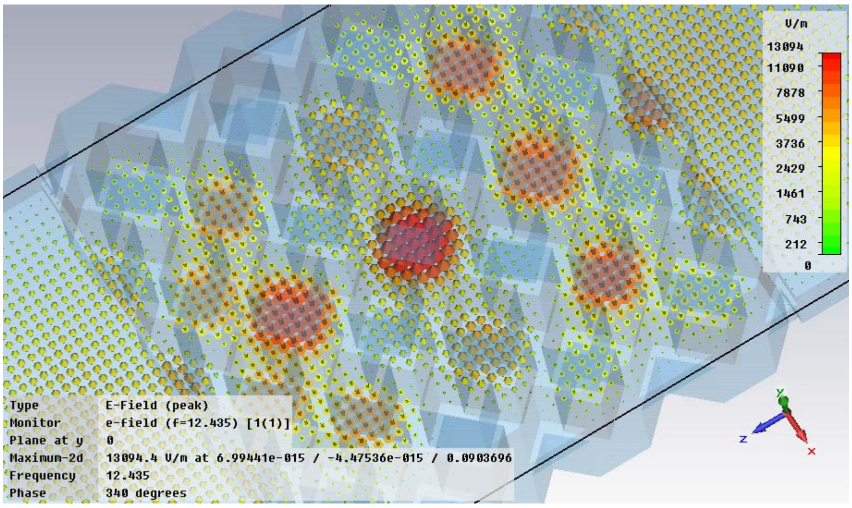

Type E-Field (peak)
Monitor e-field (f=12.435) [1(1)]
Plane at y 0
Maximum-2d 13094.4 V/m at 6.99441e-015 / -4.47536e-015 / 0.0903696
Frequency 12.435
Phase 340 degrees

(b) Quasi-TE_{103} at 12.51 GHz.

Figure 3.22: $\vec{E}$-fields of spurious cavity resonances in oblique waffle-iron filters.

of misaligned bosses that appear asymmetrical with respect to the H-plane (as shown in Fig. 3.23), exciting an x-directed $\vec{E}$-field component. Since they rely on manufacturing tolerance, they are not revealed in full-wave analysis.

Resonances of odd-ordered quasi-$\mathrm{TE}_{\mathrm{m}0}$ modes, such as those seen in Fig. 3.22, may be excited by the dominant TE_{10} mode in the presence of H-plane asymmetry, according to [74]. In this particular inquiry, the inclined faces generated by the design do cause local $\vec{E}$-fields which excite these exact modes. If these resonances occur in the buffer band (as they do for this specific example), they do not affect the filter's ability to achieve a specific pass-band or stop-band specification. This is, however, not always true (as is demonstrated in §3.6), in which case the filter has to be re-designed to move the spurious resonances out of the required stop-band or pass-band. Specifically checking for the existence and

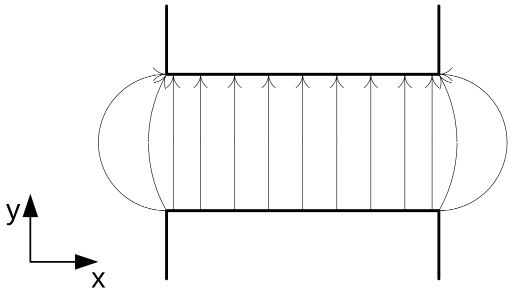

Figure 3.23: $\vec{E}$ fields for aligned (left) and misaligned (right) bosses. Note the nett $+x$-directed $\vec{E}$-field component in the latter.

frequencies of these spurious resonances is therefore a vital step in the design of oblique waffle-iron filters.

3.4.5 Suppression of higher order modes

Since this topology has never been published before, it is prudent to verify the suppression of higher order modes. The S_{11} and S_{21} of the oblique model for the TE_{20} and TE_{30} modes are shown in Fig. 3.24(a), and the TE_{10} - TE_{30} mode conversion in Fig. 3.24(b). The suppression of the TE_{20} and TE_{30} modes correspond to that of the TE_{10} mode, as expected. Significant (up to -10 dB) coupling occurs between the two odd modes (TE_{10} and TE_{30}) above the synthesised transmission band, which causes a significant amount of incident power reflected as a TE_{30} mode.

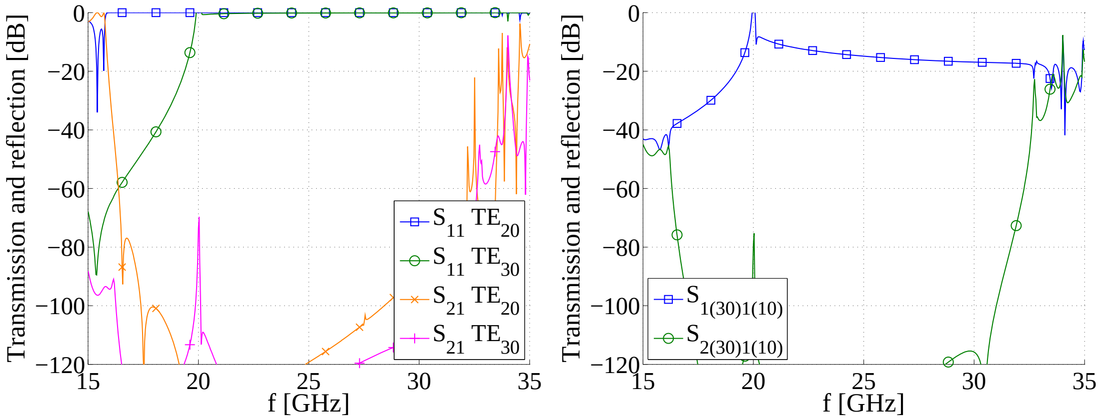

(a) TE_{20} and TE_{30} transmission and reflection responses

(b) Coupling between the odd modes TE_{10} and TE_{30}.

Figure 3.24: Higher-order modes in oblique waffle-iron filters.

3.4.6 Synthesis evaluation

The procedure represents a completely new approach to waffle-iron filter synthesis, and is capable of producing filters more compact than non-uniform filters for a given filter order. As with non-uniform filters, synthesis control over the pass-band response is achieved, which represents an improvement over the classical uniform waffle-iron filters. The first-iteration synthesis accuracy is, however, not as good as the non-uniform filter, and up to -10 dB reflected mode conversion is observed between the TE_{10} and TE_{30} modes. Of greater concern, is the spurious resonances excited inside the filter cavity, which is unaccounted for in the circuit model. This is a significant drawback to the topology, and has to be evaluated with some scrutiny in any design.

3.5 Power handling capability

Two specifications in maximum power handling capability are considered in filter design [25]. The first is maximum peak power handling capability, where the $\vec{E}$-field and *multipactor* breakdown are considered [26]. The second is peak continuous wave (CW) operation, where conduction loss and the subsequent rise in material temperature are considered.

Maximum average power handling is determined by the thermal properties of the manufacturing material, as well as the allowed rise in temperature of the component. Thermal effects can be mitigated by additional heat sinks placed around the exterior of the filter, and is not a strong function of filter dimensions. It is, therefore, omitted from the analysis. Multipactor breakdown (which relies on the mean free path of electrons) only occurs when the mean free path of electrons are of distances comparable to feature dimensions, which only occurs near vacuum conditions. For air-filled waveguide at or above 1 atmosphere, this effect may safely be neglected [26, 76]. This leaves $\vec{E}$-field breakdown the single limiting factor in power handling analysis, and will be discussed in some detail.

The breakdown $\vec{E}$-field value in air is given in [77] as

$$E_B \approx 30 \times \frac{298}{T} p \text{ V/cm RMS} \tag{3.12}$$

where T is the air temperature in Kelvin and p is the air pressure in Torr. It is important to note that this is an RMS value of field strength, and is mistakenly cited as a peak field strength in [26, 76].

E_B is found to be 22.8 kV/cm RMS ($\approx$ 30 kV/cm peak, the value used in classical texts such as [25]) only under the following conditions:

1. Still, dry air at 298K inside the waveguide.
2. Air pressure at 760 Torr (1 atmosphere).
3. Microwave frequencies ($\lambda \ll 4$m).
4. CW operation, or pulse width $\tau > 1.36\mu$s.

The particular design, however, is required to operate at an altitude of 3000 m (where the barometric equation predicts air pressure of around 522 Torr) and maximum temperature of 75°C or 348 K. Additionally, the $\vec{E}$-field inside the structure is dependent on reflections at the ports, which are not necessarily modelled in full-wave analysis. If a maximum output port mismatch of -20 dB is allowed at transmission frequencies, the maximum SWR in the internal $\vec{E}$-field is 1.22. This means that the maximum $\vec{E}$-field $E_{\max}$ is 9.91% higher than the maximum $\vec{E}$-field under matched conditions. The choice of E_B should, therefore, include a 10% safety factor, to allow for some standing wave pattern inside the filter due to port mismatch.

Having taken these conditions under consideration, a safe value of E_B is calculated as 12.1 kV/cm RMS, or 17.1 kV/cm peak. This is about half the classical “safe” value.

The nature of the input power spectrum should also be considered in evaluating the power handling capability of the filter. It is quite common for a filter to have different specifications for peak and CW power ratings in the transmission and stop-bands, or that the filter need not adhere to any power specification in the buffer band (which would relieve the condition for verifying the maximum $\vec{E}$-fields at spurious resonances).

Evaluating the maximum electric fields in the vicinity of sharp corners is no trivial matter [78]. According to analytical theory, the electric field strength approaches infinity at perfectly sharp corners [79], as shown in Fig. 3.25(a). Practical manufacturing tolerances would, however, always render some rounding.

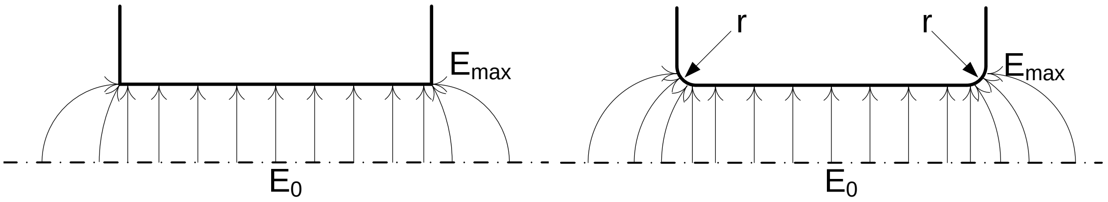

(a) Unrounded corners.

(b) Rounded corners.

Figure 3.25: $\vec{E}$-field patterns with unrounded and rounded corners.

.

Rounding outward edges and corners, as discussed in [80], can increase the power handling capability of waffle-iron filters by reducing the maximum $\vec{E}$-field around the sharp corners [76]. With E_0 and $E_{\max}$ the peak electric fields indicated in Fig. 3.25, [80] provides radii curves which guarantee an upper bound on $E_{\max}$:E_0 of 3:1 or less in the presence of an electric wall (as is the case here). Values in the region of 1.4:1 [44, 25] are commonly used in publication, since the total power handling capability of the filter is half that predicted by the breakdown in the uniform region E_0 [80]. This value is therefore used in design examples.

The rounding of edges for high power applications influence the electrical response of both oblique and non-uniform filters. The most noticeable effect is an upward shift in the stop-band, as shown in Table 3.10. This is in line with observations noted in [44]. Due to the small magnitude of shift (typically $< 5\%$), the synthesis as stated previously may be conducted with straight edges, with edge rounding only considered during final full-wave tuning.

Table 3.10: Rounding effect on filter stop-band, measured as deviation off square edged boss stop-band centre frequency.

r/b''		0	0.05	0.1	0.15	0.2
Non-uniform:	f_∞	20.402	20.539	20.661	20.802	20.973
	Deviation	0%	+0.674%	+1.272%	+1.962%	+2.801%
Oblique:	f_∞	21.311	21.687	22.000	22.219	22.443
	Deviation	0%	+1.762%	+3.233%	+4.260%	+5.311%

Decreasing E_0, irrespective of rounding, can always be accomplished (for a constant input power level) by increasing the distance d between two opposing electrical walls that support the normal $\vec{E}$-field [76]. It is therefore expected that increasing either the minimum l, w or b'' in Fig 3.7 will decrease E_0, and for a fixed radius, decrease $E_{\max}$.

3.6 Comparison of synthesis methods

3.6.1 Comparison with classical synthesis

Three sets of filters are synthesised, to compare the two new synthesis methods (oblique and non-uniform) to classical synthesis methods. In each set, four filters are synthesised to meet specification "A" in Table 3.11, which is identical to the required final filter specifications ("B") except for the omission of the third required stop-band, and allowing for a 5 dB increase[6] in reflection response by the quarter-wave matching sections required on either side. Each set consists of one non-uniform filter, one oblique filter, and two uniform filters; one designed using Cohn's corrugated data method, the other using the Marcuvitz T-junction data method, as discussed in §3.2. In each set, filters with comparative size, attenuation and power handling capability are compared on electrical response; in particular, the first-iteration synthesis accuracy. It is for this reason that no full-wave tuning was applied to any of the prototypes post-synthesis. These results are shown in Figs. 3.26, 3.28 and 3.29 respectively.

The first set compares four filters with $a \approx 22.86$ mm, total filter length $l_t \approx 22.86$ mm, $b'' \approx 2$ mm and an approximately square boss surface area of $l \times l' \approx 5$ mm^2, the dimensions of which are shown in Table 3.12. In the second set (the dimensions of which are shown in Table 3.13), all four filters have an increased $l_t \approx 2a$, to improve the stop-band roll-off. The previous dimensions of b'' and $l \times l'$ are maintained, to maintain the power handling capability. In the third set, boss spacing of the filters are all reduced to $b'' = 1$ mm and and the surface area to $l \times l' \approx 1.8$ mm, as shown in Table 3.14. This reduces the power handling capability of all four filters, but will investigate the four synthesis techniques for possible compact applications.

Table 3.11: Specification sets for waffle-iron filter synthesis.

	$\|S_{11}\|$	$\|S_{21}\|$ (1)	$\|S_{21}\|$ (2)	$\|S_{21}\|$ (3)
"A"	-30 dB	-65 dB	-60 dB	–
	8.5 - 10.5 GHz	17 - 21 GHz	22.5 - 31.5 GHz	–
"B"	-30 dB	-65 dB	-60 dB	-55 dB
	8.5 - 10.5 GHz	17 - 21 GHz	22.5 - 31.5 GHz	34 - 42 GHz
"C"	-25 dB	-30 dB	-30 dB	–
	3.6 - 4.2 GHz	7.25 - 7.75 GHz	10.75 - 12.8 GHz	–

Of the four synthesis methods, in the first set, the design based on Marcuvitz's data and the non-uniform model exhibit the best pass-band reflection response. All four designs

---

[6] See §3.7.2 for the motivation of this figure.

Table 3.12: Dimensions of four initial waffle-iron designs with $b'' \approx 2$ mm and $l_t \approx a$. Dimensions are as indicated in Figs. 3.7 and 3.20, with n_t and n_s the number of transversal and longitudinal grooves, respectively.

	Corrugated	Marcuvitz	Non-uniform	Oblique
a	21.58	22.80	22.86	22.31
b	7.96	8.30	7.68	8.72
b_T	4.67	2.42	4.49	2.80
b''	1.79	1.92	2	1.79
l or l_i	2.78	2.10	2.99, 2.55, 2.55, 2.99	1.95, 1.87, 1.87, 1.95, 1.95, 1.87, 1.87, 1.95
l' or l'_i	2.62	1.70	1.59, 3.01, 2.87, 3.01, 1.59	1.01, 2.24, 1.64, 2.24, 2.02, 2.24, 1.64, 2.24, 1.01
w or w_i	2.78	2.10	2.29	1.95, 1.87, 1.87, 1.95, 1.95, 1.87, 1.87, 1.95
w' or w'_i	2.78	1.70	2.29	1.01, 2.24, 1.64, 2.24, 2.02, 2.24, 1.64, 2.24, 1.01
l_t	21.58	22.8	23.14	22.31
n_t	5	7	4	8
n_l	5	7	6	8

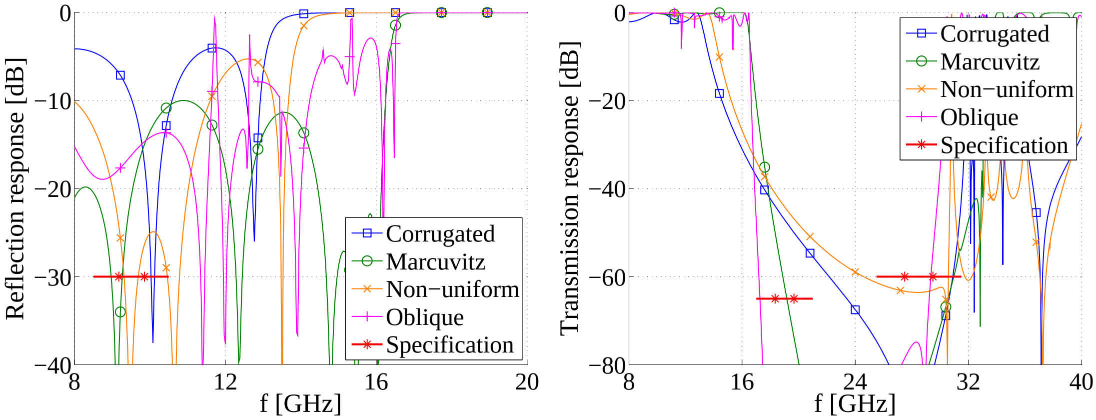

(a) Reflection response (b) Transmission response

Figure 3.26: Comparison of four synthesis methods on the same specifications before full-wave tuning, $b'' \approx 2$ mm, $l_t \approx a$.

have their stop-band centered at approximately 27 GHz, with the slower upper roll-off of the corrugated and non-uniform designs compensated for by a lower f_1. Noticeable, though, is the sharp roll-off of the oblique design. This is attributed to the increased effective order ($n = 8$, compared to 4 or 5) of the filter, whilst maintaining the same size and power handling capability. The oblique filter may therefore be presented as a more compact equivalent of traditional waffle-iron filters.

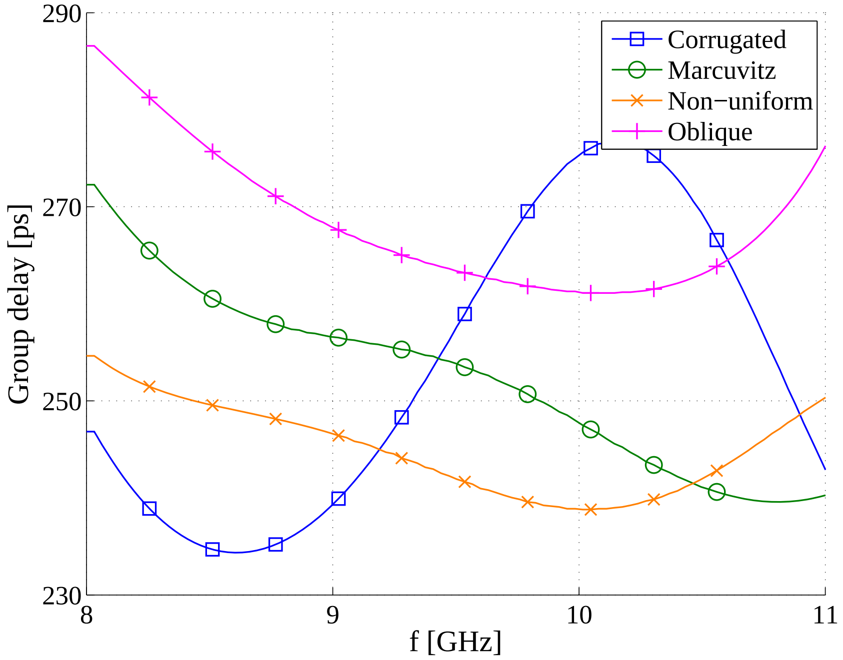

Figure 3.27: Comparison of group delay responses of four synthesis methods.

All four designs feature relatively flat group delay over the band of interest (8.5 - 10.5 GHz), due to the distance from the stop-band upper edge f_1 (as shown in Fig. 3.27). The design using Cohn's corrugated data features the largest variation, at 18.1%, followed by the Marcuvitz data design (7.7%), oblique (5.6%) and non-uniform (4.5%) designs. The effect of the spurious resonances in the oblique design are also clearly visible above 11.5 GHz.

It is immediately evident that none of the four filters satisfy the set specifications without full-wave tuning. The need for adjustments to the terminating guide height to the improve the input reflection response has been documented in both [41] and [25], and even minor adjustments to the terminating waveguide height b_T will improve the input reflection response. The stop-band performance of all of the filters may also be improved by lengthening them (adding more sections), as stated previously. It was also shown previously that the upper stop-band roll-off for the non-uniform synthesis is slower than predicted by the circuit model, and that model of the oblique filter my predict a wider stop-band than what is actually realised.

Table 3.13: Dimensions of four initial waffle-iron designs with $b'' \approx 2$ mm and $l_t \approx 2 \times a$.

	Corrugated	Marcuvitz	Non-uniform	Oblique
a	21.58	22.80	22.86	22.31
b	7.96	8.30	7.72	8.72
b_T	4.67	2.42	2.97	2.80
b''	1.79	1.92	2	1.79
l or l_i	2.78	2.10	2.34, 2.34, 2.09, 2.30, 2.42, 2.42, 2.30, 2.09, 2.34, 2.34	1.95, 1.87, 1.87, 1.95, 1.95, 1.87, 1.87, 1.95, 1.95, 1.87, 1.87, 1.95, 1.95, 1.87, 1.87, 1.95
l' or l'_i	2.62	1.70	1.38, 2.80, 2.76, 2.74, 2.67, 2.76 2.67, 2.74, 2.76, 2.80, 1.38	1.01, 2.24, 1.64, 2.24, 2.02, 2.24, 1.64, 2.24, 2.02 2.24, 1.64, 2.24, 2.02 2.24, 1.64, 2.24, 1.01
w or w_i	2.78	2.10	2.29	1.95, 1.87, 1.87, 1.95, 1.95, 1.87, 1.87, 1.95,
w' or w'_i	2.78	1.70	2.29	1.95, 1.87, 1.87, 1.95, 1.95, 1.87, 1.87, 1.95,
l_t	43.16	45.60	50.39	44.62
n_t	9	13	10	16
n_l	5	7	6	8

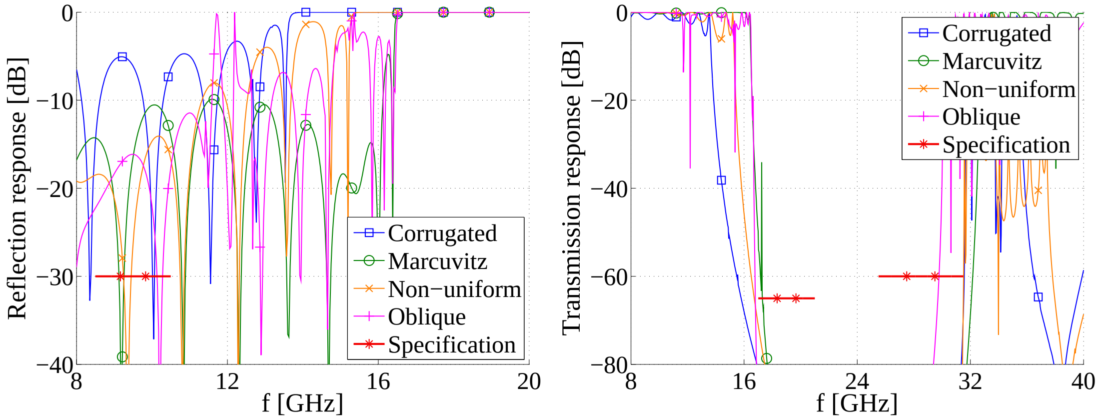

(a) Reflection response (b) Transmission response

Figure 3.28: Comparison of four synthesis methods on the same specifications before full-wave tuning, $b'' \approx 2$ mm, $l_t \approx 2 \times a$.

Doubling the length of each filter, as is done in the second set, increases the roll-off (increased order) and the maximum stop-band attenuation, as shown in Fig. 3.28. To note from this example, is that three of the four models (Cohn's corrugated data, Marcuvitz data and oblique design) are increased in length by replicating existing dimensions. In the non-uniform model, a complete redesign (without necessarily repeating values of l and l') is possible, providing additional control over the stop-band response. This is illustrated by the first-iteration accuracy of the lower cut-off frequency f_1. The non-uniform and oblique designs maintain superior in-band reflection response, with the oblique filter still exhibiting unwanted resonances in the buffer band.

Table 3.14: Dimensions of four initial waffle-iron designs with $b'' \approx 1$ mm.

	Corrugated	Marcuvitz	Non-uniform	Oblique
a	23.93	22.80	22.86	22.34
b				8.84
b_T	4.42	1.26	2.149	1.33
b''	1.02	0.98	1	0.95
l or l_i	3.54	1.70	1.40, 1.58, 1.85, 1.92, 1.92, 1.85, 1.58, 1.40	0.65, 0.77, 0.94, 1.15, 1.15, 0.94, 0.77, 0.65, 0.65, 0.77, 0.94, 1.15, 1.15, 0.94, 0.77, 0.65
l' or l'_i	1.25	1.15	0.66, 1.62, 1.42, 1.54, 1.39, 1.54, 1.42, 1.62, 0.66	0.71, 1.28, 1.12, 0.85, 0.86, 0.85, 1.12, 1.28, 1.42 1.28, 1.12, 0.85, 0.86, 0.85, 1.12, 1.28, 0.71
w or w_i	3.54	1.7	1.14	0.65, 0.77, 0.94, 1.15, 1.15, 0.94, 0.77, 0.65, 0.65, 0.77, 0.94, 1.15, 1.15, 0.94, 0.77, 0.65
w' or w'_i	1.25	1.15	1.14	0.71, 1.28, 1.12, 0.85, 0.86, 0.85, 1.12, 1.28, 0.71 0.71, 1.28, 1.12, 0.85, 0.86, 0.85, 1.12, 1.28, 0.71
l_t	23.93	22.80	25.36	22.34
n_t	5	9	8	16
n_l	5	9	11	16

When designed for $b'' \approx 1$ mm, as is done in the third set, the four filters all exhibit increased reflection response in-band. As the decrease in the dimension b'' necessarily leads to a decreased margin for error in input guide height b_T, this is to be expected. The input reflection may again be corrected by simple full-wave simulation adjustment of b_T. As expected (for a filter of higher order), the stop-band roll-off is improved in all four cases. Again, the oblique filter has the sharpest roll-off, being of highest order, and all four models feature accurate placement and width of the stop-band.

Unfortunately, the spurious resonances in the oblique filter now appear in centre of the transmission band. In an actual prototype, this would necessitate a complete redesign of the filter (changing the dimensions of the quasi-TE$_{\mathrm{m0}}$ resonant cavity) which would lead

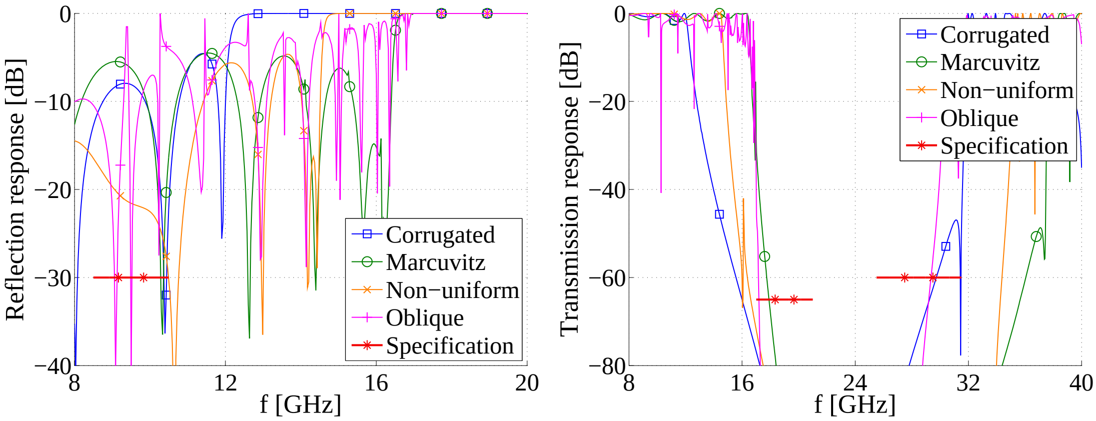

(a) Reflection response (b) Transmission response

Figure 3.29: Comparison of four synthesis methods on the same specifications before full-wave tuning, $b'' \approx 1$ mm.

to different complex Eigenmodes and relocation of the spurious resonances.

3.6.2 Comparison with full-wave optimisation methods

Present state-of-the-art designs of waffle-iron filters rely on full-wave optimisation. To evaluate the two new design methods, it is of interest to compare the two new methods to the 100% full-wave optimisation methods of [45, 46, 47]. As an test example, the specifications used in Fig. 6 of [47] (shown as set “C” in Table 3.11) are used to design both a non-uniform and an oblique filter. The designs are further constrained to maintain a similar size (waveguide width a and total length l_t) and power handling capability[7] (boss spacing b'' and minimum gap width l_{min}) as the previously published design. Lastly, it was noted during the example synthesis of the non-uniform filter that the circuit model predicts a transmission band 40% wider than what is achieved by the full-wave simulated filter. It is for this reason that the circuit model optimisation is performed with goals bandwidths 400 MHz, or 66%, wider than the required specification.

The comparative dimensions are shown in Table 3.15, with the circuit and full-wave simulation results of the non-uniform and oblique filters shown in Figs. 3.30 and 3.31, respectively. In both cases, the untuned and tuned dimensions and full-wave simulation results are shown.

This example illustrates the simplicity of the required post-synthesis full-wave tuning required for both the non-uniform and oblique filters. In both cases, an adjustment of

---

[7] Since no rounding was performed in the published design, none is performed in this design.

Table 3.15: Dimensions of previously published waffle-iron filter, and comparative oblique and non-uniform design results before and after full-wave tuning. Dimensions indicated as (–) remain unchanged.

	[47]	Non-uniform		Oblique	
		Pre-tuned	Tuned	Pre-tuned	Tuned
a	61	61	–	54.67	–
b	20.2	18.29	**19.4** (+6%)	21.08	**19.4** (-8.7%)
b_T	10	8.93	–	10.64	**8.4** (-26%)
b''	5.4	5.4	–	5.46	**5.4** (-1.1%)
l_i	4.76, 9.9, 9.9, 9.9, 9.9, 4.76	5.91, 7.11, 7.11, 5.91	–	6.83, 6.32, 6.83, 6.83, 6.32, 6.83	–
l'_i	3.2, 3.36, 3.36, 3.36, 3.2	3.14, 6.51, 6.21, 6.51, 3.14	–	3.35, 5.97, 5.97, 6.70, 6.32, 6.83, 6.32, 3.35	–
w or w_i	6.1	6.1	–	6.83, 6.32, 6.83, 6.83, 6.32, 6.83	–
w' or w'_i	6.1	6.1	–	3.35, 5.97, 5.97, 6.70, 6.32, 6.83, 6.32, 3.35	–
l_t	65.6	51.54	–	54.67	–
n_t	6	4	–	6	–
n_l	6	6	–	6	–

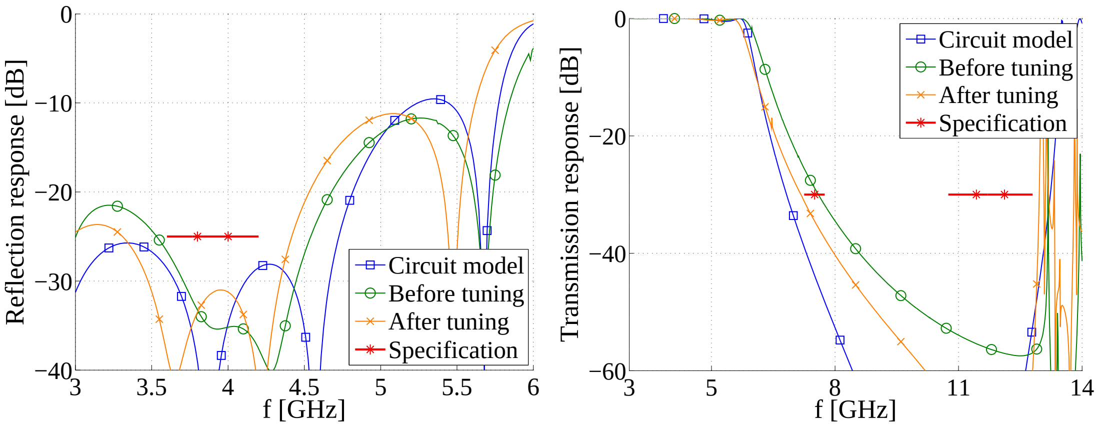

(a) Reflection response

(b) Transmission response

Figure 3.30: Development of non-uniform filter to meet specification set “C”.

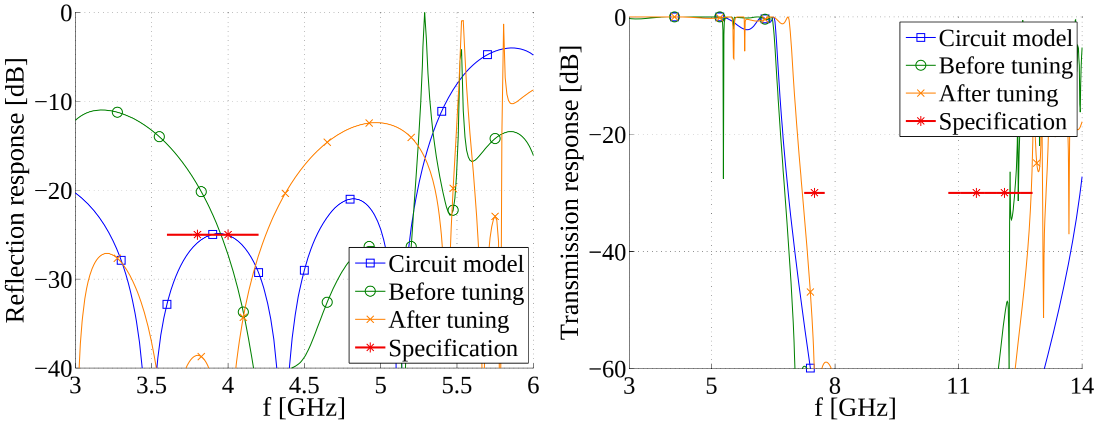

(a) Reflection response (b) Transmission response

Figure 3.31: Development of oblique filter to meet specification set “C”.

b is required to correct the stop-band centre frequency. The oblique design required adjustment of b'' to widen the stop-band, as well as a rather sizable adjustment to b_T to correct the input reflection response in-band. Both designs retained all other internal dimensions from the circuit model based synthesis, which means that full-wave adjustment to a single dimension is required in the non-uniform filter, and to three in the oblique filter.

In comparison, the method in [47] requires full-wave optimisation to all dimensions as variables. The solution space is therefore of dimension N, whereas the singular dimensional adjustments made in the proposed syntheses are, effectively, one-dimensional optimisations. The computational time required for the solution in [47] is therefore significantly more than is required for the proposed methods. Further mode, [47] requires a dedicated FEM code, whereas the proposed solutions use commercially available circuit solvers and full-wave EM simulation packages.

Both non-uniform and oblique filters are shorter (by 27% and 20%, respectively) than the prototype in [47], whilst maintaining the same boss spacing b'' and similar or wider groove widths l and w, indicating similar power handling capability.

Spurious resonances, similar to those previously observed, are visible in the oblique prototype. These resonances, clearly visible at 5.54 and 5.78 GHz, occur in the buffer band of the filter, and do not interfere with the operation of the filter otherwise.

3.6.3 Comparison of power-handling capability

A final comparison is performed between the power handling capabilities of non-uniform and oblique filters of different dimensions. In each case, the same basic dimensions are used as before, but all external edges are rounded by $r = 0.2b''$. This would ensure that the maximum electric field strength $E_{\max}$ would never exceed 1.55 times the electric field strength E_0 between opposing bosses. The tests, therefore, serve to validate the data provided in [80].

The average power incident on a TE_{10} port is given [72] as

$$P = \frac{E_0^2 ba}{4Z_{\mathrm{TE}}} \tag{3.13}$$

where a and b are the port dimensions and

$$E_y = E_0 \sin\left(\frac{\pi x}{a}\right) = -Z_{\mathrm{TE}} H_x \tag{3.14}$$

which means that the incident port power P may be derived from the known simulation port parameters $\|E_y\|$ and $\|H_x\|$, with P proportional to $\|E_y\|^2$ for a constant frequency and dimension set. If P is therefore scaled from its simulated value to the required specification value

$$P_{\mathrm{spec}} = k_1 P$$

the actual maximum electric field inside the structure will be given by

$$E_{\mathrm{actual}} = \sqrt{k_1} E_{\max}$$

which must then be smaller than the E-field breakdown strength of 17.1 kV/cm peak. This is similar to the process stated in [76]. Alternatively, the maximum scale factor $1.71 \times 10^6 = k_2 E_{\max}$ for electric field breakdown may be calculated, and the maximum input power calculated as $P_{\max} = k_2^2 P$.

Using the method described in §3.5, the power handling capabilities of all the example non-uniform filters synthesised in this section are calculated as shown in Tables 3.16, and those of the oblique filters in 3.17, compiled as per the method described in .

Of immediate interest, is that (except at the transmission band of the filters with $b'' \approx$ 1 mm), $E_{\max}/E_0$ exceeds 1.55 by a large margin, and increases with frequency. A hexahedral mesh size of $\lambda/40$ is used throughout the simulated domain in all cases, which rules out numerical inaccuracy. Since the complexity of the internal filter structure leads to greater $\vec{E}$-field concentrations than predicted by [80] for singular bosses, it would appear

Table 3.16: Power handling capabilities of different non-uniform filters with edges rounded by $r = 0.2b''$.

		$b'' \approx 2$ mm			$b'' \approx 1$ mm		
f	[GHz]	9.5	19	28.5	9.5	19	28.5
$\lvert E_y \rvert$	[V/m RMS]	3185	2796	2746	4603	4042	3970
$\lvert H_x \rvert$	[At/m RMS]	6.118	6.967	7.095	8.843	10.071	10.255
P_{in}	[W]	1	1	1	1	1	1
E_{max}	[V/m RMS]	13566	16124	14399	17442	24184	17156
E_0	[V/m RMS]	8486	7338	5489	11309	13623	8499
E_{max}/E_0		2.06	2.19	2.62	1.54	1.77	2.01
P_{max}	[W]	7955.5	5631.5	7061.6	4812.6	2503.3	4974.4
$\lvert E_0 \rvert / \lvert E_y \rvert$		2.06	2.62	2.00	2.47	3.37	2.14
b''/b_T			2.25			2.15	

Table 3.17: Power handling capabilities of different oblique filters with edges rounded by $r = 0.2b''$.

		$b'' \approx 2$ mm			$b'' \approx 1$ mm		
f	[GHz]	9.5	19	28.5	9.5	19	28.5
$\lvert E_y \rvert$	[V/m RMS]	4125	3587	3520	5967	5190	5093
$\lvert H_x \rvert$	[At/m RMS]	7.744	8.906	9.081	11.209	12.888	13.139
P_{in}	[W]	1	1	1	1	1	1
E_{max}	[V/m RMS]	18712	27029	33870	31689	31224	30929
E_0	[V/m RMS]	8486	10400	7317	20393	10922	9172
E_{max}/E_0		2.21	2.60	4.63	1.55	2.86	3.372
P_{max}	[W]	4181.5	2004.1	1276.3	1458	1501.7	1530.5
$\lvert E_0 \rvert / \lvert E_y \rvert$		2.06	2.89	2.08	3.42	2.86	1.80
b''/b_T			1.64			1.41	

prudent to verify the maximum electric field strengths in full-wave simulation for each individual filter, and not rely solely on published data.

Also of note, is that the ratio of electric field strength at the port and between opposing bosses $|E_0|/|E_y|$ is not strictly a function of the relative waveguide heights b''/b_T (as it would have been in corrugated waveguide filters). This is also due to the complexity of the structures under analysis.

The most important result from both Table 3.16 and Table 3.17 is that wider boss spacings lead to higher power handling capabilities in both the oblique and non-uniform filters. This is quite intuitive, given the inverse relationship between electric field and distance with a constant potential difference. Non-uniform filters also provide superior power handling capabilities to oblique filters for equivalent boss spacings (more than double, in each case), and is therefore the preferred topology in high-power filters.

Given the noticeable rise in the ratio E_{max}/E_0 in higher frequencies, it is important to specify the peak power handling capability in both the transmission and stop-bands, and verify each independently. Here, three frequencies are chosen, representing the three bands of specification set "A" in Table 3.11. The variation in E_{max}/E_0 within these bands is found to be less than 5%, which makes the power handling capability at the centre frequency a satisfactory measure of the power handling capability over the full band. The rise in E_{max}/E_0 at higher frequencies may either be due to a rise in E_{max} (as is the case with the oblique filter of $b'' \approx 2$ mm) or to a reduction in E_0 (illustrated for the oblique filter of $b'' \approx 1$ mm), which means that an increased E_{max}/E_0 is not necessarily an indication of decreased power handling capability. The data does, however, indicate better power handling capability in-band than out-of-band in three of the four filters (the oblique filter of $b'' \approx 1$ mm, where E_0 is reduced at higher frequencies, being the exception).

3.6.4 Final prototype model selection

In choosing a topology for development of a final prototype, the following aspects of the two designs are considered:

- First iteration synthesis accuracy (minimal full-wave tuning required post-synthesis).
- Suppression of higher order modes and internal mode conversion.
- Spurious resonances.
- Power handling capability.
- Compactness (stop-band roll-off versus size).

In the first four of the five considerations, the non-uniform filter is superior to the oblique filter. The oblique filter is certainly more compact for an equivalent stop-band roll-off, but since a maximum size is not specified, this is not an advantage for this particular case. The oblique design, however, remains a viable option for compact applications if the spurious resonances are suppressed or moved to the buffer band. For this particular prototype, however, the non-uniform filter is selected for further development.

3.7 Final prototype development

This section will discuss the development of a non-uniform waffle-iron filter prototype to meet specification set "B" in Table 3.11. Additionally, the filter is specified to operate at 8 kW peak and 500 W average power across the transmission band, with -15 dBc peak (= 252 W) and average (= 15.81 W) power handling capability in each of the three stop-bands.

3.7.1 Initial synthesis

First prototype

Initial synthesis of a prototype to meet the wider stop-band specification proceeded identically to that discussed in §3.3. In keeping with the previously noted discrepancy between synthesised and realised transmission bandwidth, the filter and matching network are both synthesised for bands 1 GHz (50%) wider than specified, to reduce the amount of post-synthesis full-wave tuning required.

The total filter (including boss pattern and two quarter-wave transitions from b_T to full WR-90 guide height of 10.16 mm) is specified to have a maximum in-band reflection coefficient of -25 dB. If possible phase interaction between the waffle-iron boss pattern and the quarter-wave transitions are ignored, and each component (both transitions, and the filter) is synthesised to contribute equally to the in-band reflection of the cascaded structure, all three are required to achieve an $-29.7 \approx -30$ dB input reflection coefficient across the transmission band. This is set as the optimisation goal for the circuit model.

An initial consideration might be to use the frequency response of the matching network to enhance the stop-band characteristics of the total structure, perhaps easing the attenuation required by the filter alone. A quick consideration of the specification "B", however, reveals that the stop-bands are located at integer multiples of the transmission band. The quarter-wave transformer is also periodic, providing a maximum of 2.8 dB and a minimum of below 0.1 dB attenuation in each of the three stop-bands. The full burden of attenuation, therefore, rests on the filter alone.

The prototype is implemented with half-inductive input steps, rather than the half-capacitive steps in previous designs. This is not only because half-inductive pattern terminations result in wider filter stop-bands (See §3.2.3), but because rounding a boss edge by radius r requires a minimum boss width of $2r$. Since half-capacitive filters require a row of reduced width bosses at either end of the boss pattern, half-capacitive filters are more constrained in the choice of r than half-inductive filters.

Finally, the total length is increased from 8 to 16 sections. It was found during circuit optimisation that extending the stop-band, without increasing the filter order, decreased both the maximum stop-band attenuation and stop-band roll-off, leading to unsatisfactory circuit optimisation results. Both stop-band attenuation and roll-off are improved by adding more filter sections. What is important to note here, is that this circuit model representation was used in the early stages of development to evaluate the filter order, and increase it as needed in a circuit simulator. Using the classical synthesis methods or full-wave optimisation, the requirement for an increase in filter order would only be ascertained during full-wave simulation.

The resulting pre-tuning dimensions are shown in column “A” of Table 3.18. Only $l_{1..8}$ and $l'_{1..8}$ are provided, with $l_{9..16}$ and $l_{9..15}$ being symmetrical around the xy-plane. Rounding of radius r is applied to enhance the power-handling capability, rendering the untuned full-wave results in Fig. 3.32.

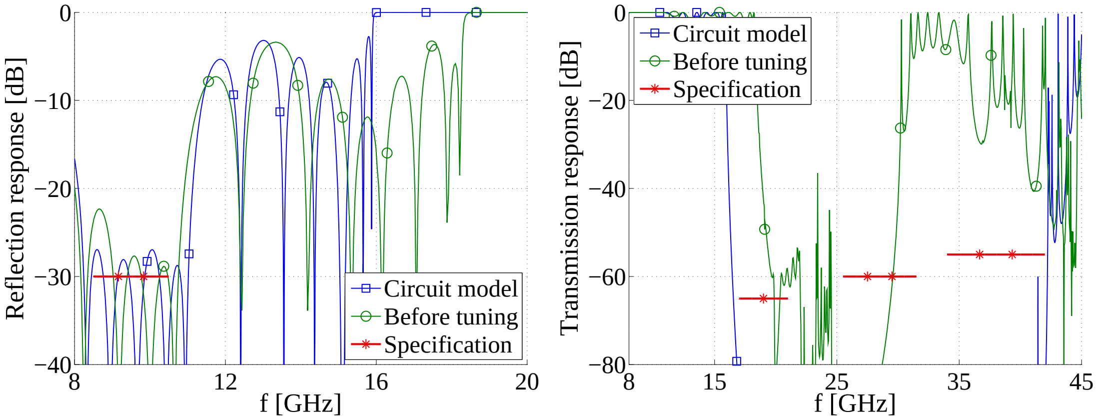

(a) Reflection response. (b) Transmission response.

Figure 3.32: Electrical response of final prototype version 1.

Despite excellent correspondence in transmission band response, the filter underperforms severely in the stop-band, especially above 30 GHz. This is due to the erosion of the $l < l'$ condition in synthesis, which in turn is caused by the severe reduction in b required to provide an f_∞ of 29.5 GHz. It is a common problem in waffle-iron filters covering three or more harmonics, which is solved by cascading two or more different waffle-iron filter sections [44, 25, 65] of different infinite cut-off frequencies f_∞, determined by different values of b. This would then necessarily lead to internal matching sections.

Table 3.18: Pre-tuned dimensions of two prototype filters to meet the final specification.

Dimension	"A"	"B"
a	22.86	22.86
b	5.85	9.29
b_1	–	5.81
b''	2.00	1.60
w	2.29	1.63
w'	2.29	1.63
b_T	4.29	2.37
l_1	1.20	0.86
l_2	3.96	1.65
l_3	2.84	1.85
l_4	3.39	1.65
l_5	2.73	1.59
l_6	3.56	2.08
l_7	3.29	2.06
l_8	3.49	1.49
l'_1	1.71	1.57
l'_2	2.08	1.68
l'_3	2.74	1.52
l'_4	2.57	1.65
l'_5	2.48	1.55
l'_6	2.31	1.61
l'_7	2.43	1.58
l'_8	2.38	1.58
r	0.40	0.32

Second prototype

An alternative to cascading and matching independent waffle-iron filters, is to use a single circuit model on the whole structure, but applying a different value of b for a number of transversal grooves inside the filter without changing the boss spacing b'' or number of transversal grooves. This section would then provide attenuation at higher frequencies, covering the fourth stop-band 34 - 42 GHz, whilst maintaining constant power handling capability.

A filter is subsequently synthesised with the middle 6 transversal grooves reduced to a height of b_1 (shown in Fig. 3.33(b)), compared to the previous model shown in Fig. 3.33(a)), to effectively synthesise two stop-bands centered at 24.25 GHz and 38 GHz, respectively. Further more, b'' is reduced to 1.6 mm to increase the effective width of each stop-band, and decreasing l and l' to avoid the "wide shallow grooves" for which the short-circuited stub model is less accurate. The number of transversal columns of bosses and longitudinal slots are increased to 7 of width $w' = w = 1.63$ mm to maintain the uniformity of the boss pattern. It is expected that this reduction will also decrease the power handling capability of the filter to below the required 8 kW $P_{\max}$ (based on the data in Table 3.16). This requirement is, however, considered secondary to the stop-band attenuation requirement, and is implemented despite the reduction in power handling capability.

The remainder of the synthesis rendered dimensions shown in "B" of Table 3.18, with electrical responses in Fig. 3.34.

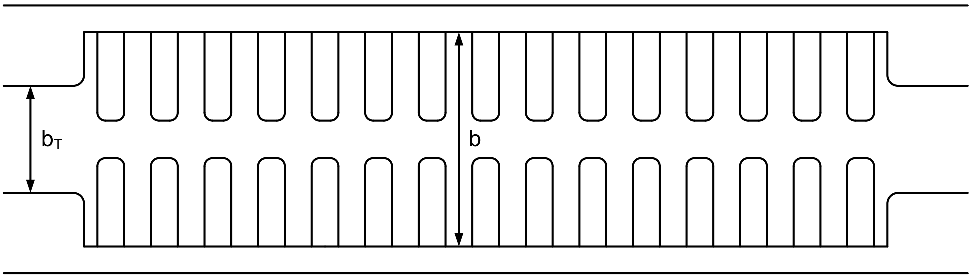

(a) No steps.

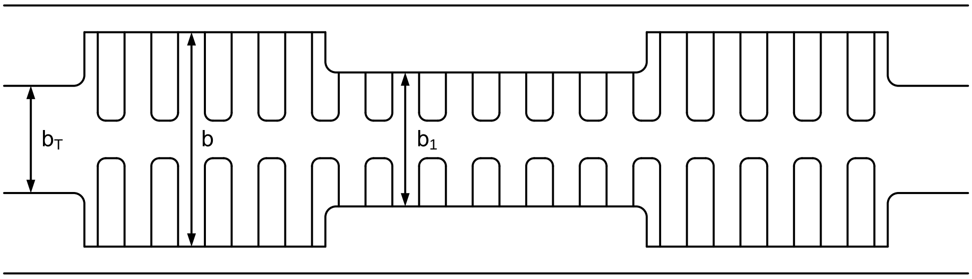

(b) Single step.

Figure 3.33: Sectioned view of waffle-iron filters with and without raised filter floors.

.

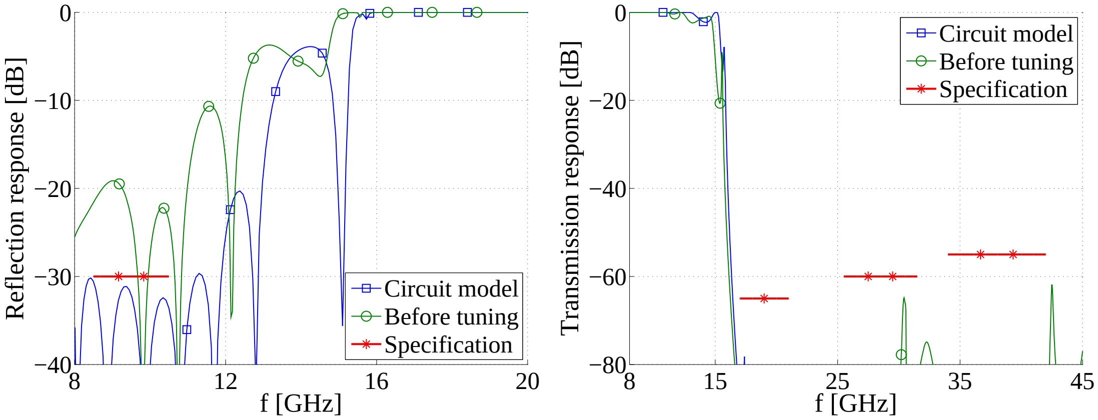

(a) Reflection response. (b) Transmission response.

Figure 3.34: Electrical response of final prototype version 2.

3.7.2 Full-wave tuning and simulation considerations

Quarter-wave matching section

After the performance of the initial dimensions are ascertained, the quarter-wave stepped-impedance transformer is included in the simulation model, and the dimensions b_2, b_3 (quarter-wave section heights), l_s (quarter-wave step length) and b_T (terminating guide height) optimised with the initial values of b_2, b_3 and l_s ascertained from classical quarter-wave stepped-impedance section matching [69]. This represents the only part of the synthesis where full-wave optimisation is used, and since an optimisation is performed over only the transmission bandwidth (as opposed to the full stop-band) for four dimensions (as opposed to all internal dimensions), this is still a computationally less intensive process than the state-of-the-art.

By optimising the waffle-iron filter and cascaded matching sections in unity, rather than simply attaching separately synthesised quarter-wave matching sections at either end of the filter, phase interaction unique to the specific filter and matching section can be used to achieve -25 dB match in the transmitted band without either matching section or filter having to achieve -30 dB input reflection match in isolation. The resulting dimensions of the quarter-wave section are shown in Table 3.19.

Table 3.19: Quarter-wave matching section dimensions.

Dimension	[mm]
a	22.86
b_1	10.16
b_2	7.52
b_3	4.29
b_4	2.94
l_s	11.4

Higher-order modes

The symmetry around the E-plane excludes the possibility of propagating even modes in the simulation. As far as odd ordered modes are concerned, the filter (without the quarter-wave matching sections) clearly suppresses the TE_{30} and TE_{50} modes (shown in Fig. 3.35(a)) with reflected energy in higher modes below -40 dB (Fig. 3.35(b)).

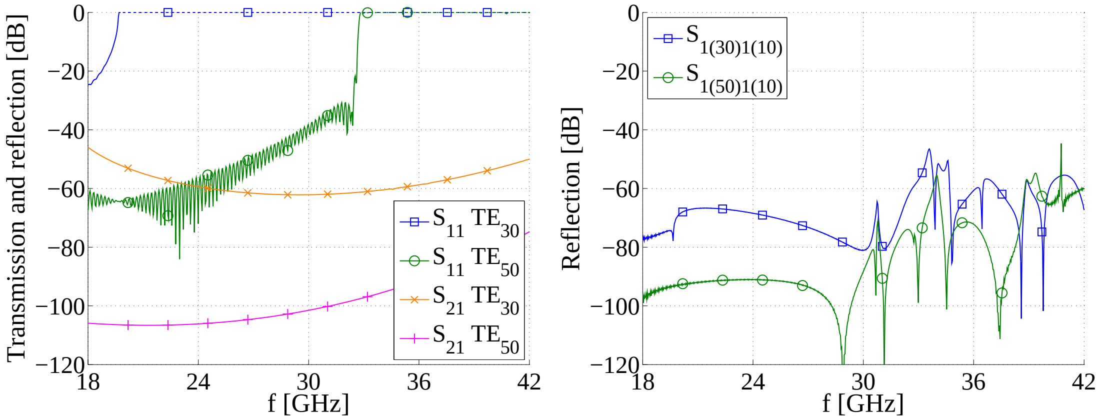

(a) TE_{30} and TE_{50} transmission and reflection.

(b) TE_{30} and TE_{50} reflection due to an incident TE_{10} mode.

Figure 3.35: Higher-order mode operation of final full-wave simulation model.

Power handling

The in-band power handling capability of the filter is below the 8 kW required, as expected. This is due to the decreased value of $b'' = 1.6$ mm used, as opposed to previous value of 2 mm. This reduction had a greater than expected effect in power handling capability. Increasing this parameter in full-wave simulation leads to a a significant decrease in stop-band bandwidth, which is deemed a more important design goal than the power handling capability.

By increasing the edge rounding from 0.3 mm to 0.5 mm, the power handling capability is increased from 3.198 kW to 4.092 kW, calculated as discussed in §3.5. Even though this is still below the 8 kW specification, it is considered adequate for an initial prototype. The increased rounding does, however, cause a upward shift in stop-band, which has to be offset by increasing the filter height b and inner section height b_1.

Tuning

Apart from the significant adjustment to input guide height b_T to improve the input match (as part of the optimisation of the quarter-wave matching section), and the minor adjustments to b and b_1 to offset the effect of boss rounding, no other adjustments to filter dimensions are required. The fact that the boss pattern was retained from synthesis to manufacturing illustrates the power and convenience of the circuit model based approach to synthesising waffle-iron filters. The final manufacturing dimensions of the filter are shown in Table 3.20, with tuned electrical response (which includes quarter-wave matching sections) in Fig. 3.36.

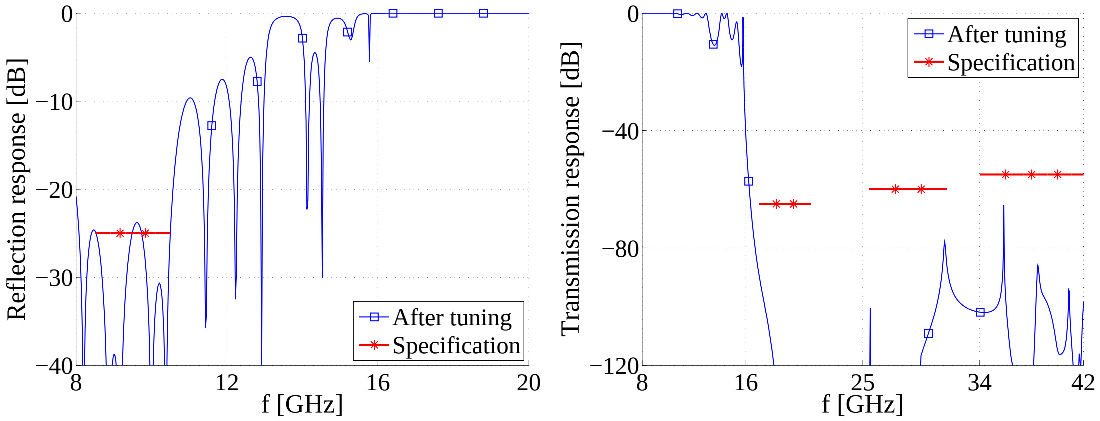

(a) Reflection response.

(b) Transmission response.

Figure 3.36: Final full-wave tuned non-uniform waffle-iron filter response, including quarter-wave matching sections.

3.7.3 Manufacturing and measured response

The filter was manufactured in four parts from Aluminium 6082, as shown in the machine sketches of Appendix A. The separate sidewalls allowed for the manufacturing of the 0.82 mm grooves required along the sidewalls. The rounding of the edge separating the b and b_1 floors was omitted, due to the increased manufacturing time required by the feature. Since the maximum $\vec{E}$-fields are concentrated between the bosses, the sharp corner in the floor step represents no risk of reduced power handling capability. Finally, the 1.5 mm radius of the machining bit is visible in the profile of the bosses along the floor height step.

To avoid excitation of the previously discussed x-directed $\vec{E}$-field modes that propagate along the longitudinal grooves (as shown in Fig. 3.23), proper alignment of the two main parts is essential. It is for this reason that eight 3 mm dowel pins were included in the assembly, two in each corner. The flange faces of the filter were also skimmed after assembly, to ensure proper contact with an opposing WR-90 flange.

The greatest construction difficulty for industrial application, however, remained the 3.9 mm bosses (where $b = 9.4$ mm). Machining an average 1.6 mm width groove to such a depth required a special elongated, re-enforced bit on the regular CNC machine. This difficulty was exacerbated in the 0.84 mm transversal grooves required by the input steps

Table 3.20: Untuned and tuned dimensions of final prototype filter. Dimensions indicated as (–) remain unchanged.

Dimension	Untuned	Tuned
a	22.86	–
b	9.29	**9.40** (+1.18%)
b_1	5.87	**6.00** (+2.22%)
b''	1.60	–
b_T	2.67	**2.94** (+10.1%)
l_1	0.86	–
l_2	1.65	–
l_3	1.85	–
l_4	1.65	–
l_5	1.59	–
l_6	2.08	–
l_7	2.06	–
l_8	1.49	–
l'_1	1.57	–
l'_2	1.68	–
l'_3	1.52	–
l'_4	1.65	–
l'_5	1.55	–
l'_6	1.61	–
l'_7	1.58	–
l'_8	1.58	–
r	0.32	**0.50** (+56%)

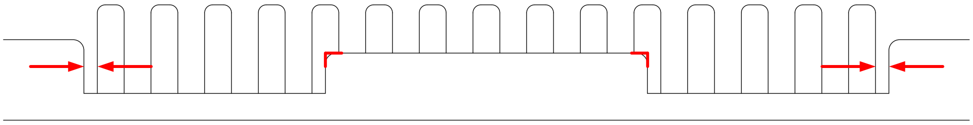

(a) Sectioned side view, showing 0.84 mm half-inductive groove and sharpened level steps.

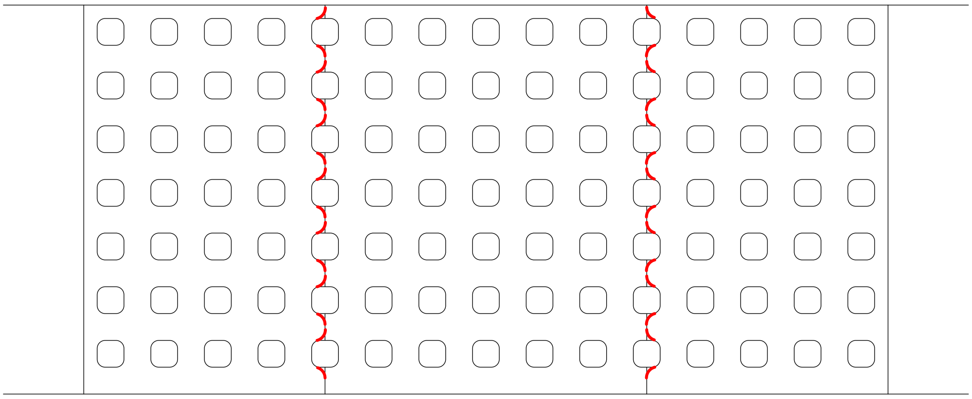

(b) Top view, showing machining bit imprints.

Figure 3.37: Manufacturing modifications to prototype “A”. Dimensions not to scale.

(Fig. 3.37(a)). Machining these grooves to a depth of 3.9 mm proved a time-consuming and expensive process.

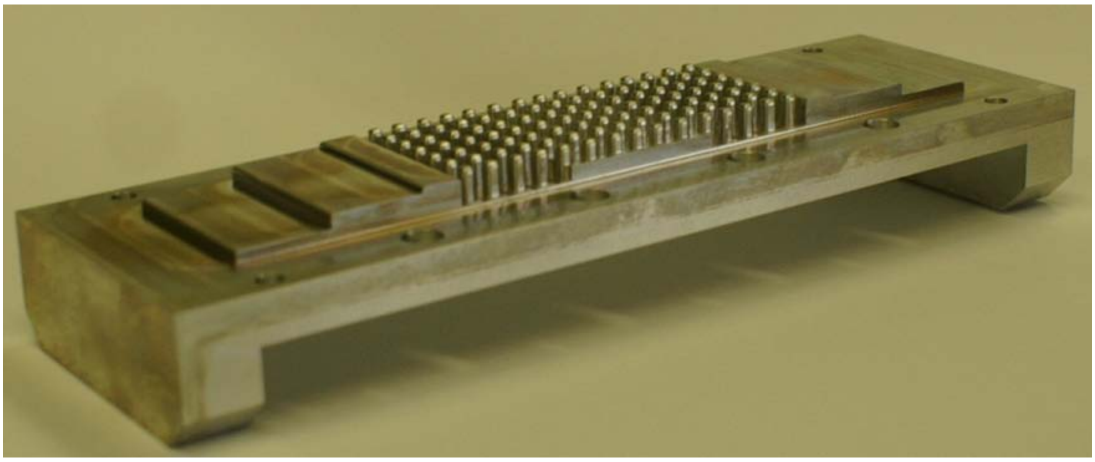

(a) Single section.

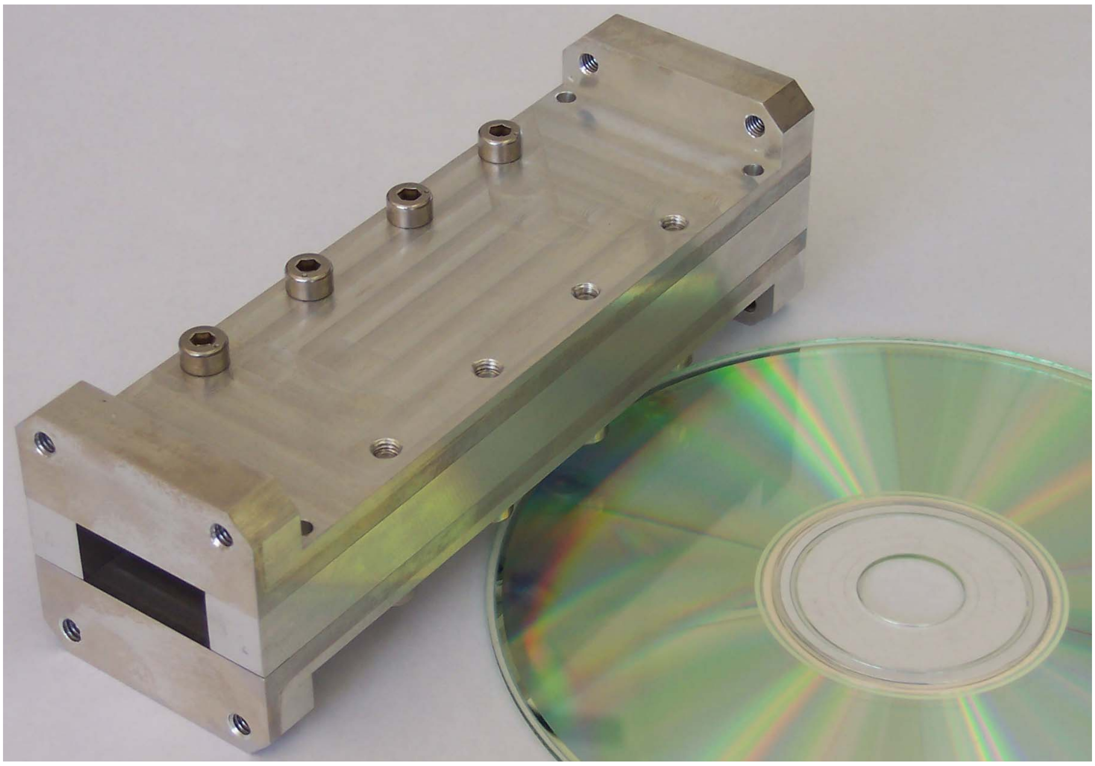

(b) Assembled filter, with compact disk for size comparison.

Figure 3.38: Photographs of constructed filter.

The electrical response of the waffle-iron filter was measured on an HP8510 VNA. The full two-port S-parameters were acquired over the transmission band using a TRL-calibration from 8 to 12 GHz. The WR-90 TRL line standard required for frequencies above X-band becomes too short to allow for practical measurements. Instead, two stop-band calibrations using SOLT standards were performed. In the band 16 - 22 GHz, WR-62

(15.80 × 7.90 mm) transitions were used at both ends of the filter, with the insertion loss due to waveguide port dimension mismatch calibrated out during post-processing. A similar procedure was performed in the band 24.5 - 43 GHz, with the two WR-62 transitions replaced by a WR-28 transition and a simple wire probe.

All measurements rely on a coaxial to rectangular waveguide transitions designed specifically for excitation of the the dominant TE_{10} mode. This is the only mode of interest, since the TWT amplifier the filter is to be used in conjunction with uses a similar transition at its output. More advanced probes and calibrations are required to measure the higher order mode operation of the filter.

The measured results of the prototype are shown in Fig. 3.39, compared to the full-wave simulated response.

The maximum in-band reflection response of the filter is 2.6 dB higher than the simulated reflection response, but is still below -21 dB across the band. More importantly, the input reflection follows the general shape of the simulated response, verifying the synthesis objective of realising a circuit optimised input reflection function. The maximum in-band insertion loss measured as 0.26 dB, which is satisfactory for the application.

The first of the three stop-band specifications (-65 dB S_{21} across 16 - 22 GHz) is met, with the stop-band roll-off frequencies predicted accurately to within 300 MHz. The second stop-band (25.5 - 31.5 GHz) features spurious resonant peaks of up to -50 dB, and the third stop-band (34 - 42 GHz) transmission peaks of up to -30 dB. These resonances are predicted by [74], and are, in part, due to some misalignment in the manufactured prototype. Another contributing factor is shallow grooves required in the centre section of the boss pattern ($l_{s1} = 2.2$ mm where $b_1 = 6$ mm) to attenuate the highest of the three stop-bands, compared to the deep grooves in the outer sections ($l_s = 3.9$ mm where $b = 9.29$ mm) for the lower two stop-bands. This decreased b_1 erodes the condition of “narrow deep grooves”, which the short-circuited series stub model is better suited for.

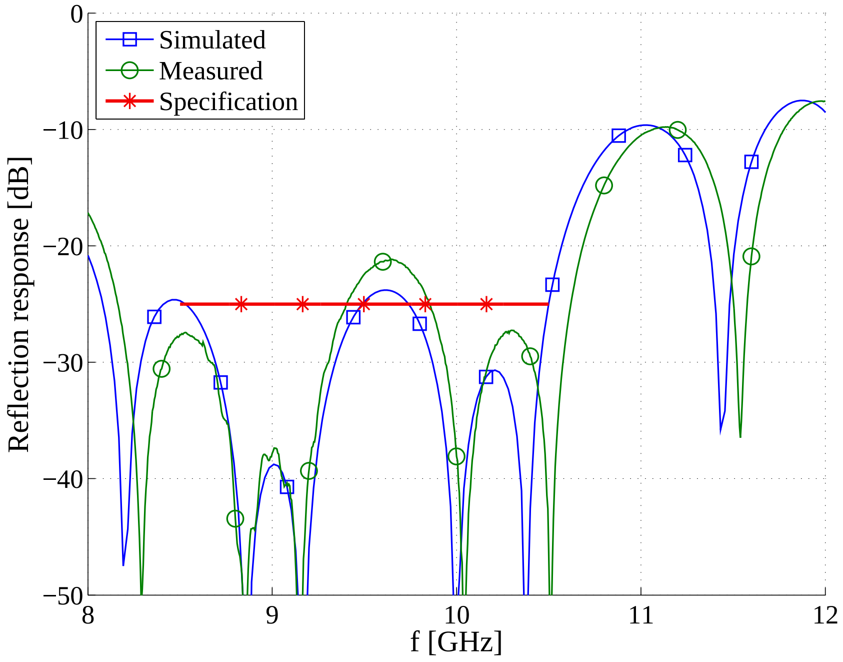

(a) Reflection response.

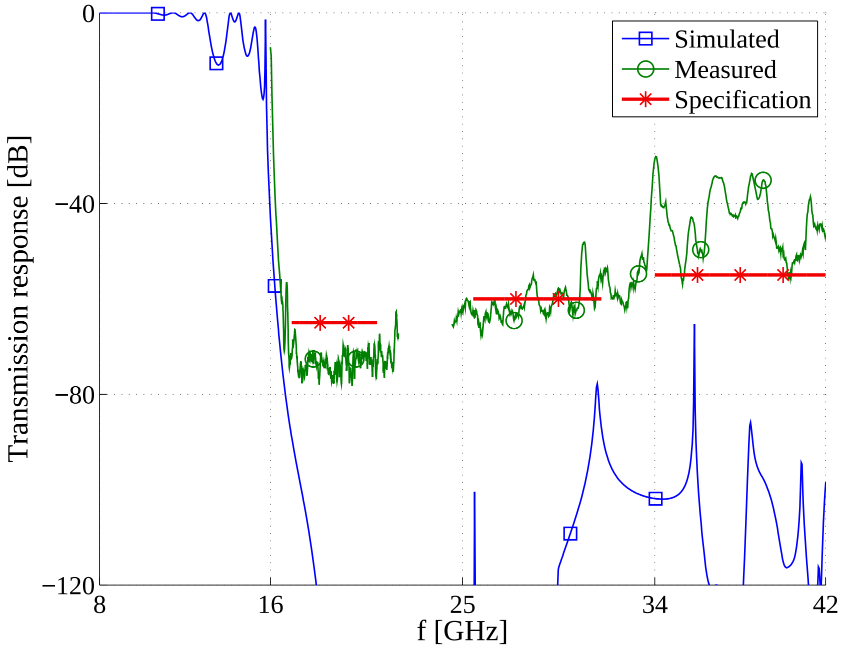

(b) Transmission response.

Figure 3.39: Measured electrical response of waffle-iron filter.

3.8 Conclusion

This chapter proposed a new approach to the synthesis of non-uniform waffle-iron filters, capable of better pass-band control than the classical methods. It also shifts the burden of optimisation to a circuit model instead of relying on time consuming full-wave optimisation using dedicated mode-matching or MoM/FEM codes. The method was used to design a waffle-iron filter to real-world specifications.

A completely new topology of waffle-iron filter was also proposed using inclined rectangular bosses, and a synthesis theory developed. This topology realises filters of orders superior to classical and non-uniform designs for equivalent sizes, but features spurious resonances and inferior power-handling capability.

Chapter 4

Cascaded waveguide slots as absorptive harmonic pads

4.1 Introduction

The second important component in the proposed absorptive filter, is the frequency-selective absorptive section. In this dissertation, this function will be implemented by cascaded waveguide slots, used as absorptive harmonic pads to absorb the energy reflected from the input of the waffle-iron filter. Details of this operating principle is discussed in §2.11.

For the application under consideration, waveguide slots coupling to an absorptive auxiliary guide will be used. Though the harmonic pad appears similar to the "distributed loss" filter in [1] (Fig. 4.1), the operating principle is quite different. Distributed loss filters achieve stop-band attenuation solely by absorption, which itself is achieved by coupling a travelling wave from the main guide to parallel absorptive auxiliary guides.

The harmonic pad, in contrast, couples a limited amount of energy from the main guide to the auxiliary guide or guides, and have a much smaller attenuation effect than distributed loss filters. By terminating the harmonic pad with a broadband reflection filter such as a waffle-iron filter, the radiating slots will couple a standing wave (created in the guide by the by the reflection of the filter) to the auxiliary guides, instead of a travelling wave as with traditional distributed loss filters. This detail is key to the operation of the pad, and will be discussed in some detail in later sections.

The operating principle also differs to that proposed in [37, 36] in that it is the reflected out-of-band energy which is coupled through the slots, and not the in-band signal. This

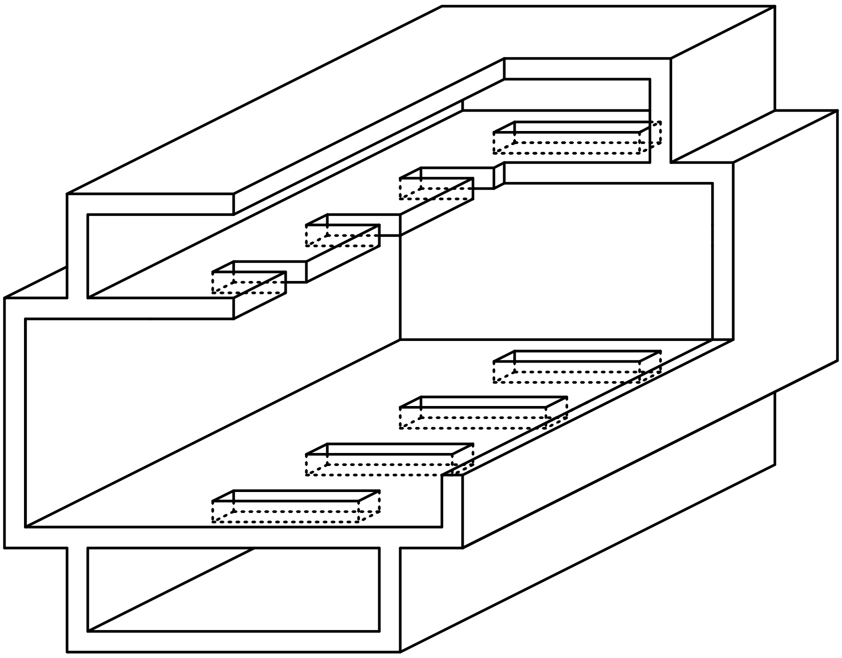

Figure 4.1: Sectioned view of distributed loss filter, which will be re-developed to operate as a harmonic pad.

approach allows for a transmission bandwidth independent of the coupling bandwidth of the slots.

The following sections will investigate both travelling and standing wave current distributions in rectangular waveguide, and establish the slot properties best suited to radiate given these distribution patterns. Approximate circuit models for these slots will be verified, and then used to synthesise a harmonic pad. Finally, a prototype system (complete with the reflective waffle-iron filter developed in the previous chapter) will be demonstrated.

4.2 Surface currents in rectangular waveguide

The equations for internal field distributions and surface currents in rectangular waveguide are well known and freely available in any number of textbooks [69, 72]. For the purpose of clarity, they are briefly repeated here.

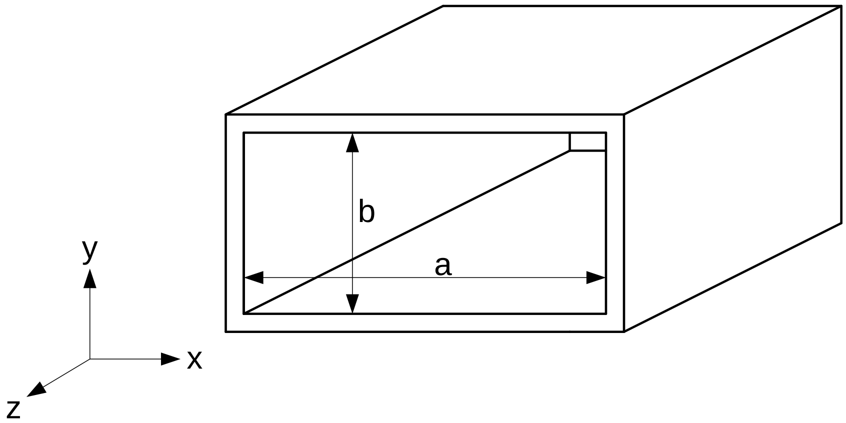

Figure 4.2: Orientation and dimensions of rectangular waveguide under consideration.

The $\vec{H}$-field distribution inside rectangular waveguide (with orientation shown in Fig. 4.2) of width a and height b is given as

$$\begin{aligned} H_x &= \frac{j\beta m\pi}{k_c^2 a} A_{mn} \sin\left(\frac{m\pi x}{a}\right) \cos\left(\frac{n\pi y}{b}\right) e^{-j\beta z} \\ H_y &= \frac{j\beta n\pi}{k_c^2 b} A_{mn} \cos\left(\frac{m\pi x}{a}\right) \sin\left(\frac{n\pi y}{b}\right) e^{-j\beta z} \\ H_z &= A_{mn} \cos\left(\frac{m\pi x}{a}\right) \cos\left(\frac{n\pi y}{b}\right) e^{-j\beta z} \end{aligned} \tag{4.1}$$

for $\mathrm{TE_{mn}}$ modes, and

$$\begin{aligned} H_x &= \frac{j\omega\epsilon n\pi}{k_c^2 b} B_{mn} \sin\left(\frac{m\pi x}{a}\right) \cos\left(\frac{n\pi y}{b}\right) e^{-j\beta z} \\ H_y &= \frac{-j\omega\epsilon m\pi}{k_c^2 a} B_{mn} \cos\left(\frac{m\pi x}{a}\right) \sin\left(\frac{n\pi y}{b}\right) e^{-j\beta z} \\ H_z &= 0 \end{aligned} \tag{4.2}$$

for $\mathrm{TM_{mn}}$ modes. Here, ω is the frequency of the wave propagating in direction $+z$, in an environment of permittivity ϵ and permeability μ. The cut-off wave number is calculated as

$$k_c = \sqrt{\left(\frac{m\pi}{a}\right)^2 + \left(\frac{n\pi}{b}\right)^2} \tag{4.3}$$

and the propagating constant

$$\beta = \sqrt{\omega^2\mu\epsilon - k_c^2} \tag{4.4}$$

If a reflective filter is placed at $z = 0$, a backward-travelling wave $\vec{H}^-$ is excited, and the total magnetic field distribution along the waveguide is given as

$$\begin{aligned}\vec{H} &= \vec{H}^+ + \vec{H}^- \\ &= H_0^+ e^{-j\beta z} + H_0^- e^{j\beta z}\end{aligned} \tag{4.5}$$

The relationship between H_0^+ and H_0^- is determined by the reflection Γ [73] which is defined differently for transversal and longitudinal field components. In the case of transversal field components (H_x, H_y),

$$\Gamma = -\frac{H_0^-}{H_0^+} \tag{4.6}$$

which allows Eq. 4.5 to be re-written as

$$\vec{H}_{x,y}(z) = H_{0(x,y)}^+ \left(e^{-j\beta z} - e^{j(\beta z+\Theta)}\right) \tag{4.7}$$

if it is assumed that, in the reflective stop-band of the filter, $\Gamma = 1\angle\Theta$ (magnitude 1, with an arbitrary angle of reflection Θ). The local maxima (in z) of the standing wave pattern is calculated as

$$|H_{x,y}(z)| = 2H_{0(x,y)}^+ \sin\left(\beta z + \frac{\Theta}{2}\right) \tag{4.8}$$

For the longitudinal field component H_z

$$\Gamma = +\frac{H_0^-}{H_0^+} \tag{4.9}$$

This leads to the further development

$$\vec{H}_z = H_{0(z)}^+ \left(e^{-j\beta z} - e^{j(\beta z+\Theta)}\right) \tag{4.10}$$

and

$$|H_z(z)| = 2H_{0(z)}^+ \cos\left(\beta z + \frac{\Theta}{2}\right) \tag{4.11}$$

Applying the relation

$$\vec{J} = \vec{n} \times \vec{H} \tag{4.12}$$

for the standing wave $\vec{H}$-fields at $y = 0$ reveals standing wave current distributions on the broadwall of the waveguide ($\vec{n} = \vec{a_y}$) to be

$$\begin{aligned}J_x &= -A_{mn}\cos\left(\frac{m\pi x}{a}\right)\left(e^{-j\beta z} + e^{j(\beta z+\Theta)}\right) \\ |J_x| &= 2A_{mn}\cos\left(\frac{m\pi x}{a}\right)\cos\left(\beta z + \frac{\Theta}{2}\right) \\ J_z &= A_{mn}\frac{j\beta m\pi}{k_c^2 a}\sin\left(\frac{m\pi x}{a}\right)\left(e^{-j\beta z} - e^{j(\beta z+\Theta)}\right) \\ |J_z| &= 2A_{mn}\frac{\beta m\pi}{k_c^2 a}\sin\left(\frac{m\pi x}{a}\right)\sin\left(\beta z + \frac{\Theta}{2}\right)\end{aligned} \tag{4.13}$$

for TE modes, and

$$\begin{aligned}
J_x &= 0 \\
|J_x| &= 0 \\
J_z &= -B_{mn}\frac{j\omega\epsilon n\pi}{k_c^2 b}\sin\left(\frac{m\pi x}{a}\right)\left(e^{-j\beta z} - e^{j(\beta z+\Theta)}\right) \\
|J_z| &= 2B_{mn}\frac{j\omega\epsilon n\pi}{k_c^2 b}\sin\left(\frac{m\pi x}{a}\right)\sin\left(\beta z + \frac{\Theta}{2}\right)
\end{aligned} \tag{4.14}$$

for TM modes. The current distributions on the waveguide sidewall is found by applying the same relation at $x = 0$ ($\vec{n} = \vec{a_x}$), which shows the current distributions to be

$$\begin{aligned}
J_y &= -A_{mn}\cos\left(\frac{n\pi y}{b}\right)\left(e^{-j\beta z} + e^{j(\beta z+\Theta)}\right) \\
|J_y| &= 2A_{mn}\cos\left(\frac{n\pi y}{b}\right)\cos\left(\beta z + \frac{\Theta}{2}\right) \\
J_z &= A_{mn}\frac{j\beta n\pi}{k_c^2 b}\sin\left(\frac{n\pi y}{b}\right)\left(e^{-j\beta z} - e^{j(\beta z+\Theta)}\right) \\
|J_z| &= 2A_{mn}\frac{j\beta n\pi}{k_c^2 b}\sin\left(\frac{n\pi y}{b}\right)\sin\left(\beta z + \frac{\Theta}{2}\right)
\end{aligned} \tag{4.15}$$

for TE modes, and

$$\begin{aligned}
J_y &= 0 \\
|J_y| &= 0 \\
J_z &= -B_{mn}\frac{j\omega\epsilon m\pi}{k_c^2 a}\sin\left(\frac{n\pi y}{b}\right)\left(e^{-j\beta z} - e^{j(\beta z+\Theta)}\right) \\
|J_z| &= 2B_{mn}\frac{j\omega\epsilon m\pi}{k_c^2 a}\sin\left(\frac{n\pi y}{b}\right)\sin\left(\beta z + \frac{\Theta}{2}\right)
\end{aligned} \tag{4.16}$$

for TM modes. Using these equations, the peak current distribution magnitudes and orientations may be calculated analytically for a given filter reflection at a specific frequency, as plotted in Fig. 4.3

The examples shown in Fig. 4.3 are selected specifically to illustrate a few properties of standing wave surface current distributions that will prove of interest in future development. Firstly, it is important to note in Fig. 4.3(a) that $|J_z|$ has a maximum at $x = a/2$ for both the TE_{10} and TE_{30} modes. This is true for all odd $\mathrm{TE}_{\mathrm{m}0}$ modes, and is a commonality which may be exploited in considering the multi-mode operation of a slot placed in the waveguide broadwall.

For a guide terminated in an ideal reflection, the maxima $|J_z|$ and $|J_x|$ in $\mathrm{TE}_{\mathrm{m}0}$ modes are not co-located on the z-axis, as seen in Fig. 4.3(b). These maxima are also dependent on frequency (Fig. 4.3(c)) and reflection phase (Fig. 4.3(d)).

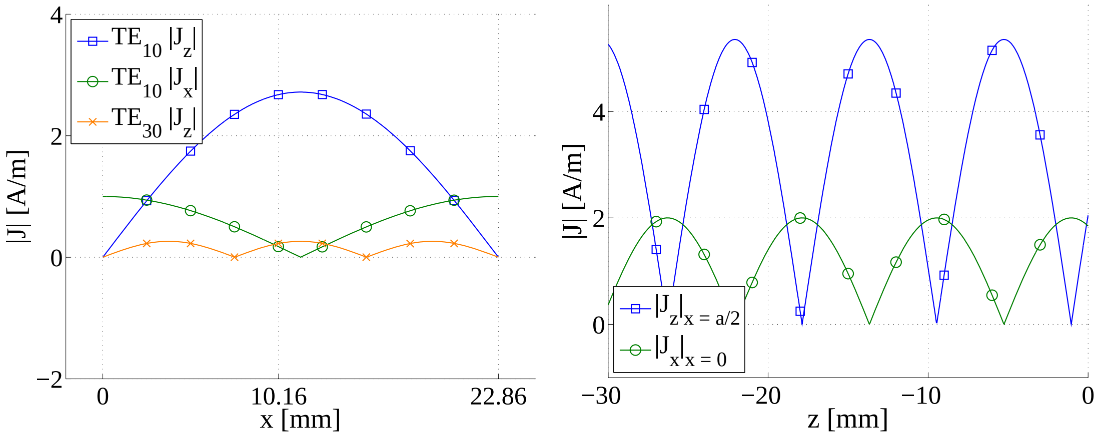

(a) $|J_x|$ and $|J_z|$ on the waveguide floor. Note the common maximum at $x = a/2$ in $|J_z|$.

(b) $|J_x|$ and $|J_z|$ at a distance z from a reflection $\Gamma = 1\angle 45°$.

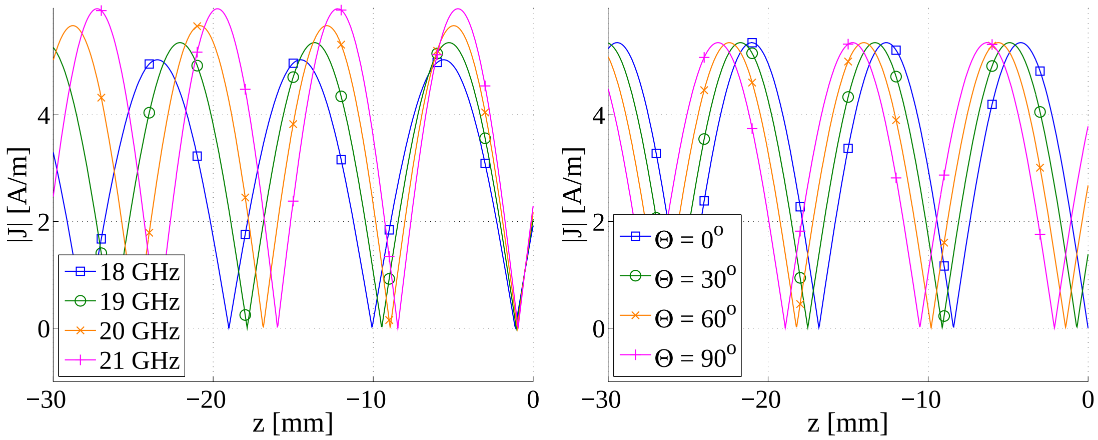

(c) Variation in $|J_z|$ as a function of f, $\Theta = 45°$.

(d) Variation in $|J_z|$ as a function of Θ, $f = 19$ GHz.

Figure 4.3: Sample surface current distributions in WR-90 waveguide, the presence of a reflection $\Gamma = 1\angle\Theta$ at $z = 0$ for a normalised wave amplitude $A_{mn} = 1$ at $f = 19$ GHz.

It is also illustrated in Fig. 4.3(c) that a given change in frequency effects a bigger change in the position of the maxima further away from the reflection source than those nearer to $z = 0$, the reflection source position. Consequently, if two points on the rectangular waveguide surface are positions of maximum standing wave current at a centre frequency f_0, the point closer to the reflection source will feature a high surface current distribution for a wider frequency bandwidth than the point further from the reflection source.

The main conclusions of this section are, therefore

- A position of maximum surface current distribution is only valid over a limited frequency bandwidth.

- The bandwidth is affected by frequency dependence of Θ, the reflection angle.
- The further the maximum is located from the reflection source, the narrower the bandwidth.

4.2.1 Modes under consideration

For a typical absorptive filtering solution spanning several harmonics, the current distributions for numerous propagating modes have to be considered. For example, WR-90 waveguide (22.86 × 10.16 mm) supports 16 propagating modes at 31.5 GHz, which is the upper cut-off frequency of the third harmonic for a system with an upper transmission frequency of 10.5 GHz. Clearly, it is impractical to consider all of these modes individually when choosing the positions and orientations of radiating slots.

The complexity of the problem may be reduced by using a reduced height waveguide, with b sufficiently low that only $\mathrm{TE_{m0}}$ modes propagate [1]. Further more, all $\mathrm{TE_{m0}}$ modes have uniform y-directed surface current along the sidewalls. If structural symmetry around the y-axis at $x = a/2$ is enforced, the existence of modes with even values of m are avoided. This ensures that there is always a local maximum for J_z in the centre of the guide broadwall, irrespective of which odd $\mathrm{TE_{m0}}$ mode is incident or excited. For the system under consideration, the required maximum for b is 4.762 mm, which places the $\mathrm{TE_{01}}$ cut-off frequency at 31.5 GHz.

Reducing the main guide height does, however, influence the coupling or radiating properties of the slots (details of which to be discussed in the next section). In the case of retention of full height guide, the number of propagating modes may also be reduced by maintaining both E-plane and H-plane symmetry. Enforcing the boundary conditions

$$\begin{aligned} E_x|_{x=0.5a} &= 0 \\ H_y|_{y=0.5b} &= 0 \end{aligned}$$

reveals that, in this case, only $\mathrm{TE_{mn}}$ and $\mathrm{TM_{mn}}$ modes of odd $m = 1, 3, 5, ...$ and even $n = 0, 2, 4, ...$ propagate. This reduces the number of propagating modes to 4 ($\mathrm{TE_{10}}$, $\mathrm{TE_{30}}$, $\mathrm{TE_{12}}$ and $\mathrm{TM_{12}}$). Each of these display a maximum z-directed surface current at $x = a/2$ on the broadwall. This commonality in surface current distribution may be exploited to design catch-all slots (which preserve the required symmetries) operating independent of the propagating mode.

4.3 Waveguide slots and absorptive auxiliary guides

Two related, but distinctly different approaches are possible when designing slots for harmonic pads. The first is to consider the slots as radiating slots, and to load the auxiliary guide sufficiently as to mimic free space. The second approach involves full consideration of the auxiliary waveguide, treating slots as coupling apertures. This section will evaluate both approaches, consider the effect of auxiliary waveguides on the slots, and select a topology for which a circuit model may be developed.

4.3.1 Review of radiating slots

Free-space radiating slots in rectangular waveguide is the subject of an extensive body of literature, of which [81, 82, 83, 84, 85, 86, 87, 88, 89, 90] is but a small sample. The vast majority of the literature aims to develop improved numerical modelling methods for these slots, which is not of concern for the problem at hand (since a commercial full-wave EM solver is available). This discussion will only focus on the properties of radiating slots relevant to the development of harmonic pads.

A narrow slot of length l and and width w (where "narrow" implies $2\log\left(\frac{l}{w}\right) > 1$, according to [81]) cut into a wall in rectangular waveguide, will radiate energy into free space. The magnitude of the radiation is proportional to the magnitude of the surface current directed normal to the orientation of the slot. Maximum radiation will therefore occur if the slot is placed at a point of maximum surface current density (for instance, the local maxima of a standing wave pattern), with a slot placed in a direction normal to the surface current direction at that point [91]

Four main slot types are of interest to this inquiry, as shown in Fig. 4.4. The broadwall inclined slot [81, 82] and transversal offset slot [82, 87] are excited by the z-directed surface current of the fundamental TE_{10} mode J_z, the broadwall longitudinal slot [82] by J_x, and sidewall inclined slot [81, 85, 92, 93] by J_y. The reason these four slots are of importance, is that special instances of each ($\theta_B = 90°$, $d_T = 0$, $d_L = a/2$, $\theta_S = 0°$) will result in maximum interruption of each of the three surface current distributions of all $\mathrm{TE}_{\mathrm{m}0}$ modes.

Maximum radiation from a slot occurs when the slot length $l \approx n\lambda_0/2$, but this is dependent on the displacement or rotation [82, 83] of the slot. Resonant lengths may, for example, be closer to $l \approx 0.52\lambda$ [84] and $l \approx 0.488\lambda$ [92] for inclined sidewall slots, 0.47λ for transversal slots [87, 94] and $0.445\lambda < l < 0.502\lambda$ for longitudinal slots in full-height

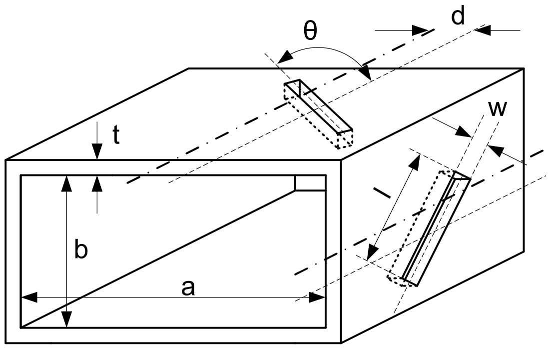

(a) General locations and dimensions of broadwall and sidewall slots in rectangular waveguide.

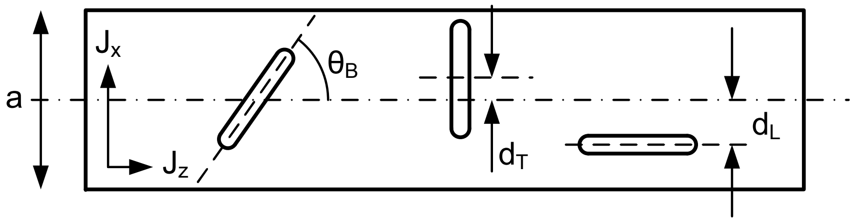

(b) Broadwall inclined (left), transversal offset (middle) and longitudinal offset (right) slots.

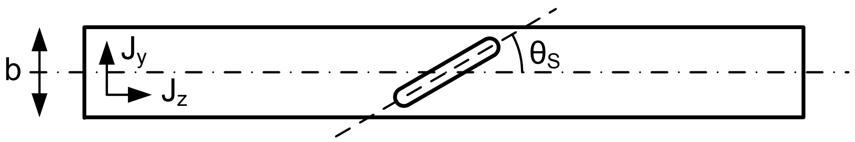

(c) Sidewall inclined slot.

Figure 4.4: Slot locations and orientations in rectangular waveguide.

guide [83, 94].

Guide height also plays a role in resonant slot length, with [95] indicating as much as 6% increase in slot resonant length by halving the guide height. Another contributing factor is the slot width [82], waveguide wall thickness [83, 86] and slot end rounding [96, 86]. Because numerous factors determine resonant slot length, it is best determined (for purpose of this inquiry) from individual full-wave analyses.

Radiating broadwall inclined and transversal offset slots may be modelled as series resonant circuits in transmission line (as shown in Fig. 4.5(a)) [82], because they interrupt J_z, the surface current component responsible for power transfer. Interrupting J_x and J_y, on the other hand, effectively places a shunt load on the transmission line. Radiating longitudinal broadwall and sidewall inclined slots are therefore modelled as shunt resonant circuits shown in Fig. 4.5(b) [82]. Generalised T-section models do not significantly contribute to the accuracy of the model, except in the case of wide slots [96], or slots of reduced guide height [83]. These circuit models will be discussed in the next section.

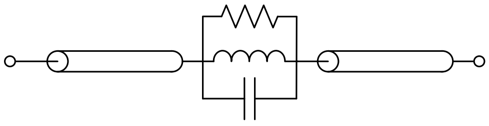

(a) Series resonator.

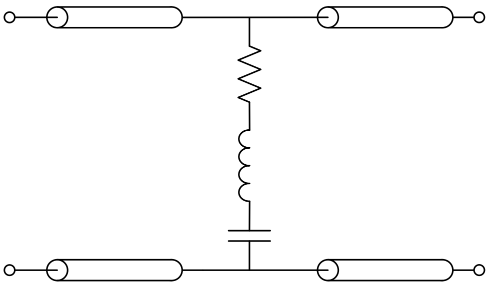

(b) Shunt resonator.

Figure 4.5: Circuit models of radiating slots.

The circuit model parameters of a radiating slot is further altered by the presence of metallisation (parallel plates [87, 89] or baffles [88, 90] being typical examples) in the near-field of the slot exterior. This effect may be as large as 4% for resonant length [88, 89] and as much as 500% for peak reflection [90] and 150% for resonant resistance or conductance [87], depending on slot displacement. The implication for the present inquiry is that the previously mentioned slot models are only valid if the auxiliary guides are sufficiently absorptive to approximate free space around the slot (ie, they do not act as tranmission lines between slots). If this condition does not hold, then the circuit model of the slot depends on the auxiliary guide dimensions a' and b'.

Guide height b has a significant influence on circuit model values. Apart from the previously noted change in slot resonant frequency, reduced guide height is associated with increased slot bandwidth [86, 87] as well as increased radiation resistance [87]. Any slot has finite reflection outside its resonant frequency, which may contribute to the total in-band reflection of the combined filter and harmonic pad. This is an important consideration in slot selection. Reduced guide height also decreases the validity of traditional circuit models [83, 97], due to asymmetric scattering from the slot [86] (an effect mitigated by the use of meandering slots [98]). This causes the frequencies of peak resistance / absorption and zero reactance / susceptance to be dissimilar, which invalidates the assumption of simple resonance absorption. A full T-network description is required in these cases [97, 99].

4.3.2 Review of coupling slots

The second main body of literature deals with slots coupling between two distinct waveguides [4, 100, 94, 92, 101, 95, 102, 103, 104, 105, 93]. Much of what is true for radiating slots, also holds for coupling slots. This section describes some differences in detail.

As with radiating slots, the coupling values of coupling slots are determined by the magnitude of surface current normal to the slot orientation, and the resonant frequency by factors similar to those stated previously (length, width, position, rotation, wall thickness and guide height). The same four basic radiating slot types can be used for coupling, but preference is given to transversal broadwall and longitudinal sidewall slots [93].

The biggest difference between radiating and coupling slots lies with the circuit modelling. Both broadwall and sidewall coupling slots and apertures are modelled in classical literature [68] as intricate networks of six reactive components, shown in Fig. 4.6(a). Later work reduces this model to a T-equivalent circuit [102], but with numerically determined impedances. An alternative approach is to represent the slot as an ideal transformer with a single shut reactance [106], or a J-inverter and a series reactance [103], both of which are based on numerically generated S-parameter data. Recent contributions [104, 105, 93] establish wide-band equivalent lumped-element series resonant models reminiscent of the traditional transverse slot model, shown in Fig. 4.6(b). Though both these models allow for resonant coupling, the latter approach may be extended to include waveguide wall thickness and coupling between non-identical waveguides [93].

These recent approaches are distinguished from earlier coupling slot models, and from almost all radiating slot models, by the absence of analytical or empirical expressions of circuit values. Instead, they incorporate data[1] obtained from a full-wave solver to establish circuit model values. This enables circuit optimisation (rather than more time-consuming full-wave optimisation) to be used in the design of coupling arrays.

Single sidewall slots have been shown to couple as much as -4.5 dB [92] from the main guide into an auxiliary guide, with -3 dB coupling possible [93] for single transversal broadwall slots, though -6 dB [101] is a more common value for both transversal and longitudinal slots. Finite wall thickness decreases the coupling bandwidth [101], but sufficiently thick slots will support propagating waveguide modes above slot resonance [94], which means that the slot acts as a waveguide above a specific cut-off frequency. For similar slot dimensions, common broadwall couplers will have a greater coupling bandwidth

---

[1] A minimum of two data points are required, but better results are achieved by averaging

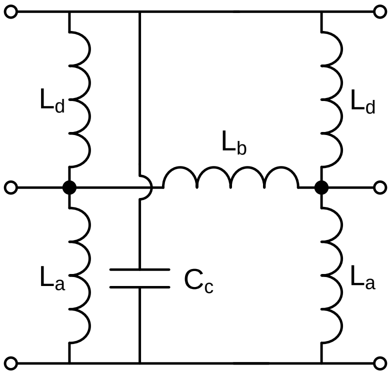

(a) Model used in [68]

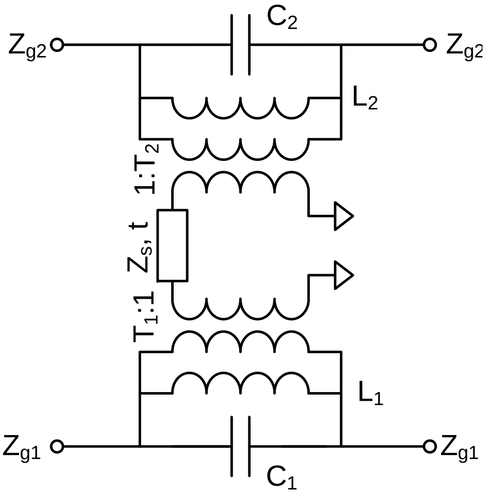

(b) Model used in [93]

Figure 4.6: Previously published circuit models of transversal broadwall slot couplers.

than common sidewall couplers [102], and the coupling magnitude is less sensitive to the dimensions of the auxiliary guide. The resonant frequency is, however, affected by the dimensions of the auxiliary guide [102].

4.3.3 Slot selection

The purpose of the selected waveguide slot is to extract as much of the reflected energy from the main guide (at harmonic frequencies) into an auxiliary guide across the absorption bandwidth, without affecting the pass-band transmission characteristics of the structure. The following aspects need to be considered when designing sets of absorbing slots.

Cascading

In cascading longitudinal slots (either on the broadwall or the sidewall), the minimum centre-to-centre spacing of the slots along the length of the guide is limited by the slot length. In transversal slots, it is limited to the slot width. A denser slot distribution is therefore possible with transversal slots, (as shown in Fig. 4.7) shortening the total length of the eventual harmonic pad.

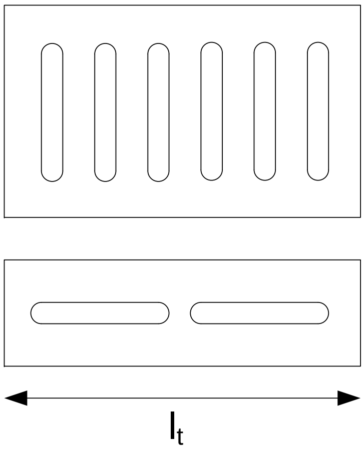

Figure 4.7: Cascade densities of transversal broadwall (top) and longitudinal sidewall (bottom) slots.

Multiple mode current distributions

It was shown previously that, by enforcing both E-plane and H-plane symmetries, all propagating modes have a common element of surface current distribution, namely the z-directed broadwall current at $x = a/2$. This commonality distinguishes centered transversal broadwall slots as the preferred slot topology.

Absorption

Absorption is defined as

$$A = \sqrt{1 - |S_{11}|^2 - |S_{21}|^2} \tag{4.17}$$

and is used as a measure of the amount of energy removed from the main guide either by radiation, coupling to an auxiliary guide, or dissipation in absorptive material. The peak absorption of individual slots determine the eventual number of slots required to achieve an matched condition of $Z_{in} \approx Z_0$ over a required frequency band.

Bandwidth

An absorption bandwidth of 20% is required by the initial problem specification in Chapter 1. The minimum number of slots needed to cover a given bandwidth would be decreased by the use of wide-band slots.

4.3.4 Characteristics of slots in unterminated waveguide

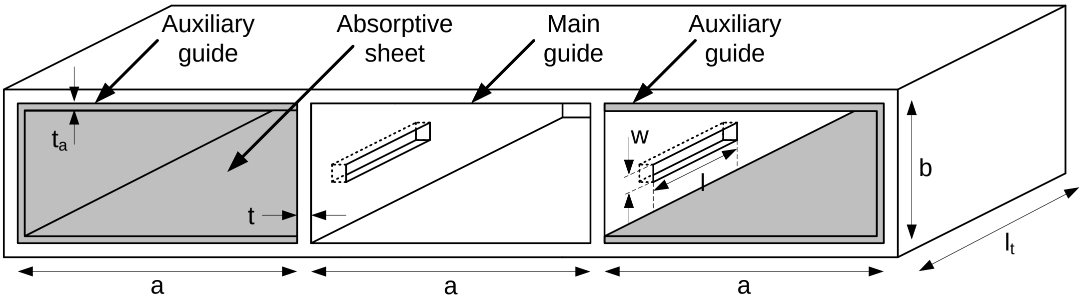

(a) Longitudinal sidewall slots.

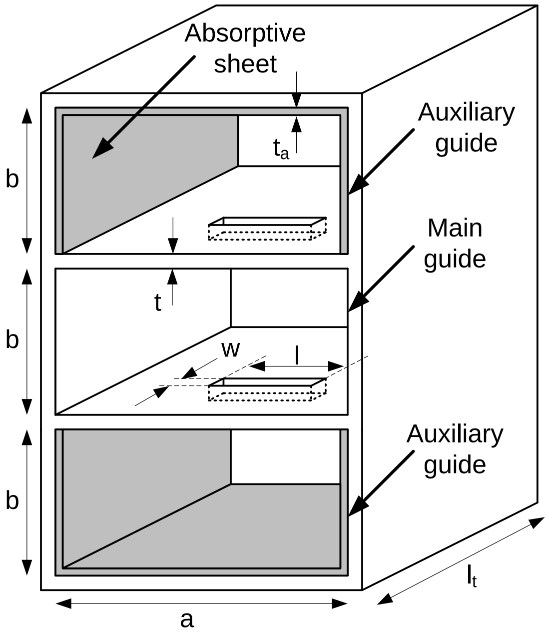

(b) Transversal broadwall slots.

Figure 4.8: Simulation models for slot selection. Note the placement of the absorptive sheet material, indicated as shaded areas.

To investigate the characteristics of various slots in terms of the criteria stated in the previous section, test slots of length $l = 8$ mm are simulated in *CST Microwave Studio 2009*. Slot width of $w = 1$ mm and wall thickness of $t = 1$ mm are used in standard WR-90 ($a = 22.86$ mm, $b = 10.16$mm) waveguide, with end rounding of $r = 0.5$ mm in all cases.

Both centered transversal broadwall and centered longitudinal sidewall[2] slots are simulated in three different test environments: free-space radiating (i.e, in the absence of the auxiliary guides shown in Fig. 4.8), coupling to an auxiliary lossless guide of identical dimensions, and coupling to a guide loaded on three sides (the common wall remaining PEC) with an appropriate absorptive sheet material (in this case, Eccosorb$^{\mathrm{TM}}$FGM-40) of thickness 1 mm, running the length of the $l_t = 60$ mm simulation cavity. To preserve the previously discussed symmetry conditions, slots are simulated as symmetric pairs.

Though slots will eventually be used cascaded with a reflected filter, both main guide ends are initially simulated ports, to investigate general absorptive properties. The effect of a short-circuited main guide will be investigated in §4.3.6. Both ends of all auxiliary guides are terminated with ports, to imitate the effect of absorptive loads.

The results are shown in Fig. 4.9.

From the comparative results, it is quite evident that the absorptive material inside the auxiliary guide is not sufficient to approximate the slot as radiating, since the scattering parameters of a slot coupling to an absorptive guide are more similar to a lossless coupling guide than to that of a radiating slot. Preference will therefore be given to coupling circuit models in later synthesis. The radiating performance of each slot topology does, however, illustrate the potential of the slot. As such, the radiating transversal slot yields more peak absorption (-3.5 dB, compared to -9.7 dB) and absorption bandwidth (16%, compared to 7.5%) than the longitudinal slot.

Also noticeable, is that the bandwidth of the coupling slots are reduced by spurious resonances (less prominent in the case of auxiliary guide loaded with absorptive material) either side of the main resonance where the slot length $l \approx \lambda/2$. However, even with these spurious resonances, it is clear that transversal slot exhibits higher peak values and larger bandwidths (6.25%, compared to the 2.8% of the longitudinal slots) of absorption than similar slots placed longitudinally. It is for this reason, as well as the cascadeability mentioned earlier, that transversal slots are selected for further development.

Spurious resonances

The spurious resonances shown in Fig. 4.9 at 16 and 24.5 GHz, coincide with the cut-off frequencies of the TM_{11} and TM_{31} modes in the auxiliary guide, both of which are excited

---

[2] Offset broadwall longitudinal slots were dismissed based on manufacturing considerations

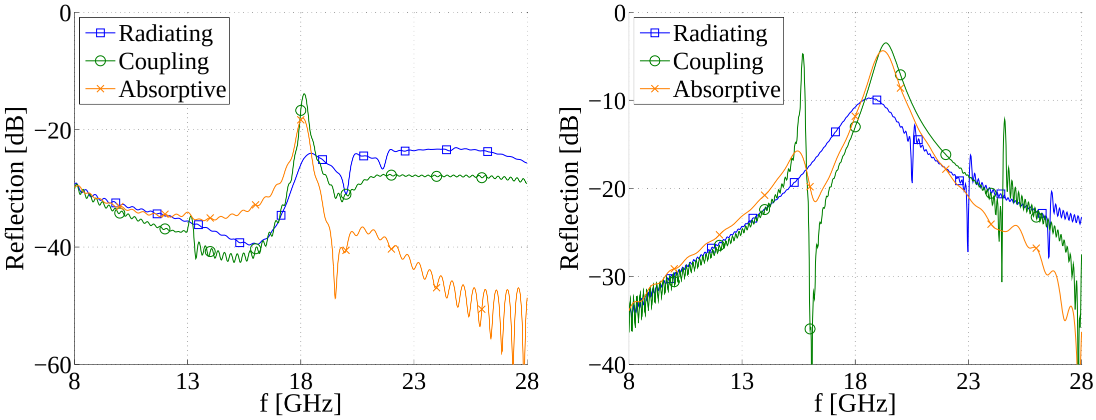

(a) Longitudinal reflection.

(b) Transversal reflection.

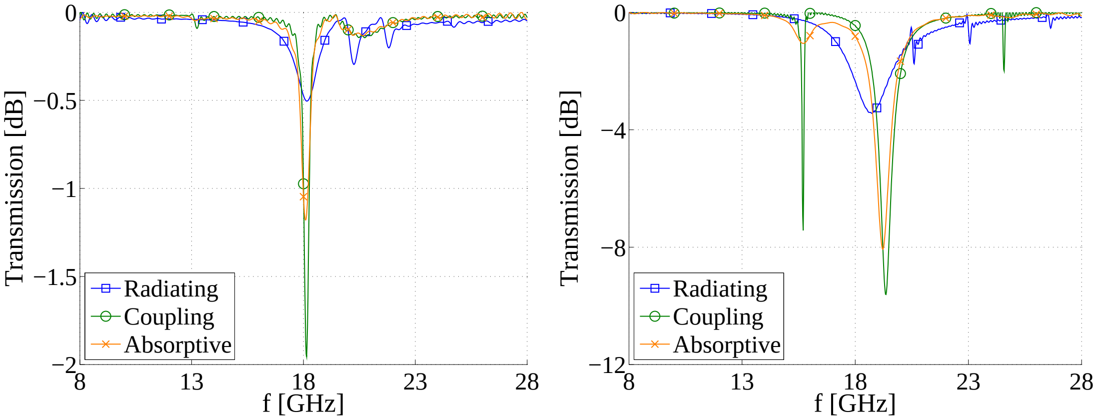

(c) Longitudinal transmission.

(d) Transversal transmission.

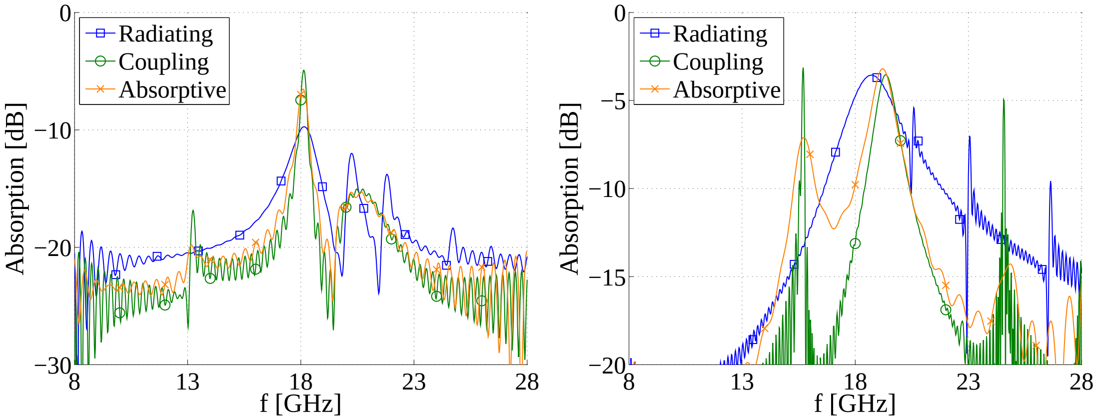

(e) Longitudinal absorption.

(f) Transversal absorption.

Figure 4.9: Electrical properties of identical symmetrically placed transverse broadwall and longitudinal sidewall slots with auxiliary guides identical to main guide.

by the resonant z-directed $\vec{E}$-field of the slot, as shown in Fig. 4.10.

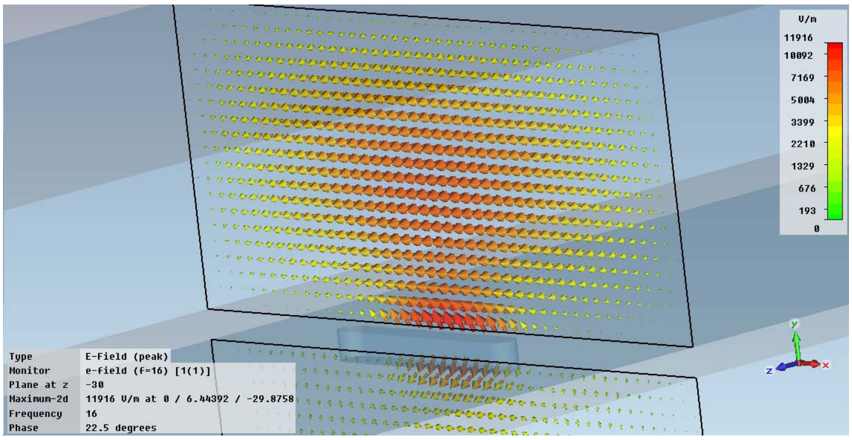

```
Type          E-Field (peak)
Monitor       e-field (f=16) [1(1)]
Plane at z    -30
Maximum-2d    11916 V/m at 0 / 6.44392 / -29.8758
Frequency     16
Phase         22.5 degrees
```

(a) 16 GHz

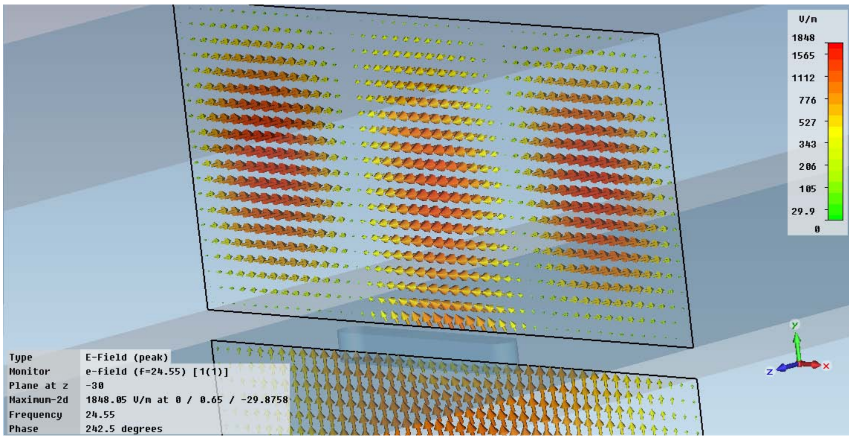

```
Type          E-Field (peak)
Monitor       e-field (f=24.55) [1(1)]
Plane at z    -30
Maximum-2d    1848.05 V/m at 0 / 0.65 / -29.8758
Frequency     24.55
Phase         242.5 degrees
```

(b) 24.5 GHz

Figure 4.10: $\vec{E}$-fields at spurious resonances in transversal waveguide slots.

At 16 GHz, the coupling between the TE_{10} mode in the main guide and the TM_{11} mode in the auxiliary guide reaches a peak value of -10 dB, which interferes with the TE_{10} mode operation of the slot (as shown in Fig. 4.11). The same happens at 24.5 GHz between the TE_{10} mode in the main guide and the TM_{31} mode in the auxiliary guide, though the spike peaks only at -20 dB.

A simple way to suppress these modes is to reduce the auxiliary guide dimensions[3], as illustrated in Fig. 4.12. This has the added advantage of increasing the $\mathrm{TE}_{\mathrm{m}0}$ cut-off frequencies of the auxiliary guide, below which coupled energy cannot propagate away from the slot. This effectively places a lower limit on the slot coupler, which avoids unwanted auxiliary guide coupling in the transmission band of the eventual cascaded absorptive filter. For the case of $a' = 13$ mm, the the TE_{10} cut-off frequency is increased

---

[3] The excitation of non-TE_{10} modes are avoided by reducing both a' and b'.

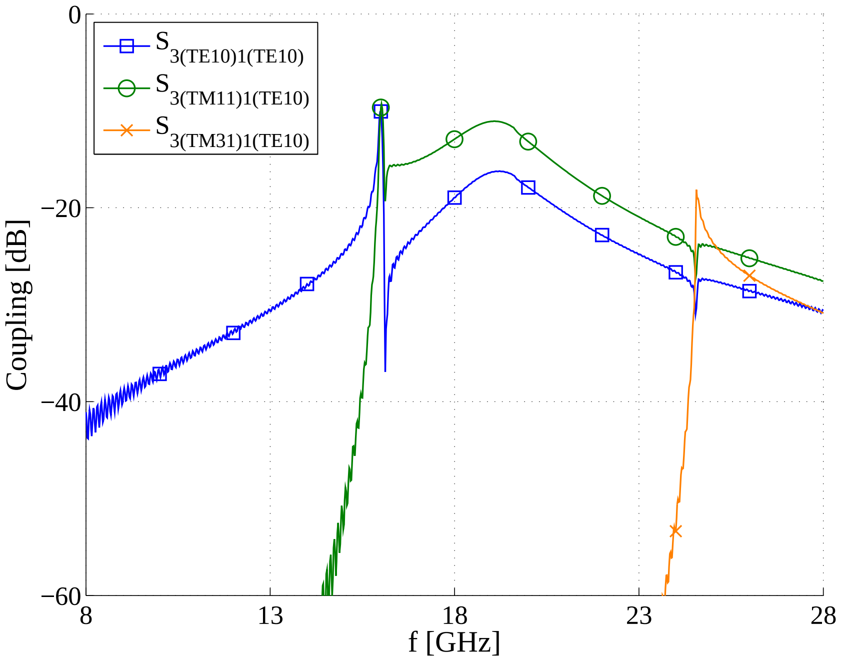

Figure 4.11: Coupling from the TE_{10} mode to higher order modes in the auxiliary waveguide. Port 3 is the auxiliary waveguide port directly above the main guide port 1.

to 11.5 GHz, which allows for near lossless operation in the eventual transmission band of the cascaded absorptive filter (8.5 - 10.5 GHz, in this case). Also, the removal of the spurious resonance has effectively increased the absorptive bandwidth of the slot to 15.6%, similar to that of a radiating transversal slot.

Reducing b' to 3 mm increases the cut-off frequency of the TM_{11} mode in the auxiliary guide to above 51 GHz. The auxiliary guide height also determines the magnitude of the absorption peak, as illustrated in Fig. 4.13. It will be shown later that b' is the single most important dimension in determining the magnitude of slot absorption, since x-axis offset d_T or rotation θ_B (as shown in Fig. 4.4(b)) excites undesirable even modes (TE_{20}, etc.). This dimension is, therefore, a synthesised dimension in an eventual cascade synthesis.

Absorptive loading of auxiliary waveguide

Fig. 4.14 shows two options for loading of the auxiliary guide by absorptive sheet material. Since the surface current distribution of the TE_{10} mode is larger on the broadwalls than on the sidewalls, loading of the broadwall alone is expected to achieve similar absorption as loading of all three walls. This is confirmed in Fig. 4.15. In all following experiments, only the structure in Fig. 4.14(b) is used.

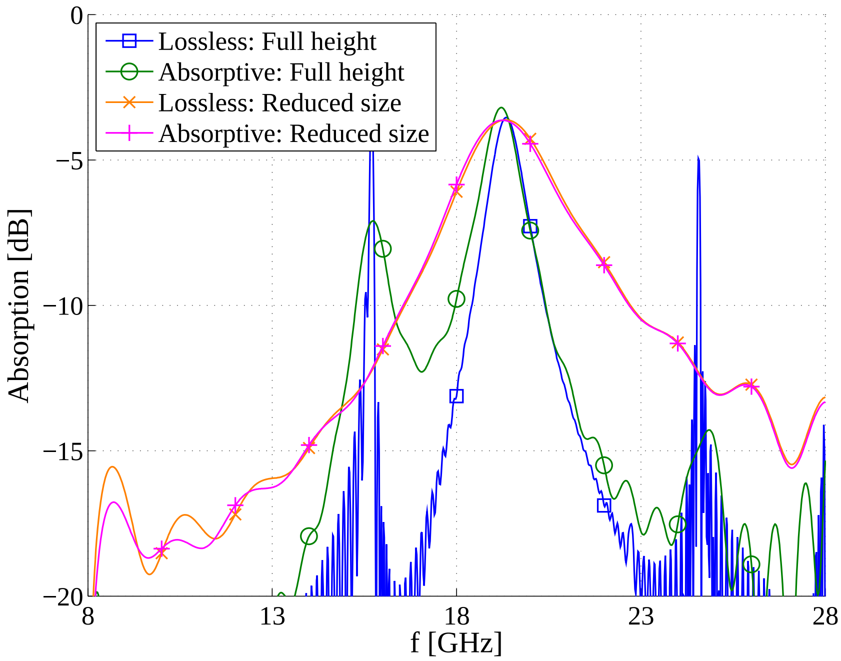

Figure 4.12: Comparison of transversal broadwall slot absorption (in absorptive and lossless auxiliary guides) with full and reduced auxiliary guide dimensions.

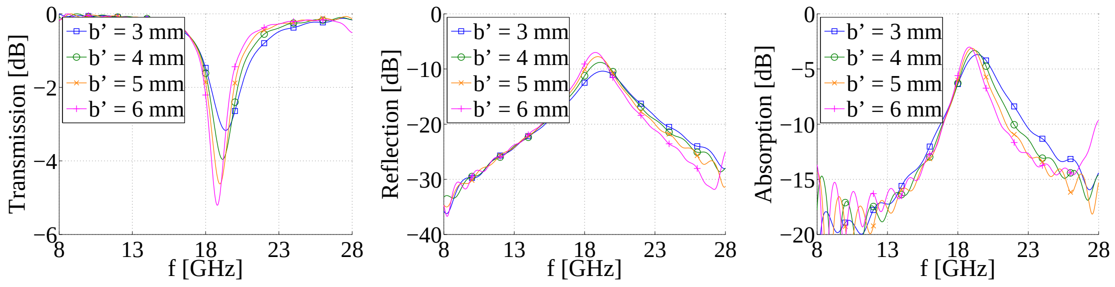

(a) Transmission. (b) Reflection. (c) Absorption.

Figure 4.13: Parametric study of auxiliary guide height b', $a' = 13$ mm.

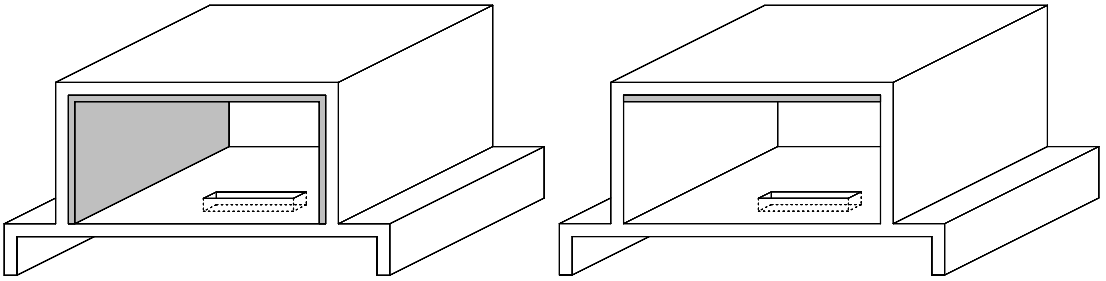

(a) Three walls. (b) Single wall.

Figure 4.14: Placement of absorptive loading in auxiliary guide.

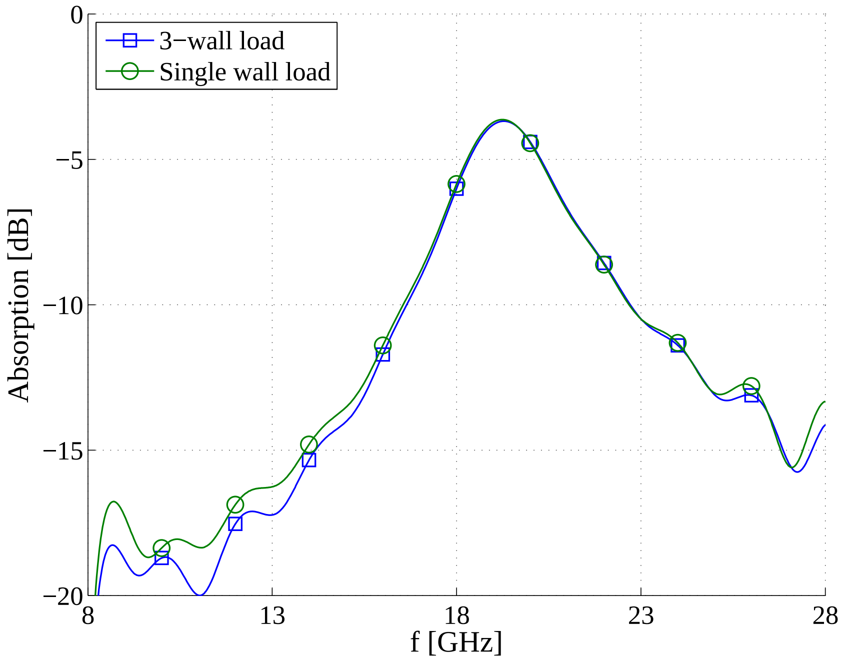

Figure 4.15: Comparison of broadwall slot absorption with single broadwall and full three-wall sheet loading for reduced size auxiliary guide.

4.3.5 Slot dimensions

Apart from the auxiliary guide dimensions, the slot itself has three independent parameters which may be altered to achieve a required electric response. The effect of varying the slot length l is shown in Fig. 4.17, and shows that l alters the resonant frequency of the absorption.

Fig. 4.18 shows that the slot width w adjusts the bandwidth of the slot. Of particular importance to the application of transversal broadwall slots in harmonic pads, is the increased reflection above and below resonance, shown in Fig 4.18(b). It is important to keep in mind that the eventual combined structure of harmonic pad and reflective filter will have a transmission band above or below the resonant frequency of the slot, and that any contribution by the slot to the total in-band reflection is unwanted. For the particular application under consideration, this eventual transmission band is at 8.5 - 10.5 GHz. To achieve a maximum contribution of -30 dB in the transmission band, the slot width has to be limited to 1 mm. For the sake of manufacturing simplicity, this means that all slots in the eventual design would be of width 1 mm.

Fig. 4.19 shows that slot thickness t has the inverse effect of slot width, decreasing the absorption bandwidth for higher values. As with the slot width, manufacturing is simplified if all cascaded slots have identical values of wall thickness. For the sake of simplicity,

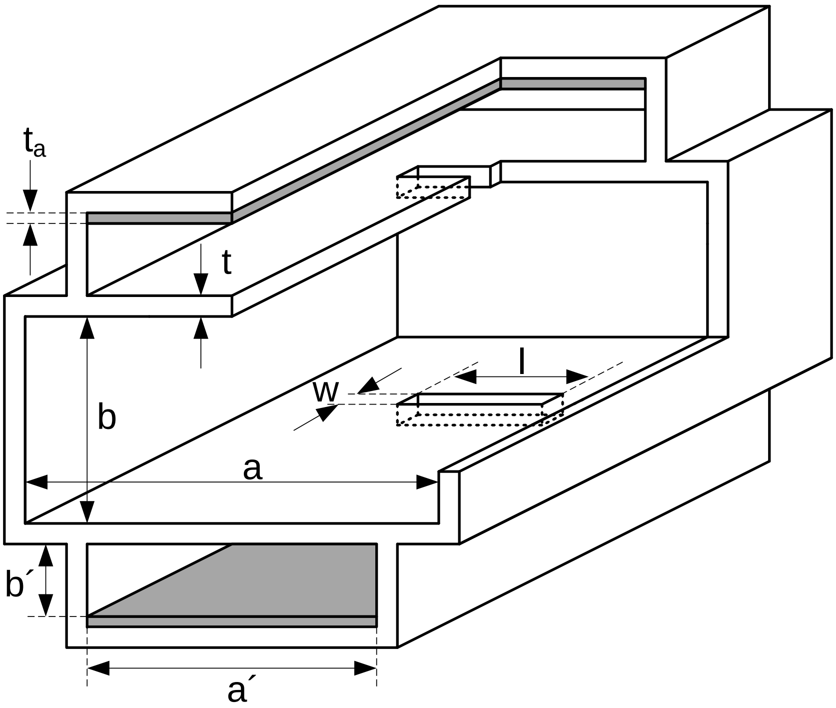

Figure 4.16: Final layout and dimensions of two transversal broadwall slots, each coupling to an absorptive auxiliary waveguide.

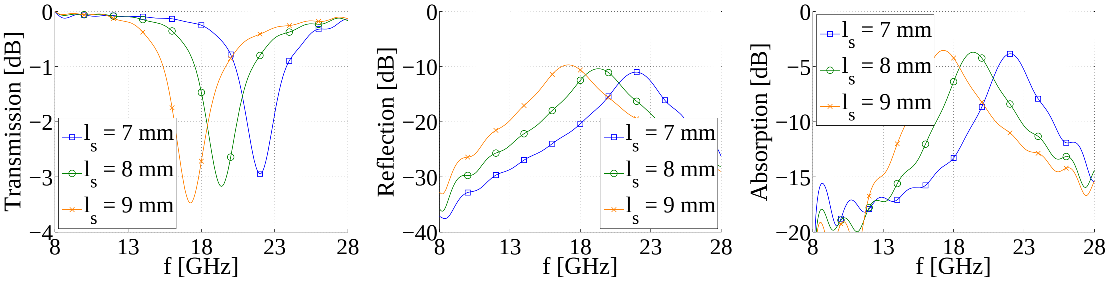

(a) Slot length, transmission.
(b) Slot length, reflection.
(c) Slot length, absorption.

Figure 4.17: Parametric study of transversal broadwall slot length.

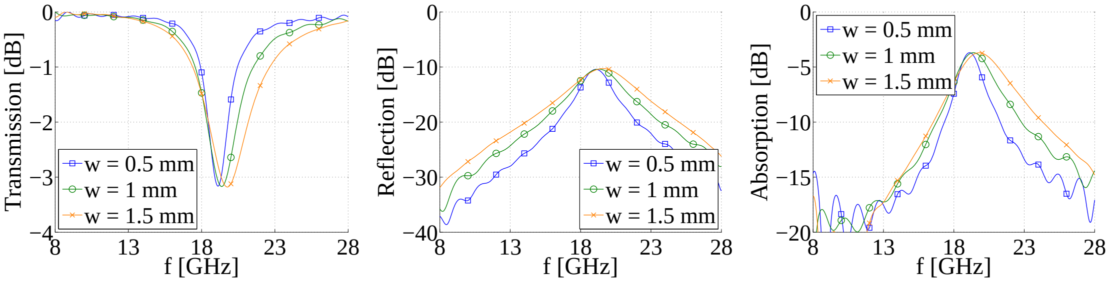

(a) Slot width, transmission.
(b) Slot width, reflection.
(c) Slot width, absorption.

Figure 4.18: Parametric study of transversal broadwall slot width.

a value of $t = 1$ mm is selected.

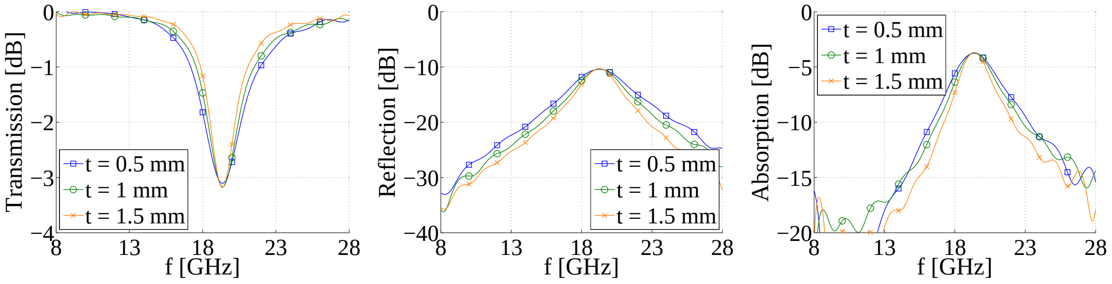

(a) Slot thickness, transmission. (b) Slot thickness, reflection. (c) Slot thickness, absorption.

Figure 4.19: Parametric study of transversal broadwall slot thickness.

An important result of the parametric study is that no single slot dimension can be used to adjust peak slot absorption without affecting other slot parameters significantly. In slotted waveguide antennas, adjustment to peak absorption is achieved by offsetting the slot from the xz axis (d_B in Fig. 4.4(b)), or by rotating the slot around the y-axis (θ_B in Fig. 4.4(b)). Both alterations disrupt the E-plane symmetry of the structure, causing the TE$_{20}$ mode to be excited. In this application, slot absorption would therefore be set primarily by auxiliary guide height (as demonstrated in Fig. 4.13), which means that all cascaded slots will (for equal wall thickness t and slot width w) have similar values of peak absorption.

4.3.6 Characteristics of slots in short-circuited main guide

Though previous results proved insightful in selecting slot position, orientation and auxiliary guide dimensions, the simulation results are not indicative of the eventual operating conditions of the slots. To examine the operation of a single transversal slot pair under standing wave conditions, the main guide is short-circuited a distance d from the centre of the slot. Maximum absorption is expected when the slot is placed at a point of maximum standing wave surface current at the resonant frequency of the slot. For $|J_z|_{x=a/2,y=0}$, this is at $d = n\lambda/2$, or multiples of 8.24 mm. Fig. 4.20 shows that both the maximum input reflection match and absorption bandwidth are achieved by placing the slot at $d = 8.24$ mm.

The effect of the standing wave on absorption is evident. Not only has the peak input match improved to below -23 dB in Fig. 4.20(a), but the -3 dB bandwidth of the absorption (shown in Fig. 4.20(b)) is now over 20%. Fig. 4.20 further illustrates that the input

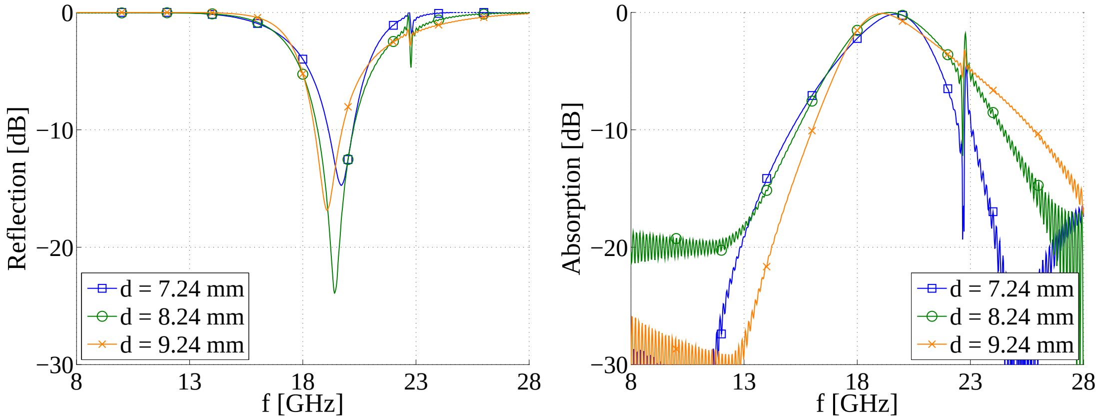

(a) Reflection. (b) Absorption.

Figure 4.20: Parametric study of transversal broadwall slot offset from waveguide short (PEC wall termination).

reflection match and the absorption bandwidth are both worsened by moving the slot away from the local maximum in standing wave surface current, whilst Fig. 4.21 shows that both parameters are also worsened by moving the slot to local maxima further away from the reflection source. This is a critial constraint on the operation of the slot, as will be seen in later synthesis examples.

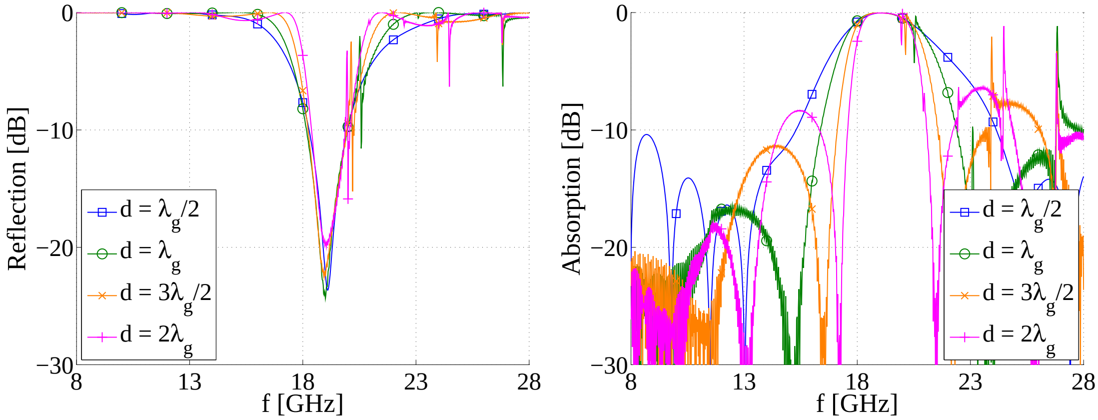

(a) Reflection. (b) Absorption.

Figure 4.21: Parametric study of transversal broadwall slot offset at different standing wave maxima from a waveguide short.

4.3.7 Higher frequency bands

The previous sections all investigated different aspects of the operation of the transversal broadwall slot for use in the band 17 - 21 GHz, the first absorptive band required by the specifications set in Chapter 1. Applying the same design to the second absorptive band at 24.5 - 31.5 GHz yields a slot length of approximately 5 mm, the results of which are shown in Fig. 4.22.

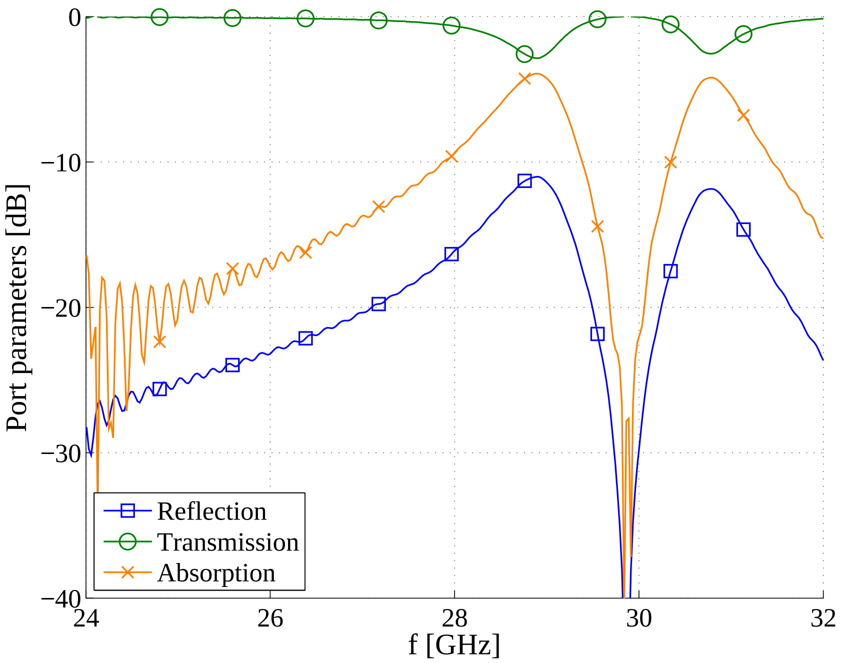

Figure 4.22: Single centered 5 mm transversal slot scattering parameters.

Apart from the reduced absorption compared to the 8 mm slot, the main concern is the null in absorption at 28.98 GHz. This coincides with the cut-off frequency of the TM_{12} mode in the main guide at 30.25 GHz. Further investigation indeed reveals the presence of a propagating hybrid TE_{10}-TM_{12} mode, excited by the z-directed $\vec{E}$-field across the slot aperture (as shown in Fig. 4.23(b)). As was previously seen with TM modes in the auxiliary guide (§4.3.4), the presence of this mode impedes the absorption of the TE_{10} mode by the slot, and has to be suppressed.

The simple approach to alleviate this problem would be to reduce the main guide height to increase the cut-off frequency of the offending TM_{12} mode. To achieve this, the main guide height b is reduced to $b_r = 9$ mm (to increase the cut-off frequency of the TM_{21} mode to above 33 GHz). Fig. 4.24(a) shows that the absorption null is no longer present for the length of length 5 mm, and that the slot of length 8 mm also operates in the reduced guide height.

The use of reduced height guide necessitates a transition from the standard WR-90 guide height $b = 10.16$ mm to $b_r = 9$ mm. A simple tapered transition, as shown in Fig. 4.25 would increase the length of the harmonic pad by $2l_t$, with $l_t = 20$ mm, to achieve a

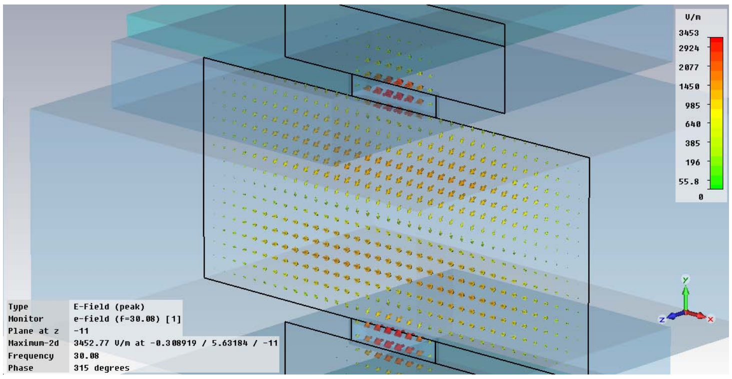

```
Type          E-Field (peak)
Monitor       e-field (f=30.08) [1]
Plane at z    -11
Maximum-2d    3452.77 V/m at -0.308919 / 5.63184 / -11
Frequency     30.08
Phase         315 degrees
```

(a) $\vec{E}$-field distribution on yz-axis.

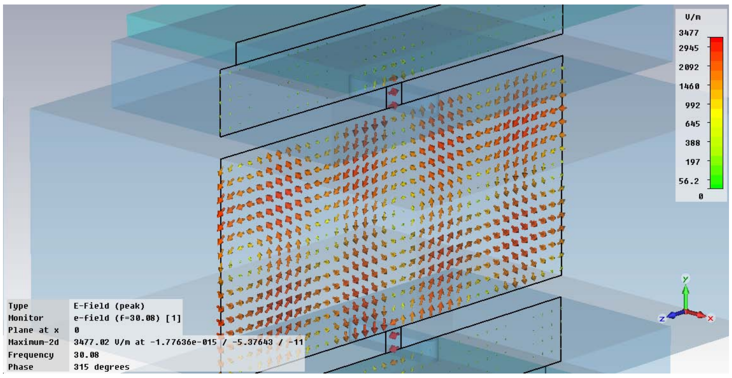

```
Type          E-Field (peak)
Monitor       e-field (f=30.08) [1]
Plane at x    0
Maximum-2d    3477.02 V/m at -1.77636e-015 / -5.37643 / -11
Frequency     30.08
Phase         315 degrees
```

(b) $\vec{E}$-field distribution on xy-axis.

Figure 4.23: Single centered 5 mm transversal slot fields.

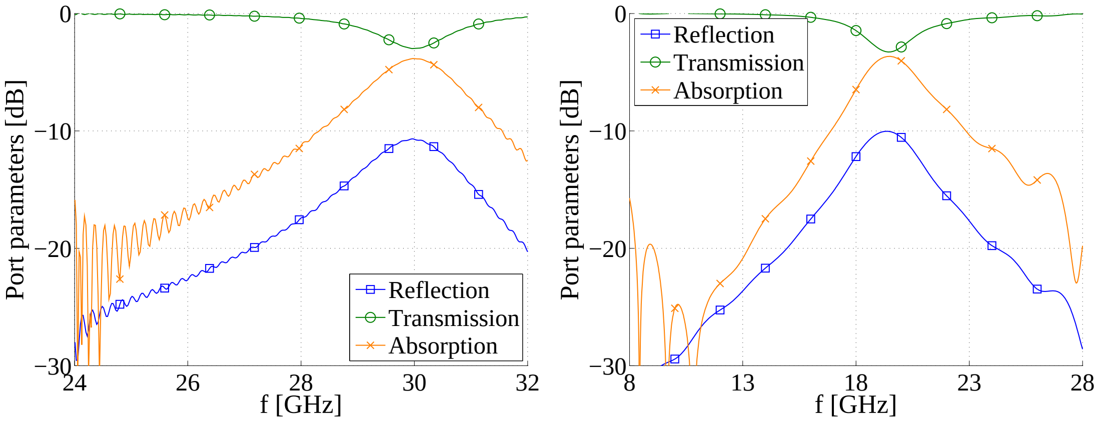

(a) $l = 5$ mm (b) $l = 8$ mm

Figure 4.24: Transversal slots in reduced main guide height $b_r = 9$ mm.

-30 dB input reflection match. Apart from the undesirable increase in component size, these transitions would place the slot array further from the short-circuit plane. As it was demonstrated in §4.3.6 that this increased distance would reduce the bandwidth of the slot considerably, this is not a preferred solution.

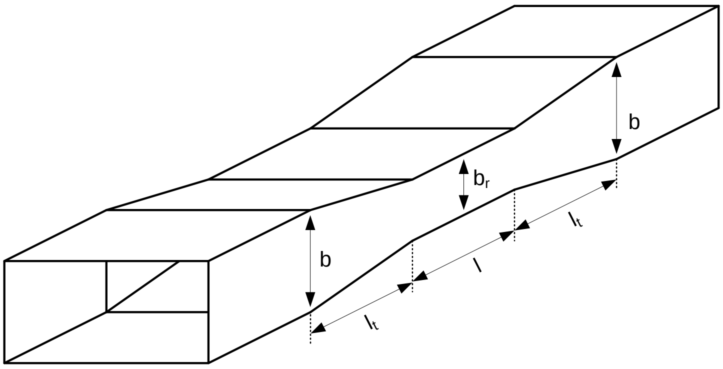

Figure 4.25: Tapered transition dimensions.

A better option is to place a PEC wall inside the normal height waveguide to suppress the TM_{12} mode without affecting the propagating TE_{10} mode. This can be done by placing two lengths of very thin ($t < 0.5$ mm) shim under the slot, separated by a distance y_s, as shown in Fig. 4.26(a).

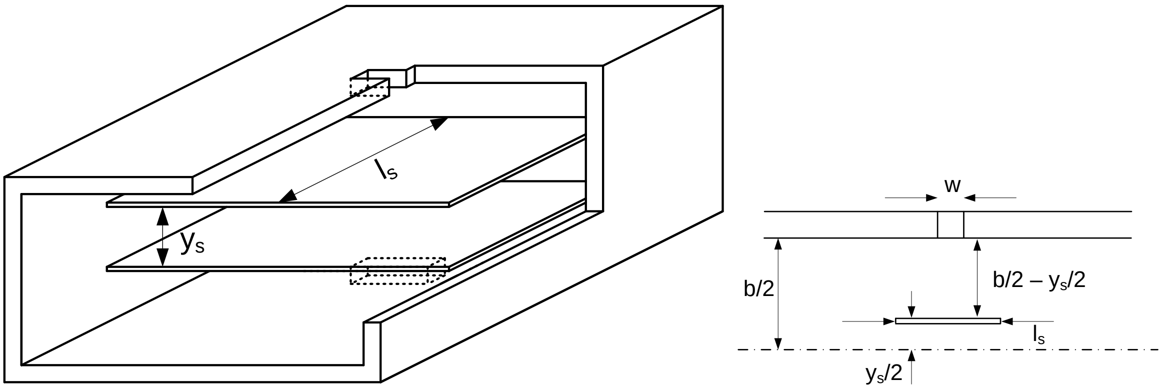

(a) Sectioned view indicating the position of the shims in waveguide. The auxiliary guides are omitted for clarity.

(b) Sectioned side view of shims.

Figure 4.26: Layout of shims between transversal broadwall slots to suppress TM_{12} propagation.

The operation of a single shim is considered by bisecting the waveguide along the xz-plane of symmetry, and considering a TM_{11} mode in this half-height guide (which is equivalent to a TM_{12} mode propagating in the full-height guide). By placing the shim at $y = y_s/2$, the effective guide height at that point is reduced to $b/2 - y_s/2$, as shown in Fig. 4.26(b). By choosing $y_s = 2$ mm, the TM_{11} mode cut-off frequency is increased to above 34 GHz, and the undesired null in absorption is removed, as is illustrated in Fig. 4.27 with two shims of length $l_s = 6$ mm in place.

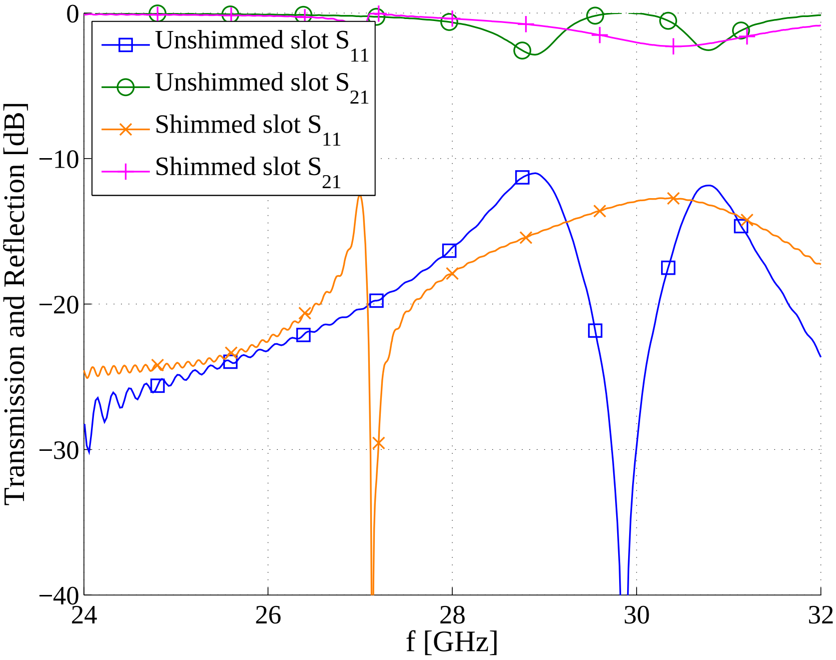

Figure 4.27: Scattering response of unshimmed and shimmed transversal broadwall slots.

Unfortunately, two new spurious resonances, corresponding to the TE_{101} and TE_{301} resonant modes in reduced height waveguide, are created at 19.8 and 27.1 GHz, as shown in Figs. 4.28 and 4.29.

These resonances are not strictly rectangular waveguide transmission line resonator modes, since the 6 mm length of the shims does not correspond to $\lambda_g/2$ for either the TE_{10} or TE_{30} modes for $a = 22.86$ mm at their respective resonant frequencies. They are, rather, combined effects of transmission line length and reactive effects associated with E-plane bifurcations, as discussed in §6.4 of [68].

These resonances do not preclude the use of shims. The contribution to input reflection of the shims is typically below -25 dB across band of interest, and if appropriate choices for y_s and l_s are made, the spurious resonances can be placed outside the absorptive bands of interest. For example, retaining y_s as 2 mm and increasing l_s to 8 mm moves the two spurious resonances to 16.5 and 24.7 GHz (shown in Fig. 4.31), which are both outside the absorptive bands of interest. The shims may be shortened to move the TE_{30} resonance above the band of interest, but this leaves a shim too short to effectively suppress the TM mode, as is indicated with a $l_s = 4$ mm shim in Fig. 4.31.

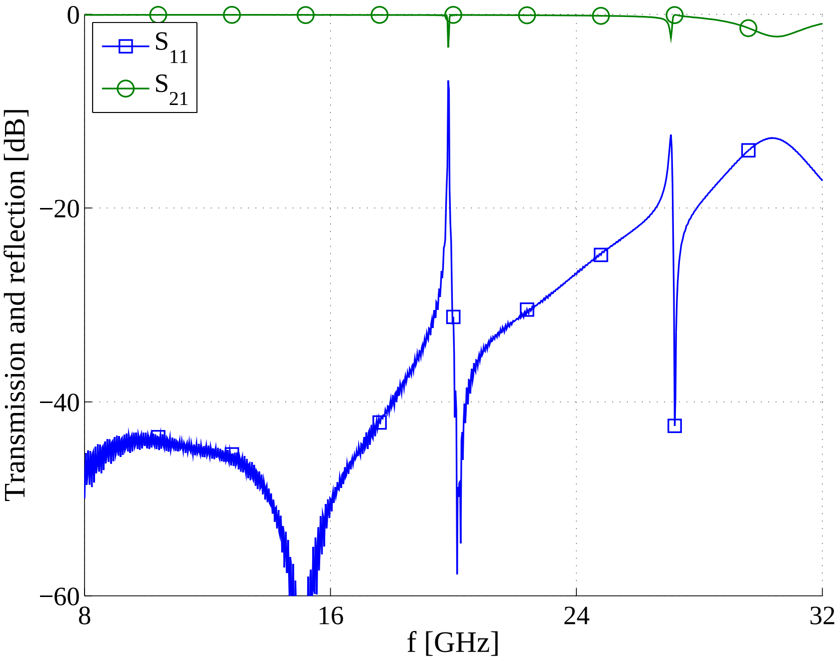

Figure 4.28: Wide-band reflection response of $l = 5$ mm transversal broadwall slots with $l_s = 6$ mm shims.

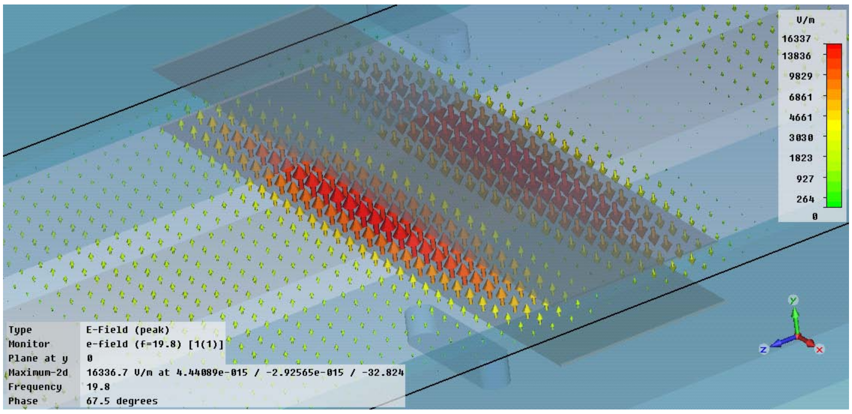

```
Type         E-Field (peak)
Monitor      e-field (f=19.8) [1(1)]
Plane at y   0
Maximum-2d   16336.7 V/m at 4.44089e-015 / -2.92565e-015 / -32.824
Frequency    19.8
Phase        67.5 degrees
```

(a) TE_{101} resonance at 19.8 GHz.

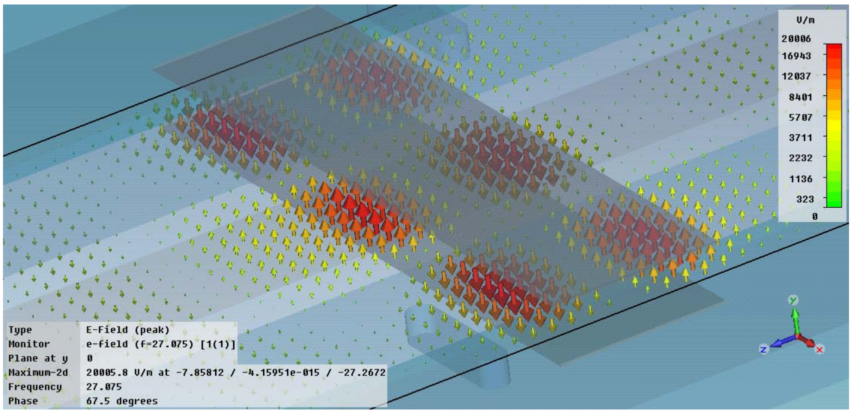

```
Type         E-Field (peak)
Monitor      e-field (f=27.075) [1(1)]
Plane at y   0
Maximum-2d   20005.8 V/m at -7.85812 / -4.15951e-015 / -27.2672
Frequency    27.075
Phase        67.5 degrees
```

(b) TE_{301} resonance at 27.1 GHz.

Figure 4.29: $\vec{E}$-field distributions on the xz-plane for spurious shim resonances.

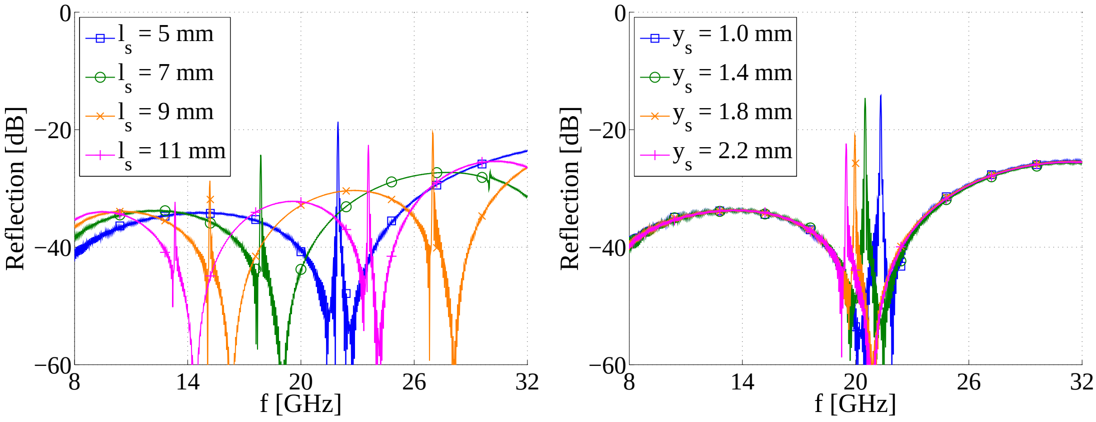

(a) Effect of shim length l_s on resonance. (b) Effect of shim spacing y_s on resonance.

Figure 4.30: Adjustment to spurious shim resonance by variation in l_s and y_s.

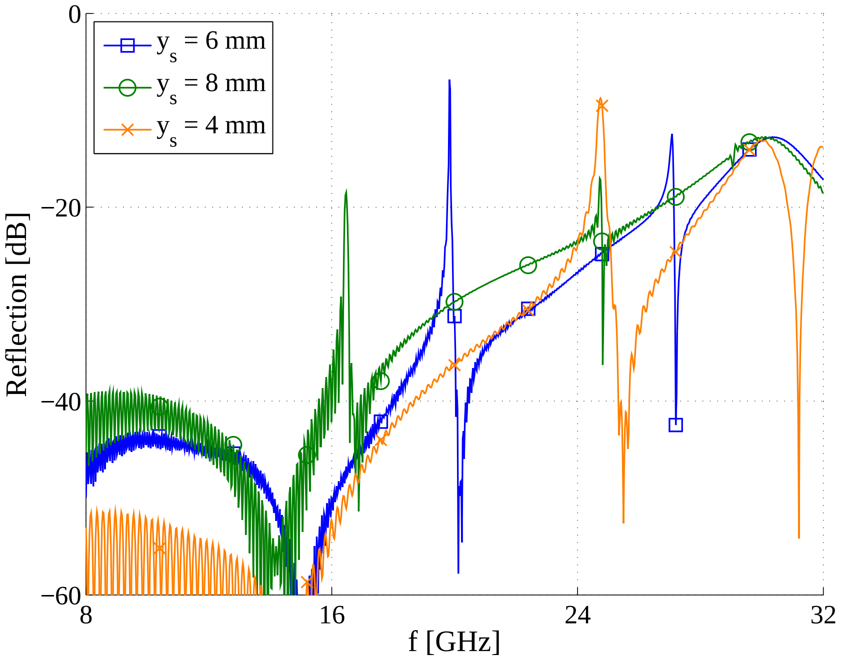

Figure 4.31: Moving the spurious shim resonances outside the absorptive bands of interest.

To improve the performance of the 24.5 - 31.5 GHz slot even further, two slots can be placed side-by-side, as shown in Fig. 4.32. Not only does this slot pattern increase peak absorption (Fig. 4.33(c)), but the peak absorption can be synthesised (without exciting the TE_{20} mode) by rotating the slots around their respective centre y axes (Fig. 4.34(a)) or, to a lesser extent, varying the distance between them (Fig. 4.34(b)).

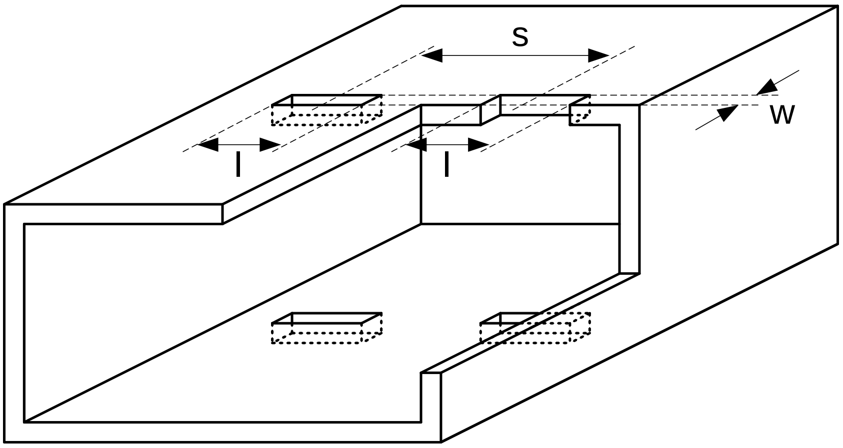

Figure 4.32: Layout of dual transversal slots. Auxiliary guides omitted for clarity.

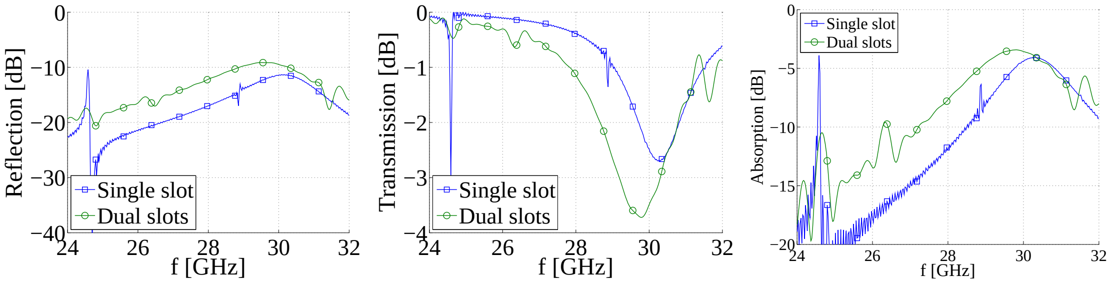

(a) Comparison of 1- and 2-slot reflection

(b) Comparison of 1- and 2-slot transmission

(c) Comparison of 1- and 2-slot absorption

Figure 4.33: Comparison of single and dual slot electrical responses.

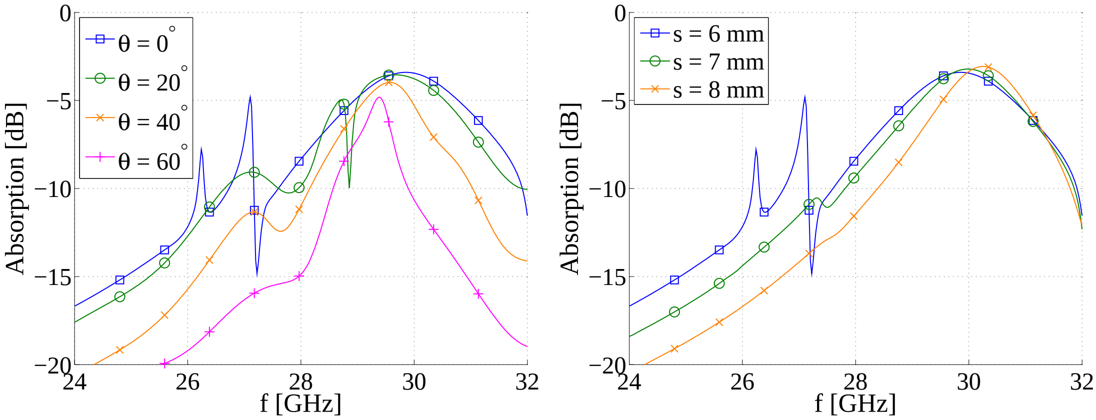

(a) Effect of varying slot rotation θ

(b) Effect of varying slot spacing s

Figure 4.34: Parametric study of relative dual slot placements.

4.3.8 Higher order modes

It was illustrated in Fig. 4.3(a) that all odd TE_{m0} modes have a common maximum in surface current, namely J_z at $x = a/2$ and $y = 0, b$. To verify that the transversal broadwall slot absorbs these modes, an $l = 6$ mm test slot was excited by the TE_{30} mode, rendering the results shown in Fig. 4.35. Note that the TE_{12} and TM_{12} modes are below cut-off ($f_c = 30.14$ GHz in WR-90) at slot resonance, and may be omitted from the analysis.

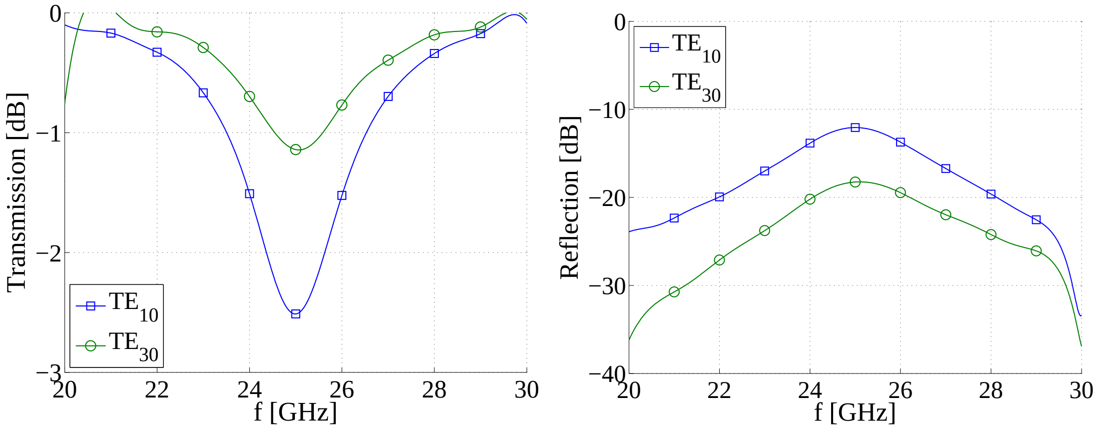

(a) Transmission. (b) Reflection.

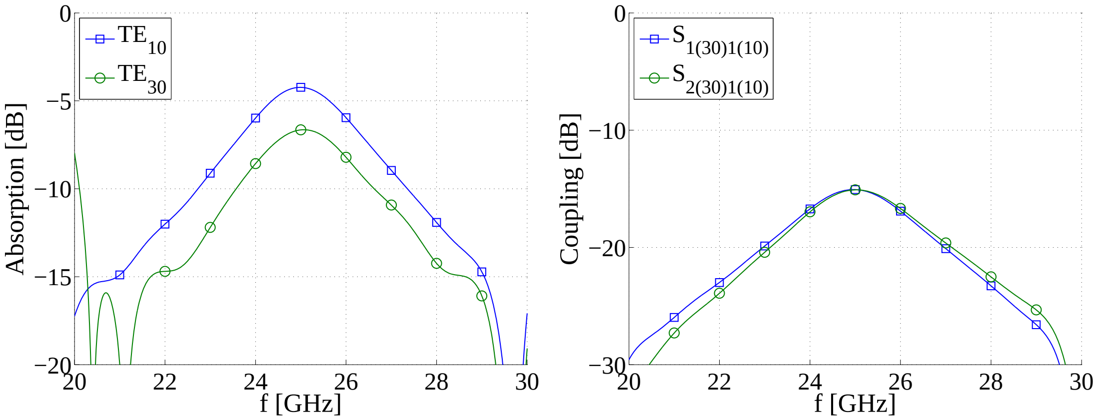

(c) Absorption. (d) Coupling to fundamental mode.

Figure 4.35: Higher order mode operation of 6 mm transversal broadwall slot.

Since the magnitude of surface current maximum is lower in the TE_{30} mode than the TE_{10} mode (shown in Fig. 4.3(a)), the absorption levels are significantly less than those of the TE_{10} mode. The general shape of the response is, however, similar, verifying the operation of the slot for odd TE_{m0} modes.

Also noticeable, is that an incident TE_{10} mode excites both transmitted and reflected TE_{30} modes of -15 dB at resonance. This effect is significant, and any final prototype performance has to be checked for acceptable levels of higher mode backscattering.

4.3.9 Power handling capability

The final required analysis of transversal broadwall slots required is an analysis of the power handling capability of the structure. Much of the theory used here is discussed in §3.5. As before, peak and average power handling capabilities are discussed separately.

Peak power

As in the previous chapter, the peak power handling capability is determined by the maximum full-wave simulated $\vec{E}$-field strength $E_{\max}$, and comparing it to breakdown $\vec{E}$-field strength E_B of 12.1 kV/cm RMS as calculated in Eq. 3.12. From simulation, the maximum $\vec{E}$-field occurs at resonance across the slot aperture, as shown in (Fig. 4.36(a)). This field strength can be used as benchmark for peak power handling capability.

Away from slot resonance, and with the waveguide terminated with a matched port, the slot exhibits maximum power handling capabilities comparable to the waveguide itself (shown in Table 4.1), and significantly more than the required 8 kW specified in Chapter 1. Since there is no concentration of $\vec{E}$-field around the slot at under these conditions (Fig. 4.36(b)), this is to be expected. In the absorption band, simulating the slot with a short-circuited main guide (similar to the conditions experienced in the filter stop-band, if the slot is cascaded with a reflective filter) at resonance indicates a heavily concentrated $\vec{E}$-field, with $E_{\max}$ increased by over 800%. The resulting decreased peak power handling capability is still more than the maximum -15 dBc = 253 W harmonic power level specified in Chapter 1, which is significantly less than the 8 kW power handling capability required under matched conditions in the band 8.5 - 10.5 GHz.

Table 4.1: Peak power capabilities of 8 mm transversal broadwall slot under different conditions. P_{in} = 1 W RMS.

		$E_{\max}$ [V/m RMS]	$P_{\max}$ [kW]
Regular, $w = 1$ mm	Shorted, $f = 19$ GHz	25184	2.31
	Matched, $f = 9.5$ GHz	3034	158.82
Regular, $w = 1.5$ mm	Shorted, $f = 19$ GHz	16694	5.25
	Matched, $f = 9.5$ GHz	2712	198.78
Rounded, $w = 1$ mm	Shorted, $f = 19$ GHz	25398	2.27
	Matched, $f = 9.5$ GHz	2711	198.93

Increasing the slot width to 1.5 mm results in the power handling capability being more

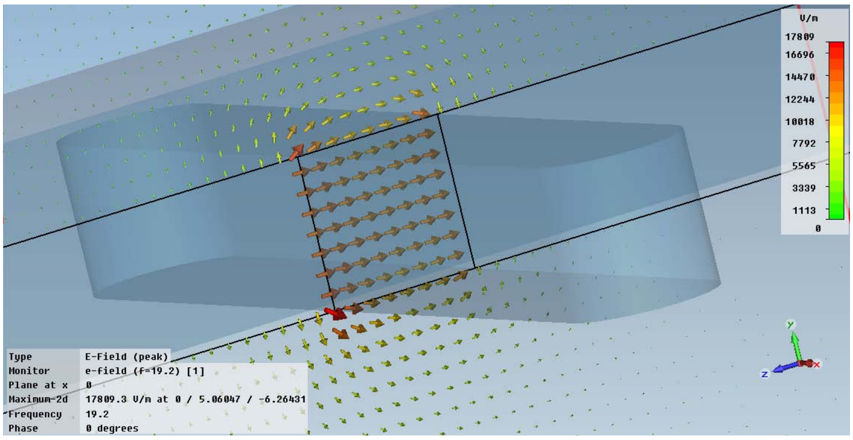

Type E-Field (peak)
Monitor e-field (f=19.2) [1]
Plane at x 0
Maximum-2d 17809.3 V/m at 0 / 5.06047 / -6.26431
Frequency 19.2
Phase 0 degrees

(a) At resonance.

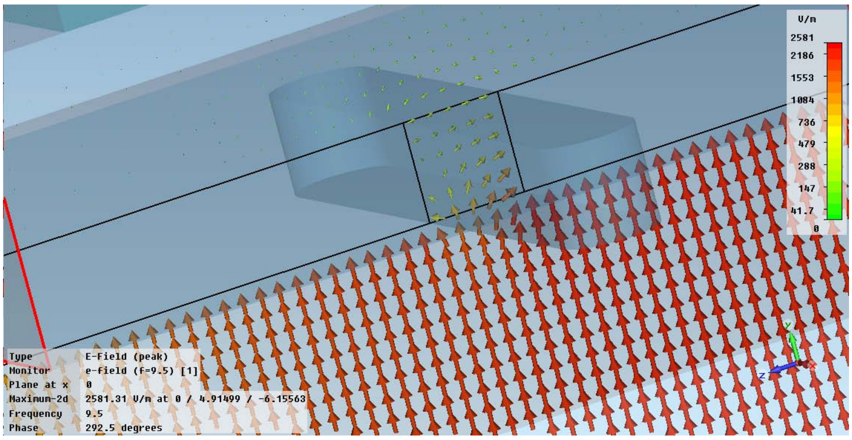

Type E-Field (peak)
Monitor e-field (f=9.5) [1]
Plane at x 0
Maximum-2d 2581.31 V/m at 0 / 4.91499 / -6.15563
Frequency 9.5
Phase 292.5 degrees

(b) Off resonance.

Figure 4.36: Slot aperture $\vec{E}$-field distribution.

than doubled, with a maximum of 5.25 kW. In contrast, rounding the outer slot edges by $r = 0.3$ mm (similar to the rounding applied to the bosses in Fig. 3.25) does not increase the power handling capability of the slots significantly. Given the increased manufacturing complexity associated with implementing this rounding, it is not considered for a manufactured prototype.

Average power

The main concern in evaluating average power handling capability is the dissipative heating of the end-load absorbers in the auxiliary guide (§4.6.1). The power absorbed in these loads is easily determined by the port parameters S_{31} and S_{41}, where ports 3 and 4 substitute end-loads in the auxiliary guide during simulation. Under short-circuited main guide conditions, these are simulated as -7.93 dB and -7.51 dB at resonance, respectively.

With the average in-band power specified as 500 W, and the average power in the second harmonic (as with peak power) no more than -15 dBc, each end-load has to absorb an average incident power in the order of -22.5 dBc, or 2.8 W. This has to be considered in conjunction with the material properties of the end-load in a final manufactured prototype.

4.4 Circuit modelling

This section will establish a circuit model representation of a single transversal slot pair (in the presence of waveguide shims), and apply it in a cascade synthesis to establish an absorptive band.

4.4.1 Single slot

Single transversal coupling slots have been studied extensively in [93, 104, 105] (Shown in Fig. 4.6(b)), and the resulting circuit models have been proven accurate over wide bandwidths. They are distinguished from classical models [68, 102] by their simplicity, but also by their reliance on accurate numerical data from a full-wave simulation of the slot[4]. Since such a solver (in this case, *CST Microwave Studio 2009*) is available, this presents no difficulty. These models will, therefore, be used as starting point of further development.

Two previous test structures will be used to verify the validity of each model. The first is two broadwall transversal slots, symmetrical around the xz-plane, of length 8 mm each, each coupling to an auxiliary guide of 13 × 3 mm from standard WR-90 guide (22.86 × 10.16 mm). The second replaces the 8 mm slot with two 5 mm slots in the side-by-side layout of Fig. 4.32, and includes two shims of thickness t_s = 0.1 mm and length l_s = 5 mm placed across the width of the main guide between the opposing slots, a distance y_s = 1.4 mm apart. All waveguide ports are de-embedded to the centre of the slot.

Resistive load model

The most reduced form of the finite wall thickness model provided in [93] is a simple loaded series resonator, shown in Fig. 4.37(a). This model makes the following assumptions:

1. The slot is resonant at the same frequency in both the main and auxiliary guides (neglecting a second LC resonator).
2. The finite wall thickness has negligible effect on the resonant characteristics of the slot.

---

[4] Classical models' circuit values are derived directly from physical dimensions

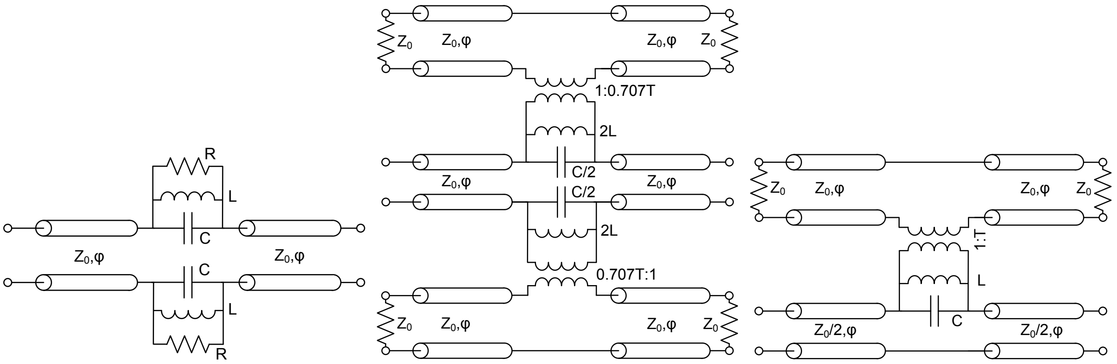

(a) Single lossy resonator. (b) Resonators coupling to auxiliary lines. (c) Electrical equivalent, in the case of *H*-plane symmetry.

Figure 4.37: Single slot circuit models under consideration.

3. The absorptive material inside the auxiliary guide suppresses propagation to such an extent that, if ports were to be placed at the ends of the auxiliary waveguide, the energy coupled to those ports would be negligible. The structure, therefore, reduces to a simple two-port.

Circuit element values are extracted from the scattering parameter $S_{11} = \Gamma$ (since all other ports are matched) produced by the full-wave solver. The resonator parameters are related simply by the resonant frequency

$$\omega_0 = \frac{1}{\sqrt{LC}} \tag{4.18}$$

which is found by the equi-phase point of S_{11} and S_{21}. The offset from 0 phase at ω_0 is the effect of the embedded line length ϕ.

Since the input impedance is purely resistive at resonance, the resistance R is calculated as

$$R = \frac{2\left|\Gamma\right|_{\omega=\omega_0}}{1-\left|\Gamma\right|_{\omega=\omega_0}} \tag{4.19}$$

Though it is possible to calculate L or C from the reflection slope at resonance

$$\left.\frac{d\Gamma}{d\omega}\right|_{\omega=\omega_0} = \frac{-j4CR^2Z_0}{4Z0^2 + 4RZ_0 + R^2} \tag{4.20}$$

this relies heavily on the accuracy of a singular full-wave simulation data points at resonance, and is complicated by the presence of embedded transmission line ϕ. A better broadband approximation is made by deriving the input reflection magnitude of the resonator from circuit theory

$$|\Gamma| = \frac{\omega LR}{\sqrt{\left(2RZ_0 - \frac{2\omega RZ_0}{\omega_0}\right)^2 + L\left(2\omega Z_0 + \omega R\right)^2}} \tag{4.21}$$

and using a broad sample of frequency points ω and reflection magnitude $|\Gamma|$ to calculate a mean value of L and, consequently, C. This method is used to calculate the results shown in Fig. 4.38 and Fig. 4.39.

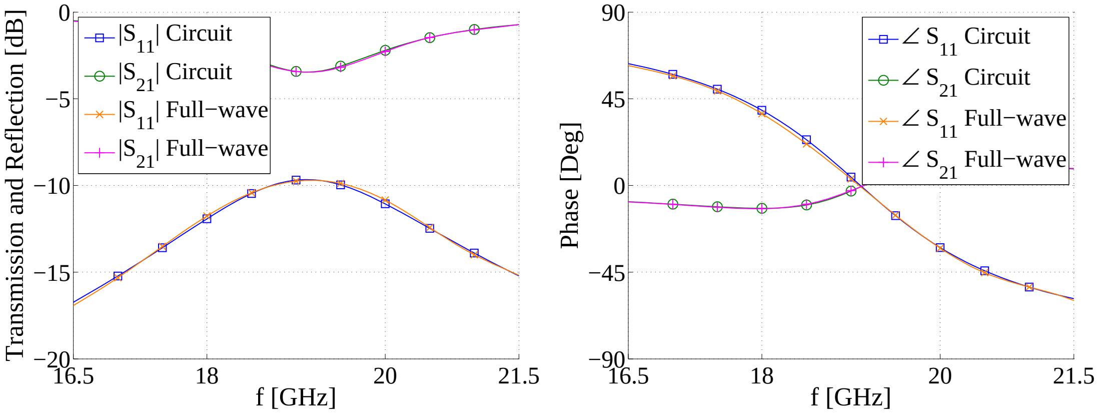

(a) Transmission and reflection magnitude. (b) Transmission and reflection phase.

Figure 4.38: Performance of single lossy resonator approximation of 8 mm transversal coupling slot, $R = 0.98\ \Omega$, $L = 800$ fH, $C = 86.62$ pF, $\phi = 0.28°$

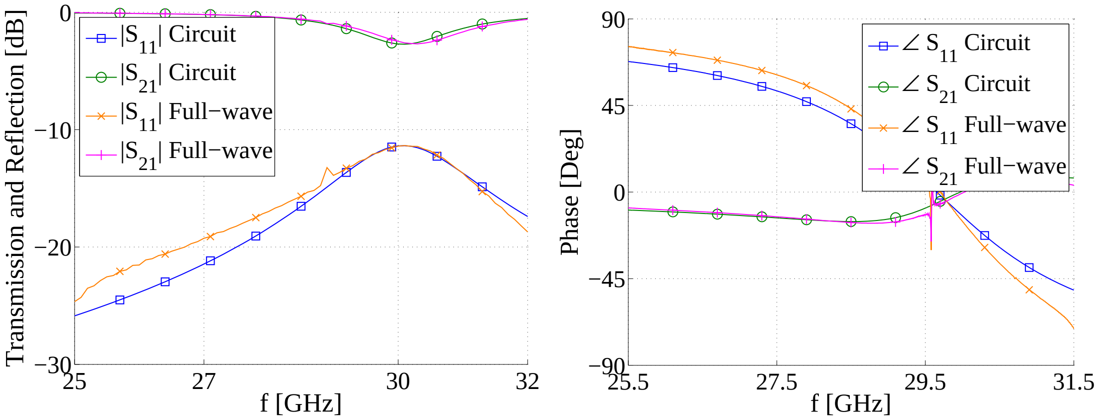

(a) Transmission and reflection magnitude. (b) Transmission and reflection phase.

Figure 4.39: Performance of single lossy resonator approximation of 5 mm transversal coupling slot, $R = 1.02\ \Omega$, $L = 384$ fH, $C = 74.48$ pF, $\phi = 1.89°$

The results in Fig. 4.38 indicate excellent correspondence between the simplified model and the full-wave simulated S-parameters in the band 17 - 21 GHz, but some deviation at 25.5 - 31.5 GHz (shown in Fig. 4.39), especially far below resonance. This may be due to unmodelled interaction between the shims and the slot, as noted previously in §4.3.7. However, the simplicity of the current model justifies its use, despite the 7° phase difference in reflection at lower frequencies.

Auxiliary TEM line model

The model coupling to external auxiliary line ports is shown in Fig. 4.37(b), with an electrical equivalent (given the H-plane symmetry in the physical structure) in Fig. 4.37(c). In the case of an isolated slot, both are electrical equivalents of Fig. 4.37(a), with the transformer value T derived from circuit theory as

$$T = \sqrt{\frac{4Z_0}{R}} \tag{4.22}$$

It is, therefore, unnecessary to evaluate it independently.

4.4.2 Cascade of two slots

Three approaches are considered in modelling cascaded slots. The first uses a cascade of lossy resonators without external coupling (Fig. 4.41(a)), the second explicitly models external coupling through the auxiliary waveguide by using TEM lines (Fig. 4.41(b)), and the third models both internal and external coupling using circuit model representations of TE_{10} propagation in waveguide (Fig. 4.41(c)). Two identical slots of $l = 8$ mm cascaded $d = 5$ mm apart (as shown in Fig. 4.40) is used as a test case. The simulated main guide also contains two shims of length $l_s = 8$ mm, separated by $y_s = 1.4$ mm.

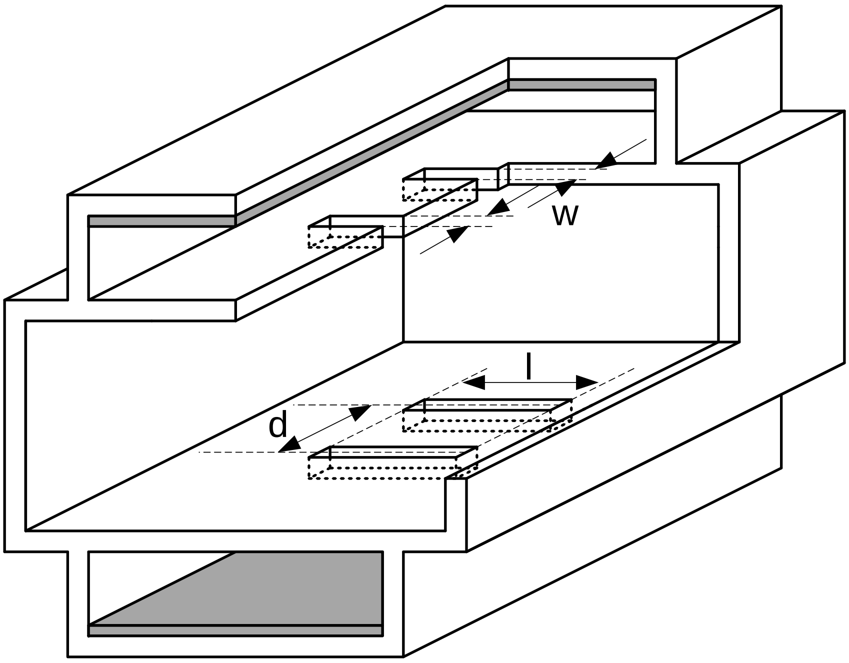

Figure 4.40: Two identical slots of length l and width w, cascaded by a distance d.

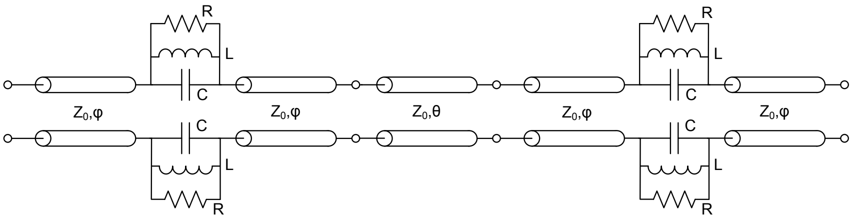

(a) Two cascaded lossy resonators.

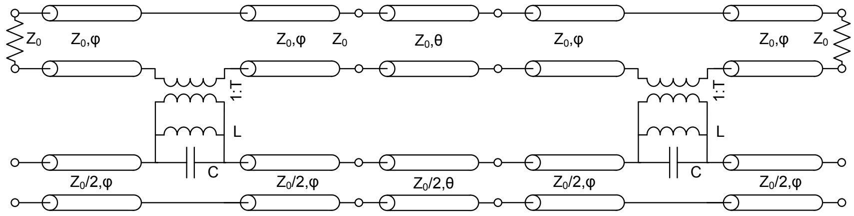

(b) Two cascaded resonators coupled by auxiliary TEM line.

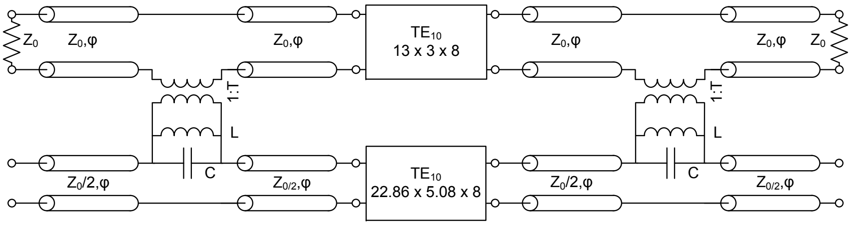

(c) Two cascaded resonators coupled by auxiliary TE_{10} waveguide. Note the bisected main guide height of 5.08 mm.

Resistive load models

In conjunction with the previously calculated circuit values for the 8 mm slot equivalent circuit, the section of waveguide between the slots is modelled as a TEM line of normalised 1 Ω impedance and length 0.299λ (since the guide wavelength at the resonant frequency of the slot is 16.69 mm). The results shown in Fig. 4.41 indicate rather poor correspondence. The accuracy of the circuit model is severely impaired by not taking exterior slot coupling through the auxiliary guides into consideration. Note that the resonant effect at 14.48 GHz is not a function of the slots, but rather a resonance of the shims, as discussed in the previous section.

Auxiliary TEM line

The second circuit model under consideration, shown in Fig. 4.41(b), includes a section of TEM line of length 0.254λ for external slot coupling, which corresponds to 5 mm line length in the reduced size auxiliary guide. The agreement shown in Figs. 4.42(a) and 4.42(b) indicate marked improvement over the cascaded lossy resonator model without external coupling.

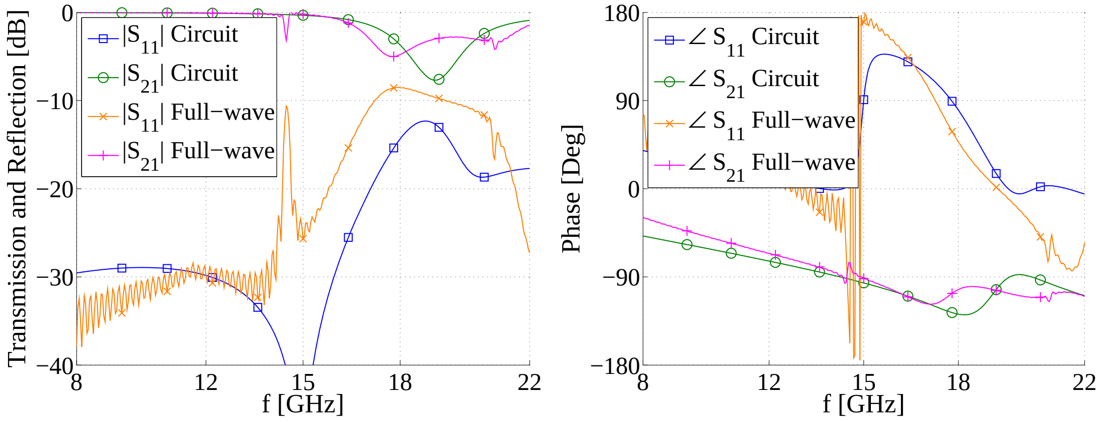

(d) Transmission and reflection magnitude. (e) Transmission and reflection phase.

Figure 4.41: Performance of cascaded lossy resonator circuit model without external slot coupling.

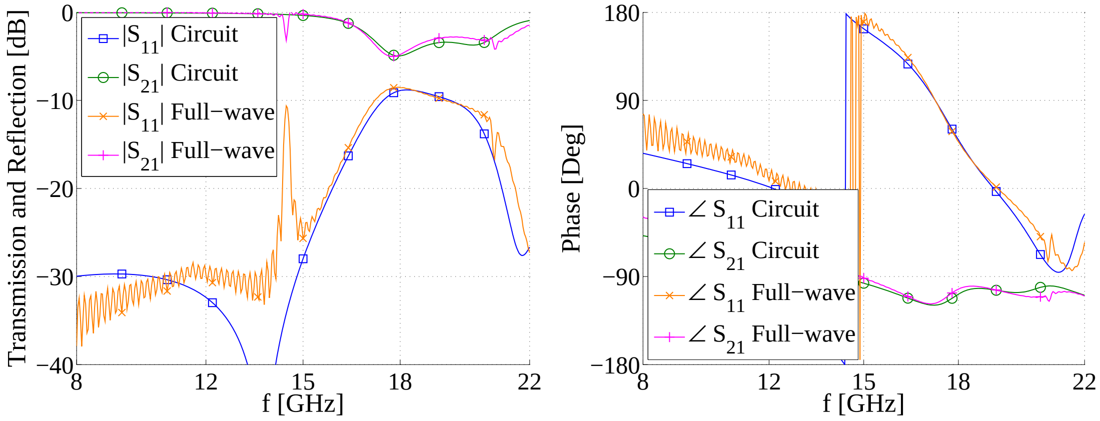

(a) Transmission and reflection magnitude, 5 mm cascade.

(b) Transmission and reflection phase, 5 mm cascade.

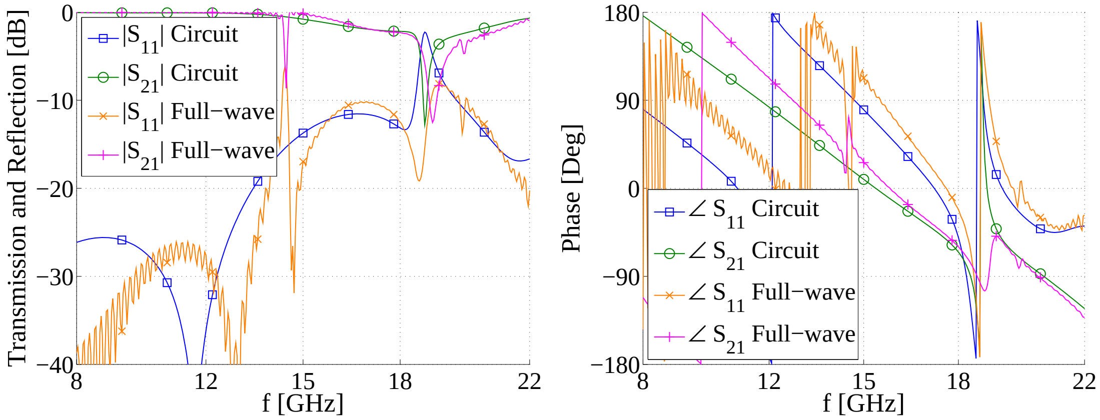

(c) Transmission and reflection magnitude, 20 mm cascade.

(d) Transmission and reflection phase, 20 mm cascade.

Figure 4.42: Performance of cascaded TEM-line coupled resonator circuit model.

In the case of increased slot separation of $d = 20$ mm, with each slot equipped with its own set of shims of length 10 mm (maintaining the shim separation of 1.4 mm) the results in Figs. 4.42(c) and 4.42(d) are obtained with the slots located 1.199λ apart in the main guide and 1.018λ in the auxiliary guide at the resonant frequency. Some differences between the magnitudes of scattering parameters are visible, but of more concern is the severe discrepancy in phase response, especially in the transmission band.

Auxiliary waveguide

The third approach models TE_{10} waveguide explicitly in both the auxiliary and main guide, as shown in Fig. 4.41(c). The broadband phase agreement for two cascaded slots of $d = 20$ mm (shown in Fig. 4.43(b)) is better than is the case when using TEM lines (Fig. 4.42(d)), though the magnitude response is little changed (Fig. 4.43(a)). This improved phase response is, however, an important consideration, since it has been demonstrated in §4.2 that the distance between the slot and the reflective source is critical to its operation. This model is, therefore, used in further development.

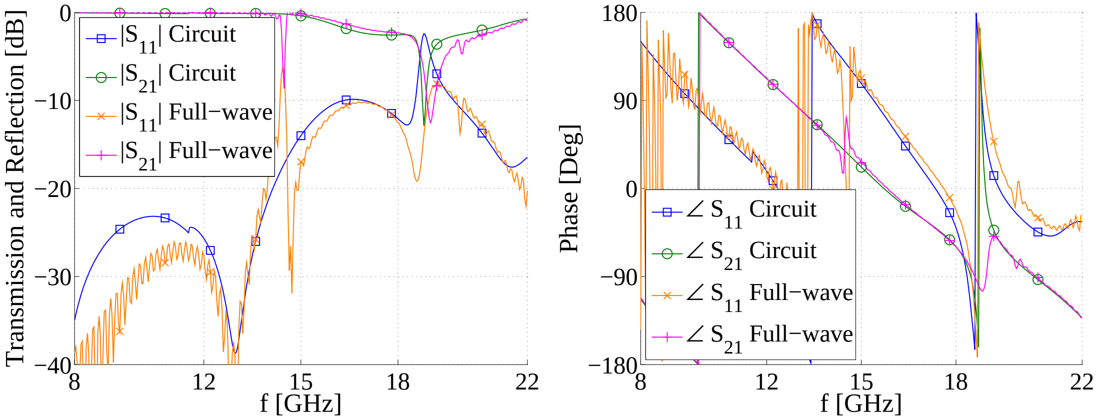

(a) Transmission and reflection magnitude, 20 mm cascade.

(b) Transmission and reflection phase, 20 mm cascade.

Figure 4.43: Performance of cascaded waveguide coupled resonator circuit model.

4.5 Synthesis examples

This section will illustrate the use of the previously established circuit models to develop harmonic pads capable of effecting a required input match over a required bandwidth, in the presence of a reflective load. The development goals for this particular application are shown in Table 4.2. In all cases, circuit modelling and optimisation are performed in *AWR Microwave Office 2008*, and full-wave simulation in *CST Microwave Studio 2009.*

Table 4.2: Input reflection specifications.

	f_1 [GHz]	f_2 [GHz]	$\|S_{11}\|$ [dB]
First absorptive band	17	21	-15
Second absorptive band	25.5	31.5	-10

4.5.1 General approach

As yet, there is no explicit synthesis technique to effect a required match for cascaded lossy shunt resonators terminated by a reflective load [23, 24, 20]. The most relevant published theory is the input reflection synthesis of multi-mode patch antennas [107], where the load on the shunt resonator is the radiation resistance of the antenna. This method relies on analytical expressions of input impedance for a limited number of resonators, and is not generally applicable to an arbitrary cascade of resonators. Analytical expressions of the absorption of Jauman absorbers [108] are similarly limited to specific orders, and grow exponentially more complex for each additional layer.

Less numerically intensive and time-consuming than full-wave optimisation, is the optimisation of a circuit model representing the cascaded transversal slots. This has the advantage that the circuit model can be designed end-loaded with the exact S-parameter data of the reflective filter the harmonic pad is to be designed for, as well as providing a reverse-tuning tool with which full-wave results can be adjusted.

The synthesis starts by selecting the initial values of resonant frequency f_i for all of the cascaded resonators to be the centre frequency f_0 of the band to be absorbed, with values of L_i, C_i, ϕ_i and T_i (shown in Fig. 4.44) to match a slot of that required length. Slot spacings d_i are chosen to place the slots at the centre frequency standing wave pattern maxima, as discussed in §4.2 and §4.3.6.

The circuit is then cascaded with the S-parameters of the reflective filter (as shown in Fig. 4.44) and the values f_i and d_i are optimised to achieve a goal input reflection match

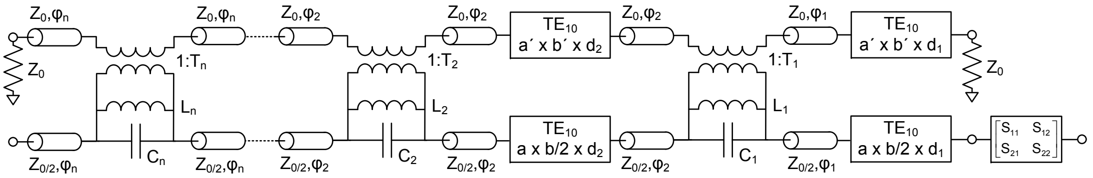

Figure 4.44: General optimisation circuit. The S-parameter block represents externally generated reflective filter data.

over a given band using a random localised optimisation algorithm. Variation in slot resonant frequency, as is done in circuit optimisation, is associated with changes in other slot circuit parameters which are not adjusted in the optimisation. It is therefore necessary to halt the optimisation periodically, full-wave simulate each individual slot to extract circuit parameters L_i, C_i, ϕ_i and T_i associated with a slot resonating at an intermediate optimised f_i, and then apply these changes in circuit parameters to the optimisation model before continuing the optimisation. An alternative is to establish values of L, C, ϕ and T for a wide range of slot resonant frequencies (and, therefore, a wide range of slot lengths l) before circuit optimisation, and apply these changed periodically to the circuit model during optimisation.

The synthesis is considered complete when the optimisation goals are achieved with values of L_i, C_i, ϕ_i and T_i that match the final optimised resonant frequency of each slot. The resonant frequencies are then used to find slot lengths l_i, and used in conjunction with the values of d_i to construct a full-wave model of the harmonic pad. These dimensions can then be fine-tuned in full-wave simulation to establish a final manufacturing model.

If the circuit optimisation fails to produce a circuit capable of reaching the specification, one of two options are available. Firstly, an adjustment to the auxiliary guide dimensions (a', b') will effect a change in the average transformer values T_i, since the magnitude of the absorbed energy is affected. More commonly, an increase in the number of slots simulated is found to improve the odds of finding an optimised solution. This is especially true if the required matching bandwidth cannot be achieved with the number of slots under consideration. On the other hand, increased slots also result in increased synthesis complexity with each additional slot leading to less performance improvement than the previous (§4.2, §4.3.6).

4.5.2 Design for first absorptive band

The procedure outlined above is applied to the first absorptive band of 17 - 21 GHz, with a top view of the physical structure shown in Fig. 4.45. The circuit model in Fig. 4.44 is terminated with the actual S-parameter data of the waffle-iron filter designed in the previous chapter.

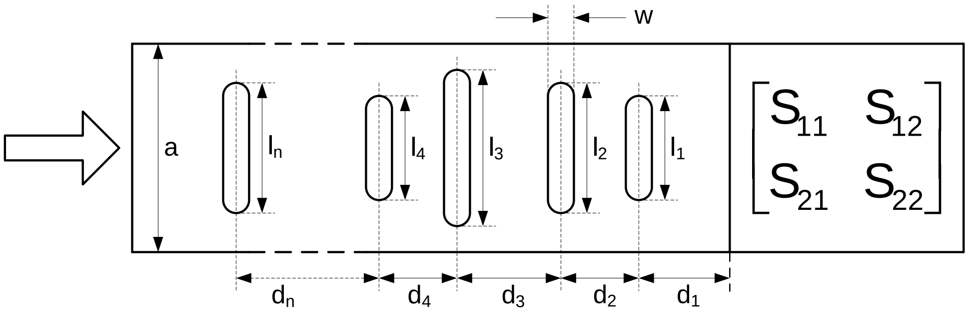

Figure 4.45: General slot dimensions for first absorptive harmonic pad.

After an initial unsuccessful optimisation[5] using a cascade of three slots, the model is increased in order to five slots. This optimisation produces the circuit values and dimensions shown in Table 4.3 and the electrical responses in Fig. 4.46. This circuit model adheres to the specification, and is implemented in a full-wave simulation model. The full-wave model is then tuned, producing the full-wave simulation results also shown in Fig. 4.46. Each slot has a width of 1 mm cut into a wall of thickness 1 mm, coupling to an absorptive auxiliary guide of 13 × 3 mm.

Apart from the 14% reduction in d_1, the circuit model renders dimensions to within 10% of those required to meet the specification.

Fig. 4.46 also shows that the harmonic pad causes a slight increase in the in-band (8.5 - 10.5 GHz) reflection response compared to that of the waffle-iron filter in isolation, namely from -25 to -22 dB.

4.5.3 Design for second absorptive band

The procedure is also implemented for the second absorptive band, using the side-by-side transversal slots and shims shown in Fig. 4.47.

The initial model is comprised of 5 side-by-side transversal slots of length $l_i = 5.15$ mm

---

[5] An optimisation that does not render a circuit model capable of achieving the input reflection specification.

Table 4.3: Progressive development of first absorptive band harmonic pad with reflective filter termination.

		Initial	Circuit optimised	Full-wave tuned
f_1	[GHz]	19	20.7	–
L_1	[fH]	435	342	–
C_1	[pF]	161	173	–
T_1		2.05	2.22	–
ϕ_1	[°]	-0.44	-0.44	–
l_1	[mm]	8.15	7.45	7.5 (+0.67%)
f_2	[GHz]	19	20.7	–
L_2	[fH]	435	342	–
C_2	[pF]	161	173	–
T_2		2.05	2.22	–
ϕ_2	[°]	-0.44	-0.44	–
l_2	[mm]	8.15	7.45	7.55 (+1.34%)
f_3	[GHz]	19	19	–
L_3	[fH]	435	435	–
C_3	[pF]	161	161	–
T_3		2.05	2.05	–
ϕ_3	[°]	-0.44	-0.44	–
l_3	[mm]	8.15	8.15	7.95 (-2.45%)
f_4	[GHz]	19	20	–
L_4	[fH]	435	389	–
C_4	[pF]	161	163	–
T_4		2.05	2.20	–
ϕ_4	[°]	-0.44	-0.44	–
l_4	[mm]	8.15	7.7	7.7
f_5	[GHz]	19	21	–
L_5	[fH]	435	310	–
C_5	[pF]	161	185	–
T_5		2.05	2.22	–
ϕ_5	[°]	-0.44	-0.44	–
l_5	[mm]	8.15	7.3	7.3
d_1	[mm]	8.42	3.67	3.15 (-14%)
d_2	[mm]	8.42	4.71	4.81 (+2.1%)
d_3	[mm]	8.42	5.44	5.24 (-3.67%)
d_4	[mm]	8.42	2.97	3.17 (+6.73%)
d_5	[mm]	8.42	1.99	1.99

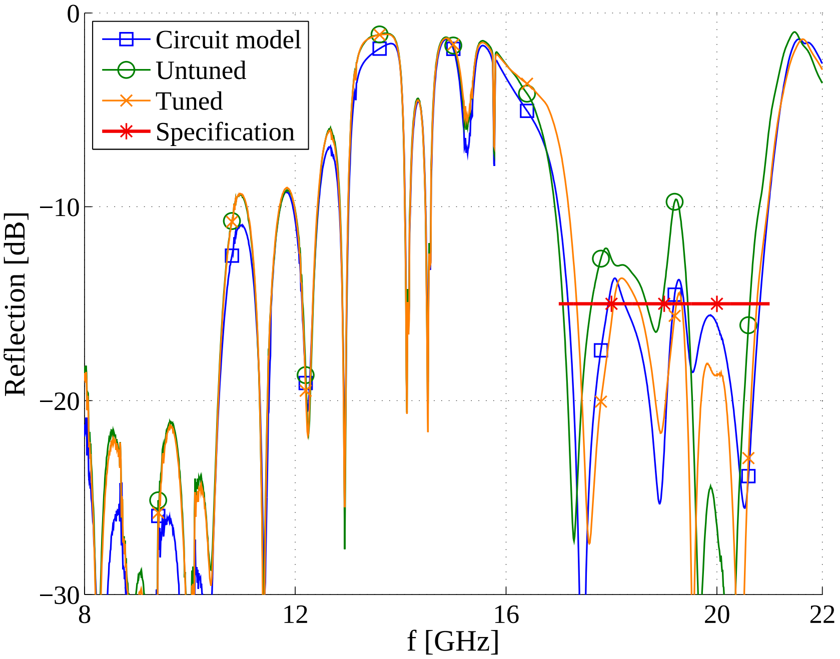

Figure 4.46: Reflection response of first absorptive band harmonic pad cascaded with a waffle-iron filter.

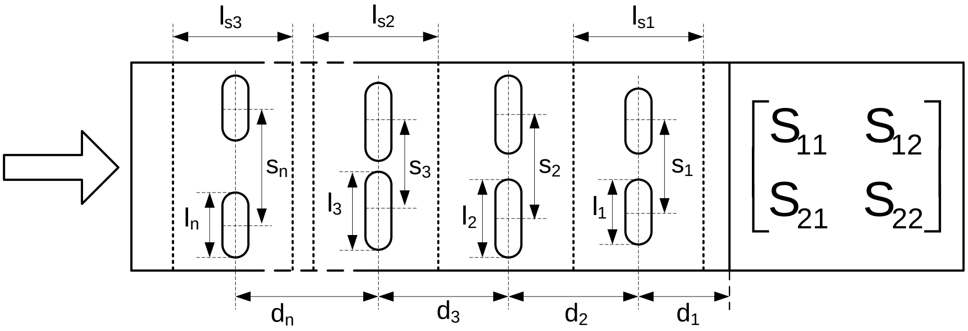

Figure 4.47: General slot dimensions for second absorptive band harmonic pad. Shim edges indicated as hidden detail.

(with centre-to-centre spacing s of 6 mm) resonating at 28.5 GHz, with cascaded spacing d_i of 5.41 (calculated as with previous designs). Full-wave simulations of isolated slots are performed with the added PEC shims of thickness $t_s = 0.1$ mm and length $l_s = 5$ mm spaced $y_s = 2$ mm apart, as shown in Fig. 4.26(a). The design proceeds as per previous examples, rendering the optimised circuit values in Table 4.4.

Due to the increased input reflection phase rate of change $\frac{d\theta}{df}$ at higher frequencies, the full 20% bandwidth cannot be achived with five slots, as was the case in the first absorptive band design. Instead of increasing the number of slots, an ammended goal of 25.5 - 30 GHz (16.2%) is chosen to illustrate the design process.

Before the initial full-wave model is considered, the cascaded effects of the shims have to be investigated. Since the slots are too closely spaced to placed to allow for an individual shim set for each, two cascaded sets of shims are placed initially. Based on the shim simulations of §4.3.7, shims of length 8 mm are selected. When simulated in isolation, however, the shims are found to introduce either spurious harmonics or reflection of up to -20 dB in the band of interest, as shown in Fig. 4.48(a).

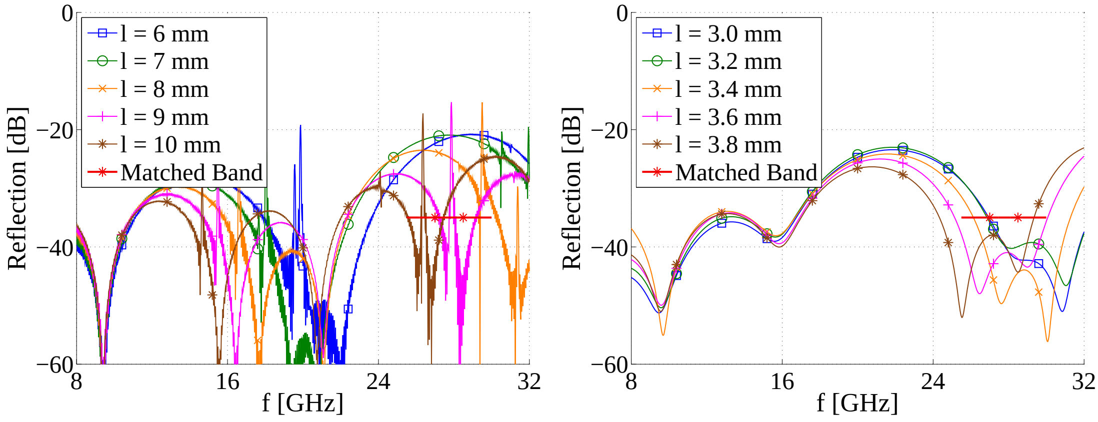

(a) Cascade of two shim pairs.

(b) Cascade of three shim pairs.

Figure 4.48: Adjustment to shim lengths for second harmonic band pad synthesis, simulated in isolation.

Replacing the cascade of two sets with a cascade of three sets (one centered at slot pair 1, one at slot pair 4, and the third at pair 5) yields a spurious-free reflection response of below -35 dB across the band of interest can be achieved for shims of length $l_s = 3.6$ mm, as shown in Fig. 4.48. The shim length is adjusted accordingly in the full-wave model, which is then tuned to the final dimensions shown in Table 4.4.

Despite considerable full-wave tuning, the third harmonic absorber does not reach even the amended specification. The overall first-iteration inaccuracy is attributed to reactive influence of the shims, since this is the only significant difference between this and the previous second harmonic designs. If the slot cascade is considered in isolation, as shown in Fig. 4.50, it is evident that same degree of first-iteration accuracy exhibited by the first absorptive band design is achieved here below 23 GHz, but is not achieved at higher frequencies. This may be due to the previously noted TE_{30} mode resonances which do not appear for shims simulated in isolation, or the mere fact that length $l_s = 3.6$ mm shims do not effectively suppress the TM_{12} mode.

Until the slot-shim interaction (as well as the shim reflection itself) is effectively modelled and accounted for in circuit optimisation, this method will be less accurate applied with

Table 4.4: Progressive development of second absorptive band pad with reflective filter termination.

		Initial	Circuit optimised	Full-wave tuned
f_1	[GHz]	28.5	26.7	–
L_1	[fH]	182	245	–
C_1	[pF]	171	145	–
T_1		2.05	1.99	–
ϕ_1	[°]	1	-0.5	–
l_1	[mm]	5.15	5.7	5.6 (-1.75%)
s_1	[mm]	6	6	6
f_2	[GHz]	28.5	29.4	–
L_2	[fH]	182	182	–
C_2	[pF]	171	161	–
T_2		2.05	2.07	–
ϕ_2	[°]	1	0.8	–
l_2	[mm]	5.15	5.15	5.15
s_2	[mm]	6	6	6
f_3	[GHz]	28.5	29.4	–
L_3	[fH]	182	182	–
C_3	[pF]	171	161	–
T_3		2.05	2.07	–
ϕ_3	[°]	1	0.8	–
l_3	[mm]	5.15	5.15	5.15
s_3	[mm]	6	6	6
f_4	[GHz]	28.5	30.95	–
L_4	[fH]	182	155	–
C_4	[pF]	171	171	–
T_4		2.05	2.1	–
ϕ_4	[°]	1	2.55	–
l_4	[mm]	5.15	4.86	3.96 (-18%)
s_4	[mm]	6	6	6
f_5	[GHz]	28.5	31.2	–
L_5	[fH]	182	145	–
C_5	[pF]	171	179	–
T_5		2.05	2.1	–
ϕ_5	[°]	1	2.55	–
l_5	[mm]	5.15	4.82	4.82
s_5	[mm]	6	6	6
d_1	[mm]	5.41	9.95	9.55 (-4.02%)
d_2	[mm]	5.41	3.11	2.61 (-16.08%)
d_3	[mm]	5.41	2.27	2.67 (+14.98%)
d_4	[mm]	5.41	5.75	5.75
d_5	[mm]	5.41	6.11	6.11

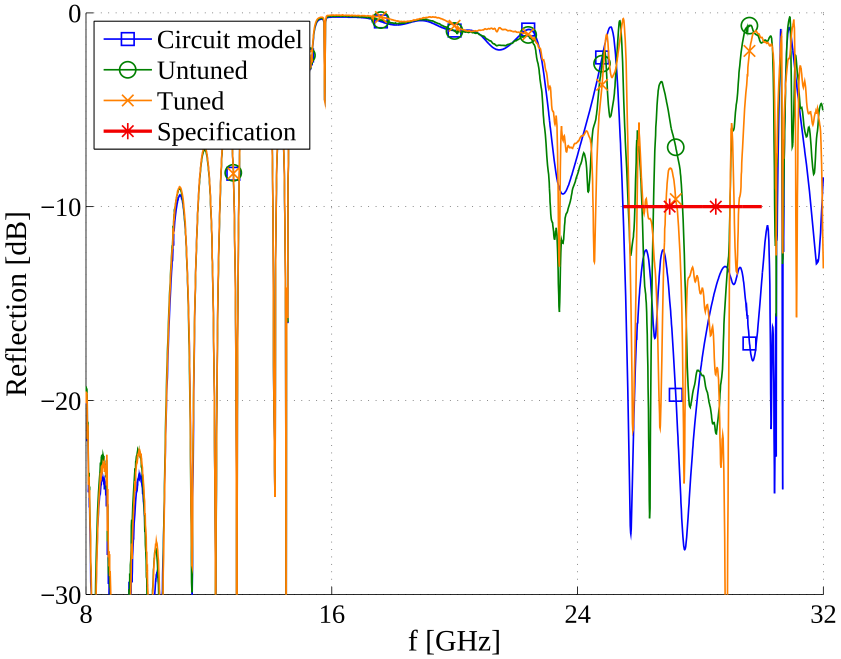

Figure 4.49: Reflection response of second absorptive band harmonic pad cascaded with waffle-iron filter.

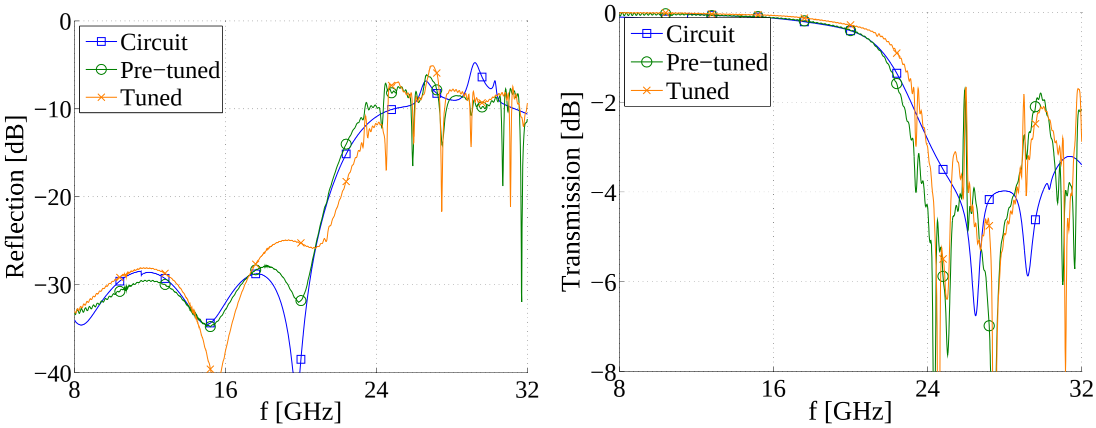

(a) Reflection.

(b) Reflection.

Figure 4.50: Comparison of transmission and reflection responses of second absorptive band harmonic pad pre- and post-tuning.

shims than without. This effectively places an upper-limit on the useful frequency band of this synthesis method in full-height waveguide.

4.6 Final prototype development

From the results in §4.5, it is clear that the first absorptive band design with a reflective source is the best candidate for implementation in a manufactured prototype. The synthesis method exhibits acceptable first-iteration accuracy (unlike the same synthesis with shimmed slots in the second absorptive band) and realistic dimensions. This section will discuss the synthesis of a manufactured prototype for the first absorptive band specification in Table 4.2, including dimensional constraints and manufacturing methods.

4.6.1 Absorptive load

The optimisation circuit model assumes characteristic termination of the the auxiliary guides at both ends. In a manufactured prototype, absorptive loads need to be placed at both ends of both auxiliary guides. The currently implemented sheet absorptive material (Eccosorb$^{\mathrm{TM}}$FGM-40) can be fashioned into a wedge-type load [109], but would require a length of at least 50 mm to provide below -20 dB reflection across the band 17 - 21 GHz.

An alternative option is to use Eccosorb$^{\mathrm{TM}}$HR, a reticulated foam sheet material. A sheet of thickness 15 mm, placed against a metal ground plane, is capable of providing below -20 dB reflection of an incident wave above 8 GHz [110]. Absorptive end-loads can therefore be implemented by inserting a block of $13 \times 3 \times 15$ mm of HR at the end of each auxiliary guide, and short-circuiting the guide behind the load (providing the metal ground plane), as shown in Fig. 4.51. The load is placed a distance d_o from the first cascaded slot, and the absorptive sheet runs the full length of the auxiliary guide above the absorptive block.

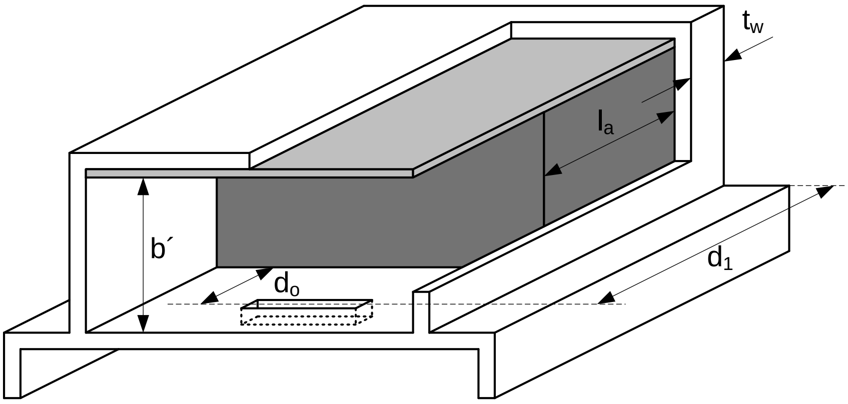

Figure 4.51: Waveguide end-load, implemented as a block of absorptive material $a' \times b' \times l_a$ against a metallic wall of thickness t_w.

An even more compact end-load can be achieved by placing the 15 mm length absorber vertically, joined to the slot by a 90° mitered E-plane bend, as shown in Fig. 4.52. Using a 45° chamfer of $d_b = 2.4$ mm (based on the optimal value calculated for WR-90 waveguide in [111]), the bend achieves better than -35 dB reflection across the band of interest, as shown in Fig. 4.52(b). For values of $b' < l_a$, this option will be more compact than the first absorber, at the cost of increased manufacturing difficulty for the 45° chamfer.

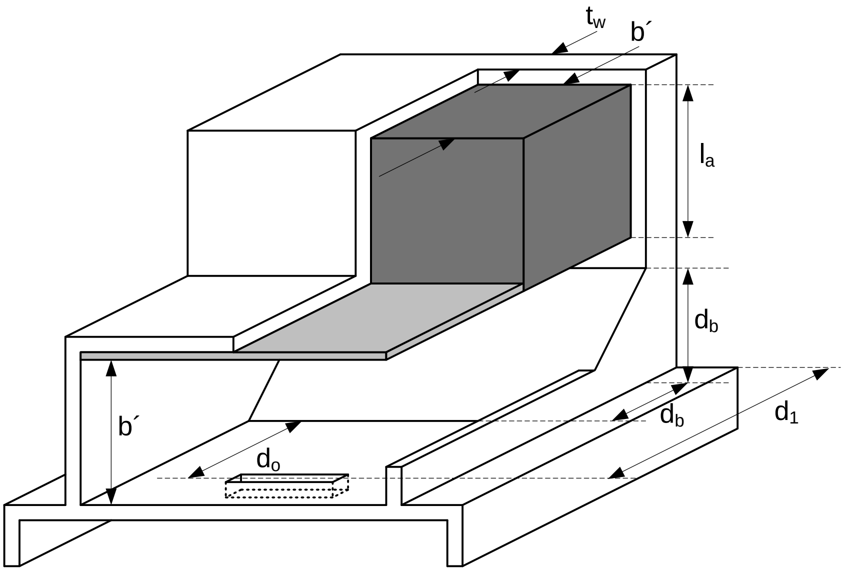

(a) E-plane bended load.

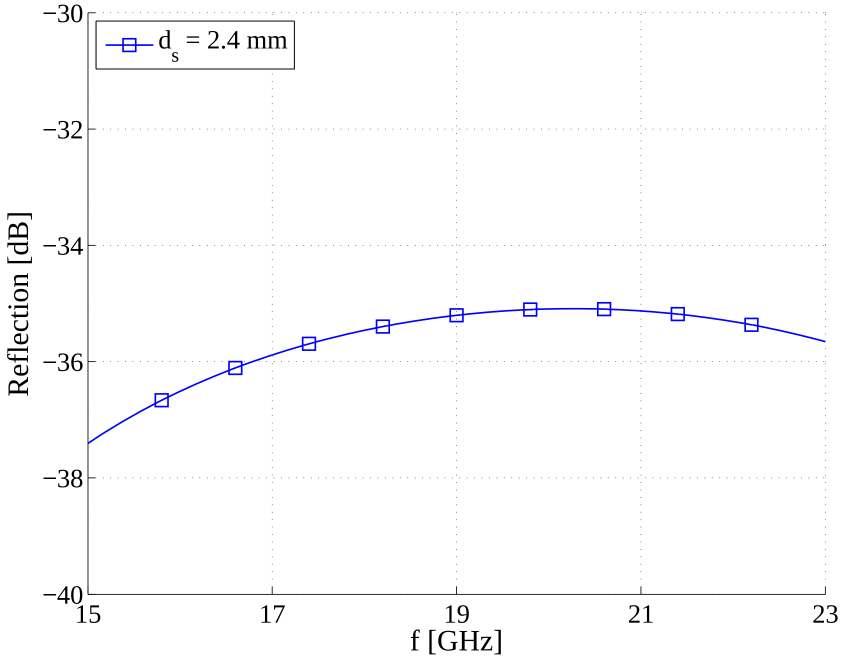

(b) Input reflection response, E-plane bend of 90° with $b = 3$ mm and $d_b = 2.4$ mm.

Figure 4.52: Layout and response of E-plane bent load.

An alternative to including an absorber is to short-circuit the auxiliary guide with an arbitrarily short guide, and terminate the auxiliary guide with an absorptive load at the opposing end. It was found, however, that the circuit optimisation did not yield better results with a shorter d_1 and short-circuited auxiliary guide, than for a longer d_1 with both ends of the auxiliary guide loaded.

4.6.2 Dimensional constraints

The synthesis completed in §4.5.2 adheres to the specification set, but the dimensions do not adhere to some physical constraints.

To allow accurate machining of the slot array, a minimum slot separation d of 2.4 mm was imposed, allowing for metallisation between adjacent slots of at least 1.4 mm. Since the previous synthesis required a minimum $d_5 = 1.99$ mm in Table 4.3, the circuit model has to be re-optimised to achieve an implementable design.

The most significant constraint on the slot synthesis is, however, a minimum distance d_1 from the first slot to the edge of the harmonic pad. In the case of the simple end-load in Fig. 4.51, d_1 has to include enough space for the end-load in the absorptive auxiliary guide l_a, as well as an electric wall of thickness t_w and a minimum offset from the first slot d_o. Even though it was found that the model suffers no ill-effect from a dimension of d_o as low as 0.5 mm, the previously established minimum value of $l_a = 15$ mm leaves a minimum initial offset value of $d_1 = 21$ mm, assuming a flange of thickness $t_w = 5$ mm. Compared to the previously synthesised value of $d_1 = 3.15$ mm, 21 mm is a significant minimum offset.

Using the vertical load in Fig. 4.52, on the other hand, only requires a minimum d_1 of 7.9 mm (5 mm flange width, 2.4 mm bend taper and 0.5 mm slot offset), which allows for the full specification to be reached with five slots.

4.6.3 Synthesis results

The synthesis proceeded as outlined in §4.5.1, with d_1 initially set to 16.84 mm, or λ_g. Under the constraints that $d_i > 2.5$ mm and $d_1 > 7.9$ mm, an optimised circuit solution was obtained for five slots. The model was tested and tuned in a full-wave simulation package, producing the dimensions shown in Table 4.5 and the electrical responses in Fig. 4.53. The auxiliary guide dimensions of 13 × 3 mm were retained.

As before, the synthesis features adequate first-iteration accuracy, with full-wave tuned

Table 4.5: Progressive development of manufacturing prototype of a first absorptive band harmonic pad with reflective filter termination.

		Initial	Circuit optimised	Full-wave tuned
f_1	[GHz]	19	22.49	–
L_1	[fH]	435	260	–
C_1	[pF]	161	193	–
T_1		2.05	2.39	–
ϕ_1	[°]	-0.45	-0.45	–
l_1	[mm]	8.15	6.75	6.42 (-4.89%)
f_2	[GHz]	19	18.15	–
L_2	[fH]	435	487	–
C_2	[pF]	161	158	–
T_2		2.05	2.13	–
ϕ_2	[°]	-0.44	-0.44	–
l_2	[mm]	8.15	8.45	8.45
f_3	[GHz]	19	20.35	–
L_3	[fH]	435	351	–
C_3	[pF]	161	174	–
T_3		2.05	2.23	–
ϕ_3	[°]	-0.44	-0.44	–
l_3	[mm]	8.15	7.5	7.5 (+3.45%)
f_4	[GHz]	19	21	–
L_4	[fH]	435	306	–
C_4	[pF]	161	188	–
T_4		2.05	2.30	–
ϕ_4	[°]	-0.44	-0.44	–
l_4	[mm]	8.15	7.25	7.23 (-0.28%)
f_5	[GHz]	19	22.11	–
L_5	[fH]	435	286	–
C_5	[pF]	161	181	–
T_5		2.05	2.35	–
ϕ_5	[°]	-0.44	-0.44	–
l_5	[mm]	8.15	6.87	6.87
d_1	[mm]	16.84	10.81	10.2 (-5.64%)
d_2	[mm]	8.42	3.87	3.75 (-3.10%)
d_3	[mm]	8.42	2.65	2.42 (-8.68%)
d_4	[mm]	8.42	3.86	3.60 (-6.74%)
d_5	[mm]	8.42	2.58	2.65 (+2.71%)

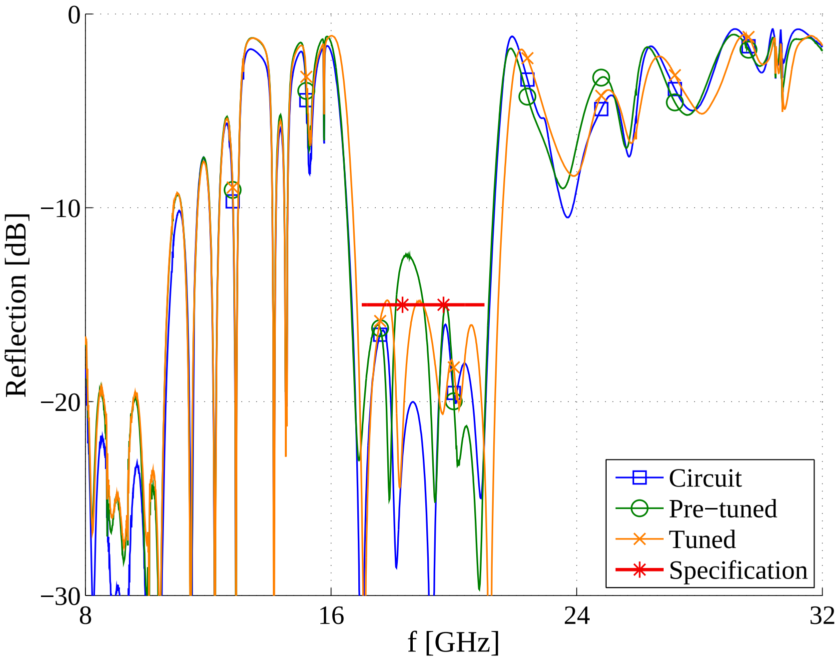

Figure 4.53: Circuit and full-wave simulated input reflection response of manufacturing prototype harmonic pad cascaded with waffle-iron filter.

parameters all within 10% of the synthesised values. As noted before, the circuit model is less accurate in describing the in-band reflection, with the full-wave solver indicating -19.5 dB ripples in S_{11} compared to the -22 dB ripples predicted by the circuit model.

4.6.4 Power handling capability

The maximum RMS $\vec{E}$-field in the matched structure is simulated as 3466 V/m at 9.5 GHz, which translates to a maximum transmission band power handling capability of 121.7 kW. At 19 GHz and short-circuited conditions (mimicking operation in cascade with the reflective filter), the field concentrates around the middle of the five slots (as shown in Fig. 4.54) and E_{max} (RMS) increases to 36996 V/m. This allows for breakdown-free operation up to 1.068 kW, which better than the required -15 dBc value of 252.98 W.

A peak S_{41} value of -6.5 dB is recorded in simulation with a short-circuited main guide, where port 4 substitutes the absorptive load closest to the reflective filter. This translates to an average power absorption requirement of 3.5 W. Although no specific absorption rate is provided in [110], the material is specified to operate up to 90°C. Since excessive heating can always be mitigated with external heat sinks, this input power is considered manageable.

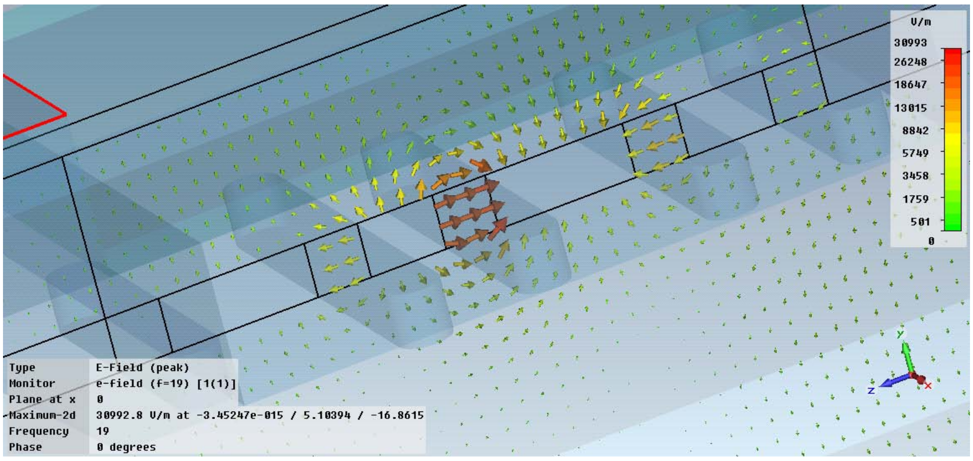

```
Type          E-Field (peak)
Monitor       e-field (f=19) [1(1)]
Plane at x    0
Maximum-2d    30992.8 V/m at -3.45247e-015 / 5.10394 / -16.8615
Frequency     19
Phase         0 degrees
```

Figure 4.54: $\vec{E}$-field distribution in the final simulation model under short-circuited conditions at 19 GHz.

4.6.5 Higher order modes

To investigate the operation of the harmonic pad in the presence of higher order modes, the cascaded simulated structure was excited by an TE_{30} mode, the results of which are shown in Fig. 4.55. Note that the cascade was only simulated from 20 GHz upward, since the TE_{30} mode is below cut-off elsewhere.

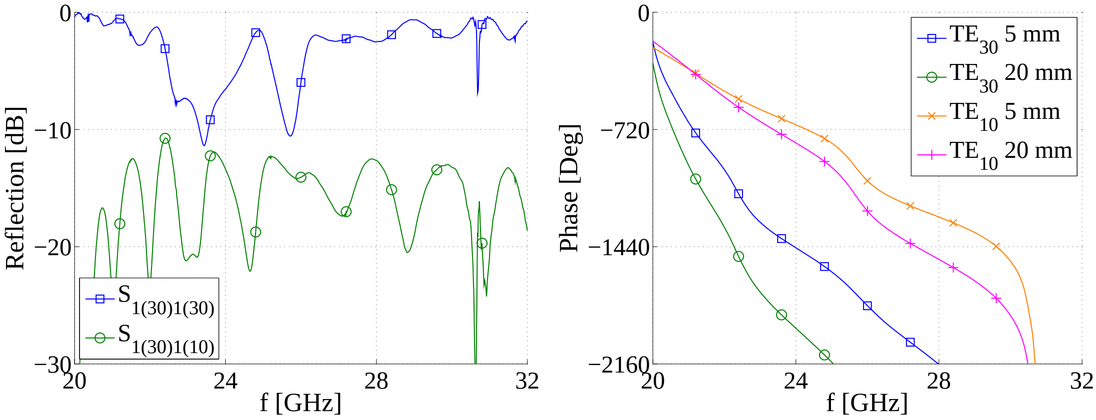

(a) Reflection magnitude.

(b) Comparison of input reflection phase.

Figure 4.55: TE_{30} response of cascaded harmonic pad and filter.

The simulation indicates almost complete reflection of a TE_{30} mode incident on the cascaded harmonic pad over the band 20 - 21 GHz, with some absorption around 23 and 25 GHz. This illustrates the reflection phase sensitivity of the harmonic pad, since the TE_{10} and TE_{30} input reflection phases are quite dissimilar, as shown in Fig. 4.55(b). Since the design is intended to absorb an incident TE_{10} mode, and not an incident TE_{30} mode, this reflection does not impact on the operational capability of the prototype.

The harmonic pad also features -11 dB ripples in reflected coupling between the TE_{10} and TE_{30} modes shown in Fig. 4.55(a). This effect, first illustrated in §4.3.8, has been exacerbated in a five slot array. However, over the band 20 - 21 GHz, the reflection is below -17 dB, which is still within the set reflection magnitude specification of -15 dB for an incident TE_{10} mode.

4.6.6 Manufacturing and measured results

The harmonic pad was manufactured in eight parts, shown in Appendix B and Fig. 4.56(a). As with the waffle-iron filter, the main guide sidewalls are manufactured as separate parts, with the broadwalls formed by two narrow plates clamped between the auxiliary waveguides (Fig. 4.56(b)). The flange and 45° chamfer transition are manufactured as a single unit, as shown in Fig. 4.56(c). All parts were milled from Aluminium 6082, with spark erosion used to create the sharp corners in the flange. This process creates a finish much rougher than milling, and less accurate than the more expensive alternative of diamond wire cutting. The Eccosorb^{TM}FGM-40 was glued to the auxiliary guide broadwall using a general industrial adhesive, with the HR blocks placed before assembly as shown in Fig. 4.56(d).

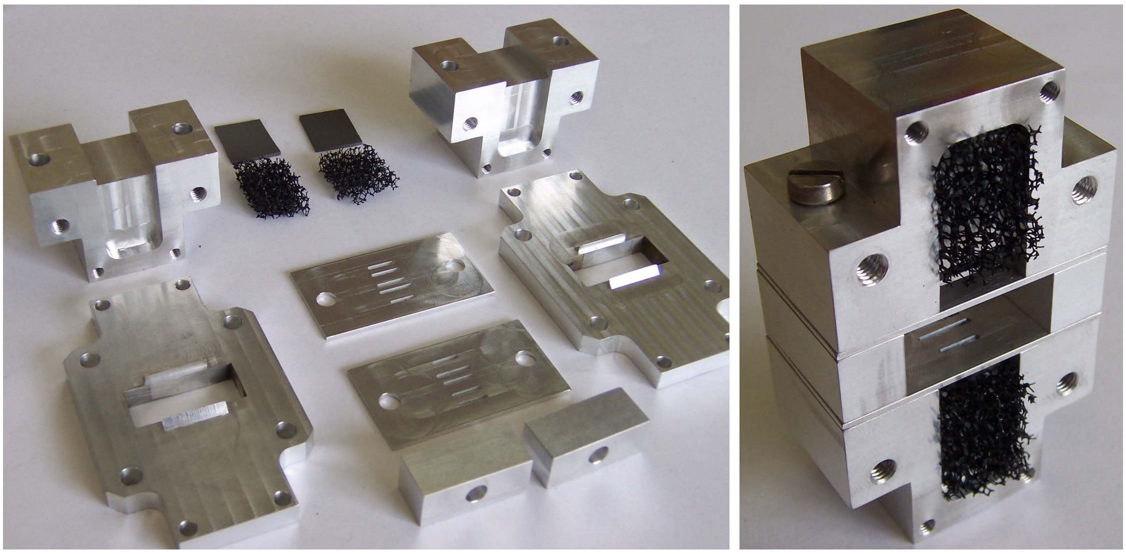

(a) Full disassembled harmonic pad

(b) Partially assembled harmonic pad, showing the main guide formed by the plates and the sidewalls.

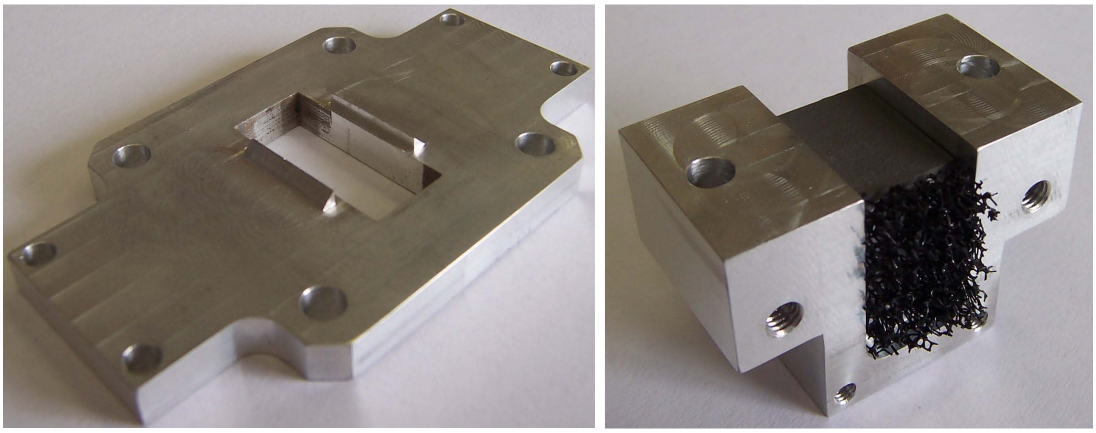

(c) Detail view of flange, showing chamfered lip and surface finish left by spark erosion of the corners.

(d) Positions of resistive sheet and reticulated foam absorbers.

Figure 4.56: Photographs of disassembled harmonic pad.

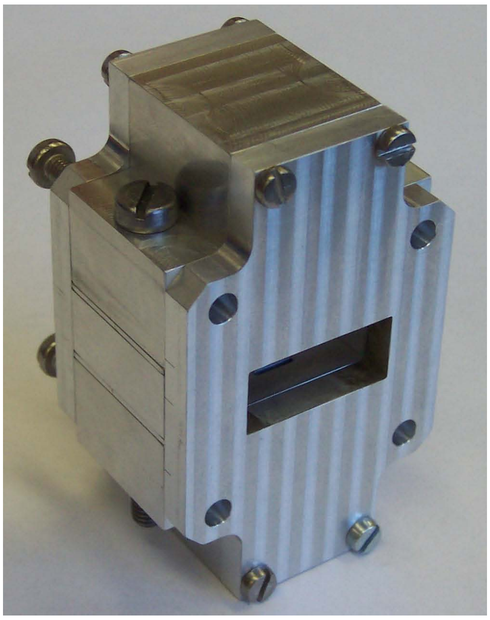

(a) Assembled harmonic pad.

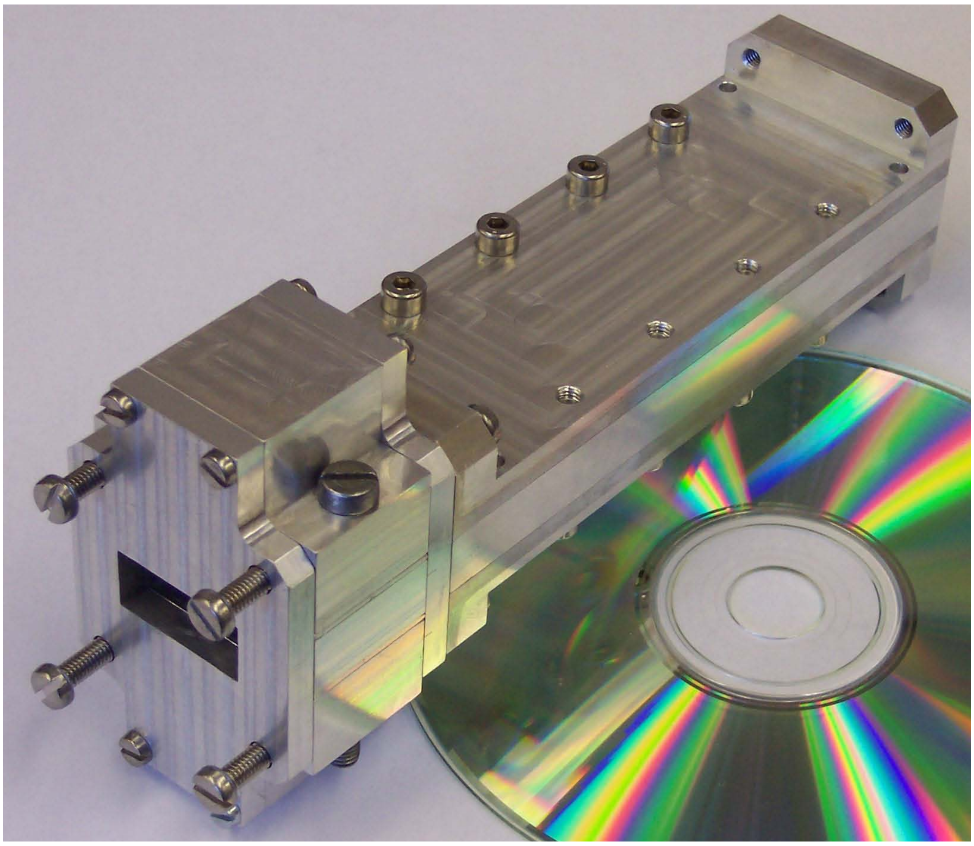

(b) Full assembled absorptive filter, with reflective filter and harmonic pad. A compact disk is shown for size comparison.

Figure 4.57: Photographs of assembled absorptive filter.

The harmonic pad was attached to the waffle-iron filter developed in the previous chapter, and two measurements were performed on an HP8510C VNA. In the first, a full two-port TRL calibration was performed over the band 8 - 12 GHz, to measure the in-band reflection and insertion loss of the combined absorptive filter. In the second measurement, a one-port SOLT calibration was performed from 16 - 22 GHz, and the input reflection of the combined device measured with a WR-62 waveguide transition, whilst the output port was backed by absorptive material. The input reflection of the transition itself, and reflection due to the WR-90 / WR-62 port mismatch, was measured by applying the WR-62 to an empty WR-90 waveguide loaded with absorptive material, and the response calibrated out of the filter measurement in post-processing.

The measured results are shown in Fig. 4.58, compared to the final tuned full-wave simulation results.

The complete absorptive filter exhibits nominally higher than anticipated in-band reflection (-18 dB, compared to the -19.5 dB simulated), as well as higher peak reflection in the stop-band (-12.5 dB, compared to the simulated -14.8 dB). Additionally, the combined structure features below 0.5 dB insertion loss in the band 8.5 - 10.5 GHz, which is better than the required 1 dB.

Some manufacturing tolerance is to be expected, given the assembly of multiple components not only in the harmonic pad itself, but also the cascaded waffle-iron filter. The in-band reflection increase, for example, can be traced back to the increased in-band reflection response of the manufactured waffle-iron filter. Considering the sensitivity to distance between the slots and the source of the reflection demonstrated in this chapter, the results achieved are quite satisfactory.

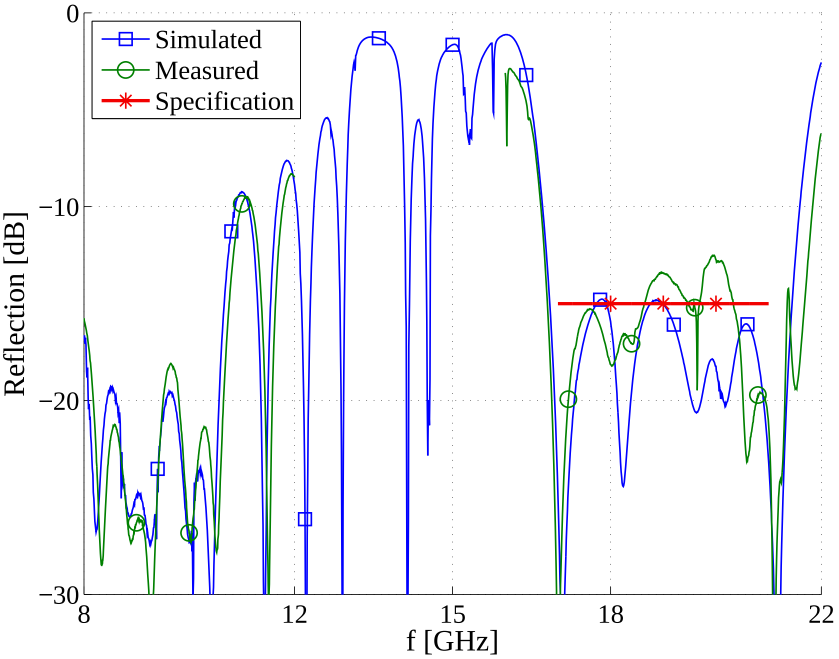

(a) Input reflection.

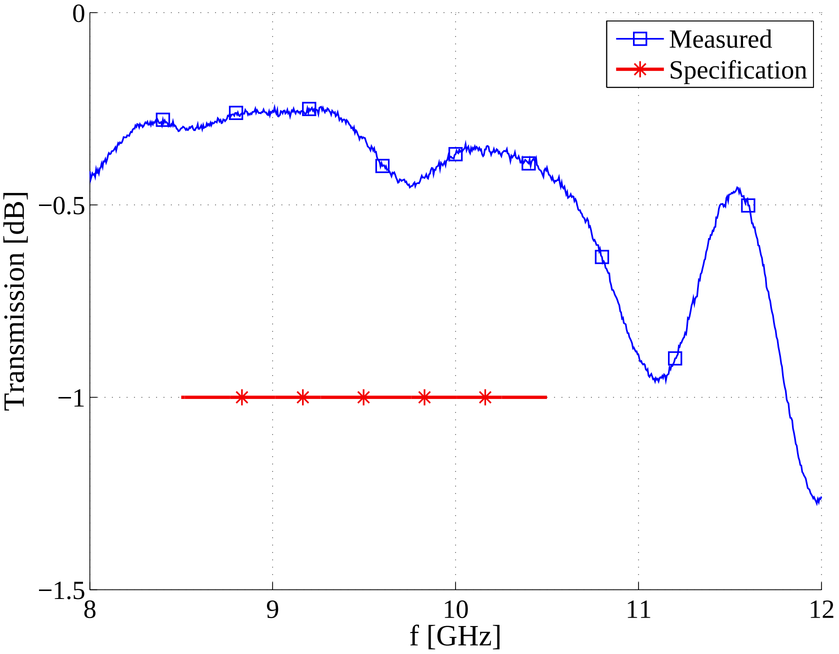

(b) Insertion loss.

Figure 4.58: Measurement of final absorptive filter.

4.7 Conclusion

This chapter presented a synthesis approach to the development of harmonic pads using transversal broadwall slots in rectangular waveguide coupling to absorptive auxiliary guides. Excellent first-iteration synthesis accuracy is achieved in a band 17 - 21 GHz, matching over a 20% bandwidth to below -12.5 dB. Diminishing returns in absorption and bandwidth are gained from adding more than five slots to the harmonic pad. The synthesis method was found less accurate in the band 25.5 - 31.5 GHz, particularly due to unmodelled effects relating to slot-shim interation. Reduced guide height has been illustrated to suppress these higher order mode effects.

Chapter 5

Conclusion

This chapter will conclude the dissertation by critically evaluating the proposed synthesis methods, with particular reference to the initial specifications and prototype strengths and shortcomings. Recommendations for future development are made.

5.1 Evaluation of synthesis methods

Two main synthesis methods were proposed in this dissertation, as discussed in Chapters 3 and 4.

5.1.1 Waffle-iron filter

The circuit model based synthesis of non-uniform filters features excellent first-iteration accuracy. The full-wave tuning required post-synthesis is related one-to-one with changes in electrical response (b_T adjusts input match, b recentres the stop-band, and no adjustments are required to boss lengths or widths), and the edge rounding causes a predictable upward shift in stop-band. Compared to similar published solutions, the method achieves the same electrical specifications with reduced form factor, and with much reduced computational requirements. Apart from the singular manufacturing difficulty created by the half-inductive input section, the machining provided no other complications. Good agreement is found in-band between synthesised and measured responses, with some spurious resonances above 34 GHz. This is due to manufacturing tolerances, but also the due to the erosion of the "narrow deep groove" condition in the reduced height (b_1) section, which adversely effects the accuracy of the short-circuited stub model. These spurious resonances may therefore also be addressed by reducing b'', l_i and l_i' (creating narrower longitudinal grooves), at the cost of reducing the power-handling capability of the filter.

In contrast, the oblique waffle-iron filters suffer from spurious cavity resonances, inter-mode coupling and inferior power handling capability compared to the non-uniform filter. It is, however, the more compact filter of the two for a given filter order, and by further investigating methods to suppress cavity resonances and mode coupling, it could find niche applications as an ultra-compact wide-band harmonic suppressor.

5.1.2 Harmonic pad

The accuracy of the simplified circuit model representation of transversal broadwall slots in rectangular waveguide is evident in the excellent first-iteration synthesis accuracy of harmonic pads in the band 17 - 21 GHz. However, each additional cascaded slot contributes less in absorption and bandwidth than the previous due to the effect of reflection plane offset. Achieving below -15 dB input reflection match, or achieving such a match over a bandwidth in excess of 20%, would require significantly more slots. As each slot contributes more synthesis complexity, this approach is not recommended for significantly wider bandwidths or lower input reflection levels.

The synthesis around 30 GHz suffers from the presence of spurious propagating modes and resonances. Though the addition of shims suppressed the offending modes, new spurious resonances are created. The presence of the shims also compromise the validity of the circuit model representation of the cascaded slots. Unless the effects of the shims are incorporated in the harmonic pad's circuit model representation, development in this frequency band are best served with reduced height main guide.

If narrower absorption bandwidths are required, the same approach could be applied to longitudinal sidewall slots. Many of the problems in spurious resonance and higher band operation can be circumvented in this way.

5.1.3 Combined approach

Using a harmonic pad custom designed for a particular reflective filter is a compact and effective approach to high-power broadband absorptive filtering. In practice, the design and manufacturing of both would benefit from the development of the harmonic pad and the reflective filter as a single unit (with combined circuit and full-wave simulation models) rather than developing two distinct components as was done in this dissertation. This method could possibly be applied to other implementations of both reflective filter (cascaded resonator, corrugated waveguide, planar structures) and harmonic pad (stainless steel chokes, etched loaded rings, dielectric stubs).

5.2 Achievement of initial specifications

The specifications set initially in Table 1.1 are not absolute requirements for the final developed prototype, but rather served as guides for the development process. However, a brief evaluation of the final prototype in terms of these specifications proves insightful into the shortcomings of the synthesis process, and is conducted below.

Table 5.1: Evaluation of target specifications for absorptive filter development.

Band	[GHz]		8.5 - 10.5	17 - 21	25.5 - 31.5	34 - 42
S_{11}	[dB]	Specified	< -25	< -15	< -10	–
		Achieved	-18	-15	0	–
		Notes	(1)	–	(2)	–
S_{21}	[dB]	Specified	> -1	< -65	< -60	< -55
		Achieved	-0.5	-66.5	-48.12	-30.2
		Notes	–	–	(3)	(3)
Power	[kW]	Specified	8	0.25	–	
		Achieved	4	1	–	–
		Notes	(4)	–	–	–

1. The circuit model of the slots is less accurate far below resonance, creating higher than anticipated in-band reflection for the combined absorptive filter structure. By allowing some margin for in-band harmonic pad reflection (which was not done in this design) an in-band reflection response specification can be achieved. The reflective filter itself also exhibited marginally more in-band reflection than predicted by simulation.

2. The development an absorptive harmonic pad for the second absorptive band was abandoned due to the inaccuracy of the circuit model representation in the presence of shims, as well as the prevalence of spurious shim and slot resonances. Both of these shortcomings may be addressed by using reduced height guide for the harmonic pad in these frequency bands.

3. The waffle-iron filter suffers from spurious stop-band harmonics, due to manufacturing tolerance in the alignment of the parts. This is known drawback of waffle-iron filters, and can only be improved by lower manufacturing tolerance and better

alignment schemes. The effect of the spurious resonances can also be decreased by decreased dimensions b'', l_i and l'_i, at the cost of reducing the power handling capability of the filter.

4. The reduction of b'' to 1.6 mm had reduced the power handling capability of the waffle-iron filter to a greater extent than had been anticipated. The power handling capability of the waffle-iron filter can easily be increased by choosing a larger value of b'' in future designs.

5.3 Recommendations for future development

This dissertation has covered a wide scope of theories and applications, and has left room for future development in many areas. The most important ones are highlighted below.

5.3.1 General absorptive filter synthesis theory

The even-odd reflection approach to absorptive filtering (§2.3) in conjunction with non-series-parallel synthesis methods, is the most evident candidate for a general absorptive filter synthesis theory. A single, unified absorptive filtering theory would allow mainstream development of absorptive filters, and is a worthy goal for future development.

5.3.2 Synthesis as a single unit

The separate synthesis and manufacturing of the reflective filter and the harmonic pad imposed limitations on the absorptive filtering capabilities of the combined structure, such as increased spacing between the reflective filter and the first absorptive slot, and increased in-band reflection response. These limitations can be overcome by modeling and optimising the full absorptive filter as a single circuit model, with a single full-wave simulation model and a single manufactured device.

5.3.3 Analytical synthesis methods

The proposed synthesis methods of both harmonic pad and non-uniform waffle-iron filter requires optimisation of a circuit model representation.

In the case of the waffle-iron filter, this synthesis requires optimisation of cascaded transmission line lengths and stub impedances, in the presence of reactive compensation. This circuit model is quite similar to transmission line filters synthesised using Kuroda's identities, except for the non-uniformity in line lengths and stub impedances. The similarity could be exploited to develop an abridged version of Kuroda's identities to suit the synthesis.

Analytical expressions are available for the input reflection of singular orders of cascaded lossy resonators, but these expressions become exponentially more complex for higher orders. An inquiry into a general absorptive filter synthesis might could also reveal a synthesis for cascaded lossy resonators. Since a number of physical structures with absorptive filtering properties represent series or shunt lossy resonators, such a theory could be used to analytically synthesise a wide variety of harmonic pads.

5.3.4 Oblique waffle-iron filters

The oblique waffle-iron filter has the potential to find niche applications where both wide stop-band attenuation and compact form factor are required, if the spurious cavity resonances and internal mode coupling can be addressed adequately. This avenue of inquiry remains open for future development.

5.3.5 Broadband slot operation

The use of shims in full-height waveguide has been demonstrated to increase the spurious-free bandwidth of transversal broadwall slots, at the expense of creating a new set of spurious resonances and complicating the circuit model representation of the slot cascade. By experimenting with shim shape, thickness and placement, the spurious resonances could be mitigated or removed altogether. Also, by incorporating the previously published reactive effects of the shims into the circuit model representation, the useful bandwidth of the harmonic pad in full-height waveguide could be increased substantially.

5.3.6 Tuning ability

The input reflection response of both the waffle-iron filter and the harmonic pad could be improved upon by installing tuning mechanisms. In the case of the waffle-iron filter, this could be achieved by tuning screws in the waveguide of height b_T leading into the filter, whereas the operation of the slots could be tuned by H-plane screws in the auxiliary guide above the coupling slots.

Appendix A

Machine sketches for manufactured waffle-iron filter prototype

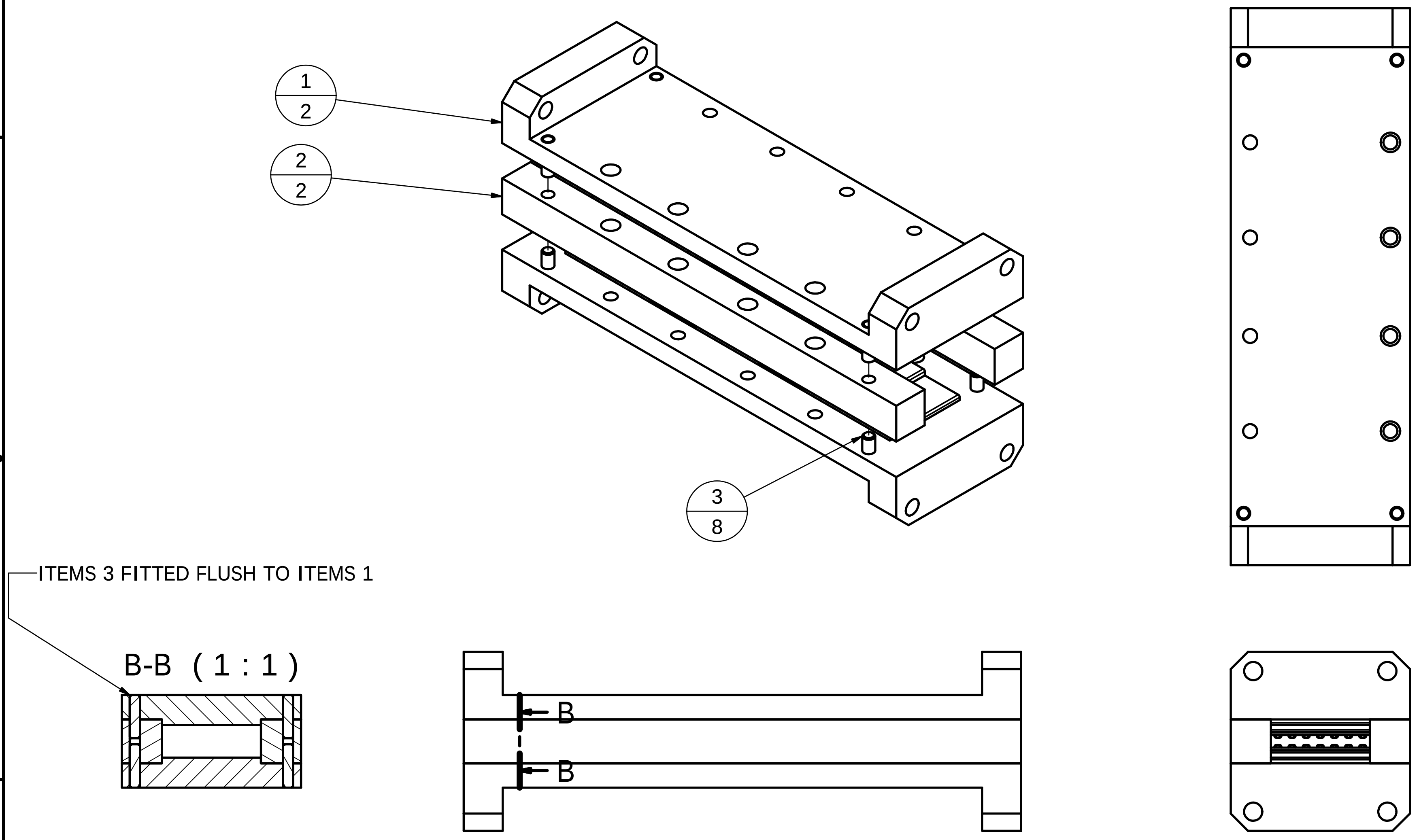

Parts List			
ITEM	QTY	PART NUMBER	DESCRIPTION
1	2	MAIN	TO BE MACHINED FROM FILE MAIN.SAT
2	2	SIDEWALL	
3	8	PIN DOWEL	DIA 3X10
4	8	SCREW CAP HEX (NOT SHOWN)	M4X20

Designed by	Checked by	Approved by	Date	Date
tstander				2009/07/05

	Edition	Sheet
WAFFLE IRON ASSEMBLY		1 / 1

NOTES:

1) DIMENSIONS ON THIS SHEET TO BE MACHINED
ONLY AFTER CNC COMPLETED

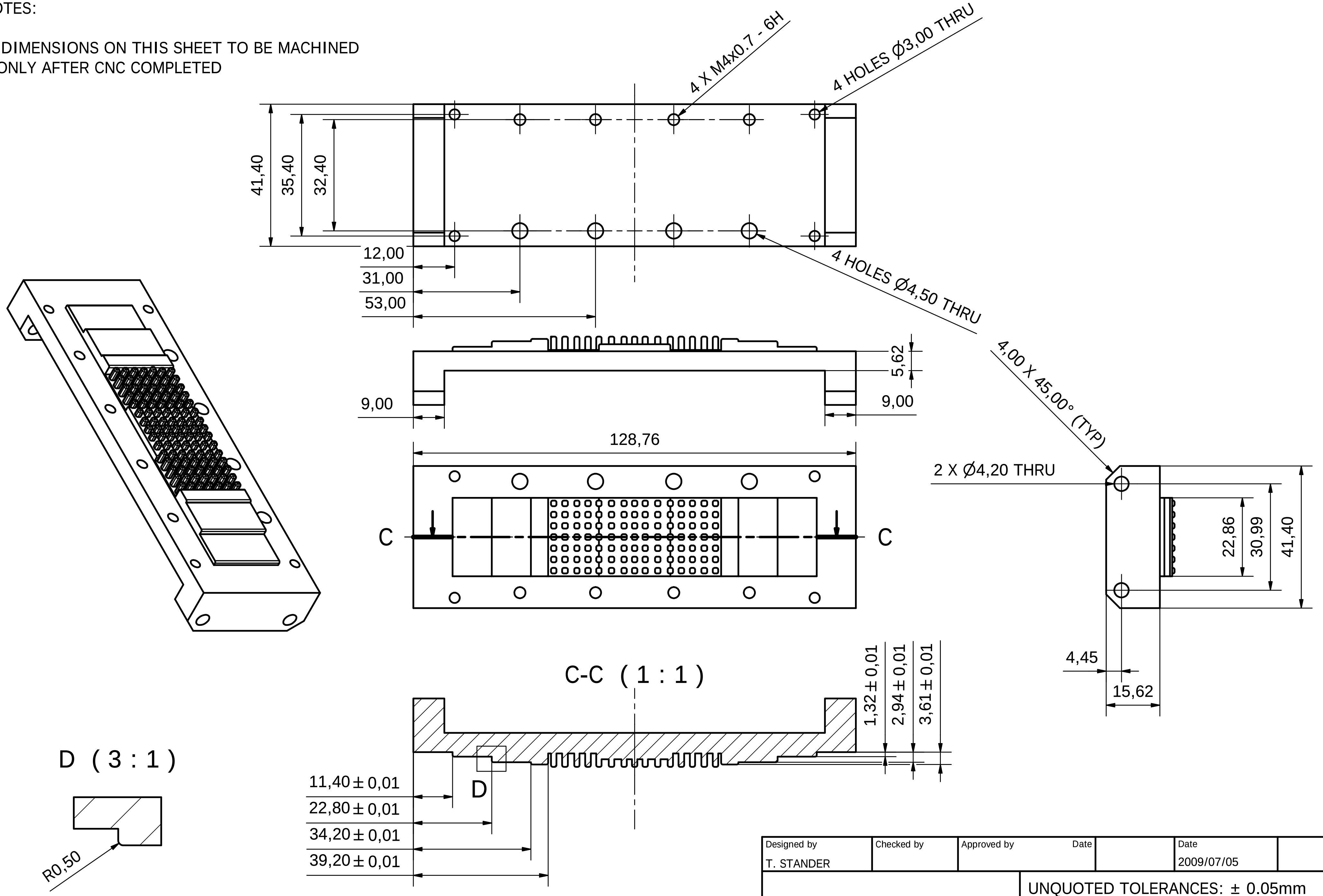

Designed by T. STANDER	Checked by	Approved by	Date	Date 2009/07/05
	UNQUOTED TOLERANCES: ± 0.05mm			
	MAIN		Edition	Sheet 1 / 2

NOTES:

1) PROTRUSIONS TO BE MACHINED FROM FILE MAIN.IGS
2) FEATURES A, B AND C NOT CRITICAL

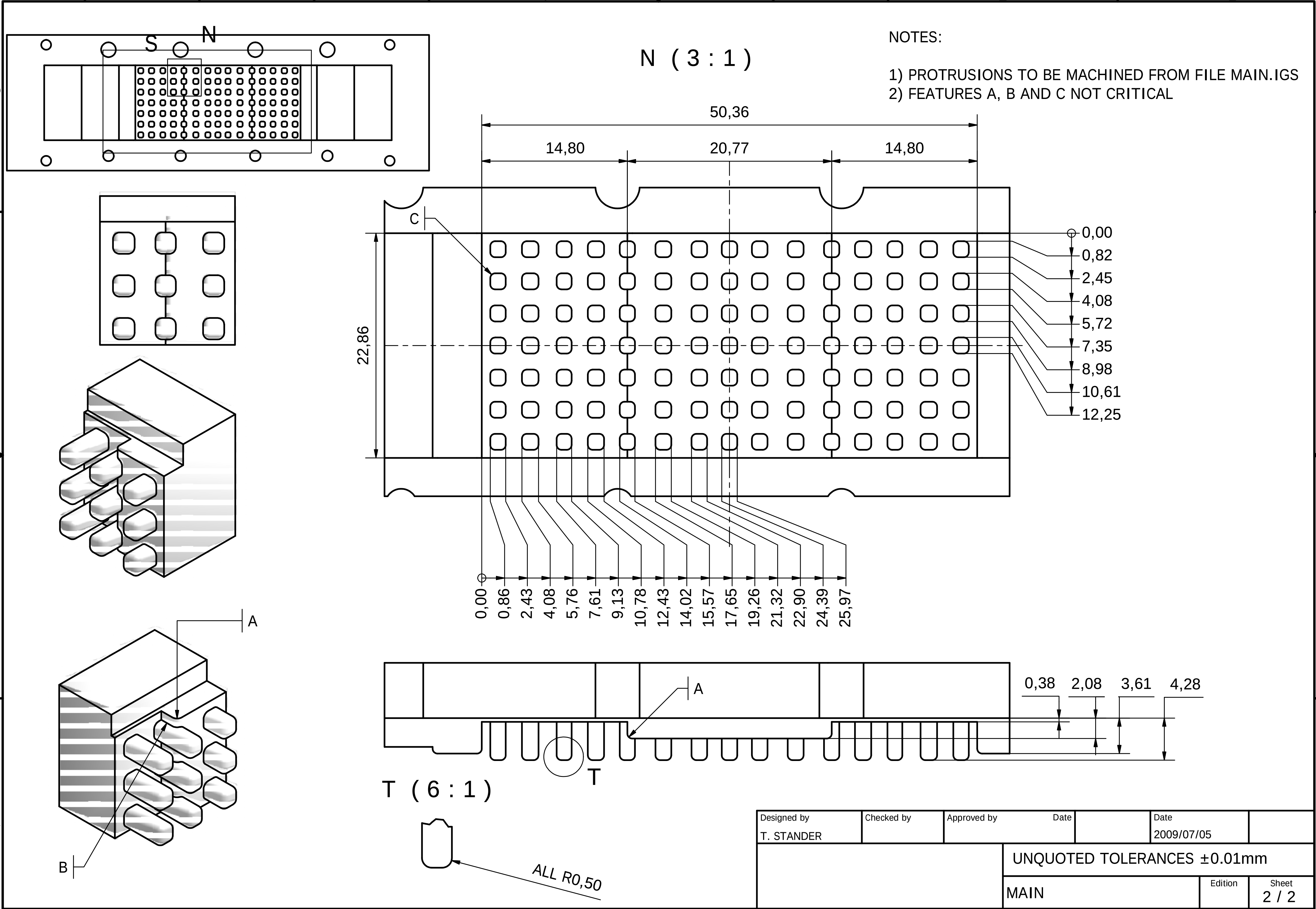

Designed by
T. STANDER
Checked by
Approved by
Date
Date
2009/07/05
UNQUOTED TOLERANCES ±0.01mm
MAIN
Edition
Sheet
2 / 2

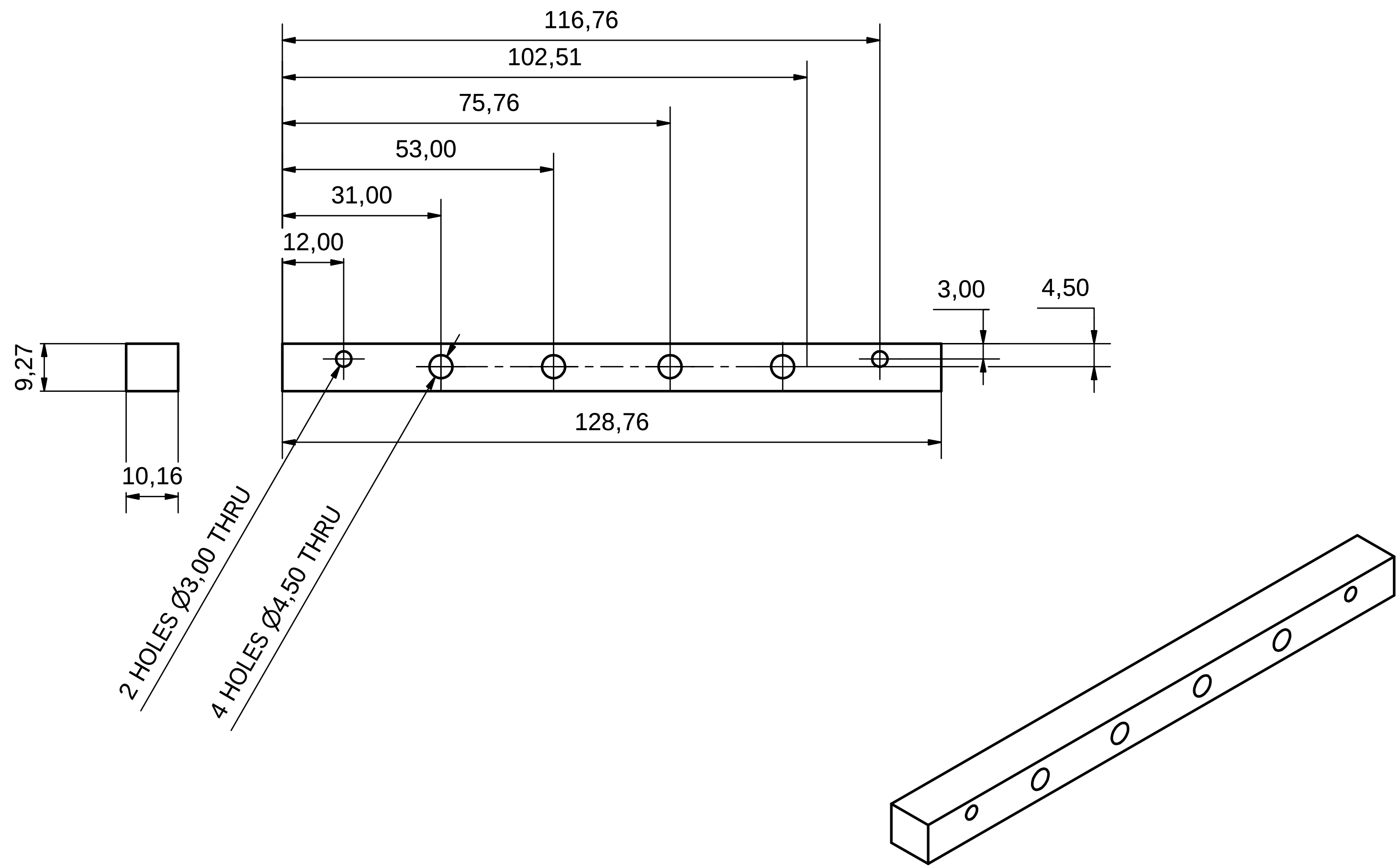

Designed by	Checked by	Approved by	Date	Date
T. STANDER				2009/07/05

UNQUOTED TOLERANCES ±0.05mm

	Edition	Sheet
SIDEWALL		1 / 1

Appendix B

Machine sketches for manufactured harmonic pad prototype

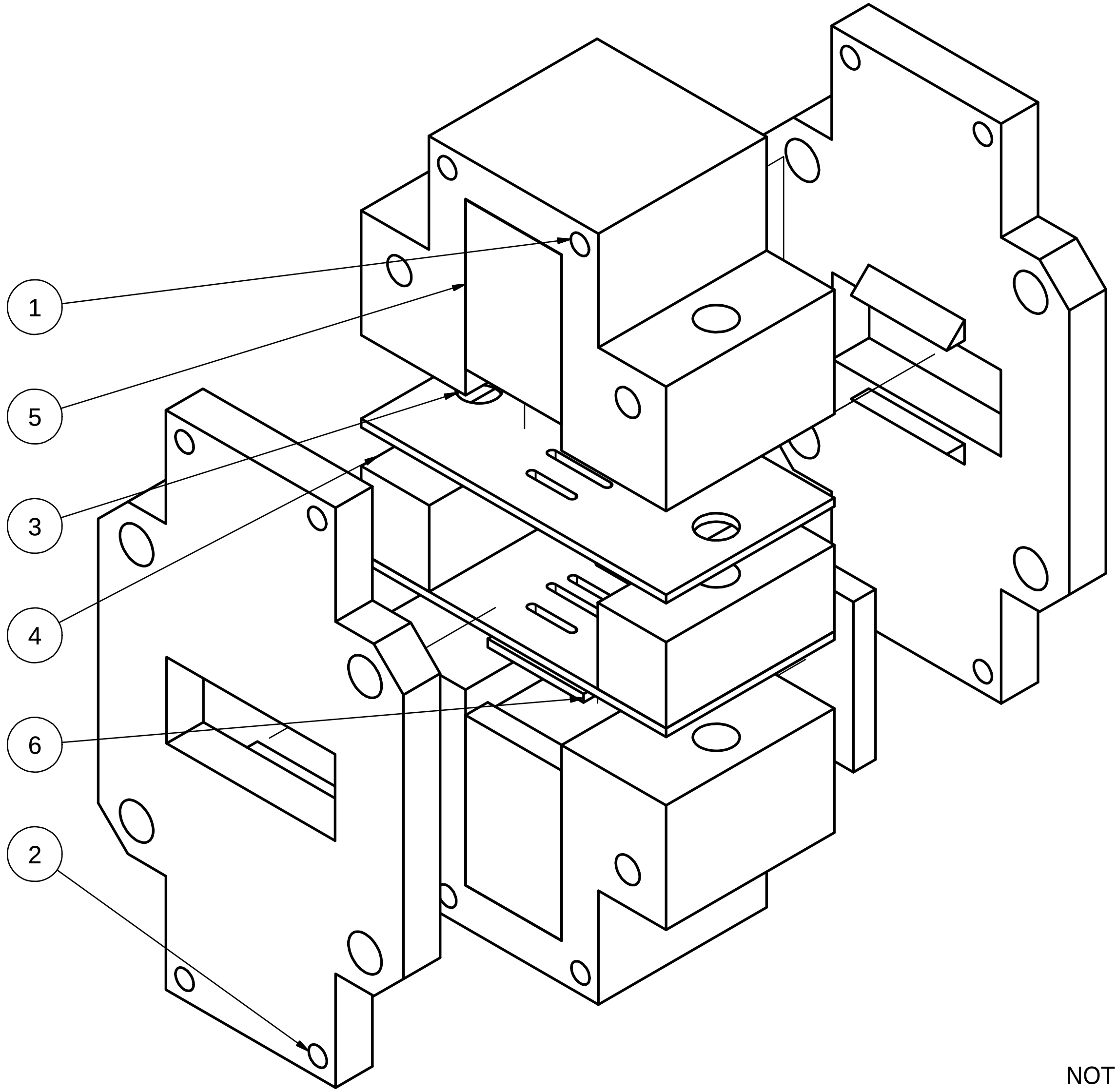

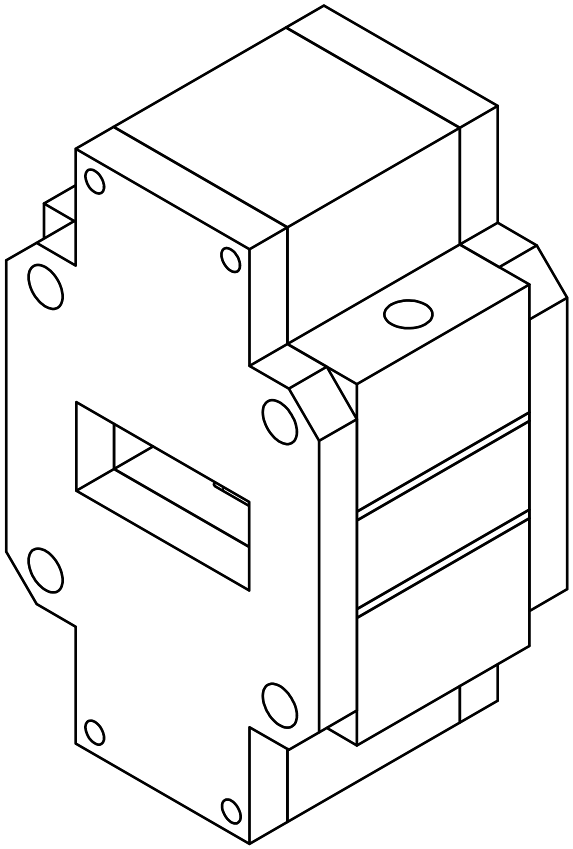

NOTES:

1) FGM-40 SHEETS TO BE GLUED TO PART 'BODY' WITH RTV-TYPE GLUE
2) HR-10 FOAM CAN BE COMPRESSED TO FIT IN CAVITY
3) FLANGE SURFACES TO BE SKIMMED NO DEEPER THAN 0.05
4) SIMILAR ORIENTATION OF PARTS 'PLATE' CRITICAL

Parts List

ITEM	QTY	PART NUMBER	DESCRIPTION
1	2	BODY	
2	2	FLANGE	
3	2	PLATE	
4	2	SIDEWALL	
5	4	ENDLOAD	ECCOSORB HR-10
6	2	GUIDE LOAD	ECCOSORB FGM-40

Designed by	Checked by	Approved by	Date	Date	
tstander				2009/08/11	

assembly	Edition	Sheet 1 / 1

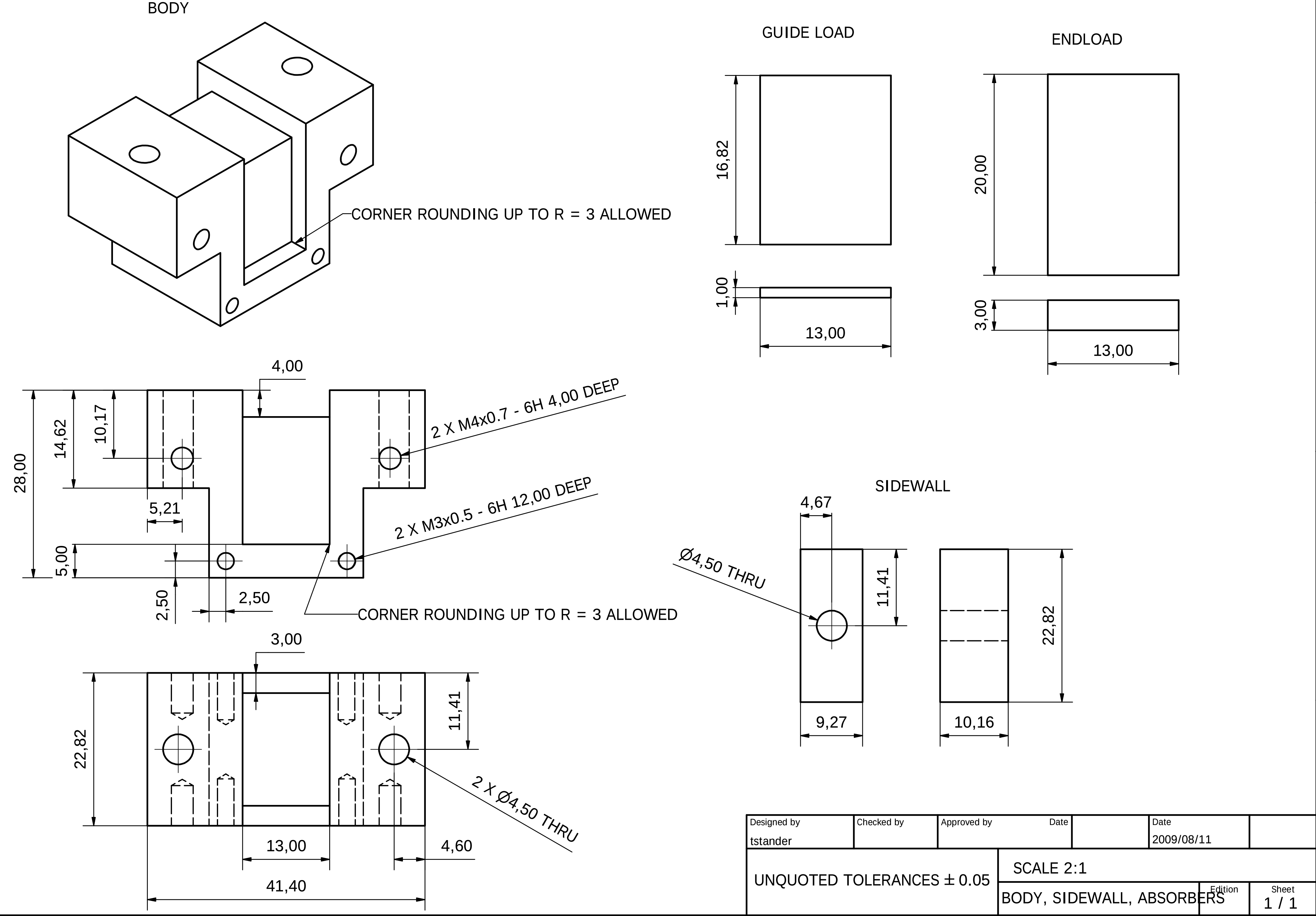

Designed by	Checked by	Approved by	Date	Date	
tstander				2009/08/11	

UNQUOTED TOLERANCES ± 0.05

SCALE 2:1

BODY, SIDEWALL, ABSORBERS

Edition

Sheet 1 / 1

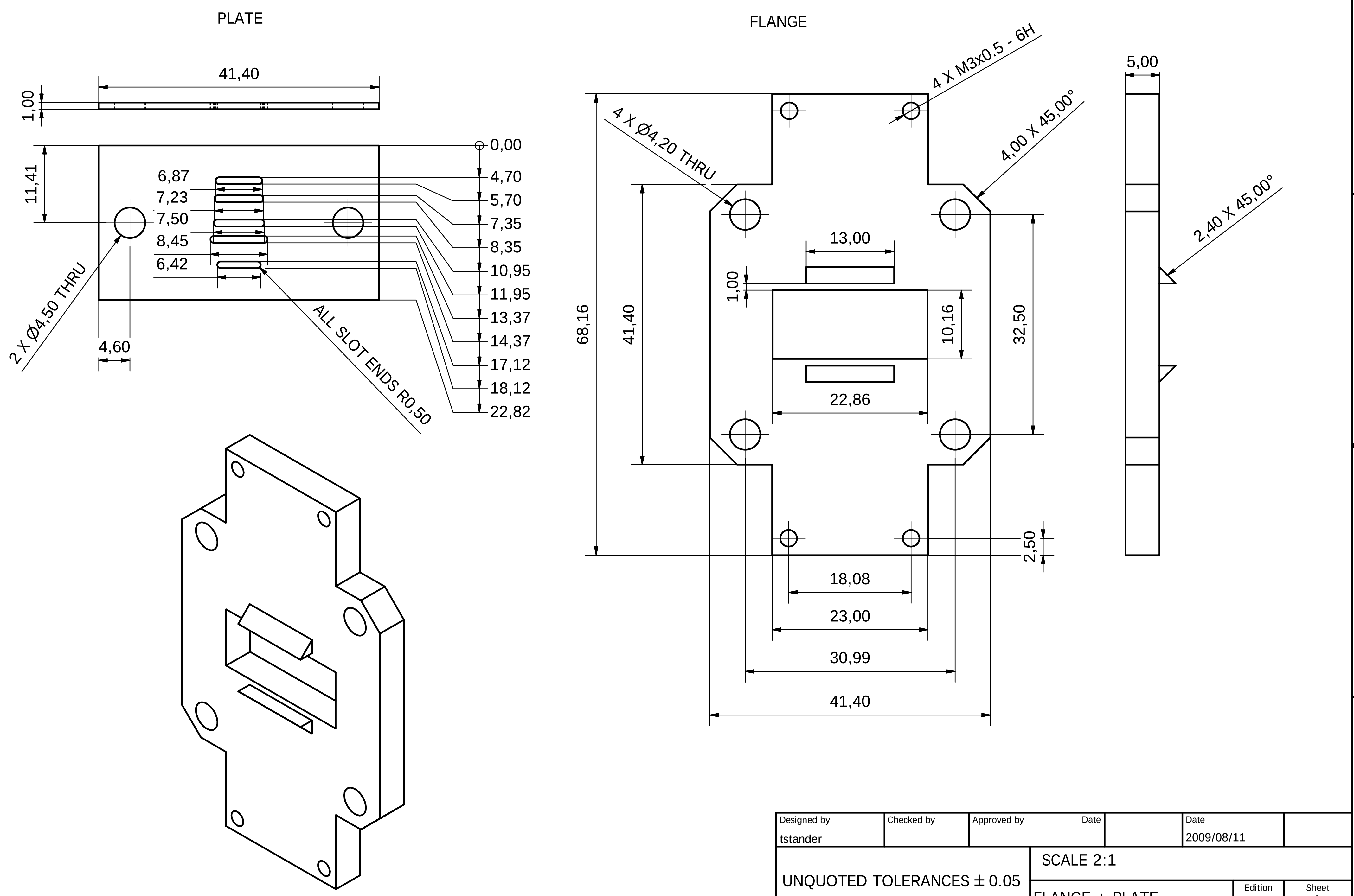

Designed by	Checked by	Approved by	Date	Date	
tstander				2009/08/11	

UNQUOTED TOLERANCES ± 0.05

SCALE 2:1

FLANGE + PLATE

Edition	Sheet
	1 / 1

Bibliography

[1] V. O. Met, “Absorptive filters for microwave harmonic power,” *Proceedings of the IRE*, vol. 47, no. 10, pp. 1762 – 1769, October 1959.

[2] I. L. Powell, “Waveguide filters,” U.S. Patent 3 916 352, October 28, 1975.

[3] S. Conning, “High-power harmonic suppression filters,” U.S. Patent 3 496 497, February 17, 1970.

[4] E. G. Cristal, “Analytical solution to a waveguide leaky-wave filter structure,” *IEEE Transactions on Microwave Theory and Techniques*, vol. 11, no. 3, pp. 182 – 190, May 1963.

[5] E. Wantuch, “A novel high-power harmonic suppressor,” *IRE Transactions on Microwave Theory and Techniques*, vol. 10, no. 6, pp. 428 – 431, November 1962.

[6] R. V. Snyder, “An improved low-pass harmonic absorber,” in *IEEE MTT-S International Microwave Symposium Digest*, vol. 76, no. 1, June 1976, pp. 122 – 124.

[7] M. E. Corporation, “Waveguide harmonic absorption filters,” Data Sheet T41C, January 2005.

[8] J. D. Rhodes, “Microwave reflection filter including a ladder network of resonators having progressively smaller Q values,” U.S. Patent 5 781 084, July 14, 1998.

[9] A. P. Gorbachev, “The Reentrant Wide-Band Directional Filter,” *IEEE Transactions on Microwave Theory and Techniques*, vol. 50, pp. 2028 – 2031, 2002.

[10] A. C. Guyette, I. C. Hunter, R. D. Pollard, and D. R. Jachowski, “Perfectly-matched bandstop filters using lossy resonators,” in *IEEE MTT-S International Microwave Symposium Digest*, 2005, pp. 517 – 520.

[11] R. D. Wanselow, “Waveguide stop-band filters utilizing hybrid circuit with lossy resonant cavities in branch arms,” U.S. Patent 3 142 028, July 21, 1964.

[12] E. N. Torgow, "Hybrid junction-cutoff waveguide filters," *IRE Transactions on Microwave Theory and Techniques*, vol. 7, no. 1, pp. 163 – 167, January 1959.

[13] V. M. Osipenkov, "The effect of total resonance absorption in microwave circuits," *Journal of communications technology & electronics*, vol. 47, no. 4, pp. 440 – 445, April 2002.

[14] D. R. Jachowski, "Passive enhancement of resonator Q in microwave notch filters," in *IEEE MTT-S International Microwave Symposium Digest*, vol. 3, 2004, pp. 1315 – 1318.

[15] ——, "Compact, frequency-agile, absorptive bandstop filters," in *IEEE MTT-S International Microwave Symposium Digest*, 2005, pp. 513 – 516.

[16] J. Breitbarth and D. Schmelzer, "Absorptive near-Gaussian low pass filter design with applications in the time and frequency domain," in *IEEE MTT-S International Microwave Symposium Digest*, vol. 3, June 2004, pp. 1303 – 1306.

[17] A. R. Djordjevic, A. G. Zajic, A. S. Stekovic, M. M. Nikolic, Z. A. Maricevic, and M. F. C. Schemmann, "On a class of low-reflection transmission-line quasi-gaussian low-pass filters and their lumped-element approximations," *IEEE Transactions on Microwave Theory and Techniques*, vol. 51, no. 7, pp. 1871 – 1877, July 2003.

[18] A. R. Djordjevic and A. G. Zajic, "Low-reflection bandpass filters with a flat group delay," *IEEE Transactions on Microwave Theory and Techniques*, vol. 53, no. 4, pp. 1164 – 1167, April 2005.

[19] M. Morgan, T. Newton, B. Hayward, and T. Boyd, "Non-reflective transmission-line filters for gain slope equalization," in *IEEE MTT-S International Microwave Symposium Digest*, June 2007, pp. 545 – 548.

[20] L. B. Minakova and L. A. Rud, "Resonance absorption in single and cascaded lossy waveguide-dielectric resonators," *IEEE Microwave and Optical Technology Letters*, vol. 36, no. 2, pp. 122 – 126, January 2003.

[21] L. A. Rud, "Properties of cascade-connected partially absorbing and reflecting waveguide resonators," in *Proceedings of the 10th International Conference on Mathematical Methods in Electromagnetic Theory*, 2004, pp. 121 – 123.

[22] C. Mias, "Frequency selective absorption using lumped element frequency selective surfaces," *Electronics Letters*, vol. 39, no. 11, pp. 847 – 849, May 2003.

[23] T. Stander and P. Meyer, "Etched ring absorbing waveguide filter based on a slotted waveguide antenna reflection response," *Microwave and Optical Technology Letters*, vol. 50, no. 4, pp. 978 – 981, April 2008.

[24] S. G. Tantawi and A. E. Vlieks, "Compact X-band high power load using magnetic stainless steel," in *Proceedings of the 1995 Particle Accelerator Conference*, vol. 4, May 1995, pp. 2132 – 2134.

[25] G. L. Matthaei, L. Young, and E. M. T. Jones, *Microwave Filters, Impedance-Matching Networks, and Coupling Structures.* McGraw-Hill Book Co, 1964.

[26] R. Cameron, C. Kudsia, and R. Mansour, *Microwave filters for communication systems.* John Wiley & Sons, Inc., 2007.

[27] I. Hunter, *Theory and design of microwave filters.* The Institution of Electrical Engineers, 2001.

[28] I. C. Hunter, "Filter design with lossy circuit elements," in *IEE Colloquium on Advances in Passive Microwave Components*, May 1997, pp. 1/1–1/6.

[29] A. C. Guyette, I. C. Hunter, and R. D. Pollard, "The design of microwave bandpass filters using resonators with nonuniform Q," *IEEE Transactions on Microwave Theory and Techniques*, vol. 54, no. 11, pp. 3914 – 3922, November 2006.

[30] A. C. Guyette, "Optimum design of microwave filters with finite dissipation," Ph.D. dissertation, The University of Leeds School of Electronic and Electrical Engineering, 2006.

[31] R. F. Baum, "A modification of Brune's method for narrow-band filters," *IRE Transactions on Circuit Theory*, vol. CT-5, no. 4, pp. 264 – 267, December 1958.

[32] V. Belevitch, "An alternative derivation of brune's cycle," *IRE Transactions on Circuit Theory*, vol. 6, no. 4, pp. 389 – 390, December 1959.

[33] S. Darlington, "Synthesis of reactance 4-poles wich produce prescribed insertion loss characteristics," *Journal of Mathematics and Physics*, vol. 18, pp. 257 – 353, 1939.

[34] W. E. Kim, "On non-series-parallel realization of driving-point function," in *1958 IRE National Convention*, 1958, pp. 76 – 81.

[35] L. Young, B. M. Schiffman, and E. G. Cristal, "High-power filters for the suppression of spurious frequencies," in *PTGMTT International Symposium Digest*, vol. 64, no. 1, May 1964, pp. 122 – 126.

[36] L. Young, "The design of branch-guide couplers, with applications to the suppression of spurious frequencies," in *PGMTT National Symposium Digest*, vol. 62, no. 1, May 1962, pp. 52 – 57.

[37] ——, "Waveguide 0-db and 3-db directional douplers as harmonic pads," *Microwave Journal*, vol. 7, no. 3, pp. 79 – 87, March 1964.

[38] J. J. McCabe and R. H. Stone, "Survey of high-power microwave filters," *IEEE Transactions on Aerospace and Electronic Systems*, vol. AES-1, no. 2, pp. 84 – 95, October 1965.

[39] L. Young, "Microwave filters to combat RF interference," *IEEE Transactions on Electromagnetic Compatibility*, vol. EMC-10, no. 2, pp. 187 – 196, June 1968.

[40] R. Levy, "Inhomogeneous stepped-impedance corrugated waveguide low-pass filters," in *IEEE MTT-S International Microwave Symposium Digest*, June 2005.

[41] S. B. Cohn, E. M. T. Jones, O. Heinz, J. K. Shimizu, B. M. Schiffman, and F. S. Coale, "Research on design criteria for microwave filters," Stanford Research Institute, Final Report - SRI Project 1331, June 1957.

[42] S. B. Cohn, C. Flammer, E. M. T. Jones, and B. M. Schiffman, "Design criteria for microwave filters and coupling structures," Stanford Research Institute, Tecnical Report 2 - SRI Project 2326, June 1958.

[43] S. B. Cohn, "Broad-band waveguide filter," U.S. Patent 3 046 503, July 24, 1962.

[44] E. D. Sharp, "A high-power wide-band waffle-iron filter," *IEEE Transactions on Microwave Theory and Techniques*, vol. MTT-11, no. 2, pp. 111 – 116, March 1963.

[45] F. Arndt and J. Brandt, "Direct EM based optimization of advanced waffle-iron and rectangular combline filters," in *IEEE MTT-S International Microwave Symposium Digest*, June 2002.

[46] F. Arndt, R. Beyer, W. Hauth, D. Schmitt, and H. Zeh, "Cascaded wide stop band waffle-iron filter designed with a MM/FE CAD method," in *29th European Microwave Conference*, 1999.

[47] M. B. Manuilov and K. V. Kobrin, "Field theory CAD of waffle-iron filters," in *35th European Microwave Conference*, October 2005.

[48] H. J. Carlin, "Darlington synthesis revisited," *IEEE Transactions on Microwave Theory and Techniques*, vol. 46, no. 1, pp. 14 – 21, January 1999.

[49] A. C. Guyette, I. C. Hunter, and R. D. Pollard, "Exact synthesis of microwave filters with nonuniform dissipation," in *IEEE MTT-S International Microwave Symposium Digest*, June 2007, pp. 537–540.

[50] B. S. Senior, I. C. Hunter, and J. D. Rhodes, "Synthesis of lossy filters," in *32nd European Microwave Conference*, October 2002, pp. 1–4.

[51] P. Phudpong and I. C. Hunter, "Nonlinear matched reflection mode bandstop filters for frequency selective limiting applications," in *IEEE MTT-S International Microwave Symposium Digest*, 2007, pp. 1043 – 1046.

[52] V. Miraftab and M. Yu, "Generalized lossy microwave filter coupling matrix synthesis and design," in *IEEE MTT-S International Microwave Symposium Digest*, June 2008, pp. 627 – 630.

[53] V. O. Met, "Microwave filter comprising absorbing structures for removing spurious wave energy," U.S. Patent 3 353 123, November 14, 1967.

[54] D. R. Jachowski, "Cascadable Lossy Passive Biquad Bandstop Filter," in *IEEE MTT-S International Microwave Symposium Digest*, 2006, pp. 1213 – 1216.

[55] C. Mias, "Frequency selective surfaces loaded with surface-mount reactive components," *Electronics Letters*, vol. 39, no. 9, pp. 724 – 726, May 2003.

[56] ——, "Varactor tunable frequency selective absorber," *Electronics Letters*, vol. 39, no. 14, pp. 1060 – 1062, July 2003.

[57] ——, "Electrically-tunable band-stop filter with mechanically variable bandwidth," *Microwave and Optical Technology Letters*, vol. 48, no. 1, pp. 53 – 56, January 2006.

[58] J. R. Wallington, "Absorptive harmonic filters using helical transmission lines," in *1st European Microwave Conference*, 1969.

[59] R. E. Stegens, "Ferrite substrate microwave filter," US Patent 4 297 661, October 27, 1981.

[60] F. Uchikoba, S. Nakajima, T. Ito, T. Miura, M. Kobayashi, T. Kurahashi, and Y. Iijima, "Electronic part using a material with microwave absorbing properties," US Patent 5 847 628, December 8, 1998.

[61] P. Bernardi, "A tunable absorbing band-stop filter: The field rotation filter," *IEEE Transactions on Microwave Theory and Techniques*, vol. 17, no. 2, pp. 62 – 66, February 1969.

[62] S. M. Daoud and P. N. Shastry, “A novel wideband MMIC voltage controlled attenuator with a bandpass filter topology,” *IEEE Transactions on Microwave Theory and Techniques*, vol. 54, no. 6, pp. 2576 – 2583, June 2006.

[63] S. Uysal and J. Watkins, “Novel microstrip multifunction directional couplers and filters for microwave and millimeter-wave applications,” *IEEE Transactions on Microwave Theory and Techniques*, vol. 39, no. 6, pp. 977 – 985, June 1991.

[64] L. Young, “Postscript to two papers on waffle-iron filters (correspondence),” *IEEE Transactions on Microwave Theory and Techniques*, vol. 11, no. 6, pp. 555 – 557, November 1963.

[65] J. Caputo and F. Bell, “Waffle-iron harmonic suppression filter,” *IEEE Transactions on Microwave Theory and Techniques*, vol. 13, no. 5, pp. 701 – 703, September 1965.

[66] L. Young and B. M. Schiffman, “New and improved types of waffle-iron filters,” *Proceedings of the IEE*, vol. 110, pp. 1191 – 1198, July 1963.

[67] S. B. Cohn, “Design relations for the wide-band waveguide filter,” *Proceedings of the IRE*, vol. 38, no. 7, pp. 799 – 803, July 1950.

[68] N. Marcuvitz, *Waveguide Handbook*. McGraw-Hill Book Co, 1951.

[69] D. M. Pozar, *Microwave Engineering*, 3rd ed. John Wiley & Sons, Inc., 2005.

[70] X.-P. Liang, K. A. Zaki, and A. E. Atia, “A rigorous three plane mode-matching technique for characterizing waveguide T-junctions, and its application in multiplexer design,” *IEEE Transactions on Microwave Theory and Techniques*, vol. 29, no. 12, pp. 2138 – 2147, December 1991.

[71] R. Levy, “Aperiodic tapered corrugated waveguide filter,” U.S. Patent 3 597 710, August, 1971.

[72] S. Ramo, J. R. Whinnery, and T. Van Duzer, *Fields and waves in communication electronics*, 3rd ed. John Wiley & Sons, Inc., 1965.

[73] C. Balanis, *Advanced engineering electromagnetics*. John Wiley & Sons, Inc., 1989.

[74] R. A. Goulouev. (Accessed 2009, September) Waffle-Iron Harmonic (Low-Pass) Filters: Why they are so bad. [Online]. Available: http://www.goulouev.com/notes/waffle.htm

[75] J. P. Rooney, “Microwave filter,” US Patent 3 271 706, September 6, 1966.

[76] M. Yu, "Power-handling capability of RF filters," *IEEE Microwave Magazine*, vol. 8, no. 5, pp. 88 – 97, October 2007.

[77] D. Anderson, M. Lisak, and T. Lewin, "Generalized criteria for microwave breakdown in air-filled waveguides," *Journal of Applied Physics*, vol. 65, no. 8, pp. 2935 – 2945, April 1989.

[78] U. Jordan, D. S. Dorozhkina, V. E. Semenov, T. Olsson, D. Anderson, M. Lisak, J. Puech, I. Nefedov, and I. Shereshevskii, "Microwave corona breakdown around metal corners and wedges," *IEEE Transactions on Plasma Science*, vol. 35, no. 3, pp. 542 – 550, June 2007.

[79] E. Weber, *Electromagnetic Fields.* John Wiley & Sons, Inc., 1950.

[80] S. B. Cohn, "Rounded corners in microwave high-power filters and other components," *IRE Transactions on Microwave Theory and Techniques*, vol. 9, no. 5, pp. 389 – 397, September 1961.

[81] A. F. Stevenson, "Theory of slots in rectangular wave-guides," *Journal of Applied Physics*, vol. 19, no. 1, pp. 24 – 34, January 1948.

[82] A. A. Oliner, "The impedance properties of narrow radiating slots in the broad face of rectangular waveguide: Part I," *IRE Transactions on Antennas and Propagation*, vol. 5, no. 1, pp. 4 – 11, January 1957.

[83] G. J. Stern and R. S. Elliott, "Resonant circuit length of longitudinal slots and validity of circuit representation: Theory and experiment," *IEEE Transactions on Antennas and Propagation*, vol. AP-33, no. 11, pp. 1264 – 1271, November 1985.

[84] C.-G. Jan and R.-B. Wu, "Moment method analysis of sidewall inclined slots in rectangular waveguide," *IEEE Transactions on Antennas and Propagation*, vol. 39, no. 1, pp. 68 – 73, January 1991.

[85] B. N. Das, J. Ramakrishna, and B. K. Sarap, "Resonant conductance of inclined slots in the narrow wall of a rectangular waveguide," *IEEE Transations on Antennas and Propagation*, vol. AP-32, no. 7, pp. 759 – 761, July 1984.

[86] L. Josefsson, "Analysis of longitudinal slots in rectangular waveguides," *IEEE Transactions on Antennas and Propagation*, vol. 35, no. 12, pp. 1351–1357, December 1987.

[87] ——, "A waveguide transverse slot for array applications," *IEEE Transactions on Antennas and Propagation*, vol. 41, no. 7, pp. 845 – 850, July 1993.

[88] K. Forooraghi, P. Kildal, and S. R. Rengarajan, "Admittance of an isolated waveguide-fed slot radiating between baffles using a spectrum of two-dimensional solutions," *IEEE Transactions on Antennas and Propagation*, vol. 41, no. 4, pp. 422 – 428, April 1993.

[89] K. Forooraghi, "Analysis of self-admittance of a longitudinal slot radiating into a parallel plate region," *Microwave and Optical Technology Letters*, vol. 1, no. 7, pp. 305 – 308, July 1988.

[90] J. Wettergren and P. Kildal, "Admittance of a longitudinal waveguide slot radiating into an arbitrary cylindrical structure," *IEEE Transactions on Antennas and Propagation*, vol. 43, no. 7, pp. 667 – 673, July 1995.

[91] T. A. Milligan, *Modern antenna design.* McGraw-Hill Book Co, 1985.

[92] A. J. Sangster and H. Wang, "A generalized analysis for a class of rectangular waveguide coupler employing narrow wall slots," *IEEE Transactions on Microwave Theory and Techniques*, vol. 44, no. 2, pp. 283 – 290, February 1996.

[93] I. A. Eshrah, A. A. Kishk, A. B. Yakovlev, and A. W. Glisson, "Generalized equivalent circuit model for transverse waveguide slots and applications," *Progress in Electromagnetics*, vol. 69, pp. 1 – 20, 2007.

[94] T. V. Khac and C. T. Carson, "Coupling by slots into rectangular waveguides with arbitrary wall thickness," *Electronics Letters*, vol. 8, no. 8, pp. 456 – 458, September 1972.

[95] S. R. Rengarajan, "Analysis of centre-inclined waveguide slot coupler," *IEEE Transactions on Microwave Theory and Techniques*, vol. 37, no. 5, pp. 884 – 889, May 1989.

[96] A. A. Oliner, "The impedance properties of narrow radiating slots in the broad face of rectangular waveguide: Part II," *IRE Transactions on Antennas and Propagation*, vol. 5, no. 1, pp. 4 – 11, January 1957.

[97] J. Gulick, G. Stern, and R. Elliot, "The equivalent circuit of a rectangular-waveguide-fed longitudinal slot," in *Antennas and Propagation Society International Symposium*, vol. 24, June 1986, pp. 685–688.

[98] F. L. Whetten and C. A. Balanis, "Meandering long slot leaky-wave waveguide antennas," *IEEE Transactions on Antennas and Propagation*, vol. 39, no. 11, pp. 1553 – 1560, November 1991.

[99] J. C. Coetzee and J. Joubert, "Analysis procedure for arrays of waveguide slot doublets based on the full T-network equivalent circuit representation of radiators," *IEE Proceedings on Microwaves, Antennas and Propagation*, vol. 147, no. 3, pp. 173 – 178, June 2000.

[100] C. J. Reddy, A. Ittipiboon, and M. Cuhaci, "Admittance characteristics of narrow radiating slots in nonradiating dielectric waveguide," *IEE Proceedings-H*, vol. 140, no. 5, pp. 407 – 413, October 1993.

[101] S. N. Sinha, "A generalised network formulation for a class of waveguide coupling problems," *IEE Proceedings-H*, vol. 134, no. 6, pp. 502 – 507, December 1987.

[102] A. Datta, A. M. Rajeek, A. Chakrabarty, and B. N. Das, "S matrix of a broad wall coupler between dissimilar rectangular waveguides," *IEEE Transactions on Circuit Theory*, vol. 43, no. 1, pp. 56 – 62, January 1995.

[103] G. A. Casula, G. Mazzarella, and G. Montisci, "A new circuital model for the longitudinal-transverse waveguide slot coupler," *Microwave and Optical Technology Letters*, vol. 44, no. 4, pp. 313 – 318, January 2005.

[104] I. A. Eshrah, A. A. Kishk, A. B. Yakovlev, A. W. Glisson, and C. E. Smith, "Wide-band lumped element equivalent circuit model for waveguide slots and applications," in *IEEE MTT-S International Symposium Digest*, 2004, pp. 607 – 610.

[105] ——, "Analysis of waveguide slot-based structures using wide-band equivalent-circuit model," *IEEE Transactions on Microwave Theory and Techniques*, vol. 52, no. 12, pp. 2691 – 2692, December 2004.

[106] G. Mazzarella and G. Montisci, "Wideband equivalent circuit of a centered-inclined waveguide slot coupler," *Journal of Electromagnetic Waves and Applications*, vol. 14, pp. 133 – 151, 2000.

[107] A. Abunjaileh, I. Hunter, and A. Kemp, "Application of dual-mode filter techniques to the broadband matching of microstrip patch antennas," *IET Transactions on Microwaves, Antennas & Propagation*, vol. 1, no. 2, pp. 273 – 276, April 2007.

[108] L. H. du Toit, "Analysis and synthesis algorithms for the electric screen Jauman electromagnetic wave absorber," Ph.D. dissertation, University of Stellenbosch, December 1993.

[109] T. Stander, P. van der Walt, P. Meyer, and W. Steyn, "A comparison of simple low-power wedge-type X-band waveguide absorbing load implementations," in *AFRICON 2007*, September 2007, pp. 1 – 4.

[110] Emerson & Cuming Microwave Products N.V., "Eccosorb$^{\mathrm{TM}}$HR-10: Data sheet EB-031," September 2009.

[111] J. M. Reiter and F. Arndt, "Rigorous Analysis of Arbitrarily Shaped H- and E-plane discontinuities in rectangular waveguides by full-wave boundary contour mode-matching method," *IEEE Transactions on Microwave Theory and Techniques*, vol. 4, no. 4, pp. 796 – 801, April 1995.